Exploring New Physics with Top-Quark Pairs: A Neural Network Approach using ATLAS Run-2 Data

Simran Sunil Gurdasani

DOCTORAL THESIS

submitted to
Albert-Ludwigs-Universität Freiburg

Supervisor
Dr. Christian Weiser
Albert-Ludwigs-Universität Freiburg
Physikalisches Institut
Freiburg, 26.04.2024

Supervisor: Dr. Christian Weiser

Research Group: Abteilung Prof. Dr. Karl Jakobs

Date of Defense: 24.06.2024

Dean: Prof. Dr. Günter Reiter

Defense Examiners: Dr. Christian Weiser
Prof. Dr. Markus Schumacher
Prof. Dr. Heidi Rzehak

Dissertation Examiners: Dr. Christian Weiser
Prof. Dr. Marc Schumann

Science makes people reach selflessly for truth and objectivity; it teaches people to accept reality, with wonder and admiration, not to mention the deep awe and joy that the natural order of things brings to the true scientist.

– Lise Meitner, Austrian-Swedish physicist

Abstract

A novel search for particles beyond the standard model produced in association with top-quark pairs using the ATLAS Run-2 pp dataset at $\sqrt{s} = 13\,\text{TeV}$ is presented. Utilising events compatible with a semileptonic decay of top-quark pairs and large missing transverse energy, the study probes direct stop quark production, spin-0 mediators decaying into dark matter particles, and effective contact interactions between top quarks and neutrinos. An innovative and inclusive analysis approach based on neural networks is introduced, enabling sensitivity to a broad spectrum of new physics models without dedicated signal region optimisation. Significant improvements in sensitivity for stop-pair production and spin-0 mediators are achieved. No significant signs of new physics have been found, exclusion limits are thus set on parameters of the simplified models probed. Stop quarks up to 1080 GeV and neutralinos up to 600 GeV are excluded at a 95% confidence level. In searches for top quarks produced in association with dark matter particles, scalar (pseudoscalar) mediators with masses up to 250 (300) GeV are excluded at a 95% confidence level. The study also interprets the data within the framework of effective vector contact interactions between top quarks and neutrinos, setting lower limits on the new physics energy scale Λ between 2.12 TeV and 2.23 TeV.

Kurzfassung

In der vorliegenden Arbeit wird eine neuartige Suche nach Teilchen jenseits des Standardmodells vorgestellt, die in Verbindung mit Top-Quark-Paaren unter Verwendung des ATLAS Run-2 pp-Datensatzes bei $\sqrt{s} = 13\,\text{TeV}$ erzeugt werden. Unter Verwendung von Ereignissen, die mit einem semileptonischen Zerfall von Top-Quark-Paaren und einer großen fehlenden Transversalenergie kompatibel sind, untersucht die Studie die direkte Stop-Quark-Produktion, Spin-0-Mediatoren, die in Dunkle-Materie-Teilchen zerfallen, und effektive Kontaktwechselwirkungen zwischen Top-Quarks und Neutrinos. Es wird ein innovativer und umfassender Analyseansatz auf der Grundlage neuronaler Netze eingeführt, der die Empfindlichkeit für ein breites Spektrum neuer physikalischer Modelle ohne spezielle Optimierung des Signalbereichs ermöglicht. Signifikante Verbesserungen der Sensitivität für die Produktion von Stop-Paaren und Spin-0-Mediatoren werden erzielt. Es wurden keine signifikanten Anzeichen für neue Physik gefunden, daher wurden Ausschlussgrenzen auf Parameter der untersuchten vereinfachten Modelle festgelegt. Stop-Quarks bis zu 1080 GeV und Neutralinos bis zu 600 GeV werden mit einem Vertrauensniveau von 95% ausgeschlossen. Bei der Suche nach $t\bar{t}$+DM werden skalare (pseudoskalare) Mediatoren mit Massen bis zu 250 (300) GeV mit einem Vertrauensniveau von 95% ausgeschlossen. Die Daten werden außerdem im Rahmen einer effektiven Vektor-Kontaktwechselwirkung zwischen Top-Quarks und Neutrinos interpretiert und es werden untere Grenzen für die Energieskala Λ der neuen Physik zwischen 2,12 TeV und 2,23 TeV festgelegt.

Contributions

This thesis presents a search for new physics using top-quark pairs and large missing transverse energy. A novel analysis technique is developed using machine learning methods. Preliminary findings from this analysis were first reported in a conference note [1] and subsequently published in JHEP [2]. This work was undertaken with the direct supervision of Dr. Daniele Zanzi and in collaboration with him, guided by Dr. Christian Weiser at the University of Freiburg. This is a result produced within the ATLAS collaboration, with emphasis on collaboration with the ATLAS SUSY physics analysis group. My individual contributions are outlined below:

1. Developed and implemented a new analysis framework to utilize the DAOD_PHYS generation of samples, including the reconstruction and processing of cut-flows.
2. Optimized pre-selection cuts through detailed studies of the DAOD_PHYS samples, evaluating the performance of different variables. Created plotting scripts for implementing various cut-flows and analysing variable distributions.
3. Conducted a comparative analysis of yields and distributions with previous similar studies, enhancing the signal-to-background ratio by introducing more complex variables.
4. Designed and set up a neural network architecture tailored for the analysis. Established a framework for data preparation, training, and evaluation of network performance.
5. Optimized the neural network design by evaluating different configurations to determine the optimal number of networks to be used in the analysis.
6. Defined Control, Validation, and Signal Regions based on the neural network scores to facilitate the analysis.
7. Implemented and executed the statistical analysis for interpretation of data in search of SUSY and DM models using the HistFitter framework.
8. Developed the statistical model employed for the interpretation and investigation of results.
9. Implemented and executed exclusion fits for $t\bar{t}\nu\bar{\nu}$ contact interactions.
10. Prepared results for integration into both the ATLAS SUSY and DM Run-2 combination results.

Several plots and tables presented in Chapters 5 and 6 are duplicated in both the JHEP publication [2] and this thesis. For the plots and tables that I created, the captions include ‘also published in [2]’. For those produced by other members of the ATLAS collaboration, the captions state ‘taken from [2]’, consistent with how other images and tables sourced from external papers are cited throughout the thesis.

Freiburg, September 2024
Simran Gurdasani

Contents

CHAPTER 1

Introduction

Humankind has tried for centuries to answer the very fundamental question of what the universe is truly made of. Theoretical efforts and experiments have yielded the Standard Model of Particle Physics, a theory which best describes the fundamental particles and interactions known today.

This state of the art theory has been probed to extreme precision by different experiments, the one providing by far the highest energies is the Large Hadron Collider (LHC) at CERN. However, there are also growing indications that the model is incomplete. Astrophysical evidence shows that the matter that is currently understood makes up only 5% of the content of the universe and is called “baryonic” matter. The rest of the content of the universe is made up of Dark Matter and Dark Energy, both of which are currently not understood.

In addition, masses of the different particles in the standard model and the scales at which the interactions become significant are spread over many orders of magnitudes, the cause of which is not well understood. Multiple proposals exist to extend the standard model to more complete theories that are mathematically well motivated.

Experimental observations are needed to shed light on the underlying theories that aim to better describe the universe. As an example, the LHC does this by smashing together protons at very high energies to probe the fundamental interactions of nature. The results of these fundamental interactions are "photographed" by different experiments at the LHC including the ATLAS experiment. This thesis uses data collected with the ATLAS detector to probe two models Beyond the Standard Model (BSM), namely particle natured dark matter and Supersymmetry.

The thesis begins with an introduction into the intricacies of the SM, introducing its known particles, interactions, and the mathematical formulation. The symmetries that underpin the SM are explored and the compelling reasons that drive physicists to search for theories that extend beyond this model are discussed. Among these extensions, Supersymmetry stands out for its potential to resolve some of the most pressing issues with the SM, including the stabilisation of the Higgs mass and the unification of forces. This is followed by the "WIMP

Miracle" and simplified models that attempt to explain the nature of dark matter and its interactions with ordinary matter.

Moving from theory to experimentation, Chapter 3 introduces the European Organization for Nuclear Research (CERN) and the LHC. This chapter provides an overview of the proton-proton physics at the LHC and focuses on the ATLAS experiment, one of the major experiments at the collider. The design and capabilities of the ATLAS detector, as well as the techniques employed in data collection and simulation are discussed.

With the stage set, Chapter 4 outlines the strategy employed to search for new physics using ATLAS data. The challenges associated with such searches are discussed and the use of top-quark pairs and missing transverse energy ($t\bar{t}$ $+E_{\mathrm{T}}^{\mathrm{miss}}$) as probes for new physics phenomena are highlighted. To tackle the complexity of data analysis, Chapter 4.3 introduces a machine learning solution, specifically neural networks. Following this, neural networks are motivated as an optimal solution to improve reconstruction of hadronically decaying top quarks and additionally to discern events that describe new physics process from known physics processes.

Chapter 5 presents the core of this thesis, detailing the search for DM production interpreted with simplified dark matter models and stop-quark pair production as a signature for Supersymmetry. Previous searches for these particles were reported by the ATLAS [3–6] and CMS [7–10] Collaborations using the Run-2 LHC pp dataset, collected in the years 2015-2018. The improvements are performed on the final state involving one lepton, previously studied in [4]. These strategies show improvements upon the results in [4] by using novel analysis techniques while probing the same dataset. These improvements are discussed including event classification using neural networks, emphasising their effectiveness in distinguishing between known physics processes and new ones. It also includes background modelling studies, statistical analysis, and concludes with a presentation of the results obtained.

Chapter 6 delves into the Effective Field Theory (EFT) interpretation, specifically focusing on $t\bar{t}\nu\bar{\nu}$ contact interactions. This chapter introduces the EFT approach and its application to the study of top-quark pair interactions with neutrinos. It discusses the theoretical background, the formulation of the contact interaction model, and presents the results of the analysis. Finally, Chapter 7 concludes the thesis by showcasing the obtained results, comparing them to previous findings and highlighting the improvements that made the improved results possible.

CHAPTER 2

The Standard Model, Supersymmetry and Dark Matter

Starting with a very brief introduction of the Standard Model (SM) of Particle Physics, this chapter provides the nomenclature of the current known particles and interactions to be used in this thesis. This is followed by a motivation to go Beyond the SM (BSM) and provides a theoretical background for the BSM theories probed in this thesis, specifically solutions to Dark Matter observations and Supersymmetry. Supersymmetry is presented as an elegant solution to the naturalnesses problem, while offering solutions to other open particle physics problems. Astrophysical evidence is shown as a leading argument for the existence of dark matter, followed by the motivation for a Weakly Interacting Massive Particle (WIMP) as a particle solution to Dark Matter.

2.1 Known Particles and Interactions

The SM is an extremely well-tested theory that describes the known particles and interactions in the universe. It is a mathematical framework, guided by special relativity and quantum mechanics, that best explains the ‘particle zoo’ that emerged in the 20th century as a result of many fundamental physics experiments. This explanation of the SM starts with an introduction to the particle content of the SM, based on [11], and is followed by an overview of the fundamental interactions the SM can explain.

The particles in the SM are all ‘elementary’ or ‘fundamental’, meaning that they cannot be broken down any further according to our current understanding. The SM categorises known fundamental particles into two main categories: fermions and bosons. Fermions make up all the known particle matter in the universe, have half-integer spin and follow Fermi-Dirac statistics. Bosons transmit fundamental forces between fermions, have integer spin and follow Bose-Einstein statistics. Three out of the four fundamental forces, namely the weak, electromagnetic and strong force are described within the SM as interactions, however, it does not provide a description of gravity. Additionally, for every particle, there exists an anti-particle that has the opposite charge[1] as compared to the particle.

Fermions comprise of leptons and quarks, each of which consist of three generations and are defined by their charge, Q, lepton number, L_X, or quark flavour and mass as listed in Table 2.1 and Table 2.2. Each fermion has a partner anti fermion that has the opposite sign of lepton number or quark flavour and charge. Each lepton generation consists of a charged, massive lepton and a corresponding neutral, very light neutrino[2]. Each quark generation has a down-type quark with charge $-1/3e$ and up-type quark with charge $+2/3e$ where e denotes the absolute value of the electron charge.

Table 2.1: Leptons in the SM [11, 12].

	Generation	**Particle**	**Q (e)**	**Lepton Number**			**Mass (MeV/c^2)**
				L_e	L_μ	L_τ	
Leptons	1st	e^-	-1	1	0	0	~ 0.5
		ν_e	0	1	0	0	$< 2 \cdot 10^{-6}$
	2nd	μ^-	-1	0	1	0	~ 106
		ν_μ	0	0	1	0	$< 2 \cdot 10^{-6}$
	3rd	τ^-	-1	0	0	1	~ 1777
		ν_τ	0	0	0	1	$< 2 \cdot 10^{-6}$

Table 2.2: Quarks in the SM [11, 12].

	Generation	**Particle**	**Q (e)**	**Quark Flavour**						**Mass (MeV/c^2)**
				D	U	S	C	B	T	
Quarks	1st	d	$-1/3$	-1	0	0	0	0	0	~ 5
		u	$+2/3$	0	1	0	0	0	0	~ 2
	2nd	s	$-1/3$	0	0	-1	0	0	0	~ 95
		c	$+2/3$	0	0	0	1	0	0	~ 1270
	3rd	b	$-1/3$	0	0	0	0	-1	0	~ 4180
		t	$+2/3$	0	0	0	0	0	1	~ 172700

Quarks have, additionally, a colour charge that leptons do not posses, yielding that each quark (anti-quark) has a red (anti-red), green (anti-green) and blue (anti-blue) version. While leptons are found to exist as individual particles, quarks have never been found to exist alone.

---

[1] While this refers most commonly to electric charge, it can also be an opposite helicity, baryon number or other physical charges.

[2] Although neutrinos are considered to be massless in the SM, neutrino oscillations, recognised by the 2015 Nobel Prize in Physics, have proven that neutrinos must have mass.

Instead, they are found to exist in colourless bound states of a quark-antiquark pair, called a meson, or three quarks (anti-quarks) each with a different colour adding up to no overall colour, called a baryon (anti-baryon). More exotic states of quarks, such as the pentaquark ($qqqq\bar{q}$) and the tetraquark ($qq\bar{q}\bar{q}$) exist additionally.

The masses of quarks and leptons increase from the 1st generation to the 3rd generation. All known matter in the universe consists of atoms that are made out of protons, neutrons and electrons, wherein protons and neutrons are colour neutral hadrons made up of up and down quarks. Hence, the 1st generations of leptons and quarks make up stable matter, while the heavier generations of leptons — which require higher energies to be produced — have been discovered by a myriad of particle physics experiments.

The SM consists additionally of spin-1 gauge bosons, that mediate the fundamental forces and the spin-0 Higgs boson, which is not a gauge boson, but is instead a quantum excitation of the Higgs field, all of which are listed in Table 2.3.

Table 2.3: Bosons in the SM [11, 12].

Force	**Mediator**	**Charge**	**Mass (GeV/c^2)**
Electromagnetic	Photon (γ)	0	0
Weak	W boson ($W^{\pm}$)	± 1	~ 80.4
	Z boson (Z)	0	~ 91.2
Strong	Gluons (g)	0	0
-	Higgs boson (H)	0	~ 125

- The electromagnetic force is mediated by the massless **photon**. Although massless, it carries energy and momentum and interacts with charged particles. These interactions are described by the theory of Quantum Electrodynamics (QED).
- The weak force is mediated by the $\boldsymbol{W^{\pm}}$ and $\boldsymbol{Z}$ **bosons**. Weak interactions are described by quantum flavour dynamics, allowing quarks and leptons to change flavour. An example of this is the β^- decay where a neutron (udd) is converted into a proton (uud) resulting in an emission of an electron and electron anti-neutrino, made possible by W bosons that allow the down quark to change flavour into an up quark.
- The strong force is mediated by eight **gluons**, which are massless and electrically neutral but carry colour charge. These interactions are described by Quantum Chromodynamics (QCD).
- The **Higgs boson** does not mediate a fundamental physics force and is the only scalar boson in the SM.

2.1.1 Theoretical Framework

The SM is built upon the foundation of symmetries, relying on the concept in Noether's theorem [13] that for every continuous symmetry of nature there is a corresponding conservation law. This is realised mathematically with the principle of local gauge symmetry using group theory.

The overall gauge symmetry group of the SM is given by $SU(3)_C \times SU(2)_L \times U(1)_Y$. Specifically, the non-Abelian $SU(3)_C$ gauge symmetry governs the strong interaction between quarks and eight massless gluons, wherein the conserved quantity is the colour charge (C). The electromagnetic and weak interactions are described by a unified $SU(2)_L \times U(1)_Y$ gauge symmetry, wherein weak isospin (I_3) and hypercharge (Y) are conserved. The unified electromagnetic and weak interaction is mediated by the photon and the $W^\pm$ and Z bosons.

Within the gauge groups, the fermions are described by spinor fields that can be further decomposed into left and right-handed components, known as chiral eigenstates. Fermion fields in the SM transform under the gauge symmetries. The fermions depicted by left and right-handed fermion fields can have different interactions and their interactions with gauge bosons are determined by the gauge coupling constants, which encode the strength of the interactions. For example, in $SU(2)_L$ the 'L' stands for left-handed, as a consequence of which only the left-handed chirality part of the fields interact with the $W^\pm$ bosons.

Electroweak Unification

The electromagnetic and weak force were recognised to be manifestations of the same underlying force and are today together called the electroweak force [14, 15]. Within this unification, the bosons associated with the $SU(2)_L$ and $U(1)_Y$ gauge symmetries are the W_1, W_2, W_3 bosons for $SU(2)_L$ and the B_0 boson for $U(1)_Y$. The W_1 and W_2 bosons are the charged components that are responsible for charged current weak interactions (like β^- decay). These W_1 and W_2 bosons mix to give $W^\pm$ as follows:

$$W^\pm = \frac{1}{\sqrt{2}}(W_1 \mp iW_2). \tag{2.1}$$

The W_3 is a neutral weak boson but could not be the Z boson, because interactions between the Z boson and right-chiral fermion fields were already observed and W_3 being a carrier of the $SU(2)_L$ was hypothesised to interact solely with left-chiral fields. In the electroweak unification, the two neutral gauge bosons, γ and Z^0, are expressed as a linear combination of W_3 and B_0:

$$\begin{pmatrix} Z \\ \gamma \end{pmatrix} = \begin{pmatrix} \cos(\theta_W) & -\sin(\theta_W) \\ \sin(\theta_W) & \cos(\theta_W) \end{pmatrix} \begin{pmatrix} W_3 \\ B_0 \end{pmatrix}, \tag{2.2}$$

where θ_W is the electroweak mixing angle, also known as the Weinberg angle. This angle has been measured precisely across a range of experiments and is an important parameter of the SM. Within this unification, the matter fermions in the SM are organised into weak isospin doublets under $SU(2)_L$ and isospin singlets under $U(1)_Y$. Each lepton and quark generation consists of one left-handed isospin doublet of an uncharged neutrino or charge $\frac{2}{3}$ up-type quark (all having $I_3 = \frac{1}{2}$) and charge -1 lepton or charge $-\frac{1}{3}$ down-type quark (all having $I_3 = -\frac{1}{2}$), and right-handed isospin singlets with $I_3 = 0$.

Mass Generation

Mass is introduced in the SM through two main mechanisms: Spontaneous Symmetry Breaking (SSB) and Yukawa couplings. The masses of the gauge bosons in the SM are generated by the spontaneous breaking of the electroweak $SU(2)_L \times U(1)_Y$ gauge symmetry via the introduction of a scalar $SU(2)_L$ doublet field, known as the Higgs field. The Brout-Englert-Higgs (BEH) mechanism [16–21] is responsible for giving masses to the $W^\pm$ and Z bosons. The Glashow-Weinberg-Salam (GWS) model, incorporates the BEH mechanism into the electroweak theory explaining how the gauge bosons acquire mass [14, 15, 22]. For the fermions, the Yukawa couplings between the Higgs field and the fermions generate their masses [23].

The SM Lagrangian

The dynamics of the SM can be described by the SM Lagrangian, drawing upon the detailed formulations provided in [24–27]. As a foundational example, the Quantum Electrodynamics (QED) Lagrangian is introduced. The fermions, are represented by spinors ψ. The dynamics of free fermions are described by the Dirac Lagrangian as follows:

$$\mathscr{L}_{\text{Dirac}} = \bar{\psi}(i\gamma^\mu \partial_\mu - m)\psi, \tag{2.3}$$

where $\bar{\psi} = \psi^\dagger \gamma^0$ is the Dirac adjoint, $i\gamma^\mu \partial_\mu$ is the Dirac operator, and m is the mass of the fermion. The QED Lagrangian is then formulated using $\mathscr{L}_{\text{Dirac}}$ as follows:

$$\mathscr{L}_{\text{QED}} = \mathscr{L}_{\text{Dirac}} - q\bar{\psi}\gamma^\mu \psi A_\mu - \frac{1}{4}F_{\mu\nu}F^{\mu\nu}. \tag{2.4}$$

Ensuring local gauge invariance of the Lagrangian for the Dirac spinor under the underlying $U(1)$ symmetry leads to the introduction of the spin-1 gauge field A_μ which corresponds to the photon field. The second term describes interactions of fermions with the photon, wherein q gives the charge of the fermion. The last term is the photon's kinematic term that is invariant under local gauge variance for a massless gauge field. Extending this definition, the electroweak Lagrangian is defined with the covariant derivative D_μ^{EW} redesigned for the electroweak symmetry group:

$$\mathscr{L}_{\text{EW}} = i\bar{\psi}_f \gamma^\mu D_\mu^{\text{EW}} \psi_f - \frac{1}{4}W_{\mu\nu}^a W^{a\mu\nu} - \frac{1}{4}B_{\mu\nu}B^{\mu\nu}, \tag{2.5}$$

where ψ_f runs over all the fermions and the gauge fields B_μ and W_μ^a (with $a = 1,2,3$) are associated with the $U(1)$ and $SU(2)$ symmetries, respectively. With the introduction of gluons in $SU(3)$, the overall Lagrangian is redefined to include EW and QCD interactions.

It is defined with the covariant derivative D_μ redesigned for the $SU(3)_C \times SU(2)_L \times U(1)_Y$ symmetry group:

$$\mathscr{L} = i\bar{\psi}_f \gamma^\mu D_\mu \psi_f - \frac{1}{4}B_{\mu\nu}B^{\mu\nu} - \frac{1}{4}W^a_{\mu\nu}W^{a\mu\nu} - \frac{1}{4}G^a_{\mu\nu}G^{a\mu\nu} \tag{2.6}$$

$$= \mathscr{L}_{\text{fermion}} \quad + \mathscr{L}_{\text{gauge}}, \tag{2.7}$$

where ψ_f runs through all left and right-handed fermions. The gauge fields B_μ, W^a_μ (with $a = 1,2,3$), and G^a_μ (with $a = 1,\ldots,8$) are associated with the $U(1)$, $SU(2)$, and $SU(3)$ symmetries, respectively. Along with the addition of the Higgs field, the full SM Lagrangian is given as:

$$\mathscr{L}_{\text{SM}} = \mathscr{L}_{\text{fermion}} + \mathscr{L}_{\text{gauge}} + |D_\mu \phi|^2 - V(\phi) + \bar{\psi}_i y_{ij} \psi_j \phi + \text{h.c.} \tag{2.8}$$

$$= \mathscr{L}_{\text{fermion}} + \mathscr{L}_{\text{gauge}} + \mathscr{L}_{\text{Higgs}} \qquad + \mathscr{L}_{\text{Yukawa}}, \tag{2.9}$$

The term $|D_\mu \phi|^2$ describes the couplings between the Higgs boson and gauge bosons, whereas the term $V(\phi)$ represents the Higgs potential and its self-interactions. The term $\bar{\psi}_i y_{ij} \psi_j \phi$ generates masses for fermions based on their Yukawa couplings y_{ij} to the Higgs field ϕ. The last term hermitian conjugate (h.c) generates masses for anti-fermions. More specifically, the Yukawa interaction terms can be broken down into specific terms that give masses to charged leptons, up-type quarks and down-type quarks as follows:

$$\mathscr{L}_{\text{Yukawa}} = \mathscr{L}_{\text{lepton}} + \mathscr{L}_{\text{up}} + \mathscr{L}_{\text{down}}, \tag{2.10}$$

$$\mathscr{L}_{\text{lepton}} = -\bar{L}_i y^e_{ij} e_{Rj} \phi + \text{h.c.}, \tag{2.11}$$

$$\mathscr{L}_{\text{up}} = -\bar{Q}_i y^u_{ij} u_{Rj} \phi + \text{h.c.}, \tag{2.12}$$

$$\mathscr{L}_{\text{down}} = -\bar{Q}_i y^d_{ij} d_{Rj} \phi + \text{h.c.}, \tag{2.13}$$

and L_i and Q_i are the lepton and quark doublets, e_{Ri}, u_{Ri}, and d_{Ri} are the right-handed charged lepton and up-type and down-type quark singlets, respectively. The Yukawa coupling matrices are y^e_{ij}, y^u_{ij}, and y^d_{ij} for the lepton, up-type, and down-type quarks, respectively.

2.1.2 The need to go Beyond the Standard Model

Although the SM has been immensely successful in describing the known particles and interactions, it does have some limitations leading to the possibility that it may be incomplete. These limitations can be described in two categories, namely theoretical limitations and those where experimental observations cannot be explained by the SM alone.

Starting with the theoretical limitations, although the SM successfully describes three of the four fundamental forces, it does not unify them into a single theoretical framework. The running of the couplings shows that a unified description of the electromagnetic and weak forces is possible, but the strong force remains out of reach. One goal of a modified SM theory would be **to unify all three forces**. Gravity, however, is still very far out of reach, as it only acquires the strength of the other forces at the Planck scale. This leads to the next theoretical limitation within the SM, in the sense that it does not provide a natural explanation for the vast difference in scales, called the **hierarchy problem**. Since the discovery of the Higgs boson, this problem has been somewhat sharpened.

The observed Higgs mass emerges as the sum of two components: the bare Higgs mass and the collective influence of quantum corrections contributed by other SM particles. To maintain the observed Higgs mass, the bare Higgs mass and quantum corrections have to cancel to an extreme degree, which implies a significant level of the so-called "fine-tuning" within the SM. This, although possible, is often considered mathematically unsatisfactory and called the SM '**naturalness**' problem. If this fine-tuning is not just an extremely coincidental feature of the natural universe, it can be solved by new BSM theories. One way is to introduce new particles, like is done in supersymmetry. Another way is to postulate the presence of extra dimensions, inspired by string theory, that modify gravity at small scales. Yet other solutions postulate that the Higgs boson is not a fundamental particle but emerges as a composite bound state of more fundamental constituents.

On the experimental side, one of the biggest open questions is the nature of **Dark Matter** (DM). According to the standard ΛCDM model of cosmology, the mass–energy content of the universe is $\sim$5% ordinary ('baryonic') matter, $\sim$27% dark matter, and $\sim$68% dark energy [28]. So far, dark matter has only been observed indirectly, through its possible gravitational interactions. Although the nature of DM is unknown so far, theoretical models describing DM to have particle nature can complete the SM and solve the so-called "missing mass" problem. Dark energy, comprises the majority of the universe's energy density and contributes to the universe's accelerating expansion but cannot be explained within the framework of the SM.

The universe also exhibits a **matter-antimatter asymmetry**, with more matter than antimatter. While the SM predicts a small imbalance, brought about by CP violation, the observed imbalance is larger, indicating that additional mechanisms are at play. **Neutrino oscillations** are another deviation from the SM. Initially thought to be massless, neutrinos have been found to oscillate between flavours, implying non-zero masses. **Anomalies** in experimental data, which don't align with SM predictions, continually challenge the theory.

These open questions have motivated the landscape of Beyond Standard Model (BSM) physics leading to BSM ideas, theories and searches. In this thesis Supersymmetry (SUSY) is probed as an answer to a combination of theoretical and experimental open questions. Additionally, a search for DM that could be produced at colliders like the LHC is performed.

2.2 Supersymmetry → a Better Standard Model?

The idea of symmetries, as seen in Section 2.1.1, has been fundamental in the formulation of the SM. Supersymmetry is the idea of introducing a new symmetry between fermions and bosons to extend the SM. This symmetry posits that for every elementary particle in the SM, there exists a superpartner differing in spin by a magnitude of 1/2. Every fermion has a bosonic, scalar superpartner, identified by putting a 's' in front of the name, yielding squarks and sleptons. Similarly, every boson has a fermionic superpartner, identified by putting an 'ino' at the end of the name yielding gluinos, winos etc. This section first motivates why a supersymmetrisation of the SM could lead to a better SM and follows up with the theoretical framework used to do so. The specific process of pair production of stop quarks, probed in this thesis, is then motivated and the phenomenology introduced.

2.2.1 Motivations

By introducing superpartners for SM particles, SUSY provides a unified description of the electromagnetic, weak, and strong forces at high energies as depicted in Figure 2.1. This unification is possible if the SUSY masses are of $\mathcal{O}(1\,\text{TeV})$ and have two Higgs doublets [29].

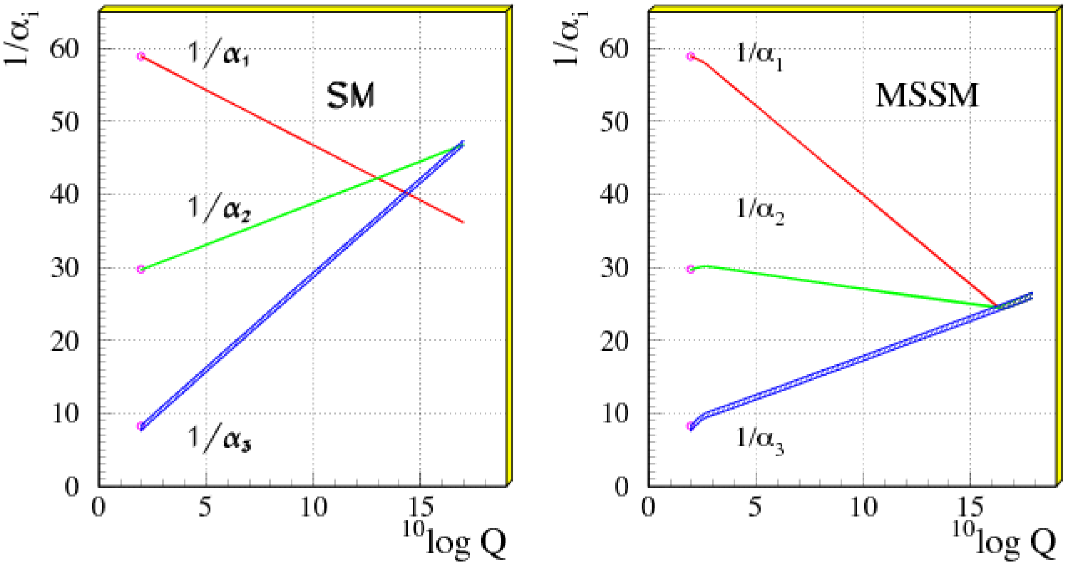

Figure 2.1: Evolution of the inverse coupling constants in the SM and MSSM. Unification is achieved only in the MSSM. SUSY particles are considered to contribute above the effective SUSY scale ($M_{\text{SUSY}} \approx 1\,\text{TeV}$), leading to a change in the coupling evolution slope, taken from [30].

SUSY can also stabilise the Higgs boson mass, m_0, against quantum corrections, addressing the fine-tuning problem inherent in the SM [31]. The quantum corrections to the Higgs mass due to a fermion field and a scalar field can be visualised as in Figure 2.2.

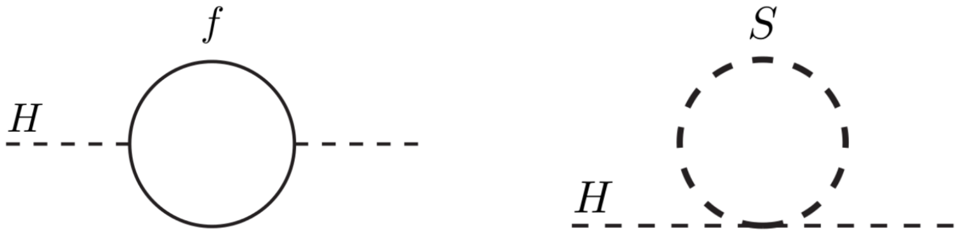

Figure 2.2: First-order quantum corrections to the Higgs propagator are represented by loops, with different contributions from fermion (left) and scalar (right) fields.

Considering a loop involving a Dirac fermion f with mass m_f and a λ_f coupling to the Higgs boson, its contribution to the physical Higgs boson mass, m_h, can be expressed as follows:

$$m_h^2 = m_0^2 - \frac{|\lambda_f|^2}{8\pi^2}\Lambda^2 + \ldots \tag{2.14}$$

where, m_0 is the bare Higgs mass and Λ serves as a momentum cut-off, representing the energy scale at which new physics might modify the high-energy behaviour of the theory. If a heavy scalar particle S exists with mass m_S and a λ_S coupling to the Higgs boson, its contribution to the Higgs mass is:

$$m_h^2 = m_0^2 + \frac{\lambda_S}{16\pi^2}[\Lambda^2 - 2m_S^2 \ln(\frac{\Lambda}{m_S}) + \ldots] \tag{2.15}$$

Each stop quark has coupling $\lambda_{\tilde{t}}$, and $\lambda_{\tilde{t}} = \lambda_t^2$ where λ_t is the top quark coupling. Hence, the leading terms cancel naturally. Specifically, the contribution from the top quark (t) is cancelled by the contribution from its two superpartners ($\tilde{t}_1, \tilde{t}_2$). In some scenarios, SUSY can also provide a natural candidate for DM. This candidate possesses all the desired qualities of a WIMP particle and aligns with observational evidence of dark matter abundance in the universe. Although the discovery of SUSY generated WIMPs satisfying the entire relic density would point to a very minimal dark sector, populated by only one type of particle, it would serve as a good starting point for DM searches.

2.2.2 Theoretical Framework

To mathematically use SUSY to extend the SM, a generator is required that connects fermions and bosons such as:

$$Q|\text{fermion}\rangle \propto |\text{boson}\rangle, \quad Q|\text{boson}\rangle \propto |\text{fermion}\rangle. \tag{2.16}$$

If the fermion-boson symmetry (supersymmetry) existed without being broken, the SM particles and their superpartners would be identical in mass, however this has been ruled out by experimental observations. Hence, this supersymmetry must be broken. The exact mechanism by which this is achieved is unknown. However, different SUSY breaking mechanisms can be possible in different models.

To search for SUSY at colliders, often the Minimal Supersymmetric Standard Model (MSSM) is employed. It provides a minimal particle content while using the idea of SUSY to extend the SM as summarised in Table 2.4. The MSSM is generally a low-energy realisation of SUSY making it more likely be accessible at the LHC. To build the MSSM, each left and right-handed SM fermion receives a corresponding spin-0 sparticle. The superpartners of the electroweak bosons are the binos and winos as they are generated before electroweak symmetry breaking when the fields W_1, W_2, W_3 and B_0 exist. For the Higgs boson, SUSY first extends the SM Higgs sector[3] to contain two complex Higgs doublets yielding five Higgs bosons[4], the lightest of which matches properties of the observed scalar Higgs particle. Superpartners of the Higgs are called Higgsinos [32].

Table 2.4: Particle Content generated by SUSY.

Particle (mass eigenstate)		**SUSY particle (flavour eigenstate)**	
Spin-1/2	quark	squark_L, squark_R	Spin-0
	lepton	slepton_L, slepton_R	
	neutrino	$\text{sneutrino}_\text{L}$	
Spin-1/2	γ	Bino	Spin-1/2
	Z^0	Wino^0	
	$W^\pm$	$\text{Wino}^\pm$	
	g	gluino	
Spin-0	Extended Higgs sector h^0,H^0,A^0,$H^\pm$	Higgsinos	

Although the particle content in the MSSM is minimal, it can have still a huge number of free parameters, especially those originating from the SUSY breaking mechanism [33]. Some parts of the parameter space can yield unphysical results. Fortunately, one can use assumptions

---

[3] This allows the generation of masses of the up and down-type quarks without creating anomalies.

[4] The two complex Higgs doublets contain eight real fields. Three of these fields provide the longitudinal degrees of freedom for the massive $W^\pm$ and Z bosons leaving five Higgs fields.

motivated by precision SM measurements to constrain the huge parameter space of the MSSM. This is done using the phenomenological MSSM (pMSSM) framework. For example, many of the free parameters in the MSSM result in flavour violation which has not been observed in experiments. For this a minimum flavour violating hypothesis is often invoked [34].

Another example is that, in the SUSY superpotential (part of $\mathscr{L}_{\text{SUSY}}$), general terms occur that violate lepton number L, and baryon number B. In the SM, B and L are conserved accidentally, meaning that this conservation is not enforced from fundamental principles but occurs as a by-product of the symmetries of the SM. Violation of B and L, as it occurs in the MSSM, would mean that proton decay is possible, which has still not been experimentally observed. To this end, an additional quantum number, R-parity, is often introduced as a function of B, L and particle spin S:

$$R = (-1)^{3(B-L)+2S} \tag{2.17}$$

With this definition, all SM fermions and bosons are R-parity even, while all SUSY particles (squarks, sleptons, gauginos and higgsinos) are R-parity odd [31]. Requiring R-parity conservation allows for B and L to be conserved in the SM without explicitly enforcing B and L conservation in the MSSM.

As a consequence of R-parity conservation, a stable LSP or Lightest Supersymmetric Particle exists. Additionally, all other supersymmetric particles, known as sparticles, must ultimately decay into the stable LSP. This serves as a dark matter candidate that is then naturally part of the MSSM. Furthermore, R-parity conservation also means that sparticles are produced in pairs, influencing the experimental signatures observable in experiments. It is important here to note, that R-parity conservation is not required fundamentally in an extension of the standard model. Searches are performed for both R-parity conserving and violating scenarios. In this thesis, the R-parity conserving case is considered.

The particle content of the MSSM is described by superfields, which are mathematical constructs that encapsulate both the SM particles and their superpartners. Similar to the SM, the dynamics of all superfields are governed by the SUSY Lagrangian, denoted as $\mathscr{L}_{\text{SUSY}}$. To break SUSY in the MSSM, "soft" breaking terms are added to the SUSY Lagrangian by hand giving the sparticles masses [35]. The soft breaking parameters consist of masses, phases and mixing angles.

$$\mathscr{L}_{\text{MSSM}} = \mathscr{L}_{\text{MSSM, unbroken}} + \mathscr{L}_{\text{soft}} \tag{2.18}$$

Once SUSY is broken by hand in the MSSM, the superpartners can undergo mixing. The superpartners of heavy SM fermions, $\tilde{f}_{L,R}$ mix to give $\tilde{f}_{1,2}$ wherein the index shows the mass ordering. For example, the superpartners of the top quark, $\tilde{t}_{L,R}$ mix to give mass eigenstates $\tilde{t}_{1,2}$, wherein $m_{\tilde{t}_1} < m_{\tilde{t}_2}$ by convention. Similarly, the neutral (charged) winos, binos and higgsinos mix to give four neutralinos (two charginos). The mass eigenstates are defined in terms of the parameters that describe the pMSSM. For example, the gaugino superfields in the MSSM are defined as follows:

$$\begin{pmatrix} \chi_1^{\pm} \\ \chi_2^{\pm} \end{pmatrix} = \begin{pmatrix} M_2 & \sqrt{2} m_W \sin\beta \\ \sqrt{2} m_W \cos\beta & \mu \end{pmatrix} \cdot \begin{pmatrix} \tilde{W}^{\pm} \\ \tilde{H}^{\pm} \end{pmatrix} \tag{2.19}$$

$$\begin{pmatrix} \chi_1^0 \\ \chi_2^0 \\ \chi_3^0 \\ \chi_4^0 \end{pmatrix} = \begin{pmatrix} M_1 & 0 & -m_Z \cdot s_W \cdot c_\beta & m_Z \cdot s_W \cdot s_\beta \\ 0 & M_2 & m_Z \cdot c_W \cdot c_\beta & -m_Z \cdot c_W \cdot s_\beta \\ -m_Z \cdot s_W \cdot c_\beta & m_Z \cdot c_W \cdot c_\beta & 0 & -\mu \\ m_Z \cdot s_W \cdot s_\beta & -m_Z \cdot c_W \cdot s_\beta & -\mu & 0 \end{pmatrix} \cdot \begin{pmatrix} \tilde{B} \\ \tilde{W}^3 \\ \tilde{H}_1^0 \\ \tilde{H}_2^0 \end{pmatrix} \tag{2.20}$$

Here, M_1 and M_2 are the gaugino mass parameters responsible for soft-SUSY breaking, μ is the Higgsino mass parameter[5], M_W is the W boson mass, M_Z is the Z boson mass. The parameters c_W and s_w stand for $\sin\theta_W$ and $\cos\theta_W$ and c_β and s_β stand for $\sin\beta$ and $\cos\beta$, wherein θ_W is the weak mixing angle, and $\tan\beta$ is the ratio of the vacuum expectation values of the two Higgs doublets. Different choices of parameters in the pMSSM parameter space lead to different mass spectra in the MSSM. The LSP introduced earlier is often a neutralino within this mass spectrum.

2.2.3 Stop-Quark Pair Production

At the onset of squark searches at the LHC, it seemed plausible that all three generations of squarks would be light enough to be produced at the LHC. However, as more of the parameter space was probed along with a lack of evidence in experimental signatures, modifications to the SUSY theory space became necessary. Solutions exist to push squark masses to above the limits set so far, however, the motivation for the stop quark to remain light has remained. Since the top quark provides large quantum corrections to the Higgs mass, the stop quark must be light and cancel for SUSY to remain a viable solution to the “fine-tuning” problem [31]. If stop quarks are to be produced within an RPC SUSY model, they must occur in pairs and eventually decay into the stable LSP, providing a DM candidate. Given these motivations, the pair production of stop-quarks is probed in this thesis.

For stop quarks to be produced as a result of proton-proton collisions, all modes of production where quarks and gluons interact to directly produce a stop-antistop pair are considered. This is possible provided the combined mass of the two stop quarks does not exceed the centre-of-mass energy of the LHC. The dominant production channels at lowest order are shown in Figure 2.3.

The decay mode of the stop quark depends on the mass spectrum of particles set by parameters of the pMSSM. In most spectra, the stop quark is the lightest sfermion and the charginos and neutralinos can have a range of masses below and above that of the stop quark. This gives rise to decay chains where the stop quark decays to the LSP with possible

---

[5] the size of the supersymmetry conserving mu-parameter must be correlated with the size of the soft supersymmetry breaking parameters [36].

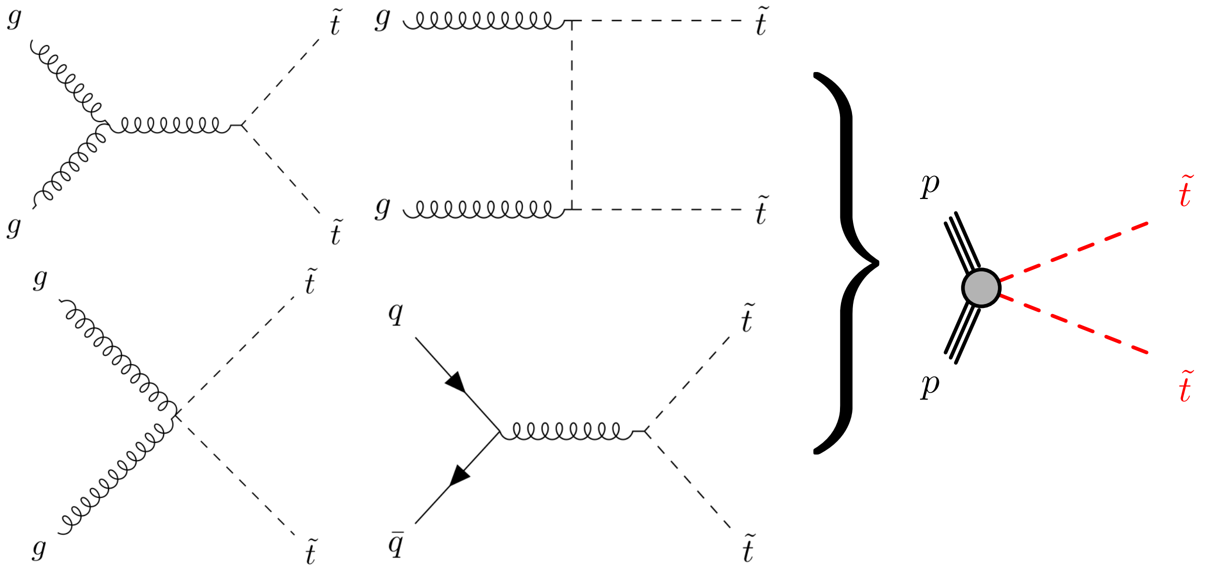

Figure 2.3: Leading-order Feynman diagrams for direct pair production of stop quarks from proton-proton collisions along with a consolidated pseudo-Feynman diagram used to depict multiple scenarios together, adapted from [37].

intermediate decays into charginos and neutralinos as demonstrated in Figure 2.4. The branching fractions of the different decay modes depend on the pMSSM parameters like the soft breaking parameters along with the mass spectrum.

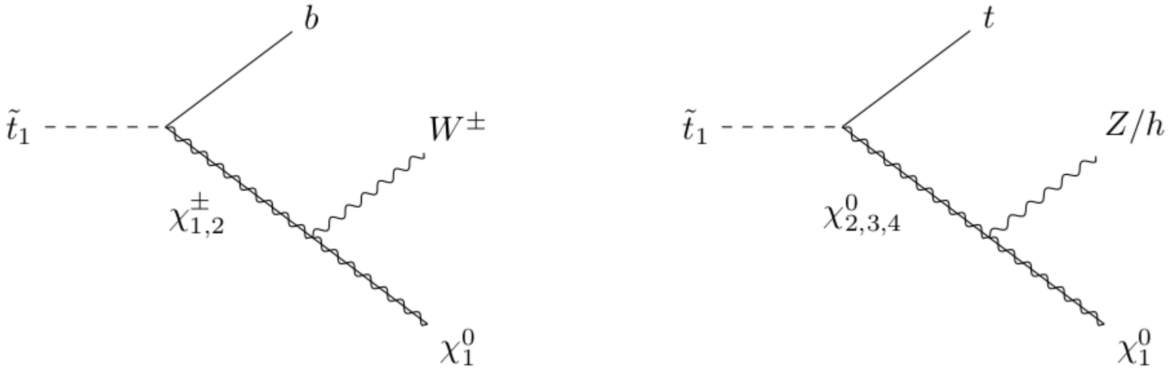

Figure 2.4: Possible decay modes of the lighter stop quark ($\tilde{t}_1$) when multiple charginos and neutralinos exist with mass less than that of the $\tilde{t}_1$.

Additionally, if the heavier stop quark is within reach of the LHC, the decay chain can start with the decay of $\tilde{t}_2$ into $\tilde{t}_1$ as depicted in Figure 2.5a wherein the probability of decaying in either h or Z is mostly influenced by the $\tilde{t}_L$-$\tilde{t}_R$ mixing. As shown in Figure 2.5b, the heavier stop can also directly decay using the decay modes of the light stop.

Since the possibilities are large and the branching ratios for individual decay modes depend

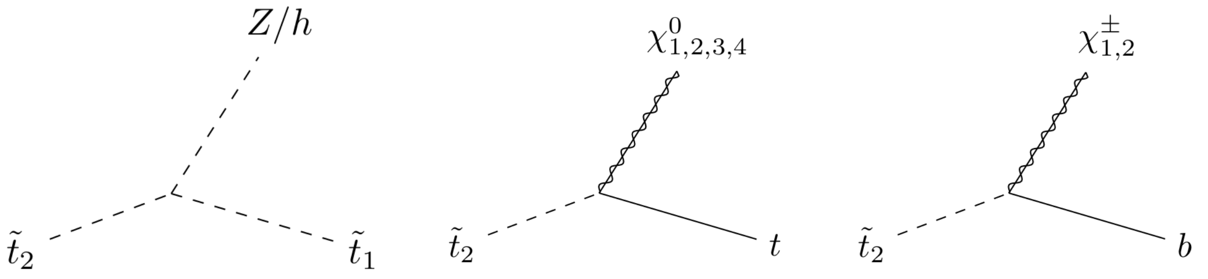

(a) (b)

Figure 2.5: Possible decay modes of the heavier stop quark ($\tilde{t}_2$) when it is light enough to be produced at the LHC.

highly on the mass spectra, a maximally simplified scenario is often considered. Here the lightest stop and lightest neutralino are lighter than all other particles and hence decoupled from the rest of the MSSM particles. This implies that the stop can decay into the lightest neutralino and SM particles and no other SUSY particles are involved. The dominant decay mode in this case is $\tilde{t}_1 \to t\tilde{\chi}^0_1$ which can occur as long as $m(\tilde{t}_1) - m(\tilde{\chi}^0_1) \geq m(t)$ as depicted in Figure 2.6a. If the mass difference is smaller, a decay via an off-shell top quark is possible as depicted in Figure 2.6b. In this thesis, the decays to on-shell and off-shell top quarks are probed. Once this decoupled scenario is probed, the results can be interpreted to allow for a more realistic mass spectrum.

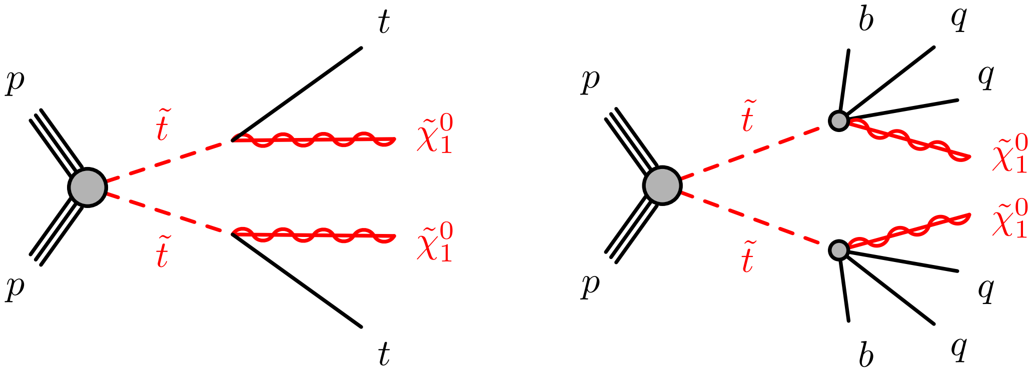

(a) $\tilde{t} \to t\,\tilde{\chi}^0_1$

(b) $\tilde{t} \to bqq\,\tilde{\chi}^0_1$

Figure 2.6: Decay modes of stop-quark pair production in the scenario where the $\tilde{t}_1$ and $\tilde{\chi}^0_1$ are decoupled from the rest of the MSSM spectrum. The Feynman diagrams representing the pair production of stop quarks as a result of proton-proton collisions are further detailed in Figure 2.3.

2.3 The Dark Matter Puzzle

The first compelling evidence for Dark Matter was presented by Fritz Zwicky in the 1930s, who noticed discrepancies in the velocities of galaxies within the Coma Cluster [38]. Subsequent observations, including rotational curves of galaxies [39], the gravitational lensing effect of the bullet cluster [40], and fluctuations in the cosmic microwave background (CMB) [41], have further solidified the need for DM.

The term 'dark' in DM means that it does not interact with ordinary matter (described by the SM) in a way that we have been able to detect so far. It must be neutral, massive and stable. What makes this problem exceptionally challenging is that a DM candidate can have a large potential mass range as depicted in Figure 2.7. These candidates can be fundamental particles or composite objects, ranging from ultralight DM to weakly interacting massive particles (WIMPs) to primordial black holes, and more. Despite extensive efforts, DM has not been experimentally detected so far, suggesting that its interactions with ordinary matter are limited, occur in unexpected ways or are entirely absent (aside from gravity).

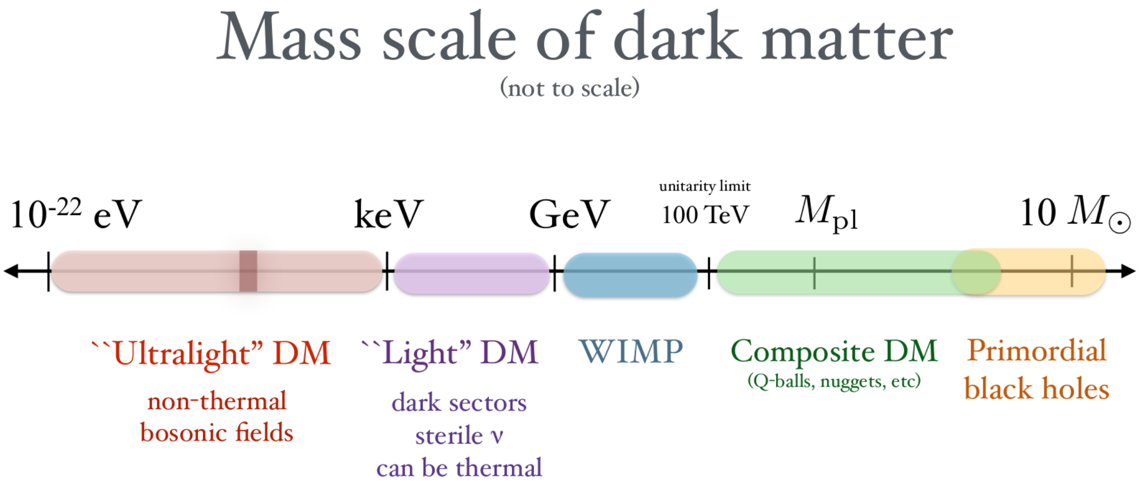

Figure 2.7: Potential mass range of DM candidates, taken from [42].

If the interaction of DM and SM particles is indeed limited to be gravitational only, an independent production mechanism may be responsible for the production of DM in the universe, one that may very well be beyond the reach of experiments with SM particles and interactions. If this isn't the case, and an interaction does exist between DM and ordinary matter, the interaction strength must be very small as no interaction has been observed so far. This scenario is often probed by experiments that posit DM to have particle nature with weak interactions[6] to the SM particles in addition to gravity. Alternative explanations for the observed gravitational effects attributed to DM also exist, including but not limited to, modifications to the law of gravity such as Modified Newtonian Dynamics (MOND) [43].

---

[6] The weak interactions include the SM weak interaction or new interactions with strength less than or equal to that of the weak force.

Ultralight DM refers to candidates with masses typically below 10^{-22} eV, exhibiting coherent wave-like behaviour. The QCD axion is a particularly weakly-coupled bosonic DM candidate within this category with several recent experiments designed for its search. Light dark matter and composite dark matter have been less explored experimentally, despite theoretical models suggesting sterile neutrinos (massive right-handed neutrinos) and Q-balls (emerging in SUSY models) as potential DM candidates. The WIMP particle is a popular DM candidate that arises in many theoretical models with mass in the TeV range, leading to what is called the 'WIMP miracle' and is the kind of DM probed in this thesis. Primordial black holes as DM candidates are probed by astrophysical and cosmological observations.

2.3.1 The WIMP Miracle

The WIMP particle is a kind of thermally produced DM candidate meaning that DM and SM particles were once in thermal equilibrium during the early stages of the Universe. As the universe expanded and cooled, the interaction rate between DM and SM particles diminished, a phenomenon often described as 'freeze-out', reducing the reaction rate. If DM was a particle with mass of $\mathcal{O}$(TeV) with an interaction strength equal to the weak force, its predicted relic density (DM content in the universe) would match what is observed today. What made the WIMP model even more attractive was that UV-complete theories like SUSY could produce a WIMP particle.

For WIMP DM, experiments are conducted in three complimentary ways as depicted in Figure 2.8: collider, indirect detection, and direct detection experiments. Collider experiments aim to produce DM particles by recreating the conditions of the early universe (colliding relativistic SM particles) and observing the resultant decay products. Indirect detection methods focus on observing the annihilation products of DM interactions. Typical experimental signatures include high-energy photons (gamma rays), neutrinos, and cosmic rays originating from regions with a high DM density, such as the centres of galaxies or galaxy clusters. On the other hand, direct detection experiments seek to capture the rare interactions between DM particles and ordinary matter. Typical experimental signatures for direct detection include nuclear recoils in sensitive detectors, which are caused by the scattering of DM particles off atomic nuclei in the detector material.

These mechanisms are complimentary to each other in searching for DM candidates. For example, at the LHC, DM would be probed using missing transverse energy ($E_{\mathrm{T}}^{\mathrm{miss}}$) signatures because they provide evidence of particles escaping undetected. However, this discovery would need to be complemented by signals in direct detection experiments confirming a DM candidate with similar properties. Similarly, finding a signal in a direct-detection experiment would raise questions about the nature of the interaction. These questions could potentially be answered by the simultaneous discovery of a new mediator particle at colliders which have the ability to probe the nature of mediators [45].

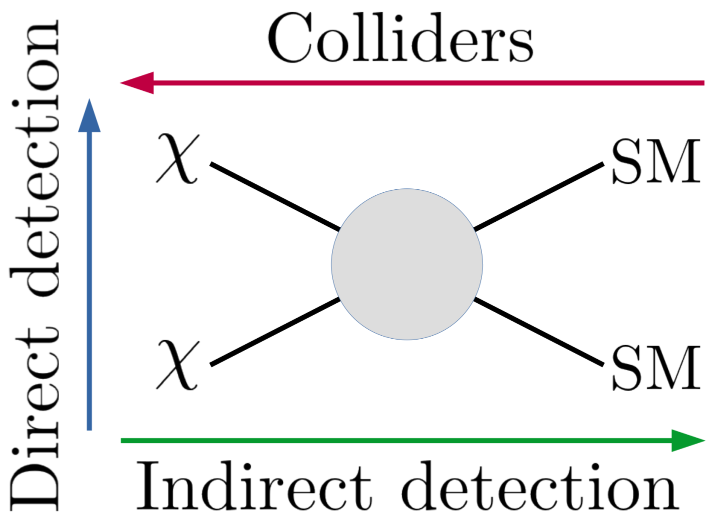

Figure 2.8: Illustration of the three different types of experimental searches for particle natured DM and how they are connected, taken from [44].

2.3.2 Simplified Models

As seen in Section 2.2.1, full theories like SUSY can yield WIMP DM candidates but come with a very specific DM candidate. An alternative general approach is the Effective Field Theory (EFT) which probes effective contact interactions between heavy DM candidates and SM particles. This approach has been proven to be too general in the past. A compromise between the two approaches leads to the Simplified Model approach wherein a benchmark interaction can be probed and then interpreted into different full theories or EFTs [46]. This allows experiments to probe a variety of interaction mechanisms, different DM candidates and interactions involving the whole spectrum of SM particles.

For searches at colliders, the two multi-purpose experiments at the LHC — ATLAS and CMS — provide the best avenue to look for multiple channels. Both experiments in collaboration with theorists have constructed a road map of simplified models to be probed at the LHC. This approach focuses on searching for kinematically distinct signals and prioritising relevant models. To ensure the interpretability of experimental results within a theoretical framework, efforts have been made to motivate assumptions based on theoretical consensus. This strategy is discussed in [45]. The specific simplified model probed in this thesis, with assumptions leading to its definition, is explained below based on descriptions available in [45, 46].

The single DM candidate in this model is a Dirac fermion[7] denoted by χ. While it is possible that DM consists of a variety of particles (just as ordinary matter does), this reductionist approach aims to probe one channel in the hope that it proves to be a starting point for DM discovery at colliders. The DM fermion interacts via a mediator with the SM particles

---

[7] The choice of the DM candidate being a fermion is arbitrary, the results obtained are applicable to a scalar dark matter case with minor modifications.

making it possible to probe as a result of proton collisions. Two types of mediators are considered: one scalar ϕ and one pseudoscalar a. Similar models with spin-1 mediators also have corresponding simplified models, further outlined in [45, 46].

The strength of these interactions is governed by coupling constants, the DM to mediator coupling g_χ and a flavour-universal SM mediator coupling g_v. The cross section for dark matter production, annihilation, and scattering to nucleons scales with the square of the product of the couplings $(g_\chi g_v)^2$. The assumption that the coupling g_v is universal across all families of quarks and leptons is made to avoid introducing large flavour violation. The coupling of the mediator to SM fermions consists of the flavour universal coupling and multiplies the SM-Yukawa coupling for each of the fermions. Within the simplified model, the couplings to W and Z bosons are possible, but small, if the mediators have an interplay with the Higgs sector and are hence ignored [46]. The implication of this assumption is that the production of mediators (ϕ, a) at the LHC has sizeable contributions though loop-induced gluon fusion or in association with heavy-flavour quarks as depicted in Figure 2.9 [47].

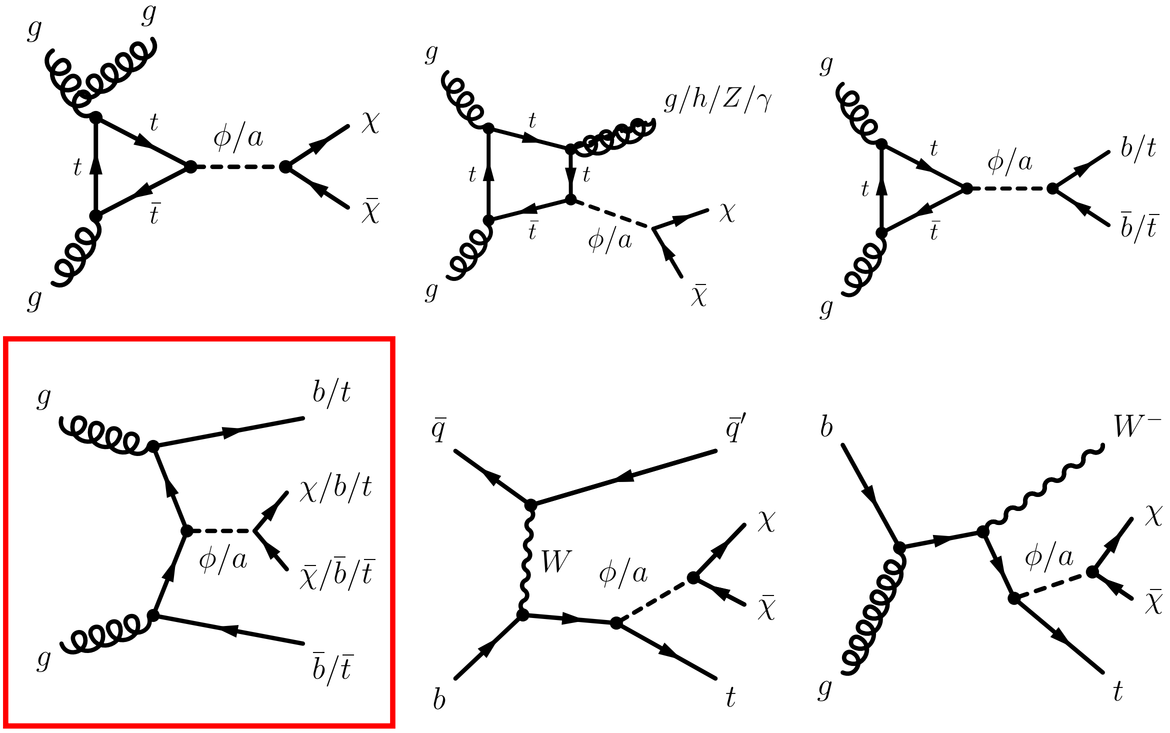

Figure 2.9: Dominant production and decay modes for Spin-0 (ϕ,a) mediators in simplified models, taken from [47].

Depending on whether the mediators decay into SM particles of DM particles, different final states are sensitive to this model. The models with top-quark interactions are especially important due to Yukawa-like couplings between the mediators and fermions. In this thesis, the channel where the mediator is produced in association with top quarks, highlighted with a red box, is probed with the specific mediator decay modes into fermionic DM candidates using the $t\bar{t}$ $+E_{\mathrm{T}}^{\mathrm{miss}}$ final state.

The parameter space of the simplified model can be described by the following free parameters: DM mass m_χ, mediator mass m_ϕ or m_a, DM-mediator coupling g_χ, flavour-universal SM-mediator coupling for quarks g_q. Within this parameter space, the choice of coupling constant has a smaller effect on the event kinematics as compared to the masses of the particles. This is explored extensively in [45] and is important to understand how these simplified models fit into a more complete DM phase space.

The width of the mediator, $\Gamma_{a,\phi}$, can theoretically be left free to accommodate additional DM particles, however here, it is assumed to be minimal meaning that only decays required in the simplified model are accounted for. As an example, the decay width of a scalar and pseudoscalar mediator decaying into 10 GeV DM fermions is shown in Figure 2.10. The primary decay mode of the mediator is into a χ-pair until the top-quark pair channel opens up at $m_{\phi,a} > 2 \cdot m_t$.

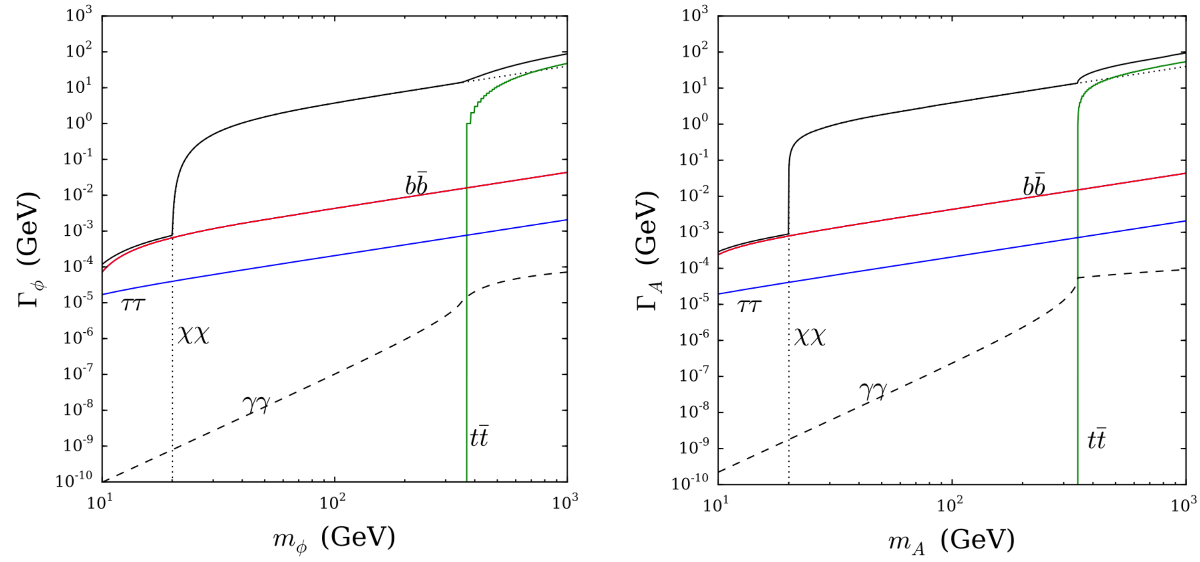

Figure 2.10: The width Γ of the scalar ϕ (left) and pseudoscalar A (right) decaying into pairs of 10 GeV dark matter particles $\chi\chi$ (black dotted), top quarks (green), bottom quarks (red), tau leptons (blue), $\gamma\gamma$ (black dashed), and the total width (black solid), plotted as a function of the parent mass m_ϕ or m_A. Widths are calculated assuming $g_v = g_\chi = 1$, taken from [46].

CHAPTER 3

CERN, the LHC and the ATLAS Experiment

The chapter begins with an introduction to CERN, detailing its historical development and its central role as a leading global institution for particle physics research. Subsequently, the Large Hadron Collider (LHC) is introduced, with a focus on its design principles, operational mechanisms, and its primary focus on proton-proton interactions. Following this, the ATLAS Experiment is detailed, starting with an explanation of the design and functionalities of the ATLAS detector, crucial for the detection and analysis of high-energy particle collisions. The chapter also introduces the methodologies utilised for data collection and simulation, followed by the complex procedures involved in object reconstruction from collision data.

* * *

3.1 CERN

CERN, the European Organisation for Nuclear Research (originally "Conseil Européen pour la Recherche Nucléaire"), was founded in 1954, 70 years before this thesis was written. CERN was established with the goal of providing a common ground for European scientists to collaborate on nuclear research after World War II. With its headquarters located in Geneva, Switzerland, CERN quickly became a hub for cutting-edge research in particle physics.

Over the decades, it achieved many milestones, including the development of accelerators like the Synchrocyclotron (SC), the Proton Synchrotron (PS) and the Super Proton Synchrotron (SPS), which were instrumental for groundbreaking discoveries such as the W and Z particles. In the 1980s, construction began on the Large Electron–Positron collider (LEP) [48], while technological innovations like the World Wide Web [49] were pioneered within its walls in the 1990s. The tunnel that housed the LEP accelerator was reused to construct the Large Hadron Collider (LHC) [50], which is the world's most powerful particle accelerator today.

Today, CERN hosts a diverse and extensive experimental program covering a wide range of topics in physics. The program encompasses studies conducted at the LHC, where nine experiments analyse particles produced by collisions. Key experiments like ATLAS [51] and CMS [52] utilise general-purpose detectors to investigate various physics phenomena, while others like ALICE [53] and LHCb [54] focus on specific aspects. Additionally, smaller experiments such as TOTEM [55] and LHCf [56] examine "forward" physics and MoEDAL-MAPP [57] searches for magnetic monopoles. Besides the LHC experiments, the accelerator complex at CERN also consists of fixed-target experiments. Under this umbrella, experiments like COMPASS [58] and NA61/SHINE [59], explore the structure of particles using beams from the SPS. Additionally, antimatter experiments, facilitated by the Antiproton Decelerator (AD) [60] and ELENA [61], study properties of antimatter.

Furthermore, experimental facilities such as ISOLDE [62], MEDICIS [63], and n_TOF [64] utilise further the capabilities of CERN's infrastructure and expertise to conduct cutting-edge research in areas such as nuclear physics, medical isotopes, and neutron-induced reactions. Additionally, CERN hosts the control center for AMS [65], and hosts experiments like CAST [66] as well as OSQAR [67] that operate independent of the CERN accelerator complex, but benefit from the collaborative environment, scientific resources, and international network available at CERN.

3.2 The LHC

The LHC consists of two circular rings[1], each with circumference 27 km designed to primarily accelerate beams of protons to collide them. The beams are accelerated in each ring in opposite directions meeting at four interaction points (IPs) where the four big LHC experiments are located. In addition to proton collisions, the LHC can also collide heavy ions and produces for example lead-lead (Pb-Pb) and proton-lead (p-Pb) collisions. ATLAS, CMS and LHCb primarily study proton-proton collisions, while ALICE focuses on heavy ion collisions.

The rate at which a physics process is produced at a collider depends on two quantities describing the collider, the centre-of-mass energy $\sqrt{s}$ and the instantaneous luminosity L. A higher center-of-mass energy allows for the production of heavier particles, in accordance with the mass-energy equivalence principle. The instantaneous luminosity describes the number of collisions delivered by the machine. The rate of a physics process produced is given by

$$R = \sigma(\sqrt{s}) \times L, \tag{3.1}$$

where σ is the cross section of the process depending on $\sqrt{s}$. A high instantaneous luminosity is desirable because it increases the probability of detecting rare events and enables precise measurements of Standard Model (SM) parameters by maximising the number of produced events.

The LHC was designed to collide protons at a centre-of-mass energy up to $\sqrt{s} = 14\,\text{TeV}$ and a maximum instantaneous Luminosity of $L = 10^{34}\,\text{cm}^{-2}\text{s}^{-1}$. Initially, during Run-1 of the LHC,

---

[1] Strictly speaking, the LHC is not a perfect circle; it is composed of eight arcs, each 2.45 km long, and eight straight sections, each 545 m long.

it operated at $\sqrt{s} = 7\,\text{TeV}$ in 2010 and 2011, later increasing to $\sqrt{s} = 8\,\text{TeV}$ in 2012. During Run-2, which lasted from 2015 to 2018, the LHC operated with $\sqrt{s} = 13\,\text{TeV}$. The data analysed in this thesis consists of all proton-proton collisions collected during Run-2 of the LHC. Since then, further upgrades to the LHC have increased its collision energy to $\sqrt{s} = 13.6\,\text{TeV}$. Since 2022, the LHC is operating at this energy and the data being collected will constitute the Run-3 dataset. Run-3 is planned to continue until the end of 2025.

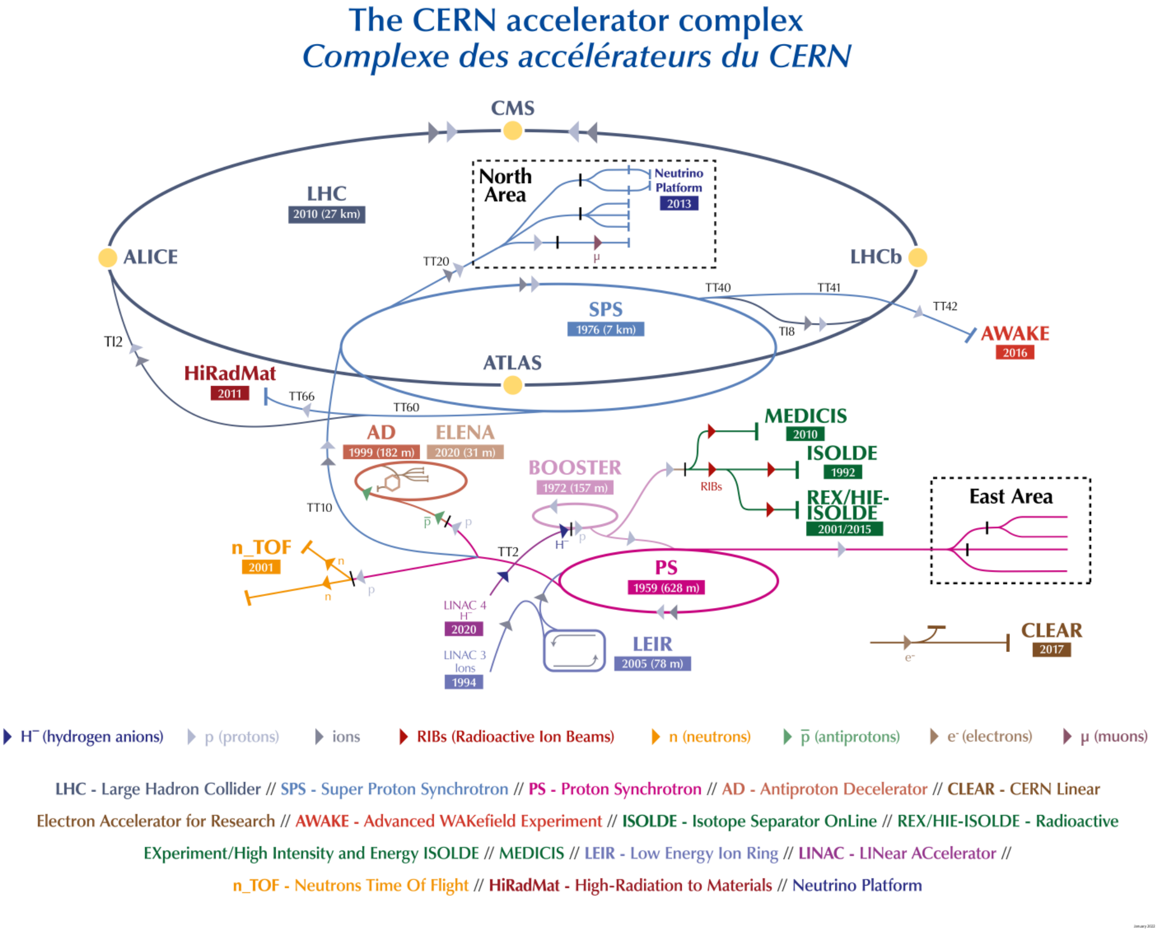

Figure 3.1: Schematic view of the chain of accelerators used at CERN to accelerate protons before colliding them at the LHC, taken from [68].

In order to accelerate protons up to their final collision energies and group them into bunches with proper time spacing for coordinated collisions, CERN utilises a complex chain of accelerators depicted in Figure 3.1. This process begins in a bottle of Hydrogen gas, from which protons are extracted using an electric field. These protons then enter LINAC 2, where they are accelerated to 50 MeV. They then pass through a series of synchrotrons - Booster, PS, and SPS - reaching energies of $1.4\,\text{GeV}$, $25\,\text{GeV}$, and $450\,\text{GeV}$, respectively. Protons then enter the LHC, and are further accelerated to $6.5\,\text{TeV}$ per beam in the case of operation at

$\sqrt{s} = 13\,\text{TeV}$. To bend the protons in the curved sections of the LHC, a magnetic field is used. This is provided by superconducting dipole magnets, cooled to a temperature of 1.9 K using superfluid Helium, installed along the ring.

The instantaneous luminosity can be expressed through beam parameters as:

$$L = \frac{N_1\, N_2\, n_b\, f_r}{4\pi\, \sigma_x\, \sigma_y} \tag{3.2}$$

where N_1 and N_2 are the number of protons per bunch in the two beams, n_b is the number of bunches per beam and f_r is the revolution frequency of the beams. The size of the beam is described by σ_x and σ_y that can be alternatively described as a function of the beam focus parameter β^*. These parameters are outlined for the different years of operation during Run-2 in Table 3.1. As seen in the last row of Table 3.1, the design luminosity has been significantly surpassed.

Table 3.1: Summary of beam parameters during Run-2 compared to the LHC design values, taken from [69].

	Design	**2018**	**2017**	**2016**	**2015**
# protons/bunch, N_1,N_2 ($\times\ 10^{11}$)	1.15	1.1	1.25	1.2	1.2
# bunches n_b	2808	2556	2556–1868	2220	2244
Bunch spacing [ns]	25	25	25	25	25
Beam focus β^* [cm]	55	30→27→25	40→30	40	80
Peak Luminosity [cm^{-2} s^{-1}] ($\times\ 10^{34}$)	1.0	2.1	2.0	1.5	0.6

3.2.1 Proton-Proton physics

While the proton is commonly approximated to consist of two up quarks and one down quark, called valence quarks, it has a more complex internal structure. Experimental evidence from deep inelastic scattering and theoretical models such as the quark model and QCD explain that protons consist of a sea of virtual quark-antiquark pairs and gluons in addition to the three valence quarks. One is particularly interested in events which have been caused by collisions of 'partons' which can be considered to be asymptotically free. Consequently, proton collisions that yield the hard scattering of partons within the proton are a powerful tool for studying fundamental physics interactions.

The total cross-section of proton-proton collisions as a function of centre-of-mass energy is shown in Figure 3.2. At high energies, the probability of having an inelastic collision increases. In an inelastic collision with large momentum transfer, the collision of protons can be viewed as a collision of two partons. The cross section of observing a particular final state X as a result of a proton-proton collisions is then given by:

$$\sigma_{pp\to X} = \sum_{i,j} \int f_i(x_i,\, Q^2) \cdot f_j(x_j,\, Q^2) \cdot \hat{\sigma}_{i,j\to X}\ dx_i\, dx_j. \tag{3.3}$$

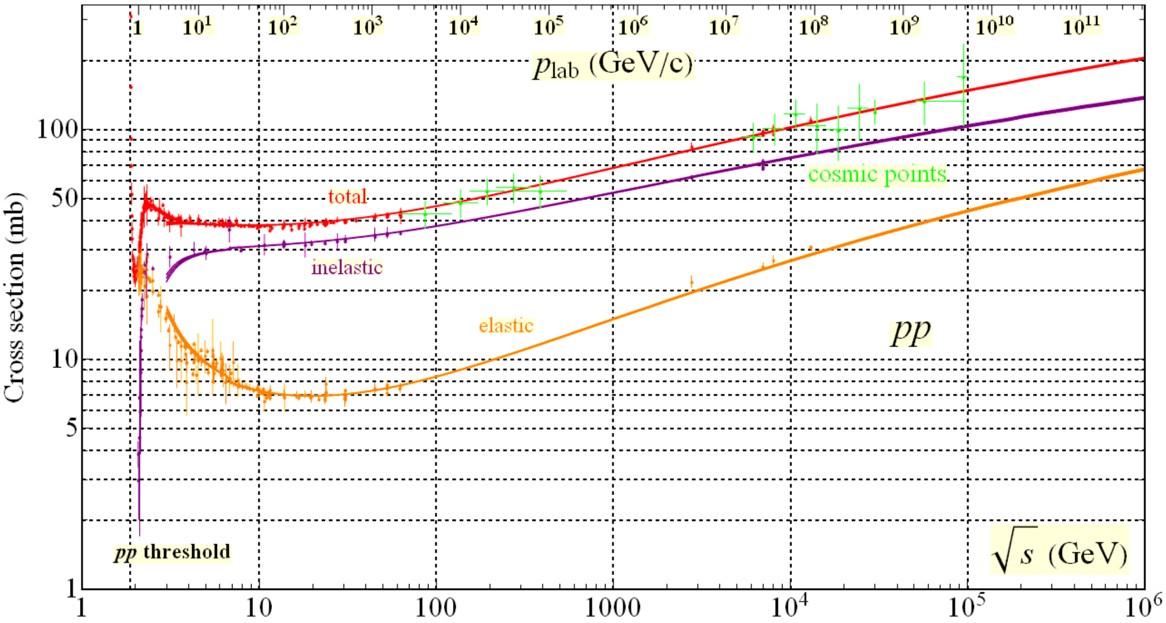

Figure 3.2: The cross section of proton-proton collisions as a function of centre-of-mass energy, taken from [12]. The elastic cross section corresponds to proton scattering where the internal structures of the protons remain unchanged and the inelastic cross section corresponds to the case where the internal structure of at least one proton is altered, leading to the creation of new particles or particle states.

with

- The Parton Distribution Functions (PDFs) are given by $f_i(x_i, Q^2)$ and $f_j(x_j, Q^2)$. The variables x_i and x_j are the Bjorken scaling variables[2] , which to a good approximation, can be interpreted as momentum fractions carried by partons within the proton. Hence, the PDFs represent the probability of finding parton types i and j carrying momentum fractions x_i and x_j within the proton. The probability to access a parton with a certain momentum fraction depends on the momentum Q that is transferred in the collision.

- The cross section of observing X as the result of the interaction of elementary partons i and j within the proton is given by $\hat{\sigma}_{i,j\to X}$.

- While i and j represent the partons participating in a given collision, the sum runs over all types of partons i and j inside the proton.

Monte Carlo generators [70] are used to model the output of proton-proton interactions and compare them with the data recorded by experiments at the LHC. The details of this modelling are provided in Section 3.3.2.

---

[2] The Bjorken x variable is a dimensionless scaling variable in Deep Inelastic Scattering (DIS) that quantifies the fraction of the momentum of the initial proton carried by the struck parton in the so-called ‘Breit’ frame.

3.3 The ATLAS Experiment

The ATLAS[3] experiment is a multi-purpose endeavour with a wide-reaching physics program aimed at discovering new phenomena and conducting precise measurements of SM processes. Independent but complementary to the ATLAS experiment is the CMS[4] experiment with its detector located on the opposite side of the LHC. Both experiments are designed to yield independent measurements, providing crucial cross checks of physics results.

The ATLAS collaboration comprises approximately 6000 people around the world including physicists, engineers, technicians, students and support staff, working together to further the understanding of particle physics. To lay the groundwork for understanding the subsequent chapters, a concise overview of key components of the ATLAS experiment is presented. This begins with a description of the ATLAS detector, which is primarily designed to identify and measure the kinematic properties of all particles produced in the collisions over a wide momentum range and solid angle. This is followed by a description of the ATLAS Run-2 proton-proton collision dataset along with a description of simulations required to understand the collected data. Lastly, there is a section on object reconstruction, which focuses on the algorithms and techniques used to reconstruct physical objects from the raw detector data, enabling the analysis of particle interactions.

Additionally, to perform all the above mentioned tasks, the ATLAS experiment requires a large amount of computing resources. The ATLAS distributed computing system [71] is anchored by the workflow management system PanDA [72] and the data management system Rucio [73]. This system processes data at CERN (called Tier-0 processing) and reprocesses it annually at Worldwide LHC Computing Grid (WLCG) [74] sites. It supports continuous Monte Carlo simulations and reconstructions. The infrastructure is monitored by shift teams for production and distributed analysis, and it is highly efficient in managing the large volume of data [71].

3.3.1 The Detector

The ATLAS detector is a large, cylindrical apparatus, depicted in Figure 3.3, surrounding one of the collision points of the LHC, with a diameter of 25 m and a length of 46 m. It consists of several layers of specialised particle detectors to capture the different particles that originate from the collision. The geometry of the ATLAS detector includes both ‘barrel’ and ‘endcap’ type regions. The barrel regions consist of layers of detector components arranged cylindrically around the beam pipe, extending radially outward. The endcap regions consist of components positioned at each end of the detector, perpendicular to the beam pipe, arranged in planes, complementing the barrel regions by extending the coverage of particle detection to a larger solid angle around the collision point.

---

[3] ATLAS - A Toroidal LHC ApparatuS

[4] CMS - Compact Muon Solenoid

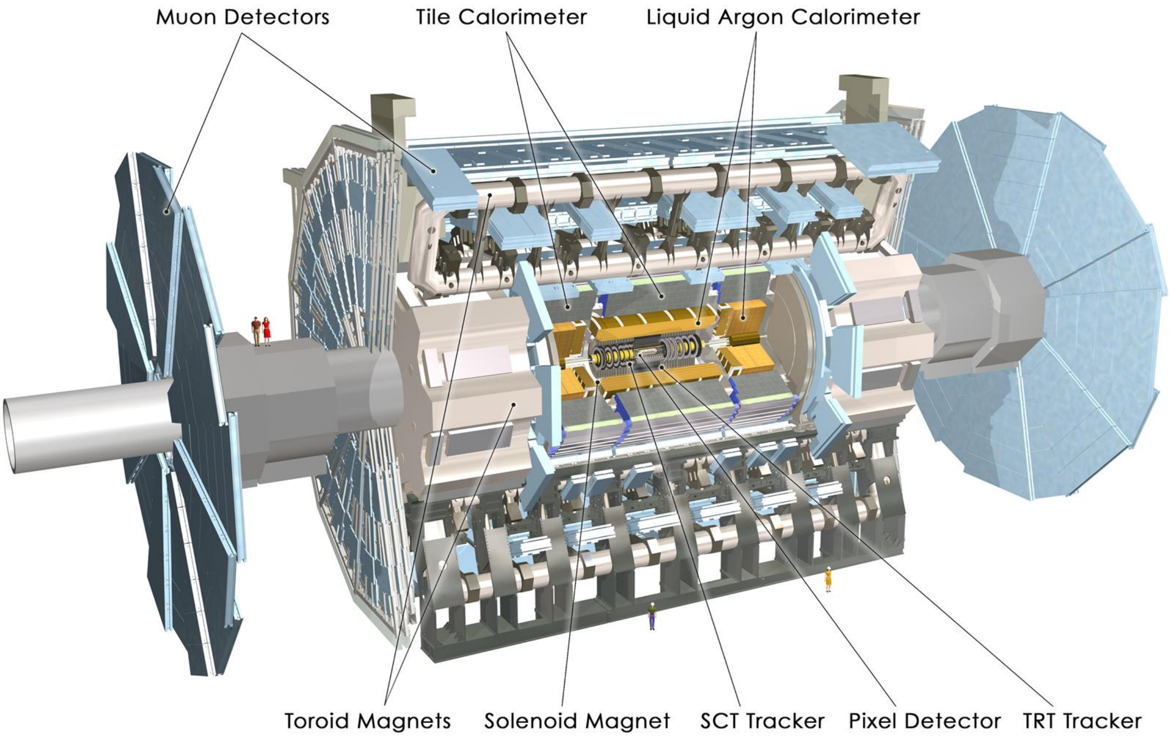

Figure 3.3: A computer generated image of the full ATLAS detector showing the Inner Detector components (Pixel Detector, SCT and TRT), Calorimeters, Muon Detectors and Magnets [75].

Closest to the beam pipe lies the Inner Detector (ID), which is surrounded by a superconducting solenoid magnet. The ID is specifically designed to perform high-precision tracking, by measuring the trajectories of charged particles originating from collisions, while ensuring minimal interference with the path of these particles. It is immersed in a magnetic field to derive kinematic information from the particles, using the Lorentz force to bend charged particles in the transverse plane. Following the solenoid, the detector comprises the electromagnetic calorimeter (ECal) and the hadronic calorimeter (HCal), which measure the energies of particles by stopping them and causing them to deposit their energy inside the calorimeters. The ECal is primarily designed to measure the energy of electrons and photons, while the HCal is designed to measure the energy of hadronically interacting particles such as protons, neutrons, and mesons. The outermost part of the ATLAS detector is the Muon Spectrometer (MS), which consists of gaseous tracking detectors and three superconducting ATLAS Toroid magnet systems, one for the barrel and one for each endcap. The MS is designed to measure the trajectories of muons, which pass through the calorimeters almost unimpeded, using the magnetic field provided by the toroidal magnets.

The coordinate system used to describe the ATLAS detector is defined using the collision point as the origin. The positive x-axis points toward the centre of the LHC, the positive y-axis points upward and the z-axis is along the direction of the beam pipe, using the right-handed

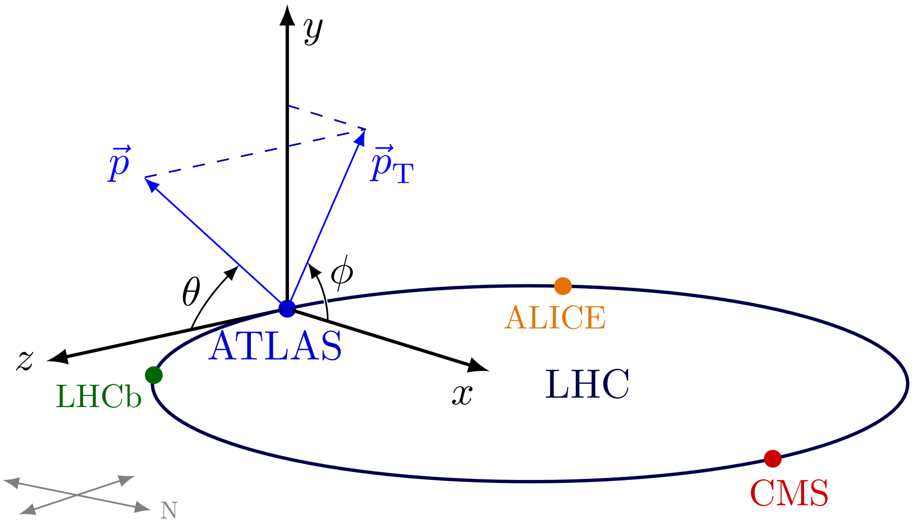

Figure 3.4: Illustration of the ATLAS detector coordinate system, taken from [76].

coordinate system as illustrated in Figure 3.4. The positive-z axis is called side-A of the detector and the negative-z axis is called side-C of the detector. In spherical coordinates, the azimuthal angle ϕ is defined to be concentrically around the z-axis with $\phi = 0$ aligning with the positive x-axis. The polar angle θ describes the angle relative to the z-axis with $\theta = 0$ aligning with the positive z-axis.

The x-y or r-ϕ plane is defined as the transverse plane. When protons collide head-on, the resulting collision may exhibit significant momentum along the z-axis but negligible momentum in the transverse plane because the protons don't have initial transverse momenta. The momentum of the collision particles in the z-direction is referred to as the longitudinal boost. The quantity 'rapidity' is introduced to provide a more suitable description of the particle's motion along the z-axis as follows.

$$y = \frac{1}{2} \ln \left(\frac{E + p_z}{E - p_z} \right) \tag{3.4}$$

Rapidities transform under Lorentz transformations as $y' = y + \text{const}$ such that differences in rapidity Δy are invariant under Lorentz transformations, making rapidity a useful variable for hadron colliders. In cases where the particle's energy greatly exceeds its mass ($m \ll E$), the pseudorapidity η is a good approximation of the rapidity. It depends only on θ and is defined as follows:

$$\eta = -\ln \left(\tan \frac{\theta}{2} \right) \tag{3.5}$$

For a value of $\theta = 0$ ($\theta = 180$), η has a value of $+\infty$ ($-\infty$) corresponding to the longitudinal directions. For a particle in the transverse plane, $\theta = 90$, η has a value of 0. The angular distance between particles is calculated with:

$$\Delta R = \sqrt{(\Delta\eta)^2 + (\Delta\phi)^2} \tag{3.6}$$

The momentum components in the transverse plane are invariant under boosts in the z-direction and thus ΔR is invariant under Lorentz transformations in the z-direction. The particle's transverse momentum (p_T) represents the momentum component perpendicular to the beam axis, calculated using the momentum components p_x and p_y as:

$$p_\mathrm{T} = \sqrt{{p_x}^2 + {p_y}^2} \tag{3.7}$$

Inner Detector (ID)

The ID consists of three sub detectors: the Pixel Detector, the Semiconductor Tracker (SCT) and the Transition Radiation Tracker (TRT) as shown in Figure 3.5 [77].

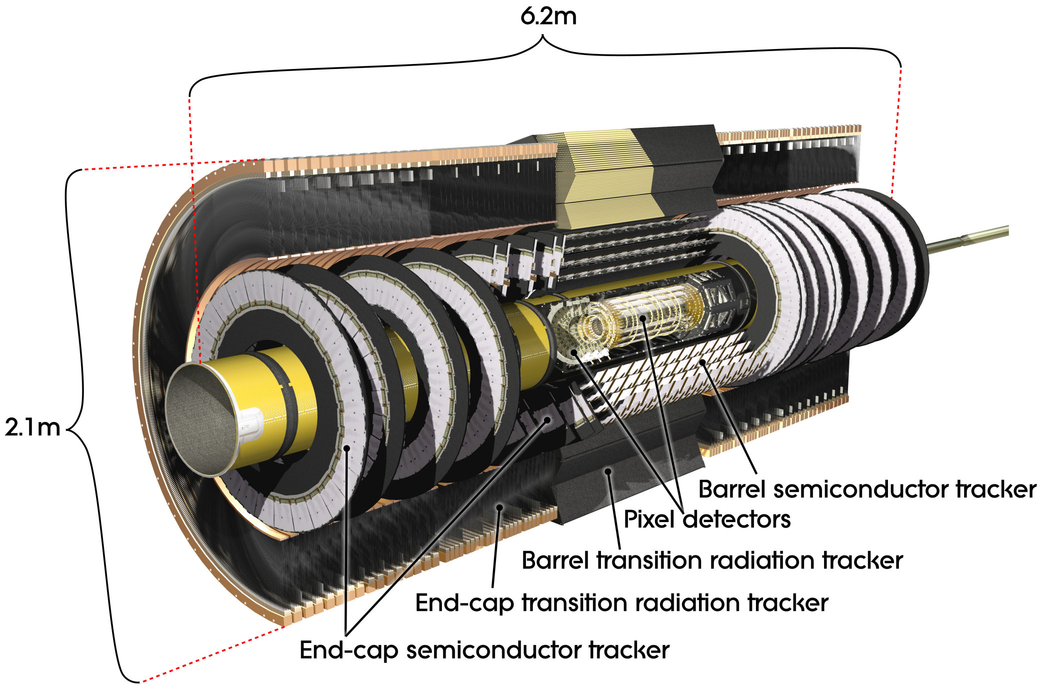

Figure 3.5: Computer generated image of the ATLAS inner detector [78].

- **The Pixel Detector** initially consisted of three concentric barrel layers and three endcap disks on either side of the barrel region. An additional barrel layer, called the Insertable B-Layer (IBL), was inserted in 2014 closest to the beampipe to further improve tracking capabilities. Each layer/disk consists of silicon pixel modules with readout electronics, mounted onto support structures that maintain positioning and operating environmental conditions. Each pixel module, typically rectangular-shaped, contains arrays of pixels on their silicon sensors that comprise the active area for particle detection. The pixel detector comprises 80 million pixels, with the outer layers featuring pixels of dimensions $50 \times 400\,\mu\mathrm{m}^2$, while the innermost B-layer has smaller pixels with dimensions $50 \times 250\,\mu\mathrm{m}^2$.

- **The SCT** consists of four concentric barrel layers and nine endcap disks on each side. The layers and disks consist of a total of 4088 SCT modules. The silicon sensors in these modules are divided into long, narrow strips. In each module, two silicon sensors are arranged back to back with a stereo angle of 40 mrad to provide three-dimensional tracking of charged particles. The pitch of the strips in the barrel layers is 80 µm and ranges from 57 µm to 90 µm in the endcap disks.

- **The TRT** is the outermost part of the ID and consists of gaseous detectors called 'straws' as the basic detector module instead of silicon modules. These straws are drift tubes, made out of kapton, each with a diameter of 4 mm. The tubes are filled with a gas mixture and have a gold-plated tungsten wire of 31 µm at their centre. In the barrel region, the straws are arranged parallel to the beam axis in 73 concentric layers. In the endcap, there are 20 disks of straws oriented radially and perpendicular to the beam axis [79]. In addition to tracking, the TRT provides electron identification using transition radiation created by inserting polymer fibres (foils) in the space between the straws in the TRT barrel (endcap) [80].

When a particle traverses the ID, it interacts with its components - silicon pixels, strips, or gas-filled straws - along its path. Each interaction is recorded as a hit with high precision and this information is then used to reconstruct the particle's trajectory or 'track'. This process allows for the determination of the particle's momentum, if its positively or negatively charged, and the origin of the particle. The particle flux is notably the highest near the collision point and decreases as one moves outward through the detector. This is addressed in the design, with the most granular pixel detectors positioned closest to the collision point, gradually transitioning to less granular detectors further from the beam axis. The Insertable B-Layer (IBL) of the pixel detector has a resolution of $8 \times 40\,\mu\text{m}$ in ($r\phi \times z$), while the remaining layers of the pixel detector maintain a resolution of $10 \times 115\,\mu\text{m}$. The SCT has a resolution of $17 \times 570\,\mu\text{m}$ [81]. For the Transition Radiation Tracker (TRT), the intrinsic straw resolution is less critical due to the large number of TRT layers and disks providing an average of 36 hits per track, which significantly aids in tracking performance [77]. The TRT achieves a hit resolution of 120 µm (130 µm) per axial (radial) straw in the barrel (endcap) region [82].

Calorimeters

The calorimeters are designed to contain entirely the showers of particles up to the TeV scale. Any energy escaping the calorimeters results in reduced energy resolution of the particles being measured and leads to residual particles punching through to the muon system. The ATLAS calorimeter system is illustrated in Figure 3.6.

- **The Electromagnetic Calorimeter (ECAL)** is a sampling calorimeter using Liquid Argon (active medium) interspaced with lead (passive medium) to produce showers and absorb the energy of particles. It is therefore called LAr corresponding to Lead-Argon. The LAr ElectroMagnetic Barrel (EMB) and LAr ElectroMagnetic EndCap (EMEC) together constitute the ECAL. The lead absorbers are designed to be accordion-shaped to increase coverage and hence the probability of interaction with all particles. The

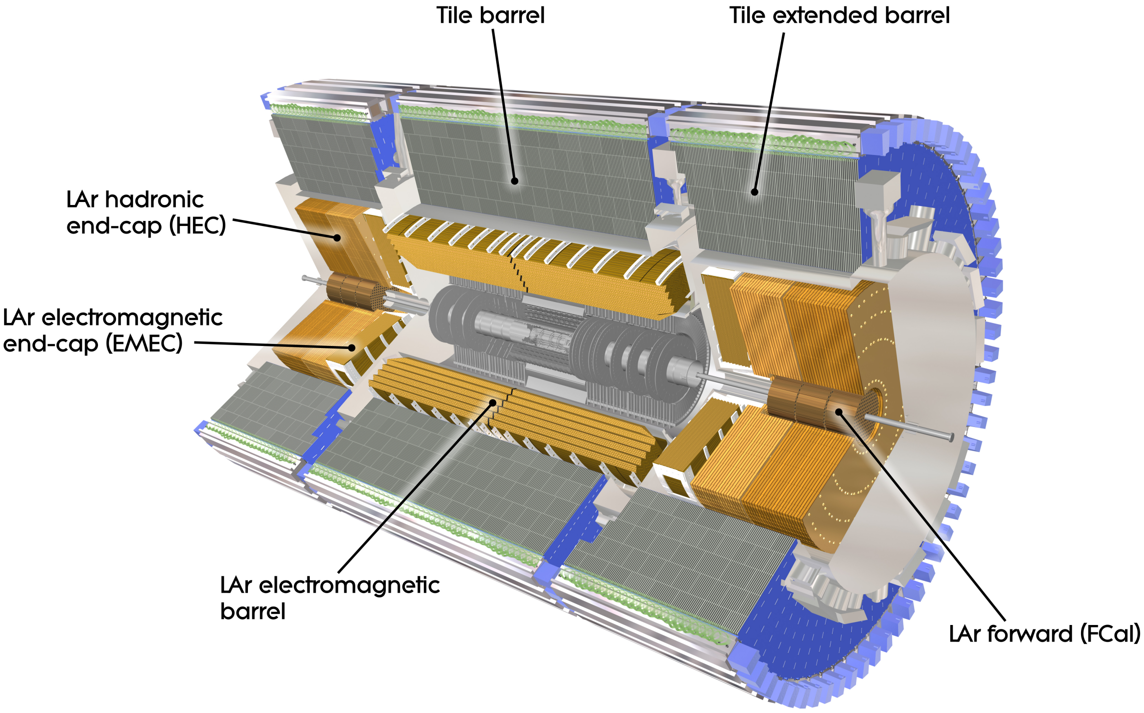

Figure 3.6: Computer generated image of the ATLAS calorimeter system [83]. The ECAL consists of the LAr electromagnetic barrel and endcap. The HCAL consists of the Tile Barrel, extended barrel and LAr hadronic endcap and a LAr Forward calorimeter (FCal).

stopping power of the ECAL can be estimated by calculating the radiation length X_0[5] of the overall material, corresponding to 22 X_0 (24 X_0) for the LAr EM Barrel (LAr EMEC).

- **The Hadronic Calorimeter (HCAL)** consists of Tile calorimeters which use alternating layers of steel absorbers and plastic scintillator tiles in the barrel regions. Additionally, the HCAL uses a LAr calorimeter with copper plates in the endcap regions, which are located at the ends of the detector and are perpendicular to the beam pipe. In the forward region, extending further along the beamline from the endcap regions and also positioned around the beam pipe but at a more acute angle, the HCAL employs LAr with tungsten, referred to as LAr FCal. The stopping power of the HCAL is estimated using the hadronic interaction length λ_{had}[6], corresponding to 11 λ_{had} for the entire HCAL at $\eta = 0$.

When a particle traverses the calorimeters, it deposits energy in the different sensitive elements of the calorimeter system. These energy deposits, called clusters, represent localised

---

[5] The radiation length X_0 is defined as the mean distance over which an electron loses all but 1/e of its energy.

[6] The hadronic interaction length λ_{had} is the mean distance over which the energy of a hadron is reduced to 1/e of its initial energy.

regions of high energy. Clusters, reconstructed from multiple hits in the calorimeter, provide a more accurate representation of the particle's energy deposition which are then used for particle reconstruction. Charged particles leave tracks in the ID and energy deposits in the calorimeters that require matching, while neutral particles, lacking tracks in the ID, contribute only to energy deposits in the calorimeters, helping to differentiate them. Particles, such as electrons and photons, deposit all their energy in the ECAL, while others, such as hadrons, deposit their energy primarily in the HCAL, further aiding particle identification. Muons leave hits in the ID and minimal energy deposition in the calorimeter but have sufficient energy to penetrate past the calorimeters.

Similar to the ID, the granularity of the calorimeters increases as the distance from the beam pipe increases. In the ECAL, there are three levels of sampling size starting with $(\Delta\eta \times \Delta\phi) = (0.003 \times 0.1)$ closest to the beam pipe, moving to (0.025×0.025) and (0.05×0.025) at the outermost layer. The HCAL has a granularity, $(\Delta\eta \times \Delta\phi) = (0.1 \times 0.1)$ except for the outer layer, which has a granularity of (0.2×0.1) [84].

Muon Spectrometer

The Muon Spectrometer (MS) is the largest and outermost part of the ATLAS detector constituting 90% of the volume of the ATLAS detector. It is designed to identify charged particles that make it through the Calorimeters (mainly muons) and accurately measure their trajectories. For high precision tracking, a magnetic field generated by superconducting toroids is used to bend the charged particles in η or the r-z plane.

Four kinds of gaseous detectors are installed in the MS as illustrated in Figure 3.7. These include Monitored Drift Tubes (MDTs), Cathode Strip Chambers (CSCs), Thin Gap Chambers (TGCs) and Resistive Plate Chambers (RPCs). As illustrated in Figure 3.7, the barrel region of the MS consists of MDTs interspaced with RPCs, while the innermost endcap consists of CSCs close to the beam pipe. The outer endcaps ("wheels") consist of MDTs interspaced with TGCs. The MDTs and CSCs are used to make precise spatial measurements for tracking, while the TGCs and RPCs are used for rapid identification to quickly tag events with muons as interesting.

The MDT chambers are proportional drift tubes while the CSCs are multi-wire proportional chambers. The MDTs are slow but precise with a maximum charge collection time of 700 ns [86]. The RPCs consist of two resistive parallel plates filled with a gas mixture in between and the TGCs are multi-wire proportional chambers with a small wire-to-cathode distance for fast readout. In comparison, the RPCs and TGCs have a charge collection time of < 25 ns. The MDTs provide measurements with a resolution of 80 μm while the CSCs provide a resolution of 60 μm [86]. For the fast TGCs and RPCs, the spatial resolution is on the $\mathscr{O}$(mm) providing less precise but fast measurements.

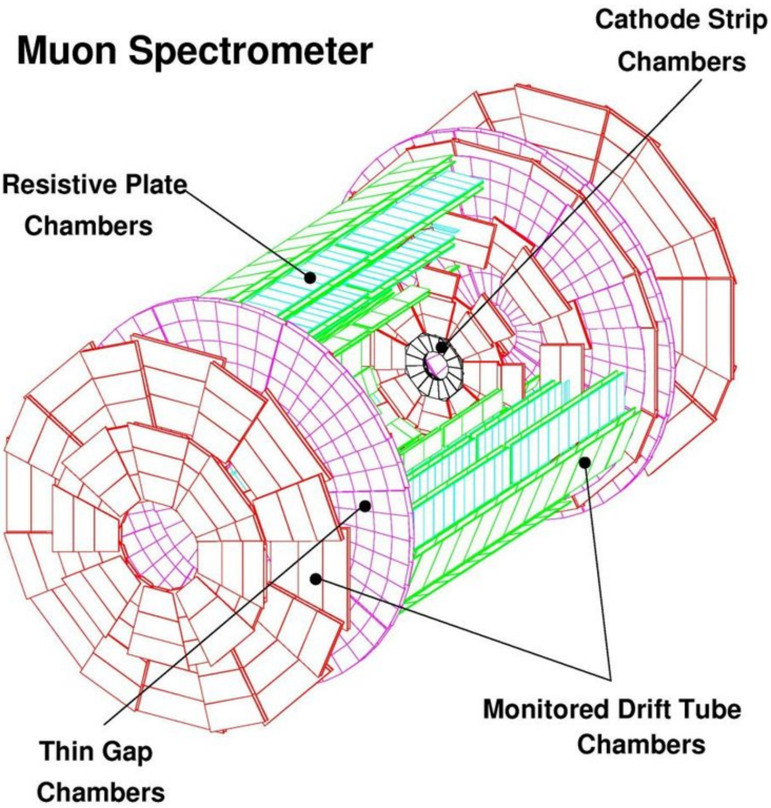

Figure 3.7: Schematic view of the ATLAS Muon Spectrometer System with its different chamber technologies, taken form [85].

Magnet System

The ATLAS magnet system illustrated in Figure 3.8 consists of the Central Solenoid surrounding the ID, the barrel toroids and the endcap toroids [87].

- The **Central Solenoid** is 5.8 m long, has an inner (outer) diameter of 2.46 m (2.56 m). It provides a 2 T axial magnetic field using 9 km of aluminium stabilised niobium-titanium superconducting wires.
- The **Barrel Toroid** is 25.3 m long, with inner and outer diameters of 9.4 m and 20.1 m, respectively. It consists of eight separate 25 m × 5 m coils. It is the largest toroidal magnet ever constructed providing a magnetic field up to 3.5 T.
- Each **Endcap Toroid** is 5 m long and consists has an inner (outer) diameter of 1.7 m (10.7 m). It provides a magnetic field of up to 4 T.

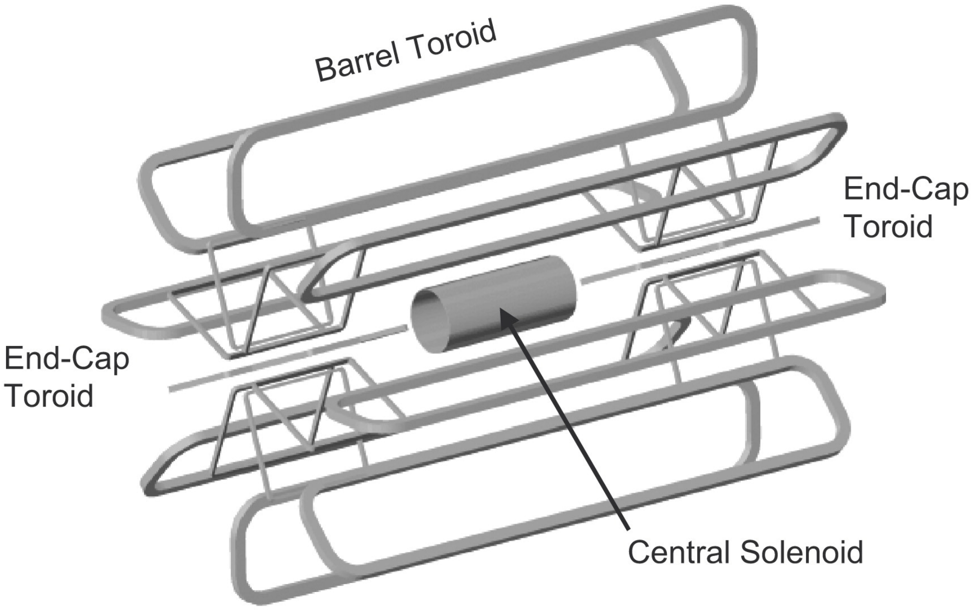

Figure 3.8: Schematic view of the ATLAS Magnet System [88].

Trigger System

During the data-taking period of ATLAS, proton bunches collide 40 million times per second in the ATLAS detector. The volume of events generated at this rate renders it impossible to save each one due to storage and readout constraints. Immense computational power is required to analyse the large number of events. Furthermore, many of the events produced with largest cross sections are not very interesting. To address these challenges, a very complex Trigger system is used to perform real-time event selection, ensuring that the most relevant events are retained for offline analysis.

The trigger system employs a two-tier system: The Level-1 (L1) Trigger which is hardware-based, followed by the High Level Trigger (HLT), which is software based. The L1 Trigger uses information from the Calorimeters and the Muon Spectrometer to make a decision if the data must be saved in less than 2.5 µs. If selected, the event is passed on to the "HLT" which is a software-based trigger. The HLT makes a decision within a few hundred milliseconds by reconstructing physics objects within the event and applying kinematic selections to them. The L1 trigger reduces the rate of accepted events from the initial maximum rate of 40 MHz down to a maximum of 100 kHz. The HLT further reduces the event rate to about 1.5 kHz. A detailed description of the ATLAS Run-2 Trigger system is available in [89].

Events that pass sequentially through both the L1 and HLT triggers are selected for recording based on the presence of specific physics signatures. This selection process involves defining a trigger chain, which corresponds to the presence of an L1 trigger item followed by a specific HLT signature. The collection of different trigger chains defined to capture the most interesting events results in a list of triggers, called the trigger menu. The trigger menu is decided upon before data is recorded. For Run-2, the trigger menus for the various years are detailed in [90–93]. Within the trigger menu, each trigger describes the selection of events it targets.

3.3.2 Data and Simulation

The ATLAS Run-2 dataset is described followed by a description of simulation techniques used by ATLAS to model different physics processes crucial for understanding and interpreting the experimental data collected by the ATLAS detector.

The ATLAS Run-2 p-p Dataset

The full ATLAS Run-2 proton-proton collision dataset recorded at $\sqrt{s} = 13\,\text{TeV}$ is used in this thesis, which corresponds to an integrated luminosity of $140\,\text{fb}^{-1}$. This quantity is defined as the integral of the instantaneous luminosity over a given period of time, denoted as L_{int} where $L_{\text{int}} = \int_0^{\tau} L\, dt$. For a given physics process, the total number of events, N, describing this process is given by $N = \sigma \cdot L_{\text{int}}$ where σ is the cross section of the physics process as produced at the LHC. This quantity is important when measuring or searching for a physics process, in order to evaluate its theoretical prediction against that observed at the LHC.

Since bunches of protons collide, multiple proton-proton collisions can occur simultaneously. Although each bunch crossing may involve several collisions, only one collision is designated as the primary collision, typically the most energetic one. This procedure is justified, given the large difference in cross section between soft inelastic pp collisions and energetic collisions shown previously in Figure 3.2, making it very unlikely that two energetic collisions occur in the same bunch crossing. An event (bunch crossing) is recorded if it contains at least one collision with large momentum transfer, that passes a trigger selection in the pre-defined trigger menu. The additional simultaneous collisions are termed pileup events and can occur within the same bunch crossing (in-time pileup) or in neighbouring bunch crossings (out-of-time pileup). The mean number of interactions per bunch crossing, denoted by μ, quantifies the pileup level. The LHC can adjust the pileup as requested by the experiments by tuning the beam configuration.

The integrated luminosity delivered by the LHC during Run-2 was $L_{\text{int}}^{\text{Run-2, LHC}} = 156\,\text{fb}^{-1}$. The ATLAS detector collected $L_{\text{int}}^{\text{Run-2, ATLAS}} = 147\,\text{fb}^{-1}$ of this data with an average value of $<\mu>= 33.7$ as depicted in Figure 3.9. From this, a dataset passing all data quality criteria and corresponding to an integrated luminosity $L_{\text{int}}^{\text{Run-2,physics}} = 140\,\text{fb}^{-1}$, is called ‘good for physics’ and used in this thesis [94].

Event Simulation

To study different Standard Model and New Physics processes, it is first required to understand how they would appear in the ATLAS detector. They are hence simulated using a chain of steps, namely: Event Generation → Detector Simulation → Digitisation. Event generation deals with modelling the expected output of proton-proton interactions based on QFT

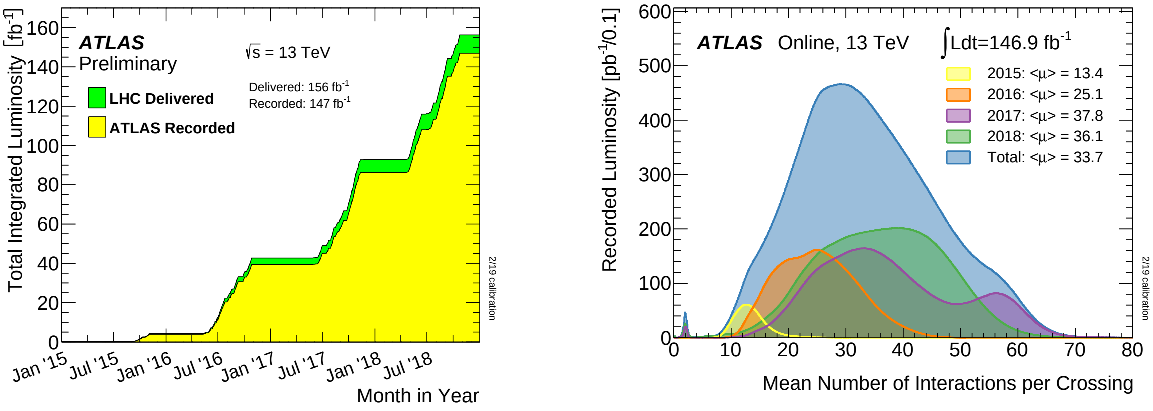

(a) (b)

Figure 3.9: (a) A depiction of the total integrated luminosity during Run-2 considering 13 TeV pp data, taken from [95]. (b) The pileup profile of the different Run-2 years and the overall Run-2 pileup profile, taken from [96].

predictions. Monte Carlo generators [70] are used for this task employing the Monte Carlo method, which is a computational technique that relies on (pseudo) random sampling to obtain numerical results.

The collision and its evolution can be visualised as in Figure 3.10, starting with the protons entering the collision described by their PDFs, followed by the hard-scattering process which describes the collision of the two partons. The parton shower phase corresponds to the radiation of additional quarks and gluons. Hadronisation refers to the formation of colour neutral states, called hadrons, from the quarks and gluons. This is followed by the subsequent decay of unstable hadrons. All these processes occur at different energy scales and the factorisation theorem in QFT allows the calculation of the processes independently.

The protons entering into the collision are described by PDFs, introduced in Section 3.2.1. The PDFs are determined using several collider and fixed target Deep Inelastic Scattering experiments. These are universal and do not depend on the physics process being simulated. The proton PDF, as annotated by $f(x,\ Q^2)$ in Section 3.2.1, depends on Q and is evaluated at $Q^2 = \mu_F^2$. The factorisation scale, μ_F, is a parameter of the factorisation theorem, that arises in the process of separating long-distance physics (PDFs) from short-distance physics (the hard scatter). Hence, the choice of setting $Q^2 = \mu_F^2$ is convenient to allow independent calculations. Nonetheless, practical applications need to be considered by varying the factorisation scale (within a defined range) to gauge theoretical uncertainties linked to the choice of scale. The evolution of the PDF for different values of μ_F is described by the DGLAP equations [98–101].

For the hard scatter itself, the cross section and subsequent particle emissions are determined via Matrix Element (ME) calculations and Parton Shower (PS) algorithms. ME calculations represent the amplitude of a given particle interaction ($ij \to X$). The calculation is performed with a fixed number of loops and real emissions in the Feynman diagram describing

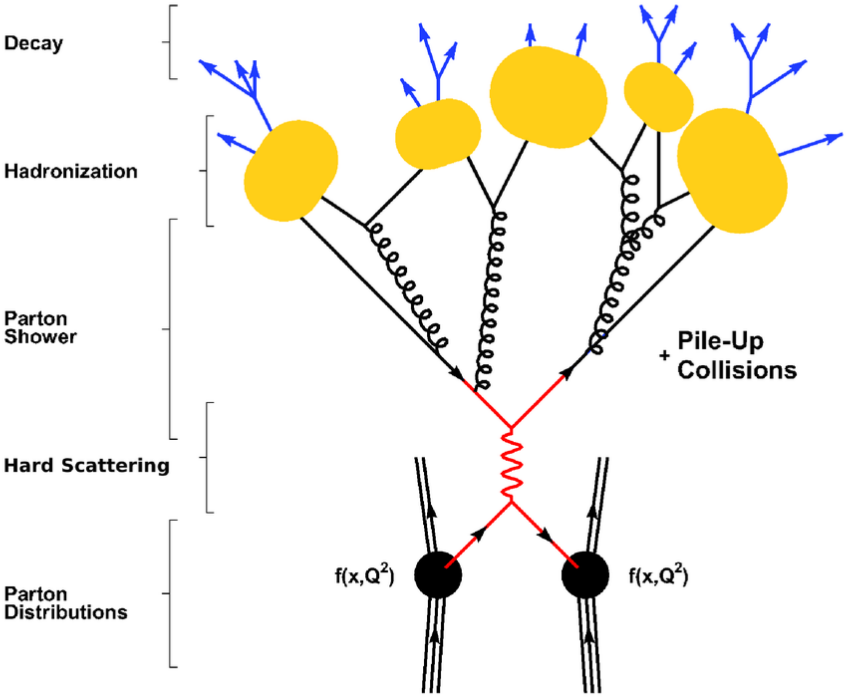

Figure 3.10: Illustration showing the evolution of a proton-proton collision. The initial state protons are described by PDFs and consist of the partons that are accessible at high energies and undergo a hard scatter. This is followed by parton showering, hadronisation, and decays of unstable particles further explained in the text. This picture is taken from [97].

the particle interaction, resulting in a ME computation at fixed order in powers of the coupling constant. This fixed order calculation requires the introduction of a renormalisation scale, μ_R, to treat divergent loop integrals that are inherent in perturbative calculations. It must be emphasised here that both μ_F and μ_R are not physical scales but rather choices made to facilitate calculations. While predictions should ideally not depend on these scales at all orders, computed cross sections as an example, can exhibit sensitivity to the choice of scale due to higher-order perturbative corrections that have not been taken into account. This artificial dependence is accounted for using theoretical uncertainties that are computed by varying the scales (using recommended factors) and observing the resultant differences in predicted cross sections. In this way, the impact of higher-order contributions, not directly calculated, on predicted observables can be accounted for as uncertainties.

The “parton shower” describes a sequence of collimated emissions from the partons appearing as a shower. Parton Shower algorithms are effective at describing soft and collinear emissions at lower energy scales, while ME calculation provide accurate descriptions of processes involving high momentum transfers. PS algorithms assist the ME computation to describe the evolution of partons in the collision as they move from the hard scatter to lower energy scales. To ensure an accurate description of both the hard scatter and softer emissions, matching techniques are used to consistently combine the hard and large angle emission in ME with the soft and collinear emissions in PS. This involves, for example, vetoing PS emissions that are too similar to emissions already present in the ME events to avoid double-counting. In this thesis, the method of Catani, Krauss, Kuhn and Webber, called CKKW, is used [102, 103].

Hadronisation is the process by which quarks and gluons form colour neutral states. Colour confinement occurs meaning that, as the particles become "observable"[7], they are in neutral colour states (hadrons). This also corresponds to the energy scale where QCD is no longer perturbative and phenomenological models are used to describe these processes. For example, in the Lund-Sting model, it is hypothesised that confinement takes the form of a string between a quark and an anti-quark. If the quark-anti-quark pair is stretched and enough energy is available, the string breaks by producing a new quark-anti-quark pair giving rise to two colour neutral states. The hadrons formed during hadronisation can be stable or decay as part of the event.

Additional particles called Initial State Radiation (ISR) and Final State Radiation (FSR) are also included in various parts of the event simulations. The initial and final state particles of the hard scatter are highly energetic and can additionally emit high and low energy partons. As the entire event evolves outward from the collision point through the detector, it lowers in energy. QED interactions like photon radiation also occur as particles lose energy.

The evolution of the leftover partons of the initial proton-proton pair, that do not participate in the hard scatter, are also described by the event generator. Additionally, pileup leads to multiple interaction vertices per bunch. These are called pileup events and their resulting partons must also be modelled. The vertex with the maximum $\Sigma {p_\mathrm{T}}^2$ is called the Primary Vertex (PV). This selection is used to tag the most interesting proton-proton collision.

After event generation, a detector simulation of the events is necessary to represent how the collision would appear within the ATLAS detector. The GEANT4 toolkit [104] is used wherein a detailed description of the ATLAS detector geometry is available and the interactions of physics particles with detector materials are modelled. A detailed description of this process is available in [105]. Digitisation converts the particle-detector interactions into electric signals that correspond to realistic measurements taken with the read out system of the ATLAS detector components. Taking the digitised outputs, first physics objects are reconstructed as described in Section 3.3.3. These objects are used to identify the physics process that occurred in the event. This is done similarly for both simulated samples (after the digitisation step) and real data as collected with the ATLAS detector.

3.3.3 Object Reconstruction

Every physics analysis requires the reconstruction and identification of particles like electrons, photons, muons etc. as physics objects used in the analysis of ATLAS data. This process, called object reconstruction, is a complex task that requires taking into account various electronic

---

[7] Coloured objects only exist at high energies and short distances.

signatures from all the sub detectors. Each detector is designed such that different types of particles interact uniquely with the different detector subsystems of ATLAS. This is exploited by reconstruction algorithms to identify physics objects in every event. An overview of the different particle signatures left in the detector is shown in Figure 3.11.

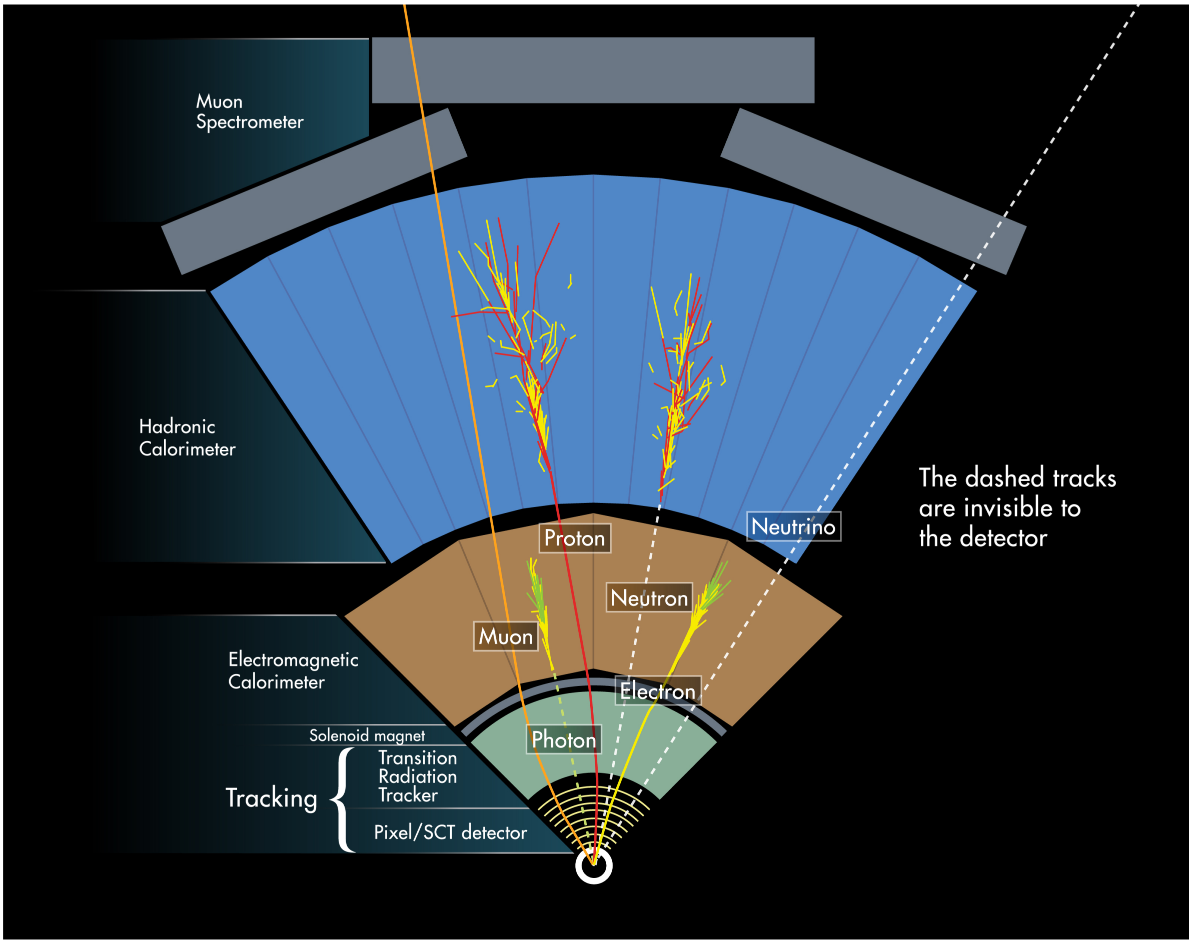

Figure 3.11: Illustration of how different particles interact with the ATLAS detector, taken from [106].

Electrons are reconstructed by matching energy deposits in the ECAL to tracks in the ID. Photons leave very similar energy deposits in the ECAL but no tracks in the ID, since they have no charge. Muons are reconstructed using hits in the MS, or hits in both MS and ID where there is an overlap in the η range between ID and MS. Quarks and gluons hadronise appearing as a collimated spray of particles, called jets, in the ATLAS detector. They are reconstructed using their energy deposits in the calorimeters matched (unmatched) to tracks in the ID for charged (neutral) hadrons. Tagging algorithms are used on these jets to further characterise if these jets originate, for example, from b quarks yielding b-tagged jets. Lastly, missing transverse energy, $E_{\mathrm{T}}^{\mathrm{miss}}$, is reconstructed as the negative vectorial sum of the p_{T} of all objects in the transverse plane to indicate the presence of invisible particles like the neutrino or new weakly interacting particles that may be produced in the collision.

The kinematic properties of each reconstructed object can be characterised using 4-vectors defined as $(E, p_{\mathrm{T}}, \eta, \phi)$. The resolution of these parameters depends on the resolution of the detector components and on the reconstruction algorithms used. The detector resolution depends in turn on the granularity. The geometrical description of the various ATLAS sub detectors is given in Section 3.3.1 along with their granularities in terms of $\Delta\eta$ and $\Delta\phi$. The ATLAS detector was designed with a required energy and momentum resolution depicted in Table 3.2 along with some benchmark resolutions achieved by specific reconstruction algorithms.

Table 3.2: Required energy and momentum resolutions for different ATLAS sub detectors along with benchmark scenarios showcasing resolution achieved with reconstruction algorithms used for specific physics objects.

Detector Component	**Required Resolution**	**Achieved Resolution (Benchmarks)**
Tracking	$\frac{\sigma_{p_{\mathrm{T}}}}{p_{\mathrm{T}}} = 0.05\%\ p_{\mathrm{T}} \oplus^{8} 1\%$	High p_{T} tracks [107] $\frac{\sigma_{p_{\mathrm{T}}}}{p_{\mathrm{T}}} \approx 5\times10^{-4} p_{\mathrm{T}} + 0.01$
EM calorimeter	$\frac{\sigma_E}{E} = \frac{10\%}{\sqrt{E}} \oplus \frac{170\,\mathrm{MeV}}{E} \oplus 0.7\%$	Electron Reconstruction [108] $\frac{\sigma_E}{E}$ = 3-4% at $E_{\mathrm{T}} = 4.5\,\mathrm{GeV}$ $\frac{\sigma_E}{E}$ = 0.1-0.3% at $E_{\mathrm{T}} = 40\,\mathrm{GeV}$
Hadronic calorimeter → **LAr FCal**	$\frac{\sigma_E}{E} = \frac{50\%}{\sqrt{E}} \oplus 3\%$ $\rightarrow \frac{\sigma_E}{E} = \frac{100\%}{\sqrt{E}} \oplus 10\%$	TileCal Pion reconstruction [109] $\frac{\sigma_E}{E} = \frac{52.9\%}{\sqrt{E}} \oplus 5.7\%$
Muon spectrometer	$\frac{\sigma_{p_{\mathrm{T}}}}{p_{\mathrm{T}}} = 10\%$ at $p_{\mathrm{T}} = 1\,\mathrm{TeV}$	Combined Muon[9]Tracks [110] $\frac{\sigma_{p_{\mathrm{T}}}}{p_{\mathrm{T}}} \approx 2\%$ at $p_{\mathrm{T}} = 100\,\mathrm{GeV}$ $\frac{\sigma_{p_{\mathrm{T}}}}{p_{\mathrm{T}}} \approx 4-10\%$ at $p_{\mathrm{T}} = 1\,\mathrm{TeV}$

In this thesis reconstructed electrons, jets, b-quark jets, muons, hadronically decaying τ-leptons and $E_{\mathrm{T}}^{\mathrm{miss}}$ are used. The specific algorithms and selection criteria used for these objects are provided in this section. The “low-level” reconstruction objects used by the algorithms are tracks, vertices and topo clusters as defined below:

- **Tracks** - Tracks are formed by connecting hits across the ID and/or MS sub detectors, to reconstruct trajectories. For a given charged particle exposed to a known magnetic field, the tracks left by this particle are circular in the transverse (x-y) plane in the ID. Tracks are characterised by five quantities in relation to a reference point as shown in Figure 3.12 [111]. The quantities d_0 and z_0 represent the transverse and longitudinal impact parameters, defined as the transverse and longitudinal distances of the single point of closest approach transverse to the reference point. The angles ϕ and θ are the azimuthal angle and polar angle of the track momentum at the point of closest

---

[8] represents sum in quadrature.

[9] Combined muons are muons that are reconstructed using ID and MS hits.

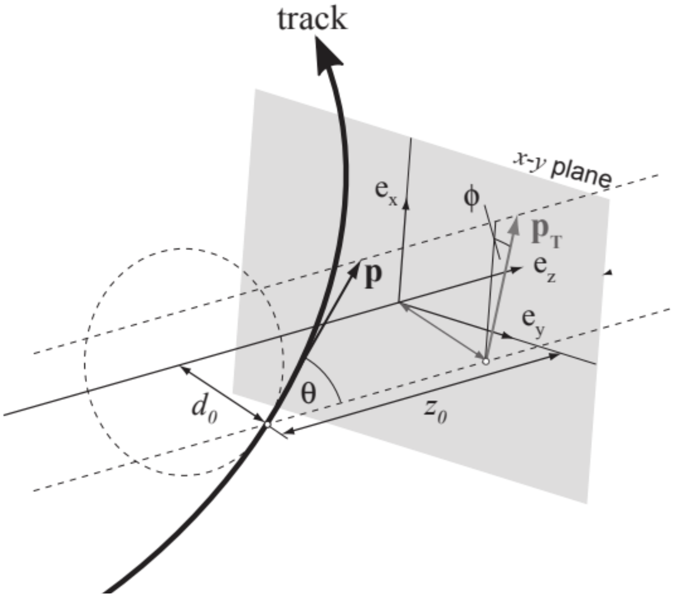

Figure 3.12: Visualization of a track defined with five parameters d_0, z_0, ϕ, θ and q/p, taken from [111].

approach. The curvature of the track gives a measure of the ratio of the charge of the reconstructed track divided by the magnitude of its momentum q/p. The reference point used is typically the average position of the proton-proton interactions.

- **Vertices** - A fitting algorithm is used to combine tracks that possibly originate from the same point in space, called a vertex. The Primary Vertex (PV) is defined by choosing the vertex with the maximum Σp_{T}^2 of the tracks associated with it. This is done to tag the vertex that most likely describes the hard scatter. Secondary vertices are sometimes reconstructed for particles, like b hadrons, that originate from the hard scatter but travel a certain measurable distance before decaying.

- **Topo clusters** - Topo clusters are formed by grouping together neighbouring calorimeter cells with significant energy deposits, likely originating from the same incident particle.

Electrons

Electron reconstruction requires matching ECAL topo clusters to tracks in the ID that describe the pattern of an electron in the ATLAS detector. The algorithms used are further detailed in [112]. Electron identification and isolation are two crucial steps required to define electrons as useful physics objects and are briefly discussed here.

Identification refers to the process of distinguishing electrons from other particles and the algorithm employed is a likelihood-based discriminant using information from the ID and

ECAL. It yields identification "selections" with increasing purity labelled as: `VeryLoose`, `Loose`, `Medium` and `Tight`. A Loose identification selection containing at least one hit in the IBL layer of the Pixel detector yields an additional `LooseAndBLayer` selection. The isolation process assesses the surrounding environment of the electron candidate. The isolation criteria are tailored to the specific requirements of the physics analysis. They aim to strike a balance between efficiently identifying prompt electrons, whether they are isolated or produced in a busy environment, while rejecting light hadrons that are misidentified as electrons [112]. Calorimeter energy deposits and track p_{T} measurements within a cone of size ΔR around the electron (and excluding the electron) are used to quantify the isolation. As examples, two isolation selections used in this thesis are defined using the energy deposited in a cone of size $\Delta R = 0.2$ around the electron for calorimeter based isolation, and the momentum sum in a variable cone size of $\Delta R = \min\left(\frac{10}{p_{\mathrm{T}}[\mathrm{GeV}]}, 0.3\right)$ for track based isolation as follows [113]:

- `Loose_VarRad` selection corresponds to an $\frac{E_{\mathrm{T}}^{\mathrm{cone20}}}{p_{\mathrm{T}}^{\mathrm{electron}}} < 0.2$ and $\frac{p_{\mathrm{T}}^{\mathrm{varcone30}}}{p_{\mathrm{T}}^{\mathrm{electron}}} < 0.15$
- `HighPtCaloOnly` selection corresponds to $E_{\mathrm{T}}^{\mathrm{cone20}} < \max\left(0.015\, p_{\mathrm{T}}^{\mathrm{electron}}, 3.5\,\mathrm{GeV}\right)$.

where $E_{\mathrm{T}}^{\mathrm{cone20}}$ is the transverse energy deposited in a cone of size $\Delta R = 0.2$ around the electron, and $p_{\mathrm{T}}^{\mathrm{varcone30}}$ is the transverse momentum sum within a variable cone size around the electron. The $p_{\mathrm{T}}^{\mathrm{electron}}$ refers to the transverse momentum of the electron candidate.

To further ensure that the signal electrons are indeed originating from the PV, a "Track to PV association" is applied using d_0 and z_0. Given the η coverage of the ID, electrons can be reconstructed within $|\eta| < 2.47$.

The true energy of an electron passing the detector may not precisely match the energy of its corresponding reconstructed electron object. Hence, a calibration process is necessary to correct for inaccuracies stemming from detector response, reconstruction algorithms etc. The calibration process involves utilising well-understood events, such as $Z \to e^+e^-$ to derive energy scale corrections and associated uncertainties essential for subsequent analyses. The efficiency of the reconstruction, identification and isolation algorithms are also evaluated on both MC simulated samples and data, where the performance may not match entirely. Scale factors (SFs) are therefore derived using well known channels ($Z \to e^+e^-$ and $J/\Psi \to e^+e^-$) and used to calibrate the performance of reconstruction algorithms in MC samples to match the performance in data. SFs are defined as follows:

$$\mathrm{SF} = \frac{\varepsilon^{\mathrm{Data}}}{\varepsilon^{\mathrm{MC}}} \tag{3.8}$$

Figure 3.13 illustrates the efficiencies of some identification and isolation algorithms in data, with the bottom panels comparing efficiencies in data and MC used to calculate SFs.

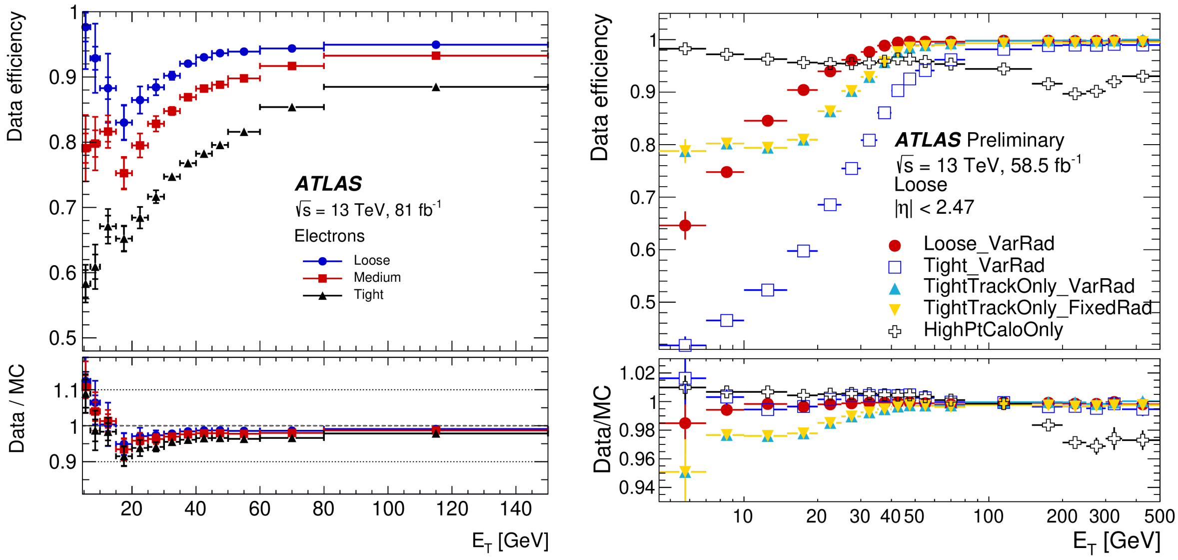

Figure 3.13: The efficiency of different electron identification (left) and isolation (right) selections in $Z \to e^+e^-$ events as a function of electron transverse energy (E_T). The bottom panel illustrates the ratio of the efficiencies measured in data and in MC simulations. The left plot uses 2015-217 Run-2 data and is taken from [112], the right plot uses 2018 Run-2 data and is taken from [113].

Jets

The spray of hadrons originating from quarks and gluons, sometimes visualised as a cone, is called a jet. It is expected to appear as a cluster of deposited energies in the calorimeters of the ATLAS detector as shown in Figure 3.14. Therefore, jets are reconstructed using the anti-k_t algorithm [114] which is a clustering algorithm that combines nearby particles, such that they yield a cone of a pre-defined radius parameter, R. The algorithm sequentially combines topo clusters to form a jet based on certain distance measures:

$$d_{ij} = \min\left(\frac{1}{k_{ti}^2}, \frac{1}{k_{tj}^2}\right)\frac{\Delta R_{ij}^2}{R^2}, \tag{3.9}$$

$$d_{iB} = \frac{1}{k_{ti}^2}, \tag{3.10}$$

where $\Delta R_{ij} = \sqrt{(y_i - y_j)^2 + (\phi_i - \phi_j)^2}$ and k_{ti}, y_i, ϕ_i are the transverse momentum, rapidity, and azimuthal angle of cluster i, respectively. R is a fixed parameter related to the jet radius and B stands for the beam. The algorithm begins by computing all possible d_{ij} and d_{iB} and selecting the smallest value. If d_{ij} is the smallest, clusters i and j are recombined. If d_{iB} is the smallest, cluster i is defined as a jet and removed from the list of available topo clusters.

This process continues until no more clusters are found. The design of the algorithm ensures that soft particles cluster around hard particles to match the expected jet configuration. This reduces the likelihood of soft particles clustering among themselves.

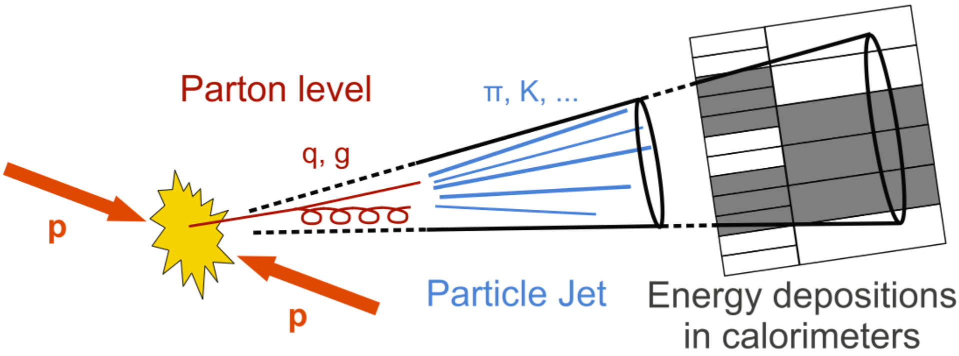

Figure 3.14: Visualisation of a jet defined as the particle-level response in a detector due to a parton-level jet produced from the collision, taken from [115].

Small-R jets are reconstructed with $R = 0.4$ using an implementation of Particle-Flow (PFlow), an algorithm that combines information from ID tracks and calorimeter clusters to improve the jet resolution [116]. Tracks are matched to clusters and then used to modify clusters by subtracting overlapping cells in different clusters or merging clusters that may originate from the same particle. Modified clusters that match tracks pointing to the primary vertex and neutral clusters that do not match any tracks are used together in the anti-k_t algorithm to reconstruct PFlow jets. In the high-energy and high-luminosity environment of the LHC, with extremely busy collision events, the accurate reconstruction of jets becomes particularly challenging. For example, fake jets reconstructed due to calorimeter noise and activity from non-collisional sources[10], are reconstructed and then need to be removed using a cleaning procedure. Additionally, algorithms are required to suppress pileup jets and to this end, a likelihood method called the ‘Jet Vertex Tagger’ (JVT) for jets within $|\eta| < 2.4$, and a supplemental ‘forward JVT’ (fJVT), for jets with $|\eta| > 2.5$ is employed [118, 119]. The JVT algorithm evaluates the compatibility of the jet with the primary vertex, providing a discriminant to distinguish between pileup and hard-scatter jets. The forward JVT extends this concept to cover the forward region of the detector.

Large-R jets are also reconstructed using the anti-k_t algorithm with $R = 1.0$, using topological clusters of calorimeter cells calibrated to the hadronic scale [120, 121]. These jets are ‘trimmed’ to remove energy deposits from pileup and activity from the proton remnants [122]. A special kind of Variable-Radius track-based ,**VR$_{\text{track}}$ jet**, reconstruction algorithm is also used where jets are reconstructed using tracks with a variable cone size. This algorithm is used to look at jets that may lie within the Large-R jet [123].

---

[10] Beam-Induced Background [117] and Cosmic Rays

The reconstructed jet energies require a more complex calibration (compared to electrons) to accurately reflect the true jet energies[11]. This calibration is necessary due to various detector effects, including dead material (energy deposited in passive areas), calorimeter non-compensation (lower response to hadronic interactions), punch-through (showers extending beyond the calorimeters), pileup (additional energy deposits from other interactions), out-of-cone radiation (part of the shower not included in the jet cone), energy deposits below the noise threshold, and simulated response mismodelling [124]. The Jet Energy Scale (JES) calibration is performed through a combination of MC-based methods and in-situ techniques from which JES correction factors are derived and applied to jets [125]. The precision with which the reconstructed jet energy aligns with the true energy is known as the Jet Energy Resolution (JER) and is also taken into account. As an example, Figure 3.15 shows the jet energy resolution and its uncertainty as a function of p_T in fully calibrated PFlow+JES jets. For Large-*R* jets the energy and mass need to be calibrated, requiring a Jet Mass Scale (JMS) in addition to JER.

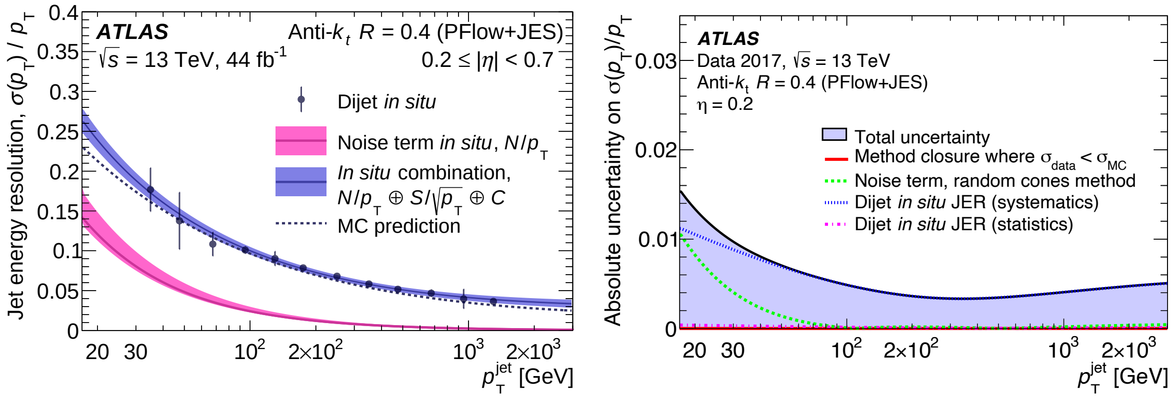

(a)

(b)

Figure 3.15: Fig. 29: (a) Relative jet energy resolution for fully calibrated PFlow+JES jets as a function of p_T. Error bars indicate total uncertainties, combining statistical and systematic components from dijet events. The resolution from Monte Carlo simulation is compared with data. (b) Absolute uncertainty in the relative jet energy resolution as a function of jet p_T, showing uncertainties from in situ measurements and data/MC simulation differences separately [125].

B-tagged jets

When a collision produces a b quark, it hadronises to a b hadron with relativistic energy and has a noticeable decay length of a few mm. This yields a specific jet configuration with a secondary vertex displaced from the primary vertex as illustrated in Figure 3.16. The DL1r b-tagging algorithm employs a deep neural network to process various input

---

[11] While the goal of jet reconstruction is to identify quark and gluon p_T, the particle jets that originate from these partons are what can be reconstructed in the event. True jet energy here refers to the true energy of jets at particle level originating from quarks and gluons

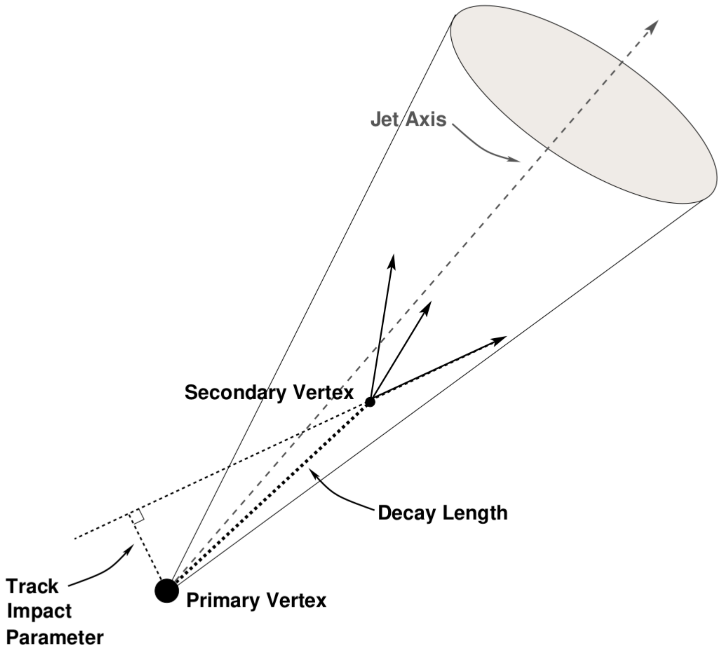

Figure 3.16: Topology of a b-quark jet originating from the primary vertex with a b hadron decaying at the secondary vertex after travelling a certain distance, taken from [126].

variables associated with the characteristics of the jet and classify the jet as b-tagged or not b-tagged [127, 128]. The inputs are selected to exploit key parameters such as lifetime, mass, and track properties for improved b-tagging performance. The DL1r algorithm uses variables that describe fundamental jet properties and high-level variables such as the signed impact parameter, d_0, the invariant mass of tracks at secondary vertices, the transverse distance between primary and secondary vertices, and the number of tracks associated with displaced vertices. Fundamental properties like jet p_T and η are used to ensure that b-quark jets across a wide range of p_T and η can be reconstructed.

The efficiency of the DL1r algorithm is measured in a sample of simulated $t\bar{t}$ events and single-cut operating points are defined. An operating point is typically defined by a certain value of the b-quark jet efficiency defined as the fraction of true b-quark jets correctly identified by the algorithm, and a corresponding misidentification rate which is the fraction of non-b-quark jets incorrectly identified as b-quark jets. For this analysis an operating point corresponding to an efficiency of 77% and a corresponding light-quark and gluon jet rejection factor of 200 and c-jet rejection factor of 6 is used. This is demonstrated in Figure 3.17. Calibrations are performed on b-tagging algorithms using $t\bar{t}$ events, yielding SFs to match performance in MC events to data and derive dominant sources of uncertainties [129]. Both small-R PFlow jets and $\mathrm{VR}_\mathrm{track}$ jets inside the Large-R jets satisfying this criteria are exposed to b-tagging for this analysis.

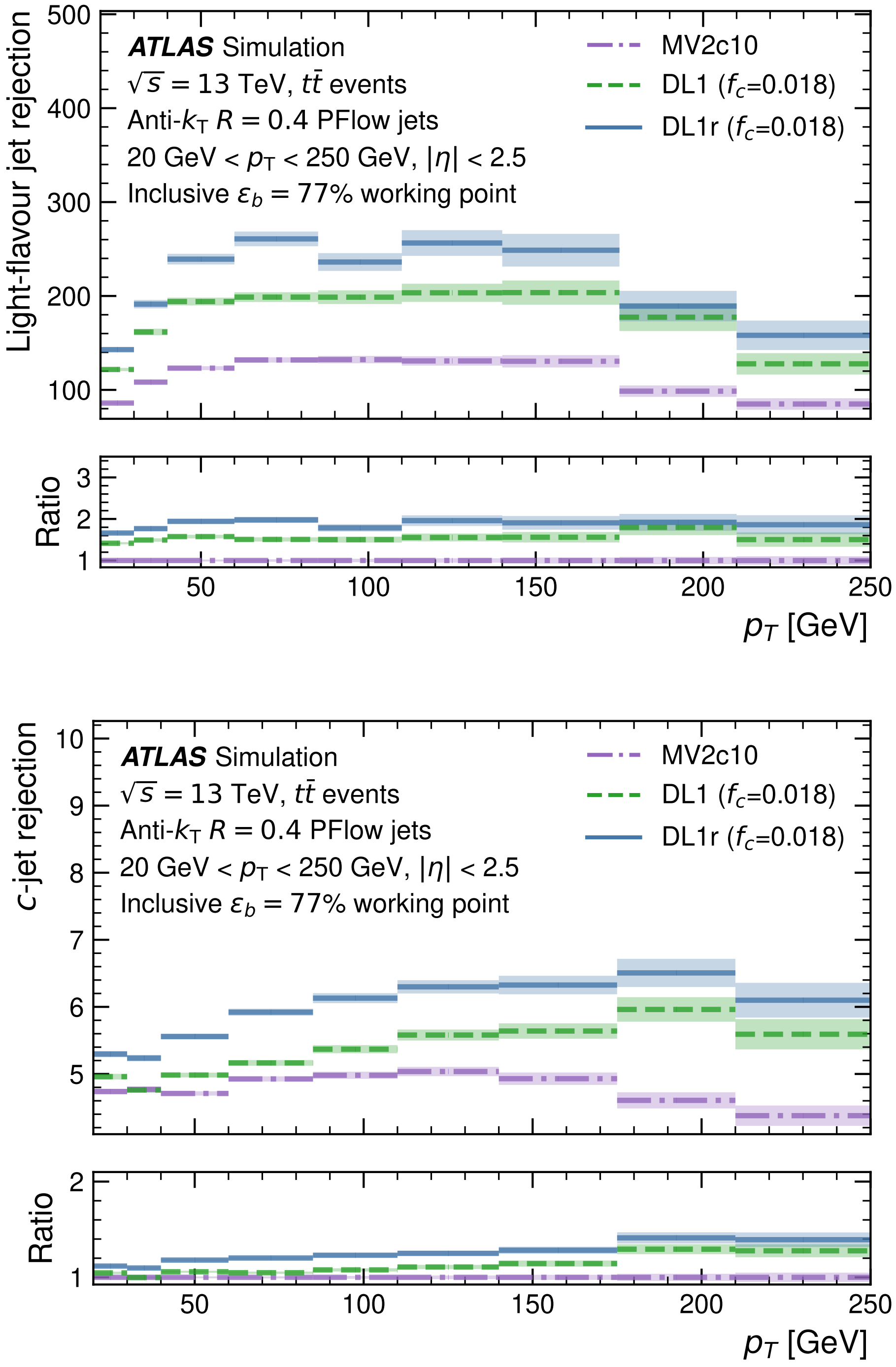

Figure 3.17: The light-flavour jet rejection and c-jet rejection for several high-level b-taggers, including DL1r, as a function of jet p_T, evaluated using simulated $t\bar{t}$ events. These are shown for various jet p_T bins at the 77% efficiency operating point, used in this thesis. The lower panels display each algorithm's performance relative to MV2c10, an older algorithm used for b-tagging [130].

Muons

Four types of muons are defined based on the sub detectors used in their reconstruction as illustrated in Figure 3.18. Combined Muons utilise a global refit combining hits from both the ID and MS, while Segment-Tagged Muons rely on local track segments in the MS chambers. Calo-Tagged Muons are identified by matching an ID track to calorimeter energy deposits, with optimised criteria for specific regions, while Standalone Muons are reconstructed solely based on MS tracks.

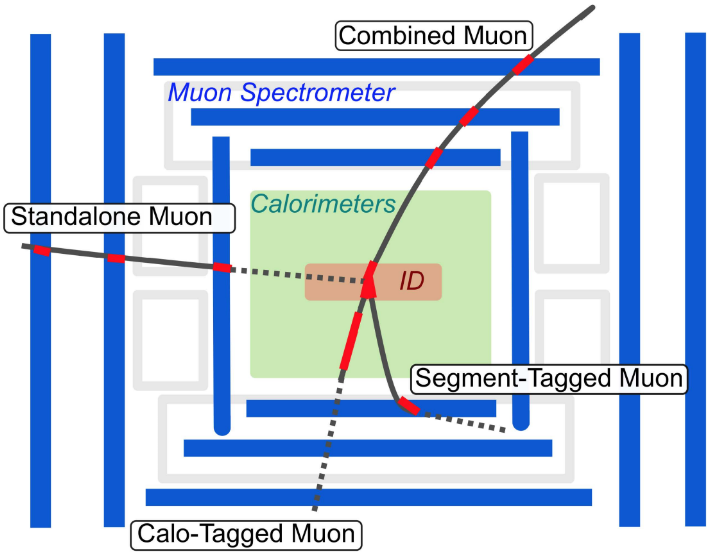

Figure 3.18: Different kinds of muons reconstructed in the ATLAS detector, taken from [131].

Muons are reconstructed using identification and isolation algorithms outlined in [132]. The identification algorithm yields selections: `Loose`, `Medium`, `Tight` and `High-`p_{T} and the medium selection is used. For isolation, a technique based on the particle-flow algorithm is employed [133] and the `PflowLoose_VarRad` isolation selection is used as defined:

- $p_{\mathrm{T}}^{\mathrm{varcone30}} + 0.4 \cdot E_{\mathrm{T}}^{\mathrm{neflow20}} < 0.16 \cdot p_{\mathrm{T}}^{\mu}$ for $500\,\mathrm{MeV} < p_{\mathrm{T}}^{\mu} \leq 50\,\mathrm{GeV}$
- $p_{\mathrm{T}}^{\mathrm{cone20}} + 0.4 \cdot E_{\mathrm{T}}^{\mathrm{neflow20}} < 0.16 \cdot p_{\mathrm{T}}^{\mu}$ for $p_{\mathrm{T}}^{\mu} > 50\,\mathrm{GeV}$

where $E_{\mathrm{T}}^{\mathrm{neflow20}}$ refers to the energy deposits from neutral particle-flow objects in a cone of size $\Delta R = 0.2$ around the muon, excluding the muon itself. The $p_{\mathrm{T}}^{\mathrm{varcone30}}$ is the transverse momentum sum within a variable cone size of $\Delta R = \min\left(\frac{10}{p_{\mathrm{T}}[\mathrm{GeV}]}, 0.3\right)$ around and without the muon. Similarly, $p_{\mathrm{T}}^{\mathrm{cone20}}$ is the transverse momentum sum within a fixed cone size of $\Delta R = 0.2$ around the muon, without the muon. The p_{T}^{μ} refers to the transverse momentum of the muon candidate.

Muon candidates can be reconstructed up to $|\eta| < 2.7$ which corresponds to the full muon detector acceptance. As an example, a set of selection algorithms and their reconstruction and identification efficiencies is shown in Figure 3.19 along with the total muon-ID efficiency. Similar to electrons, SFs are derived and calibrations performed using MC and data reconstructed muons.

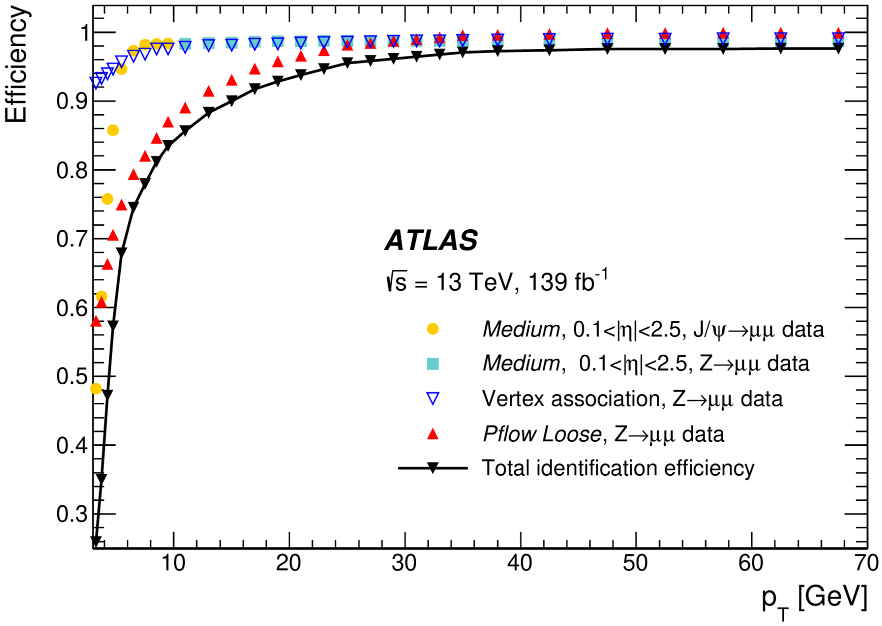

Figure 3.19: Overall reconstruction and identification efficiencies measured in data with $Z \to \mu^+\mu^-$ and $J/\Psi \to \mu^+\mu^-$ decays for prompt muons with $p_{\mathrm{T}} > 3\,\mathrm{GeV}$. The reconstruction efficiency with Medium selection is shown for both $Z \to \mu^+\mu^-$ and $J/\Psi \to \mu^+\mu^-$ decays. The Vertex association ($|d_0(\sigma)| < 3.0$ and $|\Delta z_0 \sin\theta| < 0.5\,\mathrm{mm}$) efficiency is shown for the $Z \to \mu^+\mu^-$ events. The efficiency of the PFlowLoose isolation criteria is shown for $Z \to \mu^+\mu^-$ events. Additionally, the total identification efficiency for satisfying simultaneously the Medium, PflowLoose isolation and vertex association criteria (black line) is shown together with its separate components (coloured markers). This image is taken from [133].

τ-leptons decaying hadronically

τ-leptons have a lifetime of 2.9×10^{-13} s. The decay length of a τ-lepton with p_{T} of $\mathcal{O}(10\,\mathrm{GeV})$ can be a few mm in the ATLAS detector. The τ-lepton decays 35% of the time into electrons and muons alongside neutrinos, and the remaining 65% of the time they decay into hadrons and neutrinos. The main decay modes are summarised in Table 3.3. The reconstruction of a τ-lepton depends on its decay mode.

Given the short lifetime of the τ-lepton, electrons or muons originating directly from the hard scatter (called prompt) and those originating from the decay of the τ are not always distinguishable. Hence isolated leptons, as described previously, are used to reconstruct

Table 3.3: Decay modes and branching fractions of the τ^- lepton, taken from [12] and the idea behind their reconstruction. In the decay modes, 'h' is used to denote 'hadron'.

Decay mode	Branching fraction (%)	Reconstruction
$\tau^- \to e^- + \bar{\nu}_e \nu_\tau$	17.8	Isolated leptons
$\tau^- \to \mu^- + \bar{\nu}_\mu \nu_\tau$	17.4	
$\tau^- \to h^- + \nu_\tau$	11.5	1 prong decay
$\tau^- \to h^- + \pi^0 + \nu_\tau$	26.0	
$\tau^- \to h^- + \pi^0 + \pi^0 + \nu_\tau$	9.5	
$\tau^- \to h^- h^- h^+ + \nu_\tau$	9.8	3 prong decay
$\tau^- \to h^- h^- h^+ + \pi^0 + \nu_\tau$	4.8	
$\tau^- \to$ other hadrons	3.2	

leptonically decaying τ-leptons. In the case of hadronic decays of τ-leptons, the visible component is reconstructed as $\tau_{\text{had-vis}}$ using jets from topological clusters with anti-k_t $R = 0.4$ [134, 135]. Tracks originating from the primary vertex, satisfying impact parameter requirements and selections based on a multivariate discriminant are associated to the $\tau_{\text{had-vis}}$ if they are within a cone of $\Delta R < 0.2$ around the jet axis. As shown in Table 3.3, the leading hadronic decay modes of τ-leptons contain one or three charged hadrons/pions and hence a $\tau_{\text{had-vis}}$ object must contain one or three associated tracks that together carry a total charge of ± 1. Reconstruction algorithms are used to construct $\tau_{\text{had-vis}}$ candidates given the above signature which can be mimicked by other objects like jets originating from quarks or gluons and electrons or muons. For 3-prong decays, a selection criterion of `RNN Loose` is used to reject jets from different sources misidentified as τ-leptons. Another selection of `BDT Medium` is used for 1-prong τ-lepton decays to reject electrons misidentified as τ-leptons. A selection criterion of `RNN Loose` is used to reject jets misidentified as 1-prong τ-lepton decays.

Missing Transverse Energy

The missing transverse energy, $E_{\text{T}}^{\text{miss}}$, is computed as the negative vectorial sum of the transverse momenta of all reconstructed objects in the event as well as a 'soft-term' [136, 137]. Mathematically, it can be represented by:

$$\vec{E}_{\text{T}}^{\text{miss}} = -\left(\sum \vec{p}_{\text{T}}^{\,\text{electrons}} + \sum \vec{p}_{\text{T}}^{\,\text{photons}} + \sum \vec{p}_{\text{T}}^{\,\text{taus}} + \sum \vec{p}_{\text{T}}^{\,\text{jets}} + \sum \vec{p}_{\text{T}}^{\,\text{muons}} + \sum \vec{p}_{\text{T}}^{\,\text{soft}}\right) \quad (3.11)$$

The soft term consists of tracks matched to the PV but not matched to the reconstructed objects used in the calculation. The magnitude of $\vec{E}_{\text{T}}^{\text{miss}}$ is used to quantify the amount of missing momentum in an event. It is commonly called missing transverse energy and defined as:

$$E_{\text{T}}^{\text{miss}} = |\vec{E}_{\text{T}}^{\text{miss}}| = \sqrt{(E_x^{\text{miss}})^2 + (E_y^{\text{miss}})^2} \quad (3.12)$$

Additionally. a quantity called $E_{\text{T}}^{\text{miss}}$ significance is calculated to quantify if the $E_{\text{T}}^{\text{miss}}$ originates from truly invisible particles or mismeasured energies. A likelihood based discriminant,

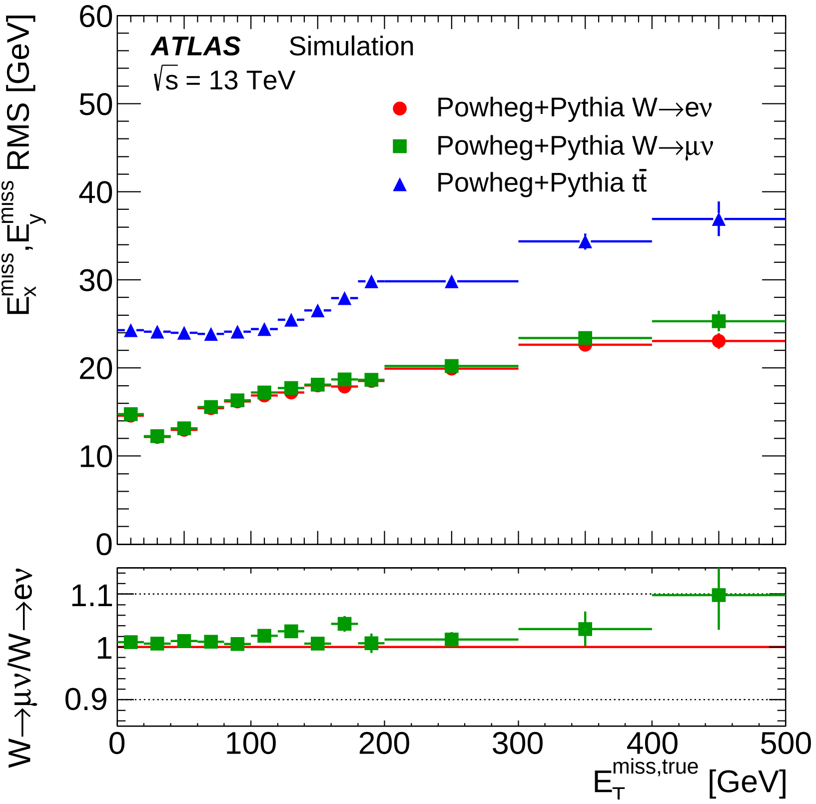

Figure 3.20: The $E_{\mathrm{T}}^{\mathrm{miss}}$ resolution measured by $\mathrm{RMS}_{x(y)}^{\mathrm{miss}}$ as a function of the true missing transverse momentum $E_{\mathrm{T}}^{\mathrm{miss,true}}$ for the $W \to e\nu$, $W \to \mu\nu$, and $t\bar{t}$ samples from MC simulations, taken from [137].

as detailed in [138], taking into account all objects in the event and their respective, resolutions is used. This object based $E_{\mathrm{T}}^{\mathrm{miss}}$ significance is defined as:

$$\text{Object based } E_{\mathrm{T}}^{\mathrm{miss}}\text{significance} = \frac{E_{\mathrm{T}}^{\mathrm{miss}}}{\sqrt{\sigma_L^2(1-\rho_{LT}^2)}} \tag{3.13}$$

where σ_L is the longitudinal resolution of all objects in the event, and ρ_{LT} is the correlation factor of the longitudinal L and transverse T resolutions. The object based $E_{\mathrm{T}}^{\mathrm{miss}}$ significance is an important discriminant in identifying events with true $E_{\mathrm{T}}^{\mathrm{miss}}$ particles, particularly important in events with a large number of jets [138]. This can be understood looking at how $E_{\mathrm{T}}^{\mathrm{miss}}$ and object-based $E_{\mathrm{T}}^{\mathrm{miss}}$ significance behave as discriminating variables in identifying events with true $E_{\mathrm{T}}^{\mathrm{miss}}$ as shown in Figure 3.21. A simpler event based $E_{\mathrm{T}}^{\mathrm{miss}}$ significance, used in other analyses, is also shown as a benchmark. Event based $E_{\mathrm{T}}^{\mathrm{miss}}$ significance is defined as $\frac{E_{\mathrm{T}}^{\mathrm{miss}}}{\sqrt{\sum E_{\mathrm{T}}}}$, wherein $E_{\mathrm{T}}^{\mathrm{miss}}$ is the missing transverse energy and $\sum E_{\mathrm{T}}$ is the scalar sum of the transverse energies of all objects in the event.

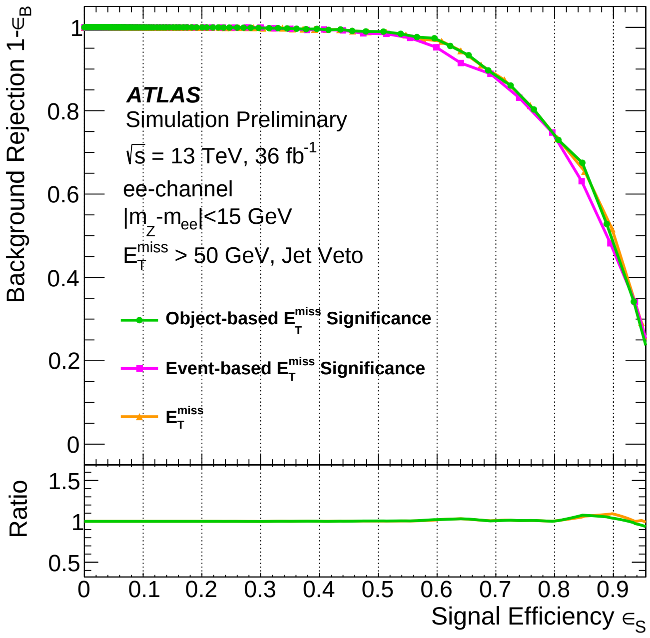

(a) Jet veto

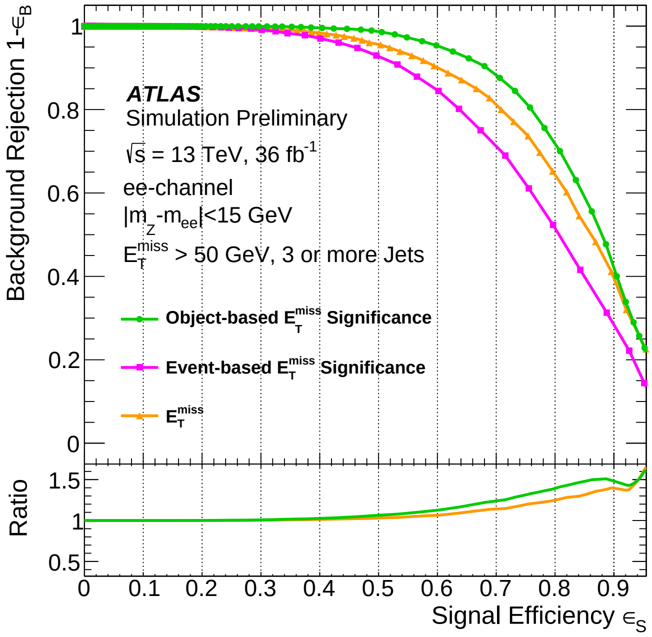

(b) Three or more jets

Figure 3.21: Background rejection versus signal efficiency in simulated $Z \to e^+e^-$ and $ZZ \to e^+e^-\nu\bar{\nu}$ samples with $Z \to e^+e^-$ selection and $E_T^{\text{miss}} > 50$ GeV. Performance is shown for E_T^{miss}, event-based E_T^{miss} significance, and object-based E_T^{miss} significance in events with (a) jet veto and (b) three or more jets. The lower panel shows the ratio of other definitions to event-based E_T^{miss} significance. This image is taken from [138].

CHAPTER 4

Strategy to find New Physics

This chapter provides a basic structure of how a search can be performed at the LHC with the ATLAS detector and describes the challenges and opportunities the $t\bar{t}$ +$E_{\mathrm{T}}^{\mathrm{miss}}$ final state signature provides for finding new physics. Following this, the case is made for why machine learning is the optimal choice to get the best results.

4.1 Structure and Challenges of a search with ATLAS data

One way to find new physics at the LHC is via model-dependent searches. This is an approach where predictions are made by specific theoretical models and then probed experimentally. The model of interest predicts a new "signal process" that can be detected by the detector. In this thesis, the signal processes that are probed predict particles of new physics produced in association with top-quark pairs, requiring top quarks to be present in the event. Some new physics particles, such as Dark Matter candidates, do not interact with the detector and their presence can only be indirectly inferred from the $E_{\mathrm{T}}^{\mathrm{miss}}$, described in Section 3.3.3. The signature left by these signal processes in the detector is henceforth referred to as the "$t\bar{t} + E_{\mathrm{T}}^{\mathrm{miss}}$" final state.

The final state, although defined to be sensitive to the signal process, is exposed to interference from other Standard Model (SM) processes that can produce a similar signature. These are called "background processes". The task is then to define an analysis strategy that retains events from the signal process while rejecting events from background processes. In reality, a perfect separation between the background and signal events will not always be possible. Rather, the goal is to simultaneously increase background rejection and signal acceptance to maximise the sensitivity of the search. To achieve this objective, it is necessary to select a variable that differentiates between background and signal events. Events can be grouped into bins so that each bin contains varying contributions of both background and signal events as illustrated in Figure. 4.1. The data can then be fit to the predicted signal and background templates to determine whether the data distribution is compatible with the background-only hypothesis or the background+signal hypothesis.

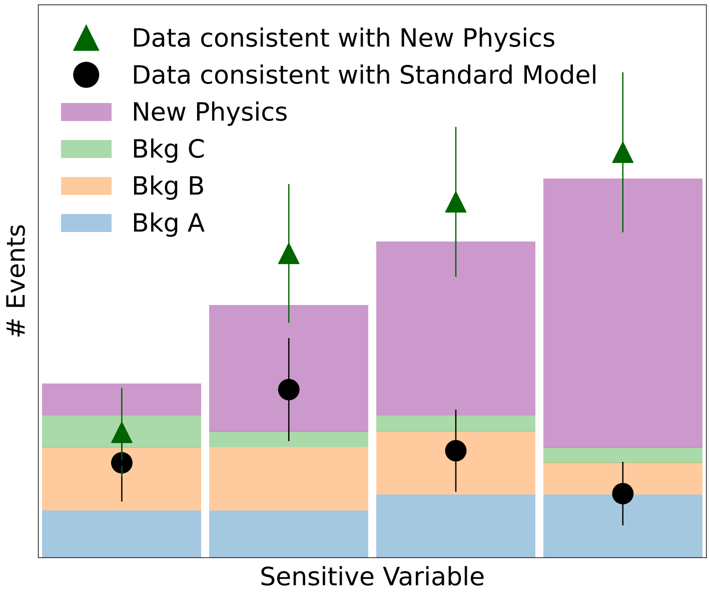

Figure 4.1: An illustration of the expected distribution of a sensitive variable for three SM processes (Bkg A, Bkg B and Bkg C) and one New Physics process. In addition, two possible distributions are shown for data representing scenarios with the presence or absence of the new physics process.

To obtain signal and background templates, Monte Carlo generators are used to simulate background and signal events as they would appear in the detector. The strategy is initially developed by studying these simulated events, deliberately avoiding the examination of real data, particularly in regions of phase space where the signal events are expected to occur. This precaution is taken to prevent potential biases in the development of the analysis strategy. Instead, a representation known as 'pseudo-data' is used to mimic the characteristics of real data and serves as a temporary substitute for optimising the analysis. In a search, pseudo-data can be constructed as a sum of background events to best model the scenario where the data describes the contributions from SM processes to describe the background-only hypothesis, or as a sum of background and signal processes to describe the background+signal hypothesis.

The Monte Carlo generated events have their own uncertainties due to limitations in the experimental and theoretical modelling. Therefore, even in a phase space where no new physics is expected, the pseudo-data and the real data may not match perfectly. The individual background processes, contributing to pseudo-data, must be adjusted for better alignment with observed data. For this, events are divided into regions where almost no signal events lie, called Control Regions (CRs), and regions enhanced in signal events, called Signal Regions (SRs). CRs are used to extract information about background processes and the corrections derived from CRs are applied to background processes in the Signal Regions. Before looking at real data in the SRs, where pseudo-data is used until the analysis strategy is fully defined, intermediate validation regions (VRs) distinct from both the CRs and SRs are defined. These regions can be used to independently verify that the corrections applied to the background processes do indeed improve the agreement between simulation of background processes and real data, before proceeding to reveal or 'unblind' the SRs.

4.2 $t\bar{t}$+$\mathbf{E}_\mathbf{T}^{\mathbf{miss}}$ as a probe for New Physics

Models that predict the production of dark matter candidates at the LHC often target WIMP DM candidates in the GeV to TeV mass range. This is rather at the heavier end of the mass spectrum of SM particles, and the top quark, being the heaviest SM particle, proves to be very interesting as a way to search for these particles. The model probed in this search postulates the presence of a mediator particle serving as a bridge between the SM and dark sector as depicted in Figure 4.2a. If the mediator particle was to have spin-0, it can be further hypothesised to have Yukawa-like couplings to satisfy stringent limits set by the LHC on flavour violation [46]. This implies that the coupling is proportional to the mass of the particles involved in the interaction. Therefore, on the SM side of the interaction, the mediator would couple to the top quark favourably as it is the heaviest known SM particle, followed by the b quark. On the DM side, the mediator is postulated to decay into a pair of fermionic DM candidates as shown in figure 4.2b. In this search the final state with top quarks is probed, and hence the process would appear as top quarks and E_T^{miss} in the ATLAS detector.

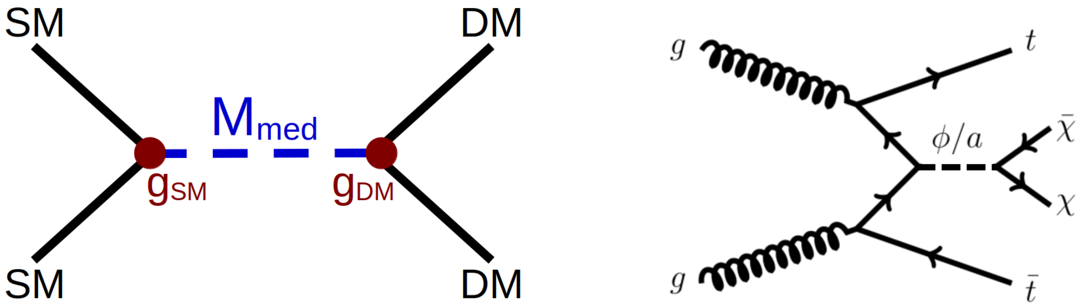

(a) (b)

Figure 4.2: (a) A general illustration of how a mediator particle can connect SM particles to hypothetical DM particles. (b) The specific case where the mediator is scalar/pseudoscalar in nature and decays into two fermionic dark matter candidates.

Additionally, stop-pair production is an important channel to search for SUSY at colliders as explained in Section 2.2. A simplified model to search for stop-pair production can be employed, where only the stop quark ($\tilde{t}$) and the neutralino ($\tilde{\chi}_1^0$) are probed. This corresponds to the case where the stop quark ($\tilde{t}$) and the neutralino ($\tilde{\chi}_1^0$) are the lightest particles in the MSSM spectra and hence decoupled from the rest of the MSSM. If R-parity is conserved, the neutralino is stable, invisible and interacts only weakly with SM particles. This makes it, additionally, a viable DM candidate. In this thesis, the scenario where the stop quark decays to a top quark (on-shell or off-shell) and a neutralino is probed. As shown in Figure 4.3, this results in the $t\bar{t}+E_{\mathrm{T}}^{\mathrm{miss}}$ final state.

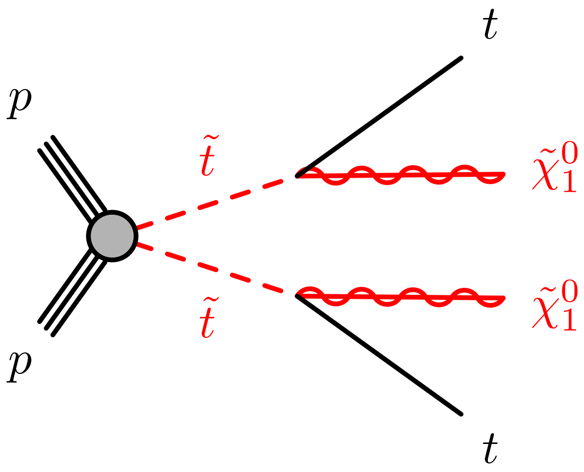

Figure 4.3: Pseudo Feynman diagram depicting the pair production of stop quarks as a result of proton collisions where each stop quark ($\tilde{t}$) decays into a top quark and a neutralino ($\tilde{\chi}_1^0$).

The LHC is a top quark production factory. Figure 4.4 presents a summary of the cross-section measurements of various top-quark processes measured with the ATLAS experiment. Stop-quark pair production, if realised in nature, could be produced at the LHC with cross sections comparable to the $t\bar{t}$ SM process for low-mass stop quarks as illustrated in Figure 4.5a. However, this cross section diminishes exponentially with increasing stop-quark mass. For simplified DM models resulting in $t\bar{t}+E_{\mathrm{T}}^{\mathrm{miss}}$, the expected cross section for a specific benchmark at $\sqrt{s}=14$ TeV is illustrated in Figure 4.5b. While these new physics models could occur with a cross section accessible to the LHC, the kinematic phase space they would be produced in is dominated by SM processes, predominately $t\bar{t}$. Nonetheless, there exist kinematic differences between the SM and new physics processes that can be exploited.

The challenge remains, firstly, in reconstructing events with top quarks and invisible particles. Furthermore, the kinematic differences between final state particles produced by SM processes and those produced by new physics processes must be exploited to give good discrimination between the two scenarios. It is expected that machine learning can perform these tasks optimally and is further motivated in Section 4.3.

4.2.1 1-Lepton (1L) Final State

The 1L final state describes a specific type of $t\bar{t}$ decays as explained in this section. Top quarks almost always (95.7%) decay into a W boson and a b quark [142]. The W boson can then decay into a lepton and neutrino, called the leptonic decay, or to two quarks , called the hadronic decay. The top quark decay is also called leptonic or hadronic based on the decay mode of the

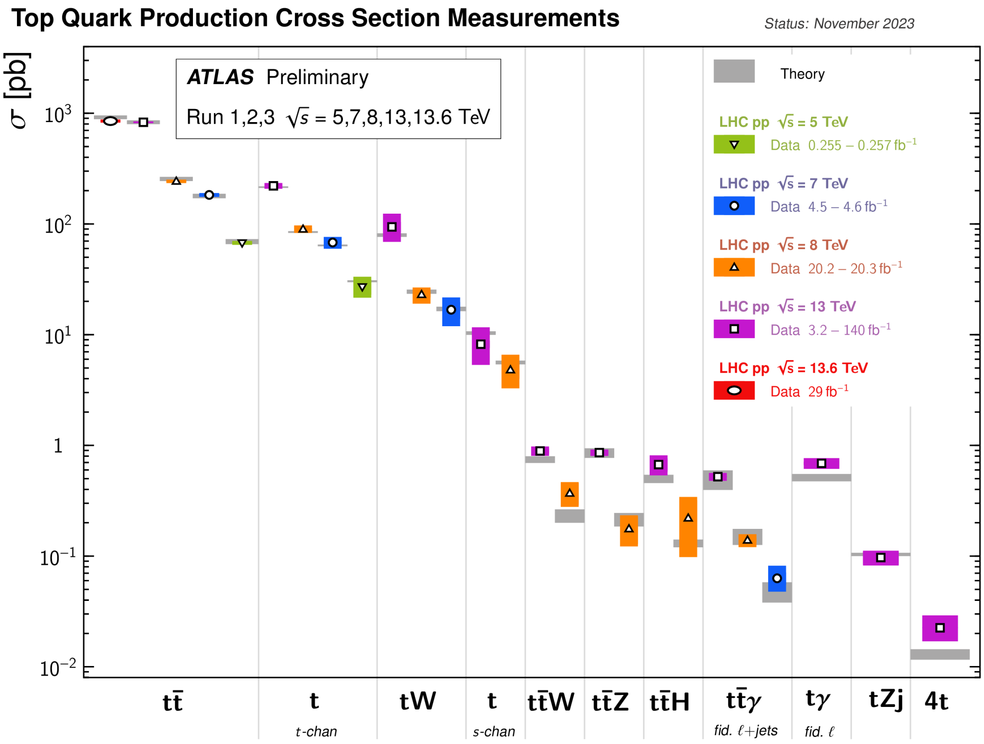

Figure 4.4: A summary of cross sections for top quark processes measured by ATLAS and compared with SM predictions, taken from [139].

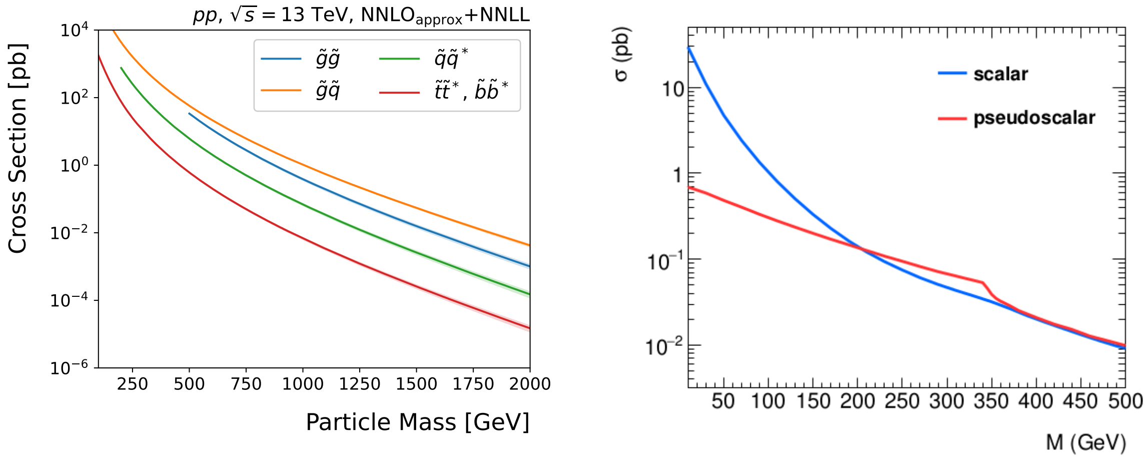

(a)

(b)

Figure 4.5: (a) The predicted cross sections of pp $\rightarrow$ sparticles as a function of sparticle mass at $\sqrt{s} = 13\,\text{TeV}$, reproduced from [140]. (b) The production cross-section for pp $\rightarrow$ $t\bar{t} + E_{\text{T}}^{\text{miss}}$ as a function of mediator mass at $\sqrt{s} = 14\,\text{TeV}$ employing $m_\chi = 1\,\text{GeV}$ and $g_{SM} = g_t = g_{DM} = 1$ with the top quark as the only SM particle in the interaction, taken from [141].

W boson. This results in three decay modes of the top-quark pair: fully hadronic: both top quarks decay hadronically; semileptonic: one top quark decays leptonically and one top quark hadronically; and lastly the leptonic: both top quarks decay leptonically.

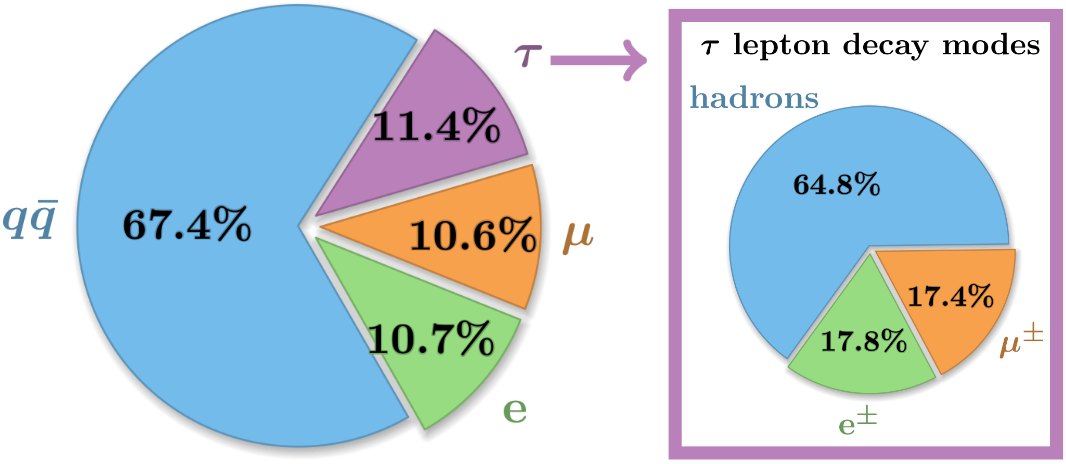

Figure 4.6: The pie chart on the left shows the decay modes of the W boson or top assuming BR(t → Wb) to be 100%. The right pie chart shows the decay modes of τ-leptons, adapted from [76].

As can be seen in Figure 4.6, the branching fraction of the hadronically decaying top quark is about twice that of the leptonically decaying top quark. So, the fully hadronic top-quark pair production has the highest cross-section of the three channels. However, in the large multiplicity environment of the LHC with many jets per event, fully hadronic final states are much more difficult to reconstruct than leptonic final states. The semileptonic channel provides a trade-off in yield and reconstructability of events. The developments presented in this thesis were performed on the semileptonic final state followed by a combination with the previously published fully hadronic and leptonic final states. It must be noted that τ-leptons decay both hadronically and leptonically. In this analysis, the hadronically decaying τ-leptons are excluded from consideration and only top quarks decaying into a muon/electron (promptly or via a τ-lepton) are considered.

4.3 A Machine Learning Solution

Reconstructing events with $t\bar{t}$ $+E_{\mathrm{T}}^{\mathrm{miss}}$ in the final state is challenging because the new physics particles as well as top quarks are not directly detected by the ATLAS detector. Top quarks need to be reconstructed from their decay products and presence of invisible particles has to be inferred from limited information:

- The top quark, unlike other quarks, is the only quark that decays before forming hadrons due to its extremely short lifetime of approximately 5×10^{-25}s [143]. It decays before interacting with the detector directly, implying that the decay products need to be found in order to reconstruct the top quark. For the leptonically decaying top quark, this requires finding the resulting b quark, charged lepton and neutrino, while for the hadronically decaying top quark, the resulting b quark and two light quarks must be found. By requiring only one lepton in the event which is reconstructed quite efficiently by the ATLAS detector, the case for the leptonically decaying top gets easier. However, for the hadronically decaying top, the task is significantly tougher.

- The new particles are invisible to the detector and can only be partially reconstructed in the transverse plane using $E_{\mathrm{T}}^{\mathrm{miss}}$. The calculation and interpretation of the longitudinal component is more complex due to uncertainties associated with the longitudinal momentum of partons within the protons that collide. The quantity of $E_{\mathrm{T}}^{\mathrm{miss}}$ attempts to measure the overall imbalance in an event, meaning that if the $E_{\mathrm{T}}^{\mathrm{miss}}$ arises from more than one undetected particle, which is often the case, the individual particles are not reconstructed separately. Furthermore, the reconstruction of $E_{\mathrm{T}}^{\mathrm{miss}}$ relies on the reconstruction of all other particles in the event and hence comes with quite some uncertainty. However, distinct kinematic distributions between new physics processes and known ones offer clues.
- Typically, kinematic variables such as combined p_{T} of particles, the relative $\Delta\phi$ between particles, etc. are used to reconstruct high level variables or complex physics objects to distinguish between different physics processes. A Machine Learning approach provides a more comprehensive utilisation of all the available information by exploiting its capability to extract subtle correlations or patterns among these kinematic variables.

In this analysis, machine learning is employed for hadronic top quark reconstruction and to provide discrimination between signal and background processes using kinematic differences. Additionally, machine learning is also used to define the CR-VR-SR strategy of this analysis.

4.3.1 Hadronic Top Quark Reconstruction

Collisions recorded by the ATLAS detector can contain a significant number of jets. In particular, for events selected to increase the probability of containing two top quarks, as was done in this search, up to 15 high p_{T} jets can be observed. These jets could originate from the top quark decay but also from the hadronisation of gluons, initial state radiation or final state radiation. Pileup jets from collisions other than the primary collision in the same bunch crossing can also have high energy and appear as jets from the collision of interest. Events that do not produce top quarks, but still produce jets, like W+jets in Figure 4.7, consist of jet combinations that may look like the decay products of the top quark but do not actually come from a top quark.

Since both a leptonic and a hadronic top quark are present in the events studied here, there should be two b-quark jets, one from each top quark, in each event. While b-quark jet tagging has limited efficiency as explained in Section 3.3.3, even in the case that both b-quark jets are

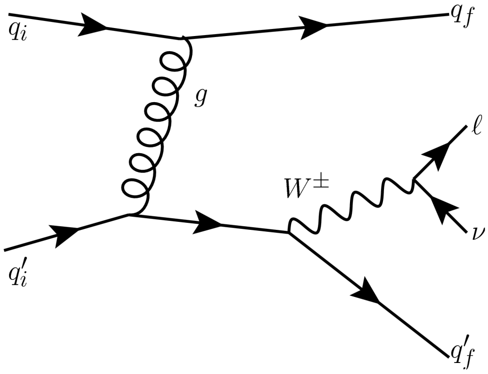

Figure 4.7: Example of a leading order diagram for the production of the W+jets SM process, taken from [144].

correctly reconstructed and identified, it is not clear a-priori which b-quark jet comes from which top quark.

These challenges are addressed traditionally by reconstruction algorithms that group together objects that are geometrically close and result in a mass close to the known top mass. Machine learning based algorithms can perform these tasks while also looking at deeper correlations in objects to reconstruct top quarks. In this thesis, machine learning is used to solve the combinatorial problem and identify the multiplet of jets which define the hadronic top candidate.

4.3.2 Discrimination of Signal and Background Processes

Typically, observables that capture differences in kinematic properties of the SM and new physics processes are used to differentiate signal events from background events. Traditionally, the approach employs a set of such variables and a combination of rectangular cuts on the individual kinematic distributions – for instance, setting a specific cut value for Observable 1 and another for Observable 2. However, the true sweet spot for separating signal from background often lies in a combination of these variables, as illustrated in Figure 4.8. Machine learning has the ability to leverage various kinematic distributions simultaneously and consider additionally their correlations to create complex shaped cuts. This advanced approach surpasses the limitations of relying solely on individual cuts on multiple kinematic variables ensuring better classification.

4.3.3 CR-VR-SR Strategy

The SRs introduced in Section 4.1 are traditionally designed for a given new physics model, with the goal of retaining the maximum number of events from the chosen model while rejecting as much background as possible. Depending on the remaining background, specific CRs can be defined to improve the prediction of these remaining background processes. This requires defining a selection orthogonal to the SR without moving too far away from the phase

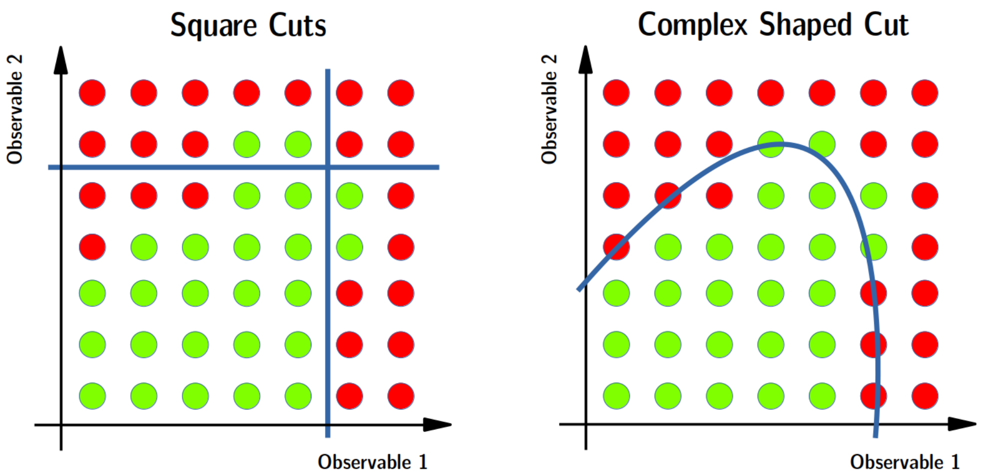

Figure 4.8: An illustration to show how a complex shaped cut provides better classification than rectangular cuts.

space where the new physics events may lie. This is because the goal of a CR is to enhance the precision of background estimation in the SR. If the CR is chosen far from the SR, the assumption that the background processes in the CR accurately represent the background in the SR may become less valid.

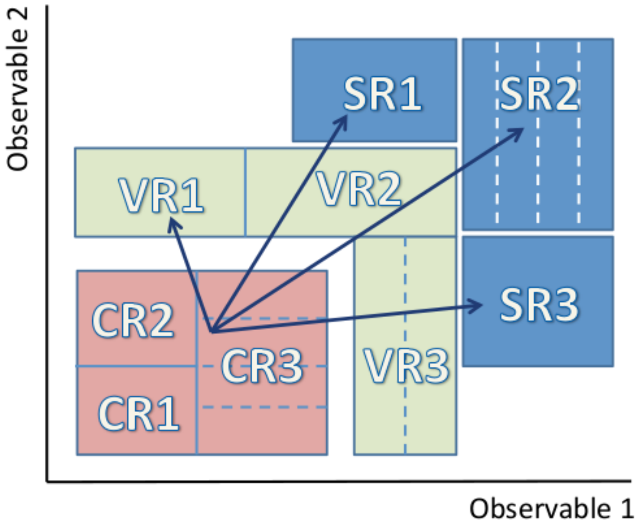

Figure 4.9: Design Schematic of Control Regions, Validation Regions and Signal Regions, taken from [145].

Figure 4.9 shows graphically one example of how this is done. The new physics models are expected to lie in the tails of the two distributions, corresponding to large values of Observable 1 and Observable 2. Multiple signal regions are designed to target potentially different new physics models. Each signal region may be dominated by different background processes. In an ideal case, SR1 manages to target a particular signal model while rejecting almost all but one dominant background process. CR1 can then be used to improve the prediction of the dominant background in SR1. To validate this process, a region called VR1 can be further defined to lie in the kinematic phase space between CR1 and SR1. It should be noted that this is an idealised scenario; it is relatively difficult to achieve high purity for a single background per control region and more often the signal regions are dominated by different combinations of background processes. More complex strategies allow multiple backgrounds to be determined across multiple control regions.

Machine learning provides a somewhat natural way to define these control, validation, and signal regions. With machine learning, the score of the classifier inherently has a distribution such that "background-like" events lie at low scores and "signal-like" events lie at higher scores. Therefore, CRs, VRs, and SRs can be naturally defined as a function of the classifier score as shown in Figure 4.10. The different processes have different shapes when binned in classifier score but the CRs are not pure in a given background processes. Within the control regions, better separation of individual background processes can be achieved by using different observables that provide separation between individual background processes. This strategy can be developed while relying on a predefined variable namely the classifier score, to smoothly transition the events used in the CR to the VR and SR.

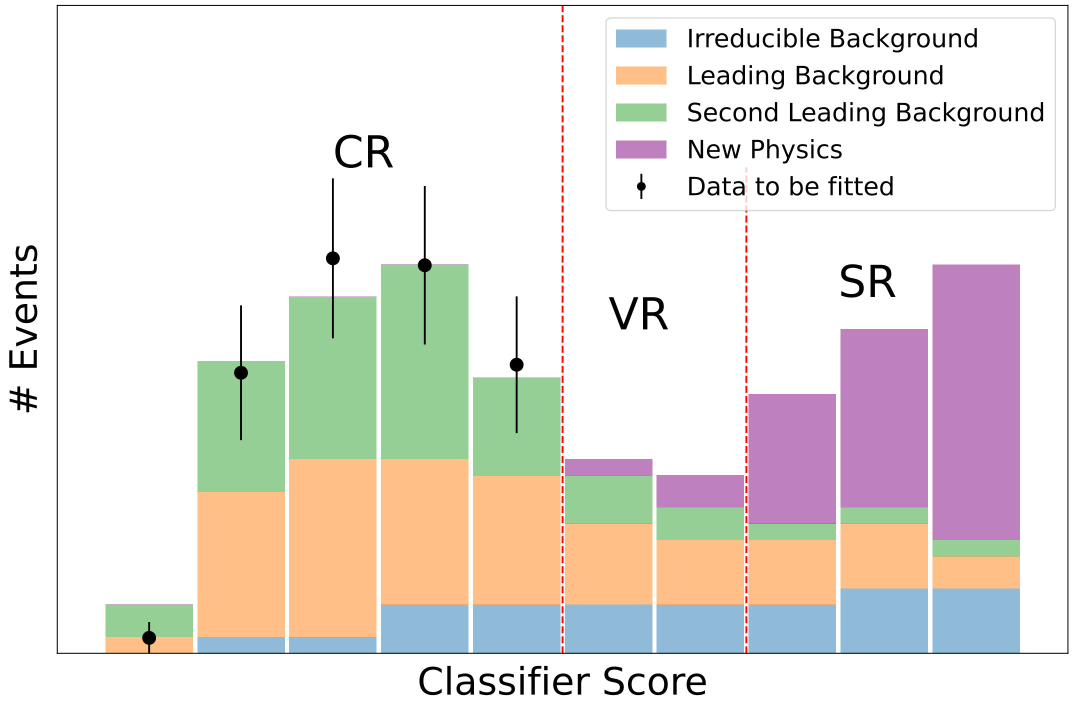

Figure 4.10: An illustration of how a CR, VR and SR can be defined as a function of Classifier Score. The data in CRs is used to enhance precision of background processes.

4.4 Neural Network Basics

In the landscape of particle physics, Boosted Decision Trees (BDTs) and Neural Networks (NNs) have dominated as the ML technique of choice [146], both of which fall under the category of 'supervised learning'. This is a family of algorithms that learns to map input data to corresponding output labels based on example input-output pairs. Unsupervised learning methods, such as clustering algorithms and anomaly detection, provide the possibility of automatically identifying patterns in the data without being explicitly told what to look for. While the idea of NNs has been around for decades, their use was limited by the available computing resources. A move to Deep Neural Networks (DNNs) and Graph Neural Networks (GNNs), bigger NNs that can learn more complex representations of data, has been made possible by advances in computing. In this thesis, the focus lies on DNNs, chosen for their adaptability to different physics tasks and this section provides an overview of fundamental concepts important to understand NNs.

4.4.1 Fundamental Components

The fundamental unit of a neural network is a **node**, sometimes also called a neuron. Each node performs a computation on the input(s) it receives and produces an output as shown in Figure 4.11. Each input quantity has a weight associated with it. The node takes a weighted sum of the inputs and adds additionally a "bias" value and passes it to an "**activation function**" yielding the node output. Akin to a neuron in the brain, once information is received by the neuron, it can decide based on the input received if the neuron must be fired or not. This firing or activation of the neuron inspires the naming of the activation function. However, mathematically, it simply provides the node, and thereafter the network as a whole, the ability to perform non-linear transformations on the weighted sum of inputs. The activation function for the nodes is defined in the network design. Some examples of activation functions are Tanh, Sigmoid, ReLU, and Leaky ReLU all of which are illustrated in Figure 4.12. The **weights** and **biases** are the free parameters calculated during the network training.

These individual nodes are arranged in **layers** which can be of three types; input, output and hidden. The input layer consists of input nodes where information, like a set of kinematic variables useful for discrimination, is provided to the network and no computation is done in these nodes. The hidden nodes are the ones that perform computations outlined above. The output layer can consist of multiple output nodes that combine the information learned in the hidden layers to provide a result. **Feed-forward** neural networks, like the ones used in this thesis, are where the information flows from input to output making it from layer to following layer. The nodes within a layer are not connected with each other and information does not cycle.

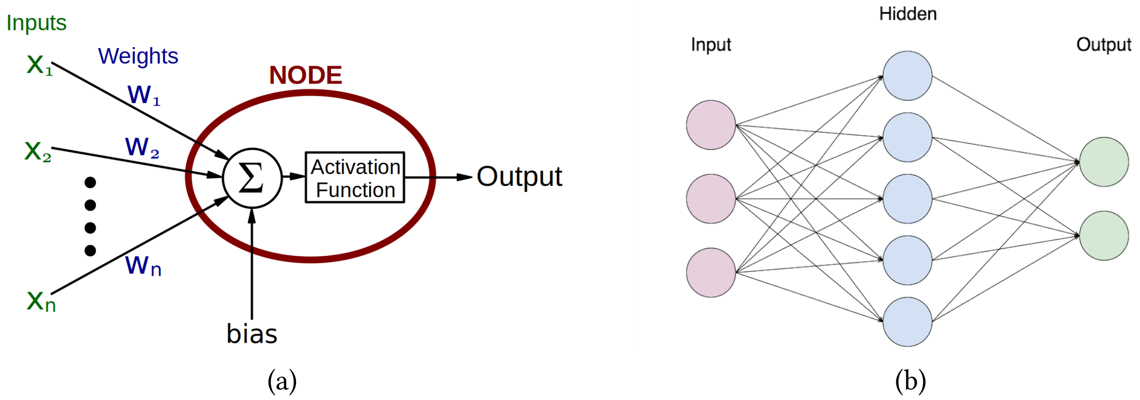

Figure 4.11: (a) Graphic depicting the computation performed inside a node of a neural network. (b) The three different types of layers in a classical neural network, taken from [147].

4.4.2 Training, Optimisation and Performance

Networks can be designed to perform a variety of tasks like classification, regression, pattern recognition etc. For a network to perform a certain task, it first requires a dataset on which it can be trained. This requires data where the true result is known and each input data point is labelled with its output, called the labelled dataset. In practice, a labelled dataset is divided into a **'training' dataset**, a **'validation' dataset** and a **'test' dataset**. A network performs a fit on the training data, meaning that it tunes the weights and biases till the predicted result is closest to the true result for a large fraction of the training data. The validation dataset is used to evaluate the model on an independent dataset and asses if the model is general enough to achieve similar accuracy on 'unseen' data as 'seen' data. The test dataset is another independent dataset used to evaluate the final performance metrics of the model.

When the training dataset is passed through the network, predicted output values are computed along with a **loss function** L, which quantifies the difference between true output values (y_i) of the dataset and predicted values (p_i) computed by the network. This loss function is used to improve the model and reduce the gap between the predicted and true values. The loss functions can be as simple as mean squared error, summed over N number of data points being evaluated, for tasks like regression:

$$\text{Mean Squared Error Loss,}\quad L = \frac{1}{N}\sum_{i=1}^{N}(p_i - y_i)^2 \tag{4.1}$$

or cross entropy for tasks like binary classification:

$$\text{Binary Cross-Entropy Loss,}\quad L = -\frac{1}{N}\sum_{i=1}^{N} y_i\cdot\ln(p_i) + (1-y_i)\cdot\ln(1-p_i) \tag{4.2}$$

or made more complex depending on the task that needs to be performed.

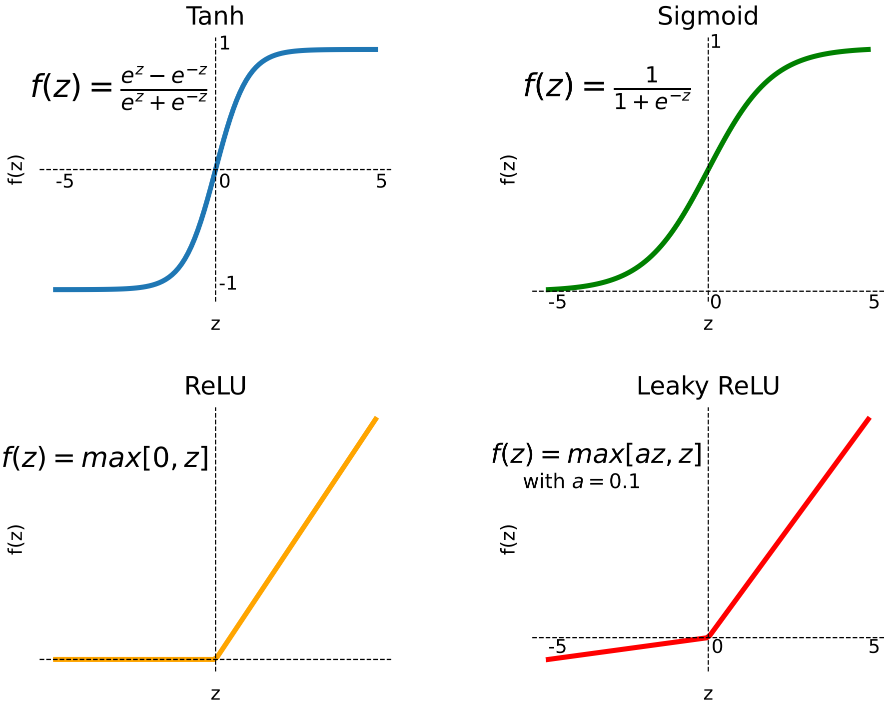

Figure 4.12: Examples of some activation functions used commonly in Neural Networks.

For every forward pass of the training data, a **backward propagation** of errors is performed to minimise the loss function by iteratively adjusting the network parameters (weights and biases). This requires computing the gradient of the loss function with respect to the model parameters. The update to the parameters is made iteratively, correcting each parameter by a certain amount at every iteration quantified by the **learning rate** (α) of the network. This is most simply realised using 'gradient descent', wherein the parameters, weight w and bias b are changed to reduce the loss as follows:

$$w_i = w_{i-1} - \alpha \cdot \frac{\partial L}{\partial w_i} \quad , \quad b_i = b_{i-1} - \alpha \cdot \frac{\partial L}{\partial b_i} \tag{4.3}$$

More advanced functions can be used to modify the parameters as explained in [148]. Examples include functions that use 'momentum' designed to consider a cumulative direction of previous updates made to each parameter.

The training dataset is passed multiple times through the network, where each pass of the full training data is called an "**epoch**". In practice, the training dataset is divided into smaller "**batches**", assuming it is large enough. The model parameters and learning rate are updated after every batch of data is passed through the network. This speeds up the processing of data and makes better use of computational resources. A small learning rate makes more precise calculations but may take much longer to reach the loss function minimum, however, with a large learning rate it is possible that the minimum is overshot. Optimisation algorithms are used to adjust the learning rate over the course of the training, for example, by starting with a large learning rate at the beginning and exponentially decaying the learning rate over batches. The Adam (Adaptive Moment Estimation) optimiser is an example of an algorithm that adapts the learning rate throughout the training and is extremely efficient for deep neural networks [148].

The following properties define the **hyperparameters** of the NN; number and type of layers, number of nodes per layer, activation functions, learning rate, loss function, number of epochs and batch size used during the training. These are parameters of the training that affect how fast a minimum is reached and also affect how close to the true minimum the network actually reaches. The bigger the number of layers and nodes per layer, the longer each epoch takes. However, the bigger a network, the more parameters it can use to describe the parameter space it is trying to fit.

During the training, loss and accuracy curves are plotted for the training and validation datasets against epochs. The loss curve is simply the value of the loss function at each epoch, while the accuracy is calculated by dividing the number of correct predictions by the total number of predictions of the model. Correct predictions are defined based on the task. For example, in the case of binary classification, a threshold of 0.5 is used to define the two classes. A well-performing model should exhibit both rising accuracy and dropping loss during the training process for both training and validation datasets as depicted in Figure 4.13a. On the other hand, Figure 4.13b illustrates an example where the value of the loss function reduces over epochs for the training dataset but starts to increase at a particular epoch for the validation dataset[1]. This points to 'overfitting', describing the scenario where the model is too big and describes details in the training data very well but is not generalisable to the validation data. The hyperparameters of the model need to be adjusted to achieve a configuration that doesn't lead to overfitting, while achieving high accuracy and reduced loss across training and validation datasets.

In order to summarise the performance of a model, the **Area Under the Curve (AUC)** metric is used often in machine learning classification tasks. Specifically, the AUC refers to the area under the Receiver Operating Characteristic (ROC) curve. The ROC curve is a graphical representation that plots the True Positive Rate (TPR) against the False Positive Rate (FPR) which are defined as follows:

$$\mathrm{TPR} = \frac{\text{True Positives}}{\text{True Positives} + \text{False Negatives}}, \quad \mathrm{FPR} = \frac{\text{False Positives}}{\text{False Positives} + \text{True Negatives}} \tag{4.4}$$

By default, a classification threshold of 0.5 is used. This means that any prediction above 0.5 belongs to the positive class and anything below 0.5 to the negative class. A perfect classifier would have an AUC of one corresponding to a ROC curve that reaches the top left corner of the plot (TPR=1, FPR=0). On the other hand, a random classifier would yield an ROC curve that follows the diagonal line from the bottom left to the top right, resulting in an AUC of 0.5 as shown in Figure 4.14.

---

[1] During the training process, the validation dataset is used solely for evaluation purposes, and the network does not utilise it for adjusting its parameters (weights and biases)

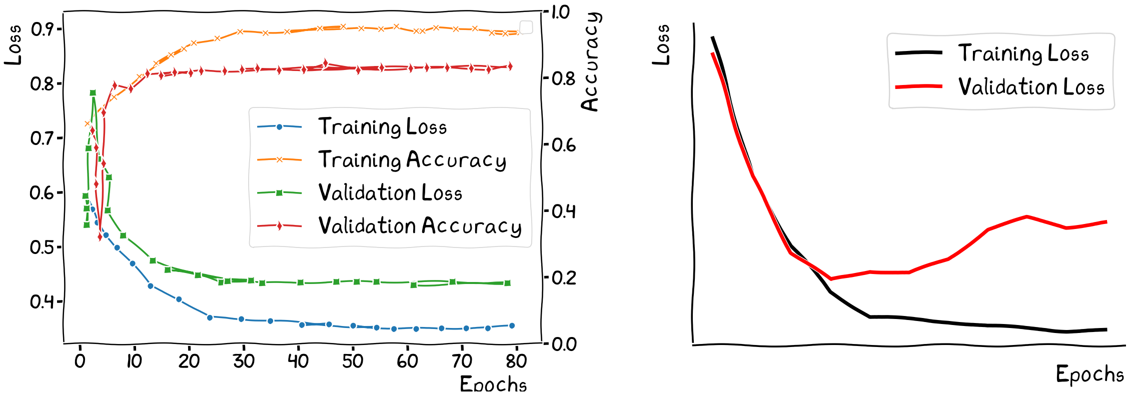

(a) (b)

Figure 4.13: (a) An example of the evolution of loss and accuracy curves over epochs for both training and validation datasets. (b) An illustration of a training configuration where overfitting is observed.

In *this thesis*, binary classification networks are used, meaning only one output node is present in the output layer. The goal of such networks is to differentiate between two classes of data. In the labelled dataset, one class is identified with output label '0' and the other with output label '1'. The desired network output is a value ranging from 0 to 1, signifying the likelihood of each data point belonging to one of the two categories. Hence, the activation function on the output node for a binary classifier is often a Sigmoid function as it has a range of [0,1]. For the hidden nodes, a ReLu activation function is used. The loss function used is binary cross-entropy widely used for binary classification networks. The hyperparameters; number of layers, number of nodes and batch size are optimised via a grid search. For number of epochs, a maximum number of epochs is set (order 100) and "**early stopping**" is used; a method that can stop the training when the performance of the network doesn't improve for the last n epochs where several values of n are tested. The Adam optimiser is left to do the definition of learning rate per epoch. When judging the network performance, loss and accuracy curves on the training and validation dataset are used, along with the "AUC" metric evaluated on the independent test dataset. A commonly used 50-25-25 split is used for dividing the labelled dataset into training, validation, and test sets.

4.4.3 Data Preparation

The kinematic input variables used to describe the events have very different numerical ranges. Consider the representation of a lepton in the ATLAS detector, it is described by four variables: Energy (E), Transverse Momentum (p_{T}), Pseudorapidity (η), and Azimuthal Angle (ϕ). E and p_{T}, typically measured in GeV, can range from values around one or even lower to several thousand, while η ranges from -2.5 to 2.5, and ϕ varies between 0 and 2π. In order to avoid that variables with higher numerical values potentially dominate what the network learns, the distribution of each variable is scaled such that it has a mean of 0 and standard deviation

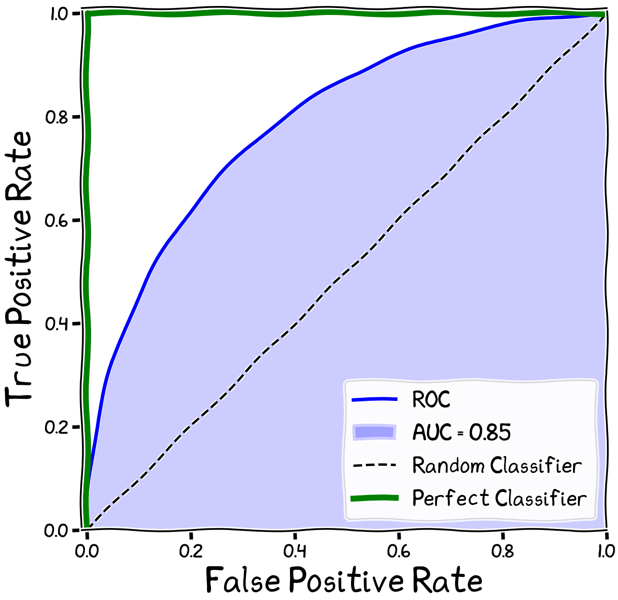

Figure 4.14: A graphic illustrating the ROC curve used to calculate the AUC metric, further explained in the text.

of 1. This is a linear transformation such that a **standardised variable** (x') is obtained by subtracting the mean (μ) and dividing by the standard deviation (σ) of the original distribution:

$$x' = \frac{x - \mu_x}{\sigma_x} \tag{4.5}$$

It often happens, in particle physics search problems, that the labelled data is not very well distributed between the two binary classes. This is called an **imbalanced dataset** and can bias the training of the network if used as is. Weights can be assigned to each data point in the input dataset such that the two classes have an equal effective weight. This ensures that there is a balanced impact on the loss function from both classes of data. This can be achieved in many ways, for example, assigning the weight of each event to be one over the total number of events in that class.

The MC simulated events are used to train the NN and are required, later, to be passed through the NN for a statistical analysis to estimate backgrounds and infer the presence/absence of new physics. Hence, random serial numbers are assigned to each event in the labelled dataset and two training datasets are defined using odd and even serial numbers. To avoid any bias coming from evaluating events with the same model they were trained on, even (odd) serial numbers are used exclusively for training one model while events with odd (even) serial numbers are evaluated with this model for statistical analysis.

CHAPTER 5

Search for simplified Dark Matter Models and Stop-Pair Production

This chapter presents the complete analysis of the $t\bar{t}$ *+*$E_{\mathrm{T}}^{\mathrm{miss}}$ *(1L) final state to probe new physics particles based on machine learning techniques also published in [1, 2][1]. Simplified models to probe dark matter and supersymmetry via top quarks are explained as the target models of this search and a description of simulations and data used follows. The strategy to reconstruct events with the help of Machine Learning (ML) based algorithms is showcased. This is followed by the classification of events in different kinematic categories wherein ML is used once again to help new physics to stand out over the background of SM processes. A dedicated strategy to understand the background modelling and systematic uncertainties is presented, all of which is used to do the final statistical analysis yielding the results at the end of the section.*

5.1 Models targeted in this search

A simplified SUSY scenario is explored in this search, focusing on the stop quark and the neutralino as the lightest particles in the MSSM. These particles are expected to be decoupled from the rest of the MSSM mass spectrum as explained in Section 2.2. Therefore, for this search, a grid of stop quark ($\tilde{t}$) and neutralino ($\tilde{\chi}_1^0$) masses is scanned. Based on the mass splitting between the stop quark and the neutralino, $\Delta m = m_{\tilde{t}} - m_{\tilde{\chi}_1^0}$, there can be 2-body, 3-body and 4-body decay scenarios described below and illustrated by the diagrams in Figure 5.1.

- 2-body ($\tilde{t} \to t\tilde{\chi}_1^0$) decay: In the kinematic range when $\Delta m > m_t$, the stop quark decays into an on-shell top quark and a neutralino. This results in the subsequent decay of the on-shell top quark into an on-shell W boson and a quark, predominantly a b quark.

---

[1] The preliminary results of the analysis presented here were first published in a conference note [1], followed by a publication in JHEP [2]. Additional results available in the paper [2] are discussed in Chapter 6.

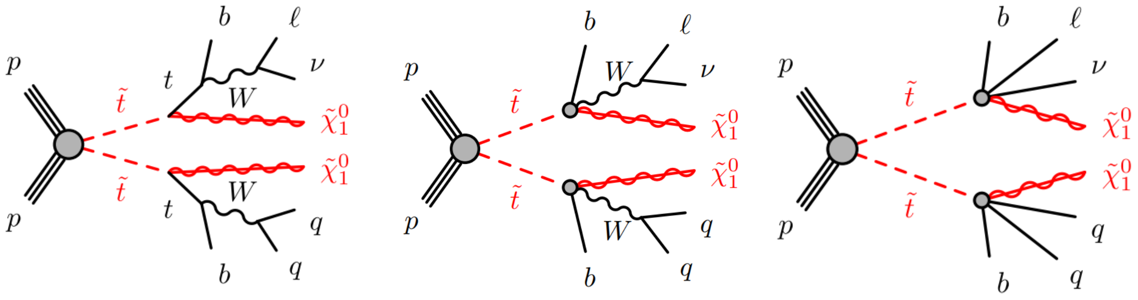

Figure 5.1: Diagrams depicting the 2-body (left), 3-body (middle) and 4-body (right) decay modes of the stop ($\tilde{t}$) pair.

- 3-body ($\tilde{t} \rightarrow bW\tilde{\chi}_1^0$) decay: In the kinematic range between $m_W + m_b < \Delta m < m_t$, the stop quark decays effectively into a b quark, a W boson and a neutralino resulting in an off-shell top quark but an on-shell W boson.
- 4-body ($\tilde{t} \rightarrow bff'\tilde{\chi}_1^0$) decay: In the kinematic range when $0 < \Delta m < m_W + m_b$, the stop quark decays effectively into a b quark and W boson daughter particles which can be a quark-antiquark pair or lepton and neutrino. Here, both the top quark and the W boson are produced off-shell.

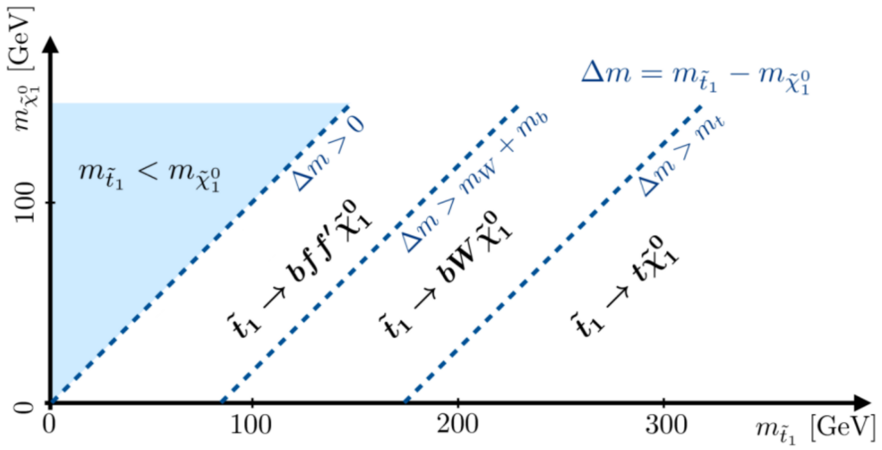

Figure 5.2: Phase space of the simplified SUSY scenario probed, spanned by $m_{\tilde{t}_1}$ and $m_{\tilde{\chi}_1^0}$, divided into the kinematic regimes that describe the 2-body, 3-body and 4-body decay modes. The 2-body regime is described where $\Delta m > m_t$. The 3-body regime starts at $\Delta m > m_W + m_b$ and ends where the 2-body regime starts. Similarly the 4-body regime starts where $\Delta m > 0$ and ends where the 3-body regime starts.

These channels occupy different regions of the phase space spanned by m($\tilde{t}_1$) and m($\tilde{\chi}_1^0$) as shown in Figure 5.2, and describe quite different scenarios of on-shell and off-shell produced top quarks and W bosons. Models with off-shell stop production are not considered as the off-shell production of stop quarks is strongly suppressed at tree level [149]. Within the 2-body (3-body) phase space, the scenario wherein the stop decays 100% of time into a $\tilde{t}_1 \to t\tilde{\chi}_1^0$ ($\tilde{t}_1 \to bW\tilde{\chi}_1^0$) is studied.

To probe DM production in association with top quarks, a simplified model, as shown in Figure 5.3, is used. This simplified model has been proposed by the LHC DM working group as a benchmark for probing many different dark matter models [45]. It can be fully described by four parameters: m_χ, m_{Med}, g_q, g_χ. The parameters m_χ, m_{Med} are the masses of the dark matter candidate and the mediator connecting the SM and the dark sector, respectively. The parameter g_χ is the coupling of the mediator to dark matter particles and g_q is a universal scaling factor of the interactions of the mediator with SM fermions. Two versions of the model are considered where the mediator can be a scalar or a pseudoscalar particle. The coupling of the mediator to SM fermions consists of the flavour-universal coupling g_q and scales additionally with the SM-Yukawa coupling for each fermion. This configuration makes the interactions of the mediator with fermions Yukawa-like, hence favouring interactions with top quarks. A specific benchmark scenario, $g_\chi = g_q = g = 1$ is used, which yields mediator decay modes as previously shown in Figure 2.10. Depending on the mass of the mediator, two scenarios are possible. Firstly, when the mediator's mass exceeds twice the top quark mass, it decays preferentially into a top-quark pair. Secondly, if the mediator mass is lower than that of the top-quark pair, it decays favourably into a pair of dark matter fermions. Within the benchmark scenario, the phase space defined by the masses of the dark matter candidate m_χ, and the mediator particle m_{Med} are explored. The motivations leading to these assumptions are explained in Section 2.3.2

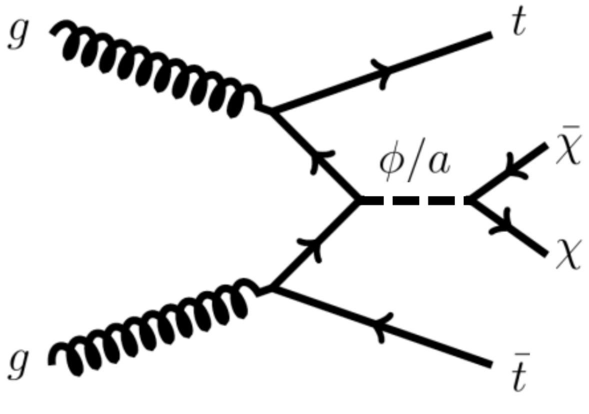

Figure 5.3: Feynman diagram describing simplified DM production. The mediator is denoted by ϕ for a scalar mediator and a for a pseudoscalar mediator. χ is the DM fermion.

As can be seen in Figure 5.4, there exists a transition line from on-shell mediator production to off-shell mediator production defined by the condition where m_{Med} is greater than or less than $2 \cdot m_\chi$. While points can be generated on the whole grid of m_χ and m_{Med}, a more simplified approach is used. The on-shell case is probed by scanning different mediator masses for a given

DM mass while in the off-shell case, different DM masses are scanned for a fixed mediator mass. This is justified because, for instance in the on-shell scenario, the final DM particles are invisible. Hence, the search is sensitive to the mass of the mediator particle and does not depend on the the mass of the DM particle it decays into. The kinematics are not expected to change drastically within the specific off-shell and on-shell divisions, implying that for the different model points not probed, a cross-section scaling of models that were probed is sufficient. A full grid can be probed to give a better understanding of the phase space but this is left to future searches.

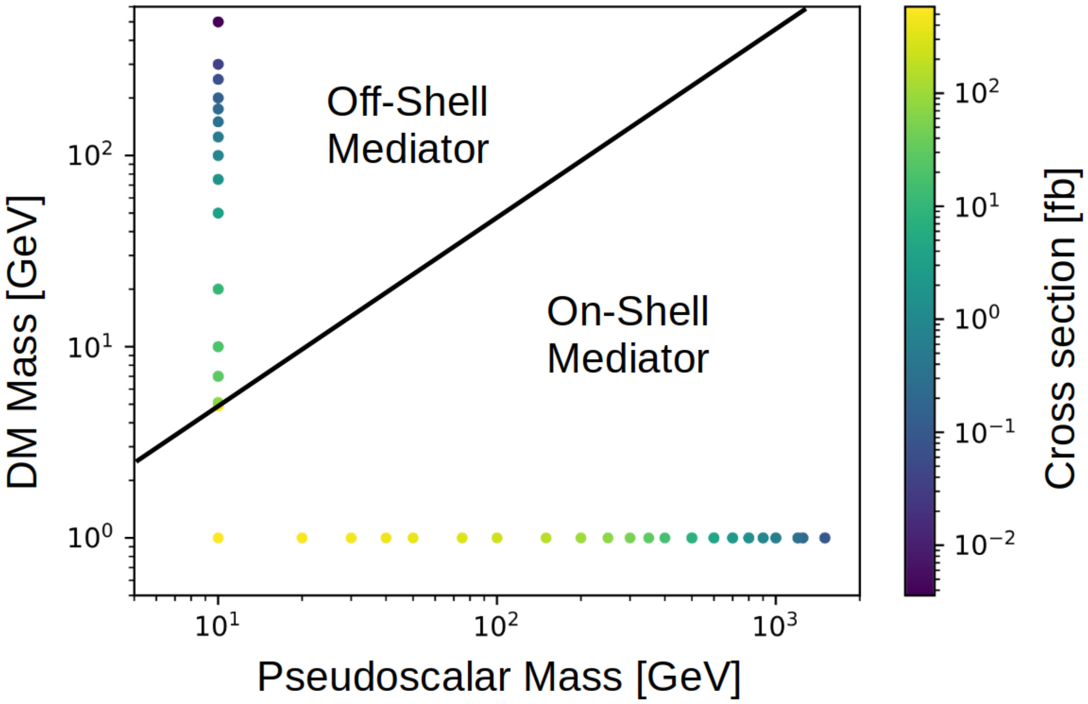

Figure 5.4: The simplified DM model phase space spanned by pseudoscalar mass and DM mass. Specific mass points considered in the analysis are shown on the grid with a colour bar showing the cross sections for the different mass points. For the scalar mediator models, the same grid points are used although they have different cross sections than the pseudoscalar models.

Additionally, it must be noted that this search is done assuming that the simplified model produces the entire relic density required by astrophysical models. However, if the simplified dark matter model is just one of several contributing channels in a more complete or complex dark matter model, the necessity for it to generate the entire relic density is relaxed. Consequently, a parameter scan is conducted to determine the upper limit on the cross section for different scenarios as a function of g. This implies that for a fixed mediator mass in the on-shell scenario, scenarios requiring a fraction of the cross section can be obtained by scaling the value of g accordingly.

5.2 Background Processes

Events describing the specific models of interest explained in Section 5.1, namely simplified DM production and stop-pair production, require the final state of the event to consist of a top-quark pair and missing transverse energy. The scenario where the top-quark pair decays semileptonically is probed. Therefore, for the leptonically decaying top quark, a b-quark jet, a lepton and missing energy is required and for the hadronically decaying top quark, significant hadronic activity is required and a dedicated strategy is employed which is explained later in Section 5.4.3. For the new physics particles, additional $E_{\mathrm{T}}^{\mathrm{miss}}$ is required. Hence, a selection criterion of at least one lepton is enforced. Additionally, some hadronic activity compatible with a hadronically decaying top quark decay and a high value of missing energy (to be compatible with having a neutrino and new invisible particles) is required. This signature, while typical for the new physics processes of interest, can also be caused by several standard model processes highlighted below:

- **Top Quark Pair Production** - The dominant background process of this search is the SM production of a top quark and anti-top quark. The $t\bar{t}$ process can be divided into $t\bar{t}$-0L, $t\bar{t}$-1L and $t\bar{t}$-2L events where the division is based on the true number of electrons and muons present in the event. This includes electron and muons from the decays of τ-leptons. All three divisions are considered, although the $t\bar{t}$-0L contribution is negligible as the final state signature requires a charged lepton to be present.

- **W+jets Production** - The next significant processes involve production of a W boson along with jets. Figure 4.7 shows an example W+jets production where the W boson decays leptonically and is produced alongside jets which satisfy the conditions above (one-lepton, jets and $E_{\mathrm{T}}^{\mathrm{miss}}$).

- **Singletop Production** - This process represents the production of a single top quark in the event which can occur in one of three ways at the LHC: s-channel production, t-channel production as well as associated production with a W boson as shown in Figure 5.5.

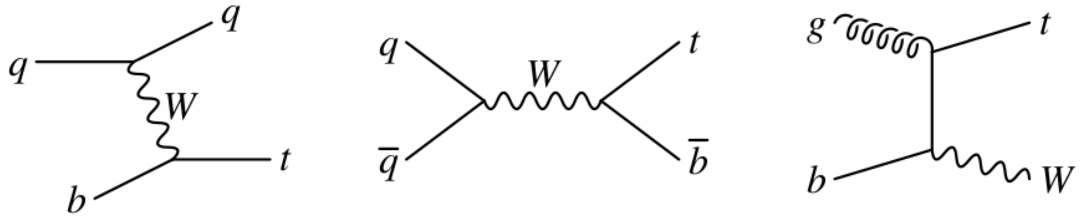

Figure 5.5: Illustration of different ways single top quarks can be produced at the LHC including t-channel (left), s-channel (middle) and associated production with a W boson (right).

- **Z+jets and Diboson (VV) Production** - Smaller contributions come from events where a Z boson is produced alongside jets or the diboson process. In Z+jets, either the Z boson decays into charged leptons and one of the leptons fails reconstruction or the Z decays into neutrinos and an additional jet is misidentified as a lepton. The Diboson processes where WW, WZ or ZZ are produced, and a charged lepton originating from the Z boson fails reconstruction, are also compatible with the event selection described above.

- **ttZ production** - This represents the production of $t\bar{t}$ in addition to a Z boson. While the cross section of this process is lower than those mentioned above, it is an important background for this analysis. This background can be divided into two:
  - **ttZ($\rightarrow ll$)** where ll denotes only charged lepton pairs as the decay products of the Z boson. This channel comprises a small contribution.
  - **ttZ($\rightarrow \nu\nu$)** - the specific case where the Z boson decays into neutrinos is considered separately. This process is very difficult to discriminate against as it has exactly the same signature as the DM and SUSY events and is therefore denoted as the "irreducible background" and depicted in Figure 5.6.

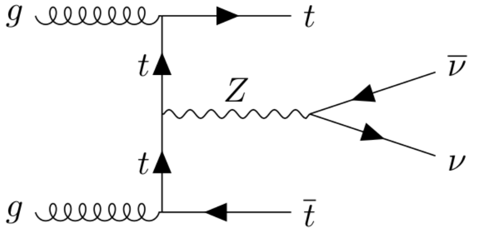

Figure 5.6: Illustration of the ttZ physics process where the Z decays invisibly into two neutrinos.

5.3 Simulation Details

For background processes which are all well known SM processes explained in Section 5.2, different generators are used for different processes. Details of the simulation samples used, including the ME event generator, its QCD accuracy, the PDF set used, the PS and hadronisation model, and the accuracy of the cross-section calculation, are summarised in Table 5.1.

After event generation, all samples were processed through the step of detector simulation using the "full simulation" description of the ATLAS detector [185] made using GEANT4 [186] software. Samples generated by the MADGRAPH5_aMC@NLO [176] and POWHEG BOX [166–169] tools incorporated EVTGEN [187] for b hadron decay modelling. For these samples, PYTHIA [170] facilitated parton showering and hadronisation, with the A14 tune [188] and the NNPDF2.3LO PDF set [189]. The description of pileup was modelled by overlaying the simulated hard-scattering event with inelastic pp collisions generated with PYTHIA 8.186 [190] using the NNPDF2.3LO set of PDFs and the A3 set of tuned parameters [191].

Table 5.1: Overview of the configurations used to simulate background processes, also published in [2].

Process	ME event generator	ME QCD accuracy	ME PDF	Parton shower and hadronisation	Cross-section calculation
$t\bar{t}$	Sherpa 2.2.12 [150]	0,1j@NLO +2,3,4j @LO[154–157]	NNPDF3.0nnlo [158]	Sherpa [102, 103, 151–153]	NNLO+NNLL [159–165]
Single-top					
tW	Powheg Box v2 [166–169]	NLO	NNPDF3.0nlo	Pythia 8.307 [170]	NLO+NNLL [171, 172]
s- and t-channel	Powheg Box v2	NLO	NNPDF3.0nlo	Pythia 8.230	NLO [173, 174]
V+jets ($V = Z, W$)	Sherpa 2.2.11	0,1,2j@NLO +3,4,5j@LO	NNPDF3.0nnlo	Sherpa	NNLO [175]
$t\bar{t}V$	MadGraph5_aMC @NLO 2.3.3 [176]	NLO	NNPDF3.0nlo	Pythia 8.210	NLO QCD +EW [177]
VV'	Sherpa 2.2.1, 2.2.2	0,1j@NLO +2,3j@LO	NNPDF3.0nnlo	Sherpa	
SUSY signals	MadGraph 2.8.1 , 2.9.9 [176]	0,1,2j@LO	NNPDF2.3lo	Pythia 8.240, 8.307	NNLO+NNLL [178–182]
DM signals	MadGraph 2.7.3	0,1j@LO	NNPDF2.3lo	Pythia 8.244	NLO [183, 184]

The MadGraph [176] package was used to simulate $\tilde{t}_1\tilde{t}_1$ production at leading order (LO) with up to two additional partons. MadSpin [192] software was used to simulate the decays of the stop quark, which mimics kinematic distributions without full ME computations. Cross-sections for $\tilde{t}_1\tilde{t}_1$ production were approximated at next-to-next-to-leading order (NNLO+NNLL) in QCD, factoring in soft gluon emission resummation [178–182]. A nominal cross section and its uncertainty were determined using the PDF4LHC15_mc PDF set, following the guidelines outlined in [193]. For $t\bar{t}$+DM production in the benchmark scenario with $g = g_\chi = g_q = 1$, MadGraph was employed at LO with one additional parton, complemented by MadSpin for the top quark decay. The cross sections were computed at next-to-leading order (NLO) in QCD [183, 184].

The $t\bar{t}$ and W+jets processes were simulated using the Sherpa 2.2.12 and Sherpa 2.2.11 [150] generators, respectively. The $t\bar{t}$ production simulation incorporated NLO MEs with one extra parton and LO MEs with up to four additional partons, computed via Comix [154] and OpenLoops [155–157]. Likewise, W+jets production utilised NLO MEs with two extra partons and LO MEs with up to five extra partons. Event weights were applied to introduce approximate NLO EW corrections, using the electroweak virtual approximation and the additive method. These simulations were integrated with the Sherpa parton shower [151] using the MEPS@NLO method [102, 103, 152, 153], incorporating parameters fine-tuned by the Sherpa team.

The tW production was modelled by Powheg Box v2 [166–169] at NLO in QCD using the five-flavour scheme. The diagram removal technique [194] was employed to eliminate interference with $t\bar{t}$ production. An alternative diagram subtraction scheme [194, 195] was also used to estimate uncertainties related to resolving the overlap. The $t\bar{t}W$ and $t\bar{t}Z$ processes were simulated using MadGraph5_aMC@NLO 2.3.3 [176] at NLO. Other sources of background events that are considered in this search are diboson production (VV', where

$V = W, Z$). Events describing Higgs boson production in association with a top-quark pairs are simulated with Powheg Box v2 [167–169, 196, 197] at NLO using NNPDF3.0nlo [158]. Pythia 8.230 [198] with the A14 tune[188] and NNPDF2.3lo [158] handled event generation, and EvtGen 1.6.0 [187] managed b and c hadron decays. Additional small backgrounds include the production of tZ and tWZ and the production of three and four top quarks, all simulated with MadGraph5_aMC@NLO+Pythia 8.

The use of the Sherpa simulation for $t\bar{t}$ production was tested during the course of this analysis, as described in Section 5.6.1. The performance was compared against the nominal Powheg Box v2 simulations, as used in [4], yielding that it provides improved modelling of events in the high transverse momentum region relevant for this search. Similarly, for tW production, samples that use dynamic scales rather than fixed scales in the calculation of the ME were studied as detailed in Section 5.6.2.

5.4 Event Selection and Reconstruction

Starting with $140\,\text{fb}^{-1}$ of data corresponding to the entire Run-2 dataset of “good physics” outlined in Section 3.3.2, a step of event cleaning and primary vertex reconstruction is performed. This is accompanied by the selection of trigger chains that would record the type of events most suitable for probing the desired signal events. This trigger chain selection is also applied on MC simulated events to provide a set of simulated events that can be used to understand the data. An offline object reconstruction is done on events that pass the triggers and higher level variables are built using these objects to maintain high signal acceptance while rejecting background events.

5.4.1 Trigger Selection

The main signature that differentiates the signal and background events is the presence of large quantities of $E_{\mathrm{T}}^{\mathrm{miss}}$ corresponding to new invisible particles. Hence $E_{\mathrm{T}}^{\mathrm{miss}}$ triggers are used primarily for the selection of relevant events. The trigger menu, which differs over the various data-taking years within Run-2, provides a list of the trigger chains under which events have been saved. As explained in Section 3.3.1, the trigger chain corresponds to the presence of an L1 trigger item followed by a specific HLT signature. For $E_{\mathrm{T}}^{\mathrm{miss}}$ triggers, the trigger chains used are listed in Table 5.2.

The naming of a trigger chain reflects the selection criteria an event must satisfy to pass it. For instance, “HLT_xe” signifies a trigger chain employing $E_{\mathrm{T}}^{\mathrm{miss}}$ reconstruction at the HLT, followed by a number denoting the minimum $E_{\mathrm{T}}^{\mathrm{miss}}$ threshold. Subsequent strings like “mht” or “pufit” specify which $E_{\mathrm{T}}^{\mathrm{miss}}$ reconstruction algorithm was used. Additionally, “L1XE” indicates the Level-1 $E_{\mathrm{T}}^{\mathrm{miss}}$ trigger item followed by its threshold. In 2018, triggers combine “pufit” and “cell” algorithms for improved pileup mitigation. The “cell” algorithm utilises calorimeter cells, while “mht” uses jets to calculate $E_{\mathrm{T}}^{\mathrm{miss}}$. The “pufit” algorithm employs calorimeter cells corrected for pileup to compute $E_{\mathrm{T}}^{\mathrm{miss}}$ [199].

Table 5.2: Description of $E_{\mathrm{T}}^{\mathrm{miss}}$ Trigger Chains. In years where the trigger changes over the course of the year, lumi-blocks denoted for example by (A-D3), describe time periods within data-taking years.

Year (lumi-blocks)	Trigger Name	HLT algorithm	L1 threshold [GeV]	HLT threshold [GeV]
2015	HLT_xe70_mht	mht	50	70
2016 (A-D3)	HLT_xe90_mht_L1XE50	mht	50	90
2016 (D4-F1)	HLT_xe100_mht_L1XE50	mht	50	100
2016 (F2-end)	HLT_xe110_mht_L1XE50	mht	50	110
2017 (B1-D5)	HLT_xe110_pufit_L1XE55	pufit	50	110
2017 (D6-end)	HLT_xe110_pufit_L1XE50	pufit	50	110
2018 (B-C5)	HLT_xe110_pufit_xe70_L1XE50	pufit, cell	50	110, 70
2018 (C6-end)	HLT_xe110_pufit_xe65_L1XE50	pufit, cell	50	110, 65

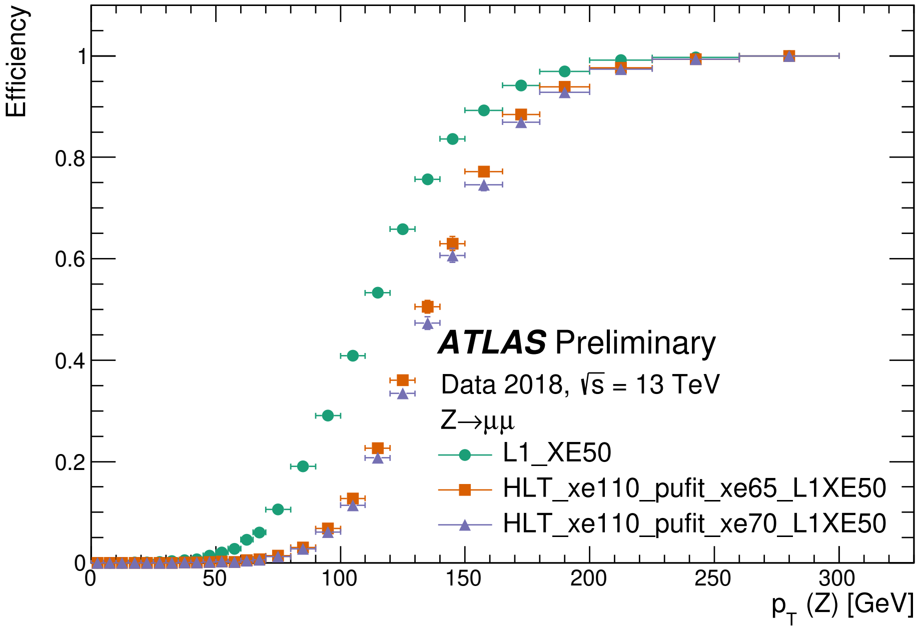

Figure 5.7: Efficiency of the two $E_{\mathrm{T}}^{\mathrm{miss}}$ trigger chains used for 2018 data as listed in Table 5.2. The efficiency of the L1 item alone and that of the combined HLT and L1 trigger chains are shown. Here $Z \to \mu\mu$ events are used to evaluate the efficiency of the $E_{\mathrm{T}}^{\mathrm{miss}}$ reconstruction algorithm used by the trigger. The muon momentum is known and provided as invisible to the algorithm, the efficiency is plotted as a function of p_{T} (Z), taken from [93].

The efficiency of these triggers is measured in events with a “known” wide range of $E_{\mathrm{T}}^{\mathrm{miss}}$ to understand its performance. An example of such an efficiency curve for the $E_{\mathrm{T}}^{\mathrm{miss}}$ trigger used in 2018 is shown in Figure 5.7. It shows that the trigger has high efficiency (100%) for $E_{\mathrm{T}}^{\mathrm{miss}}$ above 230 GeV. This efficiency is similar across the other Run-2 data-taking years.

While studying the phase space of signal events, it was concluded that considering events with $E_{\mathrm{T}}^{\mathrm{miss}}$ as low as 70 GeV would be desirable to increase the acceptance of signal events. As can be seen in Figure 5.7, the $E_{\mathrm{T}}^{\mathrm{miss}}$ trigger efficiency is very low in this range and single-lepton triggers are used for events with $E_{\mathrm{T}}^{\mathrm{miss}}$ between 70 and 230 GeV instead. Single lepton triggers where the lepton is either an electron or muon are used and τ-lepton triggers are not used. This is because the events with τ-leptons decaying leptonically would make it into the event selection using single-lepton triggers and events with hadronically decaying τ-leptons are not studied in this analysis. Table 5.3 and Table 5.4 provide a list of the electron and muon trigger chains used during the specified years.

Table 5.3: Description of Electron Trigger Chains.

Year	Trigger Name	HLT threshold E_{T} [GeV]	ID algorithm selection	Other
2015	HLT_e24_lhmedium_L1EM20VH	24	LH medium	L1EM20VH
	HLT_e60_lhmedium	60	LH medium	-
	HLT_e120_lhloose	120	LH loose	-
2016-18	HLT_e26_lhtight_nod0_ivarloose	26	LH tight	No d_0, loose isolation
	HLT_e60_lhmedium_nod0	60	LH medium	No d_0
	HLT_e140_lhloose_nod0	140	LH loose	No d_0

Table 5.4: Description of Muon Trigger Chains.

Year	Trigger Name	HLT threshold p_{T} [GeV]	ID algorithm selection	Other
2015	HLT_mu20_iloose_L1MU15	20	Loose	L1MU15
	HLT_mu40	40	-	-
2016-18	HLT_mu26_ivarmedium	26		medium isolation
	HLT_mu50	50	-	-

Similar to $E_{\mathrm{T}}^{\mathrm{miss}}$ triggers, the naming convention for single-electron triggers describes the properties of the electron present in the event that passes the corresponding trigger. For instance, the trigger HLT_e26_lhtight_nod0_ivarloose requires the electron to meet a minimum E_{T} threshold of 26 GeV, pass the tight likelihood (LH) identification criterion, have no requirements on the transverse impact parameter (nod0), and satisfy a loose isolation criterion (ivarloose). Similarly, the muon triggers follow a similar naming convention, with ‘mu’ indicating the muon object and the corresponding p_{T} threshold. For example, HLT_mu20_iloose_L1MU15 requires a muon to have a p_{T} greater than 20 GeV, meet a loose identification criterion, and satisfy the L1 trigger requirement of $p_{\mathrm{T}} > 15\,\mathrm{GeV}$.

A combination of single-lepton triggers to provide a p_{T} dependent reconstruction is depicted in Figures 5.8 and 5.9

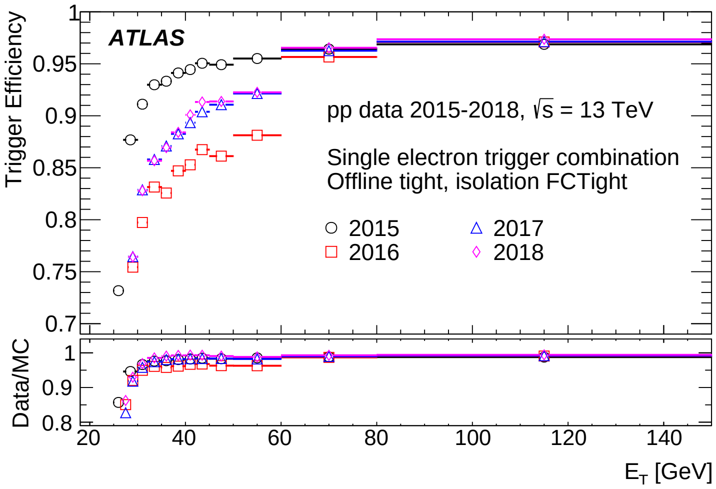

Figure 5.8: The efficiency for the single electron trigger as a function of the electron E_{T}, taken from [200].

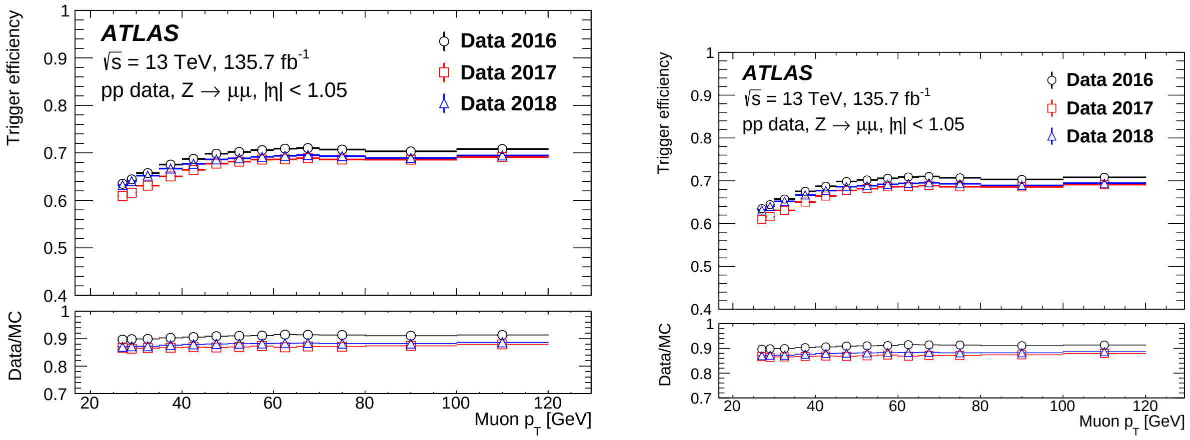

Figure 5.9: Efficiency of passing either the HLT_mu26_ivarmedium or the HLT_mu50 trigger in the barrel (left) and endcaps (right) as a function of the muon p_{T}, computed using data taken in 2016–2018. The error bars show the statistical uncertainties only, taken from [201].

5.4.2 Offline Event Reconstruction

The events selected by either the $E_{\mathrm{T}}^{\mathrm{miss}}$ triggers or single-lepton triggers are then reconstructed offline. Further cuts are applied to leptons and $E_{\mathrm{T}}^{\mathrm{miss}}$ such that the triggers are used in the highly efficient range. Depending on object quality and kinematic requirements, reconstructed electrons and muons are labelled as either baseline or signal, where the latter is a subset of the former that passes tighter selection criteria. The selection criteria for signal and baseline electrons and muons are given in Table 5.5 and Table 5.6

Table 5.5: Baseline and signal electron selection criteria, using algorithms and working points defined in Section 3.3.3.

Feature	Baseline	Signal
Identification	`LooseAndBLayer`	`Medium`
Isolation	`None`	`Loose_VarRad` at low-p_{T} `HighPtCaloOnly` at High-p_{T}
Track to PV association	`None`	$\lvert d_0/\sigma(d_0))\rvert < 5.0$ $\lvert z_0 \cdot \sin\theta\rvert < 0.5\,\mathrm{mm}$
Pseudorapidity range	$\lvert\eta\rvert < 2.47$	$\lvert\eta\rvert < 2.47$
Transverse momentum	$p_{\mathrm{T}} > 4.5\,\mathrm{GeV}$	$p_{\mathrm{T}} > 20\,\mathrm{GeV}$

Table 5.6: Baseline and signal muon selection criteria, using algorithms and working points defined in Section 3.3.3.

Feature	Baseline	Signal
Identification	`Medium`	`Medium`
Isolation	`None`	`PflowLoose_VarRad`
Track to PV association	`None` $\lvert d_0/\sigma(d_0))\rvert < 0.5\,\mathrm{mm}$	$\lvert d_0/\sigma(d_0))\rvert < 3.0$ $\lvert z_0 \cdot \sin\theta\rvert < 0.5\,\mathrm{mm}$
Transverse momentum	$p_{\mathrm{T}} > 4\,\mathrm{GeV}$	$p_{\mathrm{T}} > 20\,\mathrm{GeV}$
Pseudorapidity range cut	$\eta < 2.7$	$\eta < 2.7$

Baseline leptons are used to remove overlapping objects and compute the missing transverse momentum. Signal leptons are used to select events and construct discriminating variables. To further tune these events to match the signal signature, it is required that one and only one signal lepton (electron/muon) is present in the event. Hadronically decaying τ-leptons are reconstructed to reject events containing them. The selection used to reconstruct τ-leptons is given in Table 5.7. Some fraction of events where the τ-lepton decays leptonically make it into the event selection, as desired.

Table 5.7: Hadronic τ-lepton selection criteria, using algorithms and working points defined in Section 3.3.3.

Feature	Criteria
Track selection	1 or 3 tracks
Jet rejection	RNN `Loose`
Electron rejection	BDT `Medium`
Transverse momentum	$p_{\mathrm{T}} > 20\,\mathrm{GeV}$
Pseudorapidity range	$(\lvert\eta\rvert < 1.37) \quad \lvert\lvert \quad (1.52 < \lvert\eta\rvert < 2.5)$

Additionally a selection on reconstructed jets is required, for this it is first required to understand how hadronic top quarks appear in the event. The higher the p_{T} of the top quark, the more collimated and the lower the p_{T}, the more spread out are the decay products as depicted in Figure 5.10. The jet selection has to allow for different configurations of the top quarks to allow reconstruction of top quarks over a wide range of p_{T}. For the leptonically decaying top this is not very relevant as the lepton coming from the top can be reconstructed and identified quite well. However, for the hadronically decaying top, this affects the event selection strategy.

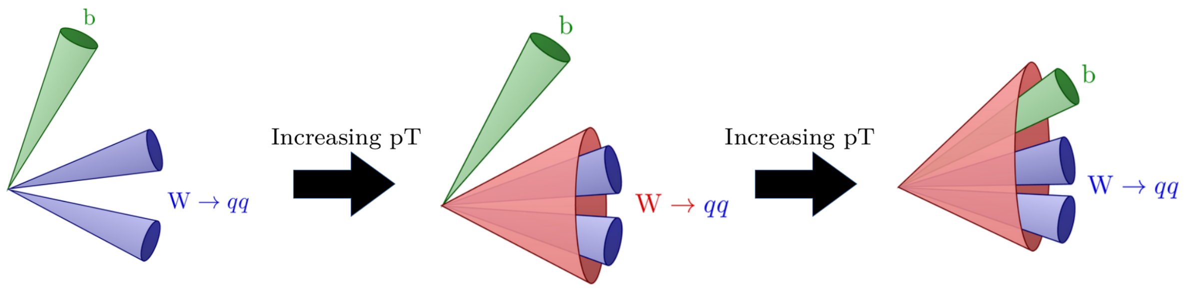

Figure 5.10: Based on the p_{T} of the hadronically decaying top quark, it can appear as three spatially resolved small radius jets at low p_{T} and evolve to one large radius jet at high p_{T}, adapted from [76].

A high p_{T} top, called “boosted”, appears as one jet with a large radius, possibly having some sub-jet structure, while in the low p_{T} or “resolved” case, this appears as three small radius jets. Jets are reconstructed in the event using the anti-k_t algorithm explained in Section 3.3.3. Hence, both small radius jets, described by anti-k_t radius of 0.4, and Large Radius (LR) jets, described by anti-k_t radius of 1.0, are reconstructed in the event. Events are divided based on the configuration and p_{T} of the hadronic top quark produced. Generally the event has to have either a boosted or resolved top and how this is achieved is explained in detail in Section 5.4.3.

Algorithms to tag jets as b-quark jets are used to further identify the jets present in the event and help to reconstruct the two top quarks. In the analysis, a b-tagging working point corresponding to a b-tagging efficiency of 77%, as estimated on simulated $t\bar{t}$ events, has been chosen. A large fraction of signal events will therefore have only one tagged b-quark jet. To retain these events, a minimal selection of at least one b-quark jet is used but events are later divided based on the number of b-quark jets ("multiplicity"). Additionally the b-quark jet can originate from either the hadronic or leptonic top and both possibilities have to be considered. For the boosted category, this leads to a further complication, namely if a b-quark jet is reconstructed to be within the *LR* jet or outside its cone. Within the *LR* jet the b-quark jet has quite likely a smaller radius (due to being collimated at high p_{T}) than when it lies outside the *LR* jet. Therefore, a variable radius reconstruction for b-quark jets is used within the Large-R jet. Table 5.8 outlines the reconstruction algorithms and selection criteria for small-*R* jets, *LR* jets and Variable Radius (VR) jets.

Table 5.8: Jet reconstruction criteria, using algorithms and working points defined in Section 3.3.3.

Feature	small-R Jet	Large-R (LR) Jet	Variable Radius (VR) Jet
Reconstruction algorithm details	anti-k_t 0.4 using PFlow (track corrected) EM clusters	anti-k_t 1.0 on LCTopo (trimmed and calibrated) clusters	anti-k_t VR jets for R between 0.2 and 0.4 using tracks
p_{T}	$> 20\,\mathrm{GeV}$	$600 < p_{\mathrm{T}} < 2500\,\mathrm{GeV}$	$20\,\mathrm{GeV}$
$\lvert\eta\rvert$	< 4.5	< 2.0	< 2.5
Mass		$40 < m < 600\,\mathrm{GeV}$	

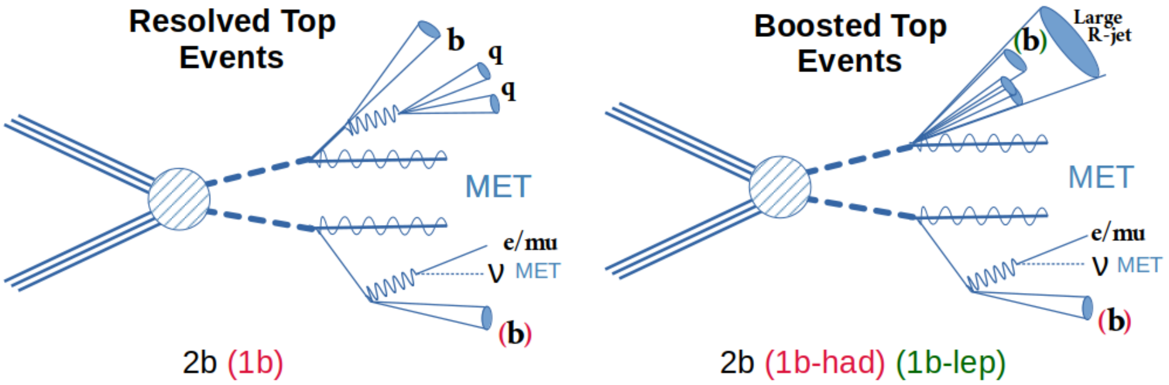

Figure 5.11: The ideal event is showcased where both b-quark jets are identified, called "2b". In events with resolved top quarks, if one of the b-quark jets is missing it is retained but falls into a separate "1b" category. Similarly for events with boosted top quarks, the "2b" category is ideal, while if only one b-quark jet is found in the event, it is divided such that if the b-quark jet is found inside (outside) the *LR* jet, it is considered a "1bhad" ("1blep") event.

The different jet configurations for events with hadronically decaying, boosted and resolved top quarks, alongside the leptonically decaying top quark and invisible particles are depicted in Figure 5.11. As illustrated, the b-quark jets within *LR* jets can have variable radius and those outside the *LR* jet are fixed to be small-R jets.

After all objects are reconstructed offline, the $E_{\mathrm{T}}^{\mathrm{miss}}$ is recalculated using these objects as described in Section 3.3.3. It is the negative sum of baseline electrons and muons and small-R jets present in the event. A soft term using tracks associated with the primary vertex but not assigned to any reconstructed object is also subtracted to mitigate activity from high pileup events.

Overlap Removal

It is possible that two different physics objects can be reconstructed from the same detector signatures as overlapping objects. Hence, during event reconstruction, after all objects are reconstructed, they have to go through overlap removal to ensure no double counting of particles. The overlap removal procedure used in this thesis, similar to the one used in [4], is summarised in Table 5.9.

Table 5.9: Overlap removal criteria in the order in which they are applied.

Sequence	Reject	Against	Criteria
1	Muon	Electron	shared ID track and Muon is a CT Muon
2	Electron	Muon	shared ID track
3	Jet	Electron	Not a b-jet, electron with $p_{\mathrm{T}} < 100$ GeV and $\Delta R < 0.2$
4	Electron	Jet	Sliding ΔR cone
5	Jet	Muon	`NumTrack` < 3 and (ghost-associated or $\Delta R < 0.2$)
6	Muon	Jet	Sliding ΔR cone
7	Tau	Electron	$\Delta R < 0.2$
8	Tau	Muon	$\Delta R < 0.2$
9	Jet	Tau	$\Delta R < 0.2$

In steps 1 and 2, overlaps between muons and electrons are addressed using shared ID tracks and the type of muon reconstructed. In step 3, any jet, *not* tagged as a b-quark jet, is rejected if it lies inside a $\Delta R = 0.2$ of an electron with $p_{\mathrm{T}} < 100$ GeV. Step 4 requires removal of any electron found within a sliding ΔR cone around a jet. A sliding ΔR cone is a p_{T} dependant cone radius, $\Delta R = \max(0.04 + 10/p_{\mathrm{T}}, 0.4)$ to better accommodate the spread of different p_{T} objects. In step 5, a jet may be considered to overlap with a muon if it has less than three tracks associated to it and is either "ghost-associated" [202] with the muon (i.e., associated with a hypothetical ghost particle representing the muon) or if it is found within a close proximity ($\Delta R < 0.2$) to the muon. Step 6 uses the previously described sliding ΔR cone. Steps 7-9 address overlap of τ-leptons with other objects using a minimum distance between objects. Additionally, small-R jets that lie within the *LR* jet, hence satisfying $\Delta R < 1.1$ from a Large-R jet, are discarded. Leptons are allowed to overlap with Large-R jets.

Both resolved and boosted top quarks are reconstructed using Deep Neural Networks (DNNs). In the case of a resolved top quark decaying hadronically, its decay products, namely the b-quark jet and the two light jets, need to be identified. For this a DNN classifier is designed that evaluates the different combinations of jets in an event to identify which configuration is most likely to originate from the top quark. This procedure is detailed in Section 5.4.3. In the case of boosted top quarks, the decay products are not individually reconstructed. Instead, what needs to be judged is whether the LR jet reconstructed in the event has the properties of a boosted top quark. For this, a DNN that evaluates sub-structural components of the top quark is used. This procedure is detailed in Section 5.4.4.

5.4.3 Resolved Hadronic Top Reconstruction using Neural Networks

Jet Combinatorics

To design a dedicated DNN with the goal of finding the correct combination of small-R jets that originate from the decay of the hadronically decaying top quark, combinations of jets in the event need to be constructed. Hence, in each event, two to six jets are considered in the reconstruction of a resolved top quark. These two to six jets consist of one to two b-tagged jets and one to four non b-tagged jets. If more than two b-tagged jets and four non b-tagged jets are present in the event, the two highest p_T b-quark jets and the four highest p_T non b-tagged jets are considered. All jets are required to have a p_T above 20 GeV. Events that do not contain at least one b-tagged jet and one non b-tagged jet with this p_T requirement are not considered. While the decay products of the hadronic top consist ideally of three jets (one b-tagged), a configuration of two jets, wherein one is a b-tagged jet and one that is non b-tagged is also considered for two reasons. Firstly, this allows the scenario where one of the two non b-tagged jets is missed in reconstruction because it lies outside the acceptance of the detector, has a p_T below 20 GeV or has been misidentified as another object. Secondly, in the case of high p_T top quarks, it is possible that the two jets coming from the decay of the W boson are, in reality, merged into one jet. Hence, the combinations constructed in the event can consist of either one b-tagged jet and one non b-tagged jet called a “pair” or one b-tagged jet and two non b-tagged jets, called a “triplet”. This gives every event between one and 20 possible combinations that are candidates to describe the decay products of the hadronic top quark. These combinations, collectively called multiplets to include pairs and triplets, are illustrated in Figure 5.12.

Input Definitions

The network should ideally be able to reconstruct which decay products originate from the top quark for top quarks at a wide range of p_T. Different p_T top quarks are Lorentz boosted differently inside the detector. Additionally, top quarks of different transverse momenta can be produced pointing in various directions. Given a large enough DNN, and top quarks in all rotations and with different boost configurations, the network can in principle learn these symmetries itself. However, one can modify inputs by exploiting these known symmetries, such that the network does not need to learn them. Furthermore the p_T at which the hadronic top quark is produced in the event causes the decay to appear differently. It is expected

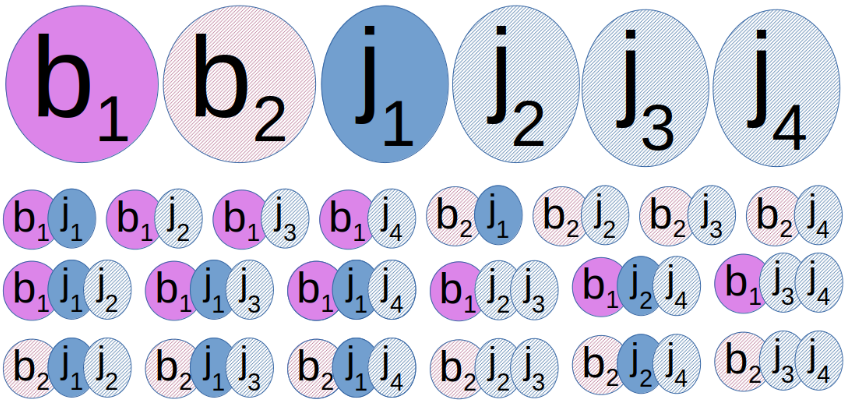

Figure 5.12: The top row shows the two to six jets in the event used to reconstruct the hadronic top. One b-quark jet and at least one additional jet is a required condition, giving minimally one pair. The shaded circles show cases for when the additional jets are present in the event. Below the row of jets considered is a visualisation of one to 20 multiplets formed from making pairs and triplets from the available jets. These multiplets are candidates for the hadronically decaying top quark.

that with increasing top quark transverse momentum, the reconstruction using resolved jets suffers.

The top quark candidate multiplets used in the training are boosted into their rest frame yielding two advantages: removing the Lorentz boost that the network should, in principle, be able to learn, and reducing the Lorentz boost dependence of the top quark reconstruction on its momentum. It must be noted here that the multiplet p_{T} is retained and provided to the network additionally as this does affect the reconstructability of the top quark. In order to additionally ensure that the network performs well for a wide range of transverse momenta, the weight of events used in the training are modified such that the effective number of events used has a uniform p_{T} distribution.

The multiplets are also rotated to exploit rotational symmetries, further reducing the aspects that the network needs to learn. The rotation is done such that the b-quark jet in the multiplet is aligned with the positive z-direction. After this, the multiplet is rotated around the b-quark jet (or z-axis) until the highest p_{T} non b-tagged jet lies in the x-z plane. This retains the relative orientations between the (two) three jets while removing rotations not relevant for the classifier. As seen in Figure 5.13, this reduces the number of input quantities from twelve to six non-trivial kinematic parameters listed in Table 5.10. This is beneficial in reducing the complexity of the DNN training so that one can work with smaller networks.

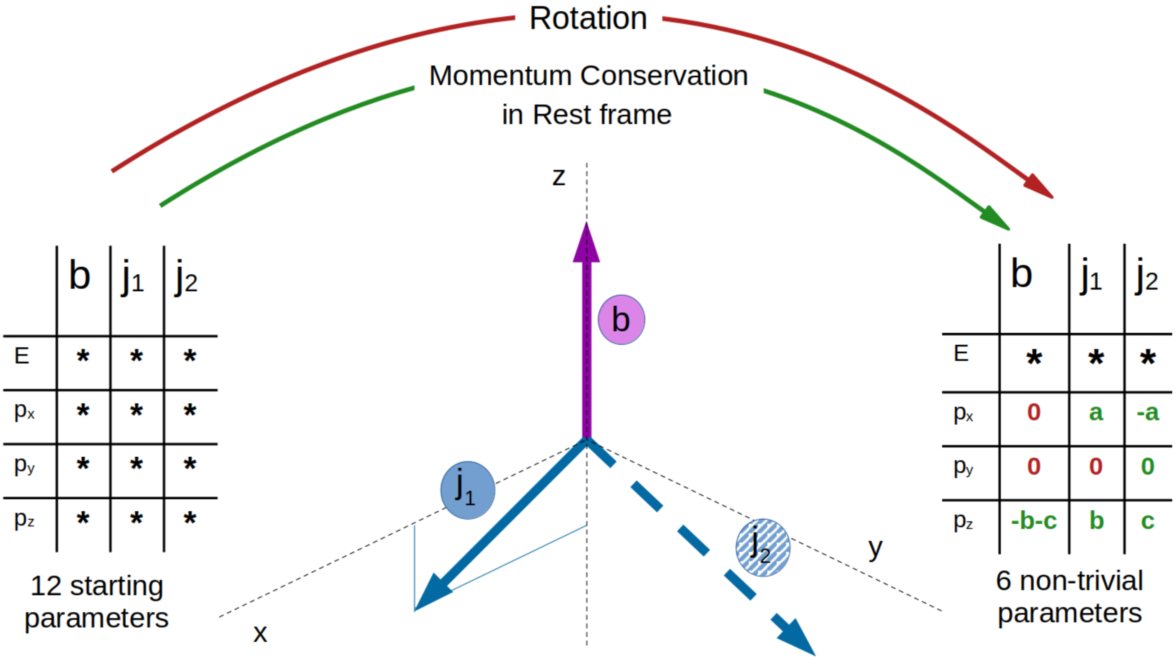

Figure 5.13: Reduction of twelve parameters required to represent 4-vectors of three jets, giving six non-trivial parameters by applying the transformations outlined in the text. In triplets, j_1 is the highest p_T non b-jet. A '*' is used to represent the original quantities and consistently show the parameters that remain unchanged after the transformation. The graphic in between the two parameter tables shows the orientation of the multiplet after the rotation.

Table 5.10: List of the six non-trivial input variables for the resolved top NN.

Object	Vector Component
b	E
j_1	E p_x p_z
j_2	E p_z
p_T^{top}	$p_T(b+j_1+j_2)$ - triplet $p_T(b+j_1)$ - pair

Truth Matching

For a classification network to be able to distinguish a multiplet that comes from a top quark and one that does not, truth labelled multiplets are required to train the network with. The label is simply '1' defining a signal multiplet (top) and '0' defining a background multiplet (not top). These binary labels are provided in the labelled data as target values in the training. The output of the classifier on unlabelled data then lies between 0 and 1 to give it a probability of being background or signal like.

Multiplets from signal processes (DM and SUSY) are used in the training. Truth matching is done using truth information available in the generated Monte Carlo (MC) samples. In the MC samples, true particles kinematics are present for the top quarks, W bosons and leptons. The true flavour of jets and leptons are also available. However, the information of which jets/lepton come from which top or W boson is absent. In future iterations it would be possible to improve on this by saving jet origin information in the Monte Carlo events. Nevertheless, to label the multiplets, the following strategy is employed with the information available. A maximum of one multiplet in an event can be labelled as a true (and therefore signal) multiplet, ensured by the matching criteria.

A multiplet is considered to be a signal multiplet if:

- The reconstructed b-quark jet in the multiplet is a true b-quark jet
- The reconstructed non b-quark jets are true light jets
- The true top quark momentum is compatible with the vectorial sum of the reconstructed b-quark jet and true hadronically decaying W boson. This is achieved as follows:
  - The W boson has to have a charge opposite to that of the true lepton in the event to rule out the W boson originating from the leptonically decaying top quark.
  - The combination of the b-quark jet in the multiplet combined with the true W_{had}, called a Wb pair, must be the closest to the top quark momentum when compared to other Wb pairs in the event. This is relevant only when more than one b-quark jet exists in the event and achieved with:
    - The value of $\Delta R(t, Wb) = \sqrt{(\eta_t - \eta_{(Wb)})^2 + (\phi_t - \phi_{(Wb)})^2}$ for this Wb pair must also be the minimum compared to other Wb pairs in the event.
    - Additionally, the condition $\Delta R(t, Wb) < 2.1 \cdot (m_t / t_{p_\mathrm{T}})$ is used to ensure that (within some margin) the Wb pair lies inside a cone which is expected to contain the decay products of the top quark[2] .

---

[2] To determine the expected cone size of boosted objects such as W, Z, and top quark, a rule of thumb to determine the jet size of the truth object is given by $\Delta R = 2 \cdot (m/p_\mathrm{T})$, where m is the mass of the object and p_T is its transverse momentum [124].

- Similarly, the true hadronically decaying W boson has to be compatible with the vectorial sum of the reconstructed light (jet)s.
  - Here $\Delta R(W, j)$ ($\Delta R(W, jj)$) is calculated for the jet(s) in the pair(triplet). $\Delta R(W, jj) < 2.1 \cdot (m_W / W_{p_\mathrm{T}})$ such that the jet is inside the expected W boson cone.
  - Additionally $\frac{m_W - m_{jj}}{m_W} < 0.3$, meaning that the invariant mass of the light jet system has to be within 30% of the W boson mass.

Multiplets satisfying the above conditions are given label 1 for being a signal multiplet, the rest are labelled as 0 for being a background multiplets. Stop and DM events are used to get top candidates for training. This is done because the top quarks in stop and DM events are produced across a wider range of p_T when compared to $t\bar{t}$ events. It is possible that the truth matching procedure does not find the true hadronic top even when one exists in the event. This can happen because the p_T and η requirements on the jet candidates used to make the multiplets are too strict. The truth matching procedure has an efficiency of $\sim 66\%$ in the p_T range below 600 GeV, which drops to $\sim 40\%$ in the p_T range between 600 GeV and 900 GeV, when calculated with stop events, as shown in Figure 5.14. Since the matching process is done to create training data for the top DNN, this strict process is considered the best way to provide a high purity of true top quarks that can be trained on.

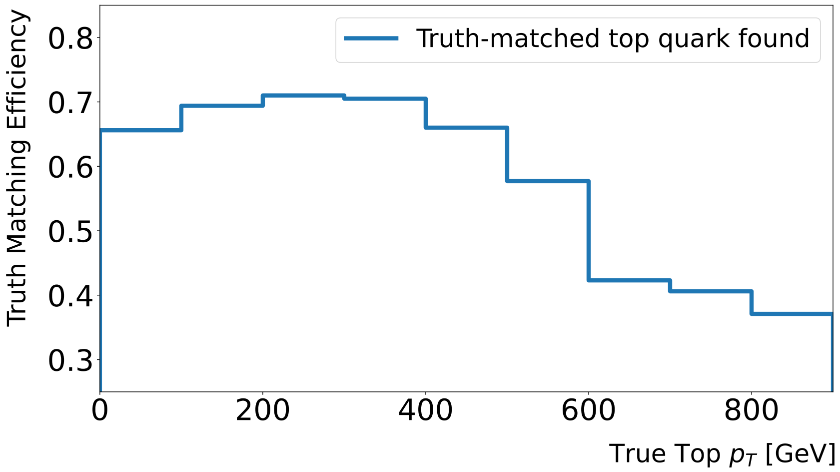

Figure 5.14: The number of events where the true hadronic top quark is matched as a result of truth matching procedure detailed in Section 5.4.3 divided by the total number of events with a true hadronic top quark.

The distributions of the input quantities provided to the network capture fully the kinematic properties of the top quark decay. The distributions of the six non trivial input quantities and the p_T of the top used in the training are shown in Figure 5.15. As discussed in Section 4.3, the Neural Network can learn differences in the input distributions and higher order correlations between them. The triangle plot (Figure 5.15) shows 1-D and 2-D distributions of the signal events in blue and background events in red showing how these multiplets occupy the input kinematics phase space. The flat distribution of top p_T, mentioned previously, is also visible.

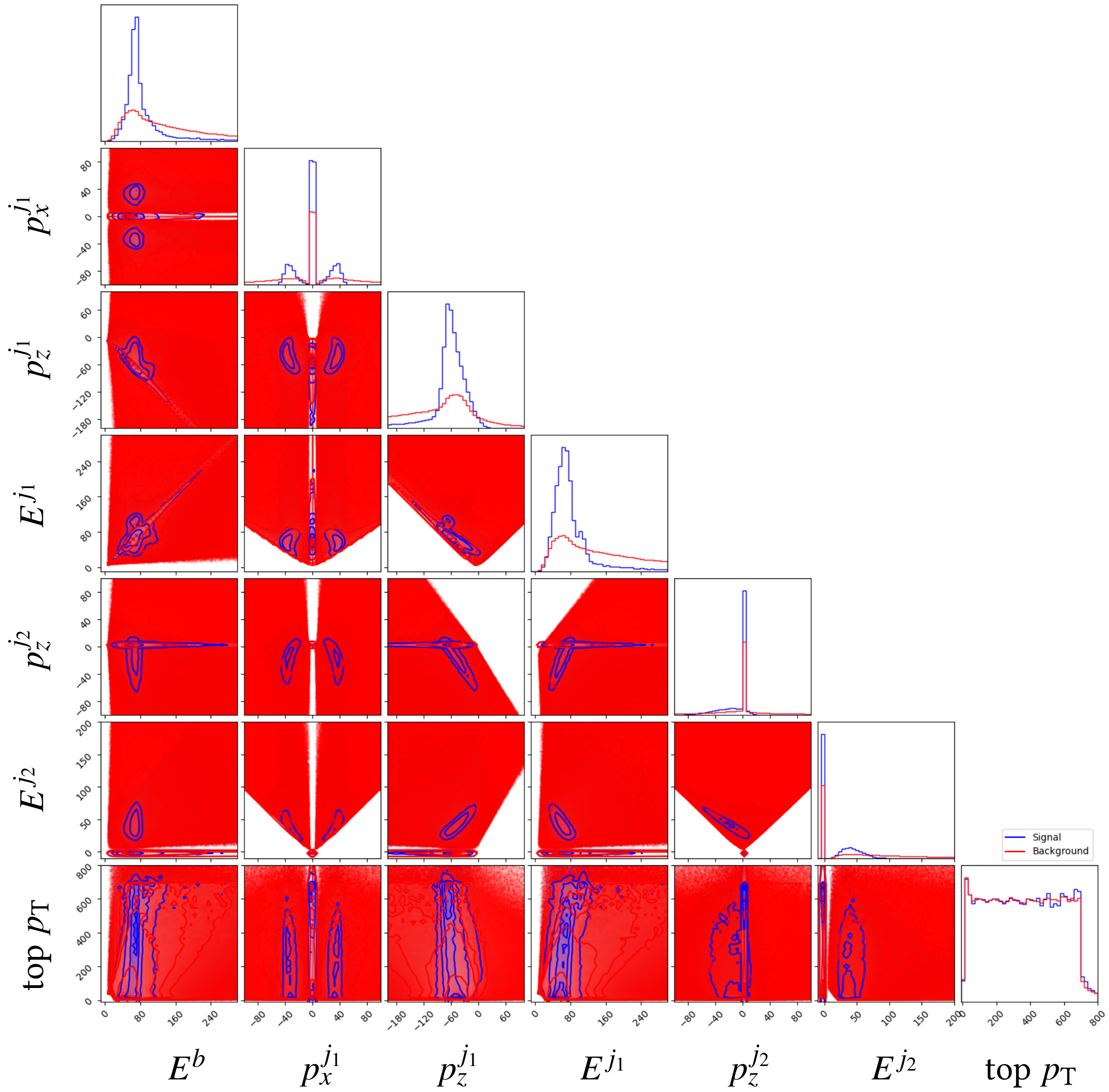

Figure 5.15: Distributions of the input variables used in training the resolved top DNN with signal multiplets depicted in blue and background multiplets in red. All inputs but the top p_T describe the six non trivial kinematic variables required to the relative configuration of the jets within the top decay. The top p_T which is removed from the multiplet by boosting it into the rest frame is provided additionally. This is made to have a flat distribution by providing weights to events as a function of the p_T.

DNN Training

Each stop and DM event consists of a true hadronic top quark which may or may not be identified by the truth matching process defined in Section 5.4.3. Within events with a truth matched hadronic top (signal multiplet), up to 20 background multiplets that are not the hadronic top, can be found. Since all multiplets from stop and DM events are used to develop the DNN, a very imbalanced labelled dataset is created. Hence, during the training, weights are applied to each multiplet such that the effective number of background and signal multiplets are equal, called 'training weights'. This is a common approach used to deal with imbalanced dataset as explained in Section 4.4.

A Keras [203] implementation of DNN is used and the network consists of four fully connected hidden layers with 64 nodes per layer. This configuration is chosen after scanning a grid of two to four layers and 16 to 64 nodes per layer and evaluating which configuration gives the highest AUC value. Each training is done on a CPU and the maximum number of allowed epochs is set to 200. Early stopping is used to stop the training when the performance of the network doesn't improve for the last 10 iterations. In this particular network, the best performance is obtained after $\simeq 60$ epochs. The labelled dataset was divided into training, test and validation using a 50-25-25 split, as explained in Section 4.4. The 2-fold cross-validation also explained in Section 4.4, yields the two classifier labelled '_0' and '_1'. The NN loss and NN accuracy are plotted for the training and validation datasets of both networks in Figure 5.16. The output of the DNN as evaluated on the test dataset is shown in Figure 5.17 where the 'Bkg' class describes multiplets that have label 0 and 'Sig' describes multiplets that have label 1. The test dataset is a part of the labelled dataset used to test the DNN performance as explained in Section 4.4. The reconstruction algorithm has an AUC value of about 0.91 calculated using the test dataset as shown in Figure 5.18.

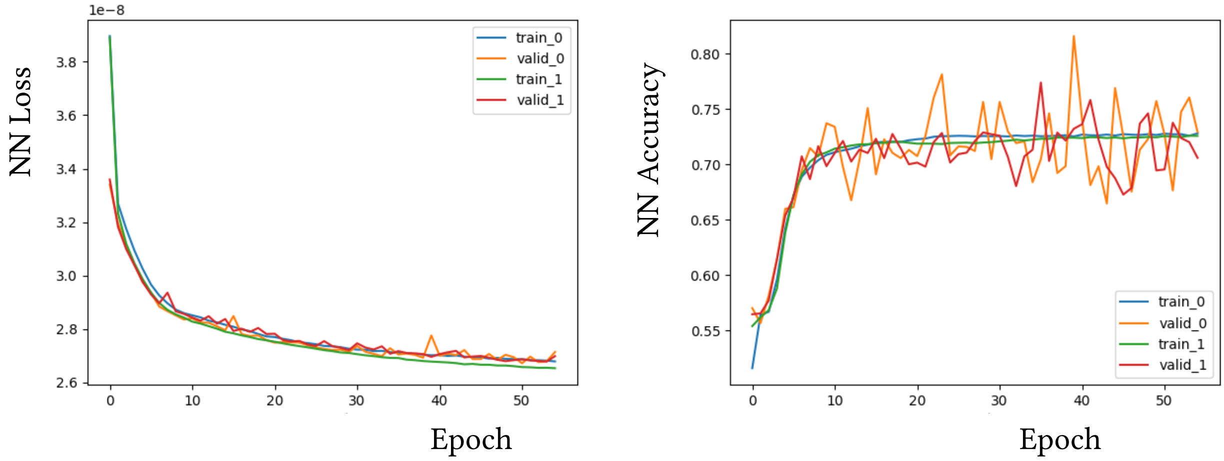

Figure 5.16: NN loss and accuracy versus training epochs of the resolved top DNN.

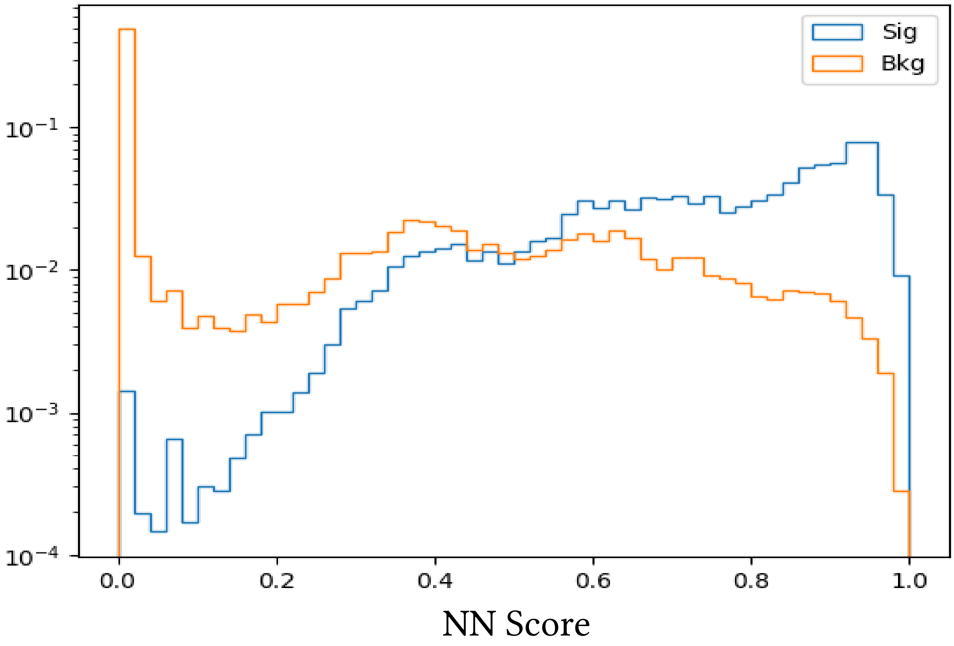

Figure 5.17: Output of the resolved top DNN in the test dataset.

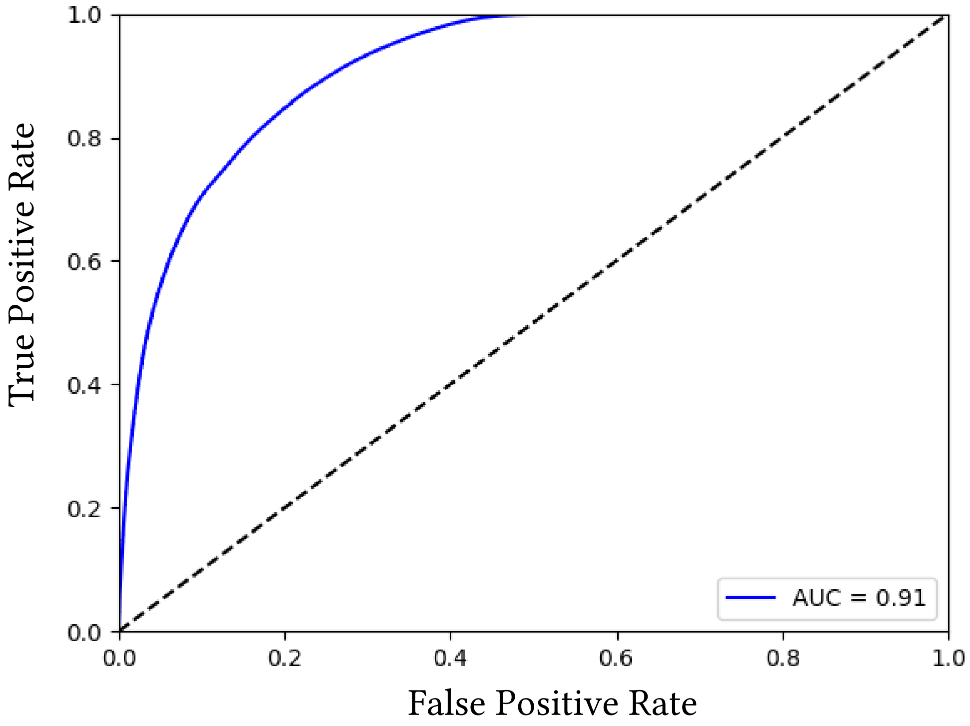

Figure 5.18: ROC curve along with the computed AUC value of the resolved top DNN.

DNN Performance

The performance of the DNN is evaluated on a subset of stop signal events. Within this dataset, each event with a multiplet having DNN score above 0.2 is studied. In both $t\bar{t}$ and signal events, such a cut of $\text{top}^{\text{DNN}}_{\text{score}} > 0.2$ corresponds to the selection of at least 99.5% of events with a real hadronically-decaying top. The multiplet with the highest NN score in the event is considered as the hadronic top candidate identified by the DNN. To understand further how the top NN performs, a few studies are done as depicted in Figures 5.19-5.22. Each event in the studied dataset falls into one of five categories:

- No truth-matched Top: The true top multiplet in the event is not found by the matching procedure (blue).
- DNN missed Pair: The true top multiplet, in the form of a pair, is found by truth matching but **missed** by the DNN (orange).
- DNN identified Pair: The true top multiplet, in the form of a pair, is found by truth matching and **correctly identified** by the DNN (green).
- DNN missed Triplet: The true top multiplet, in the form of a triplet, is found by truth matching but **missed** by the DNN (red).
- DNN identified Triplet: The true top multiplet, in the form of a triplet, is found by truth matching and **correctly identified** by the DNN (purple).

The distribution of these categories as a function of true top p_{T} is shown in Figure 5.19.

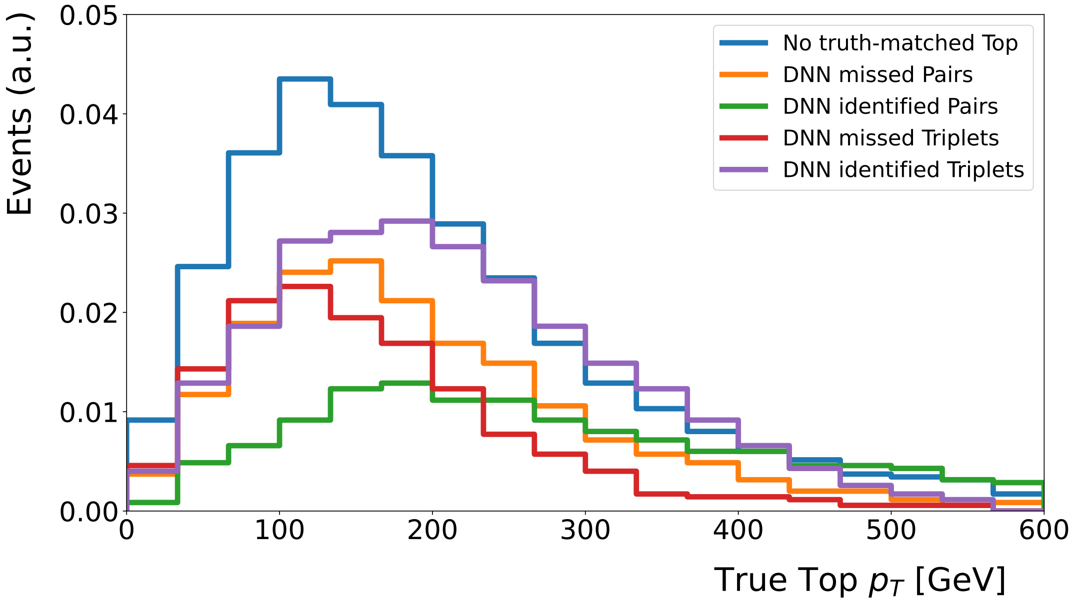

Figure 5.19: Distribution of the different subcategories of events with hadronic top quarks as a function of true top p_{T}.

To understand the efficiency of the DNN, the ratio of events that fall into each of the five different categories is plotted in Figure 5.20. The ratio is defined as follows:

$$\text{Ratio (category)} = \frac{\text{Number of events with top}_{\text{score}}^{\text{DNN}} > 0.2 \text{ in category}}{\text{Number of events with true hadronic top quarks with top}_{\text{score}}^{\text{DNN}} > 0.2} \tag{5.1}$$

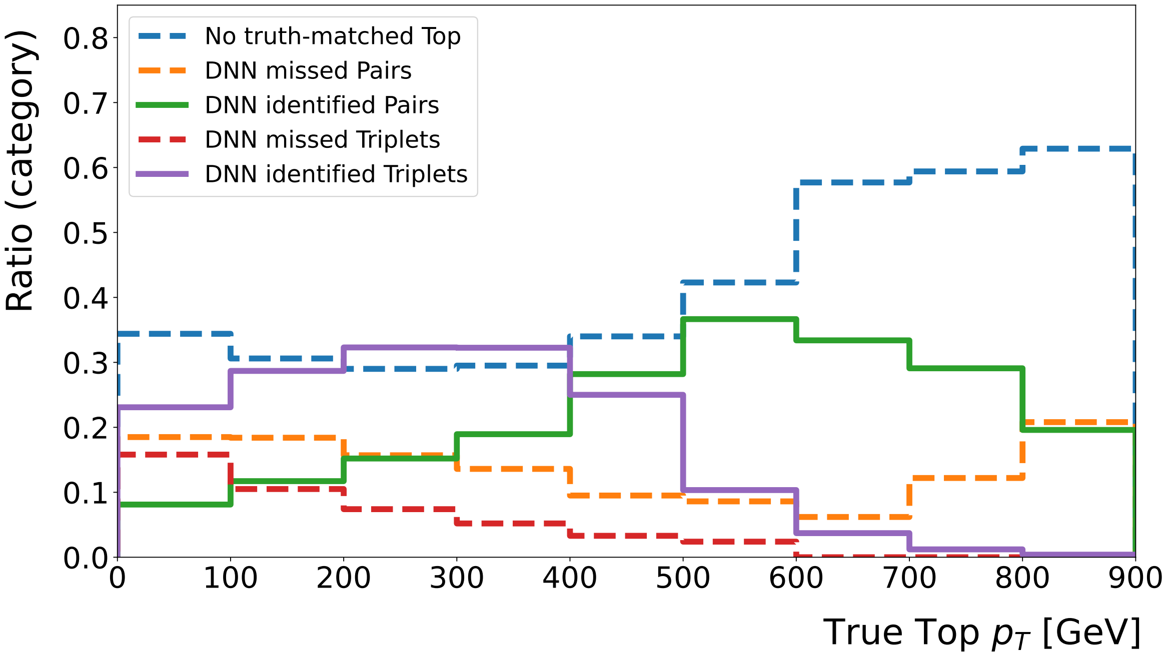

Figure 5.20: Ratios of the top DNN for the different subcategories of events with hadronic top quarks as a function of true top p_T.

The DNN is most successful at identifying the truth top triplet in the p_T range of 200 to 400 GeV and pairs in the p_T range of 400 to 600 GeV. Hence the DNN can be considered to be most successful for multiplets (pairs and triplets together) in the mid-p_T range of 200 to 600 GeV. A high fraction of non-truth matched top quarks exist across p_T, as demonstrated in Figure 5.20, suggesting that the truth matching procedure has some room for improvement. In an event, the multiplet with the highest score is taken as the hadronic top quark. Hence, even in events where a true top quark isn't found as a result of truth matching, a top candidate can be found by the DNN. However, to verify that the candidate chosen by the top DNN is a true top quark, more truth information is required in the MC samples which is not possible at this stage. A plot of the same event categories as a function of NN score is shown in Figure 5.21.

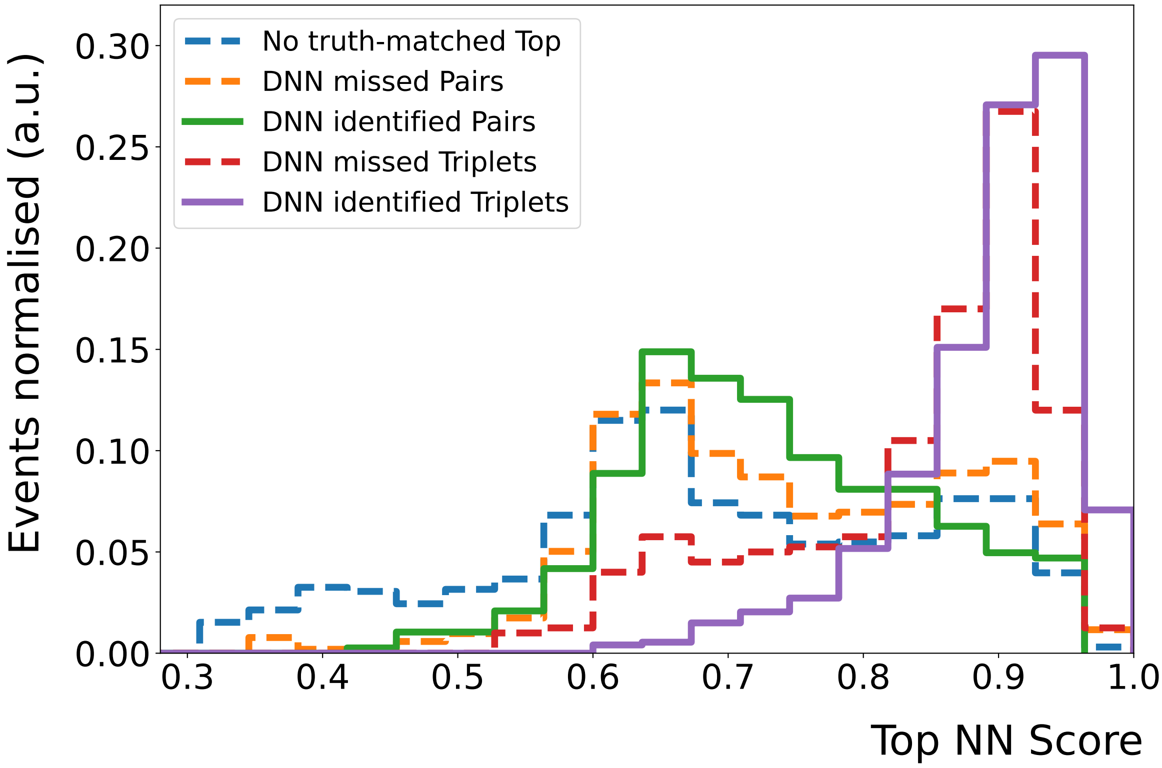

Figure 5.21: Normalised distributions of the different subcategories of events with hadronic top quarks as a function of top NN Score.

Without better truth information, some studies are performed using mass distributions of the top candidate mass and the W candidate mass to understand where the events in the different categories lie. In the pairs, the W candidate mass comes from m(j), while for triplets it comes from m(jj) . Figure 5.22 indicates that within the pairs that the DNN tags successfully (green), a larger fraction of events are those with m(j) < m(W). These can be explained by a missed second jet or one that is reconstructed as part of the b-quark jet. The DNN identified pairs also cluster at a lower value of top candidate mass, when compared to DNN identified triplets, as shown in Figure 5.22. The top candidate mass is defined as m(bj) for pairs and m(bjj) for triplets. Given that the DNN identified pairs still lie within the top mass peak, it can be concluded that that m(bj) gives a value close to top mass, even if slightly lower. This suggest that the pairs consist of a b-quark jet that is actually a merged bj pair or a j that is actually a merged jj pair. However, more in depth studies, ideally with more truth information, are required to draw more conclusive statements.

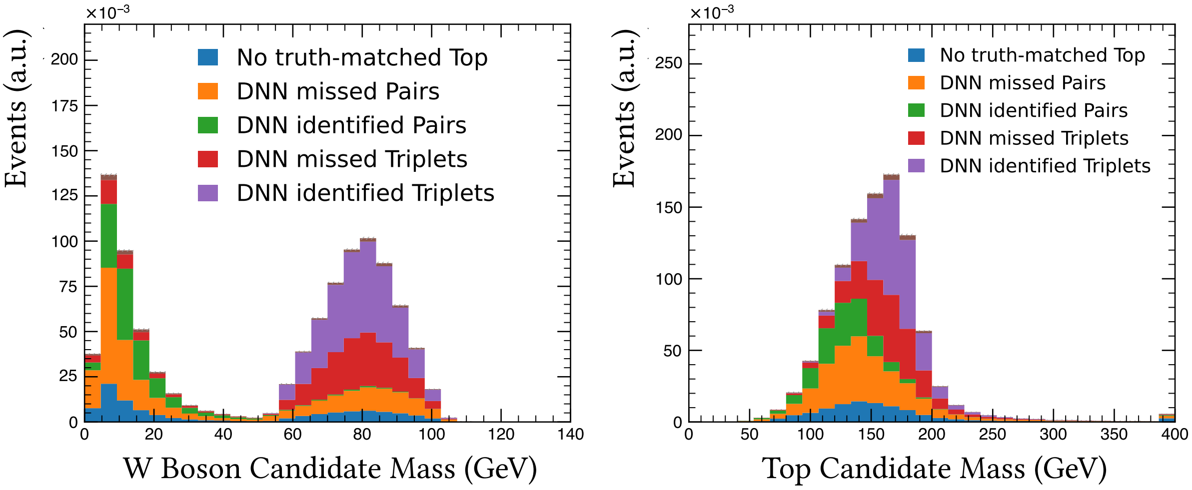

Figure 5.22: Distributions of the different subcategories of events as a function of W boson candidate mass defined as $m(jj)$ for triplets and $m(j)$ for pairs (left) and top candidate mass defined as $m(bjj)$ for triplets and $m(bj)$ for pairs (right).

5.4.4 Boosted Hadronic Top Reconstruction

For boosted top quarks, a multivariate classifier is used to identify the Large-R jets from hadronic top decays using a working point with a top-tagging efficiency of 80% [204, 205]. This classifier uses jet substructure observables as input. The algorithm is designed for top quarks with p_{T} above 350 GeV. The resolved top tagger performance is compared with the boosted tagger as a function of true top quark p_{T} for the top quarks in this analysis as shown in Figure 5.23. The efficiency of the resolved top tagger is defined using events with a DNN selected multiplet having a score above 0.2. From these events, the fraction where the DNN identified multiplet (pair + triplet) is the one also selected by truth matching is used as follows[3]:

$$\varepsilon_{\text{Resolved Top Tagger}} = \frac{\text{Events where DNN identifies truth-matched multiplets, top}^{\text{DNN}}_{\text{score}} > 0.2}{\text{Events with true hadronic top quarks, top}^{\text{DNN}}_{\text{score}} > 0.2} \tag{5.2}$$

For boosted top quarks, events with a LR jet with $p_{\mathrm{T}} > 300$ GeV are considered and those with true hadronic top quarks are used to define the algorithms efficiency. A simpler truth matching can be done for boosted top quarks as compared to resolved top quarks. The LR jet with minimum $\Delta R(t, LR)$ that also has $\Delta R(t, LR) < 2 \cdot (m_t / t_{p_{\mathrm{T}}})$ is identified as the true hadronic top quark. Using this truth matching, the efficiency of the boosted tagger is defined as follows:

---

[3] This efficiency can be considered as a lower bound because of a possible truth-matching inefficiency discussed earlier.

$$\varepsilon_{\text{Boosted Top Tagger}} = \frac{\text{Events where DNN identifies truth matched } LR \text{ jet with } p_{\mathrm{T}} > 300\,\text{GeV}}{\text{Events with true hadronic tops, } LR \text{ jet } p_{\mathrm{T}} > 300\,\text{GeV}} \tag{5.3}$$

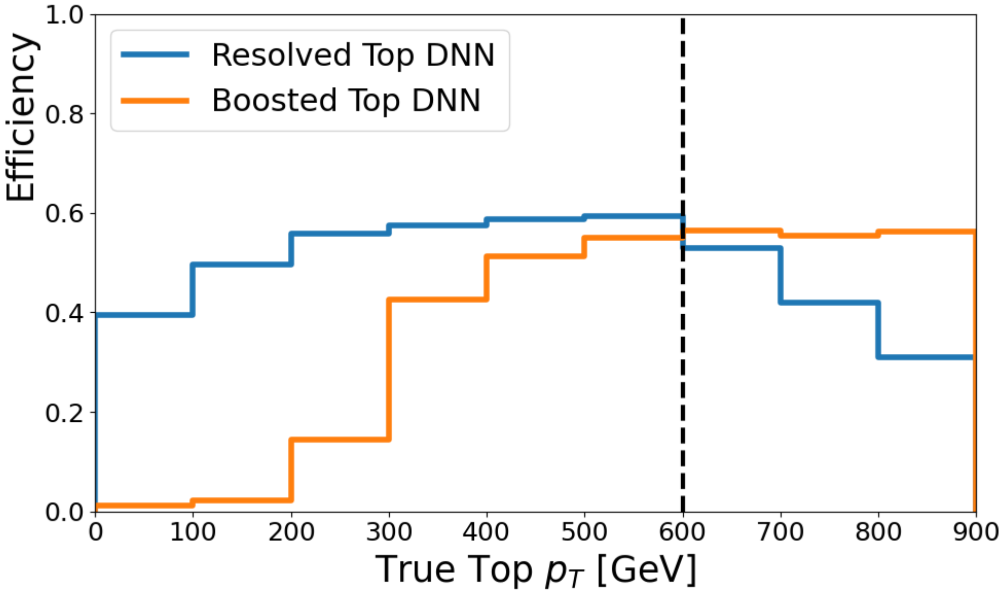

Figure 5.23: Efficiency of the two DNN algorithms used to tag resolved and boosted top quarks.

It can be seen that 600 GeV is the p_{T} at which the efficiencies of resolved and boosted top quarks cross. It is concluded that this will be used as the transition point between the two taggers. This means that if a *LR* jet is found in the event with a $p_{\mathrm{T}} > 600\,\text{GeV}$, the boosted DNN top tagger is used. In events with no *LR* jet and those with a *LR* jet of $p_{\mathrm{T}} < 600\,\text{GeV}$, the resolved DNN is employed to find a resolved hadronic top candidate. This top reconstruction strategy is summarised in Table 5.11.

Table 5.11: Table summarizing the event selection wherein the different Top DNN strategies are employed.

Preselection	$E_{\mathrm{T}}^{\mathrm{miss}}$ or single-lepton trigger Exactly one signal lepton [e (Table 5.5) or μ (Table 5.6)] No baseline τ-leptons (Table 5.7) $N_{\text{jet}} > 1$ can be small-R or *LR* jet (Table 5.8)	
Top Reconstruction	Resolved top DNN 0 *LR* jet ($p_{\mathrm{T}} > 600 GeV$) ≥ 2 small R jets	Boosted top DN ≥ 1 *LR* jet ($p_{\mathrm{T}} > 600 GeV$) any config of small R jets

5.5 Event Classification using Neural Networks

5.5.1 Definition of Analysis Categories

The selections described in the previous section cover a very large phase space. In order to subdivide this large kinematic space, kinematic variables are used to define eight independent analysis categories. At first, events are separated into those that contain a Large-*R* jet, called "Boosted". In the case of absence of Large-*R* jets, a tighter $E_{\mathrm{T}}^{\mathrm{miss}}$ cut of 230 GeV is applied and these events are called "High-$E_{\mathrm{T}}^{\mathrm{miss}}$" events. Events with $70\,\mathrm{GeV} < E_{\mathrm{T}}^{\mathrm{miss}} \leq 230\,\mathrm{GeV}$ were initially studied as "Low-$E_{\mathrm{T}}^{\mathrm{miss}}$" events but later dropped because they didn't provide significant improvement in the results.

Within the high-$E_{\mathrm{T}}^{\mathrm{miss}}$ events, the configuration of b-quark jets is used to further split categories into events with only one tagged b-quark jet falling into the 'High-$E_{\mathrm{T}}^{\mathrm{miss}}$-1b' category and for events with at least two b-tagged jets falling into the 'High-$E_{\mathrm{T}}^{\mathrm{miss}}$-2b' category. In the boosted categories, three configurations of b-quark jets are considered. The first type of event consists of 2 b-quark jets called the 'Boosted-2b' category. If only one b-quark jet is found in the event, its location with respect to the *LR* jet is evaluated. If the b-quark jet is found inside the *LR* jet, the event is considered to be in the 'Boosted-1bhad' category denoting that the b-quark jet originates from the boosted hadronic top. On the other hand, if the b-quark jet is found to be outside the *LR* jet, it falls in the 'Boosted-1bhad' category denoting that the b-jet likely originates from the leptonically decaying top quark in the event.

The *LR* jet top tagger is used in all three sub-categories of boosted events, namely the Boosted-2b, Boosted-1blep and Boosted-1bhad categories. Events with and without a positive top tag are used for the analysis. However, the categories are further split further into one with a top tag (-1t) and one without a top tag (-0t). The events without a positive tag are retained because a significant fraction of the signal events lie inside the selection of *LR* jets, above a p_{T} of 600 GeV, without a top tag. This leads to six boosted analysis categories, splitting each of the three b-quark jet configurations into one with a top tag (-1t) and one without a top tag (-0t). The eight analysis categories thus obtained are High-$E_{\mathrm{T}}^{\mathrm{miss}}$-1b, High-$E_{\mathrm{T}}^{\mathrm{miss}}$-2b, Boosted-1blep-1t, Boosted-1blep-0t, Boosted-1bhad-1t, Boosted-1bhad-0t and Boosted-2b-1t, Boosted-2b-0t. The kinematic selections that define these categories are shown in Table 5.12.

As explained in Section 5.4.2, VR jets are used to find b-quark jets inside the *LR* jets. This selection is defined using the definition $N(\mathrm{VR\ trk\ bjet}, \Delta R(\mathrm{bjet}, \mathrm{LR\ jet}) < 1.1)$, leading to the b-quark jet configuration required for the 'Boosted-1bhad' categories. Small-*R* jets are used to find b-quark jets outside the *LR* jets. This selection is defined using $N(\mathrm{PFlow\ bjet}, \Delta R(\mathrm{bjet}, \mathrm{LR\ jet}) > 1.1)$, leading to the b-quark jet configuration described by the 'Boosted-1blep' categories. In the high-$E_{\mathrm{T}}^{\mathrm{miss}}$ events, where the top DNN is used to select the hadronic top, a configuration of three light jets is required. This can be one b-quark jet and two light jets for the High-$E_{\mathrm{T}}^{\mathrm{miss}}$-1b category or two b-quark jets and one light jet for High-$E_{\mathrm{T}}^{\mathrm{miss}}$-2b category. Such a selection ensures that one b-quark jet and one light jet, as required by the resolved top DNN is present and an additional jet used to reconstruct the leptonically decaying top quark is also present.

Table 5.12: Summary of the analysis categories, also published in [2].

Preselection	Event cleaning, primary vertex $E_{\mathrm{T}}^{\mathrm{miss}} > 70\,\mathrm{GeV}$ MET or single lepton trigger Exactly one signal lepton and no additional baseline leptons. No taus.							
Analysis Regions	High $E_{\mathrm{T}}^{\mathrm{miss}}$		Boosted					
	1b	2b	1bhad-0t	1bhad-0t	2b-0t	1bhad-1t	1bhad-1t	2b-1t
$E_{\mathrm{T}}^{\mathrm{miss}}$	$> 230\,\mathrm{GeV}$		$> 70\,\mathrm{GeV}$					
$N(\mathrm{LR\ jet})$	0		≥ 1					
$N(\mathrm{VR\ trk\ bjet}, \Delta R(\mathrm{bjet}, \mathrm{LR\ jet}) < 1.1)$	-		0	≥ 1	≥ 1	0	≥ 1	≥ 1
$N(\mathrm{PFlow\ bjet}, \Delta R(\mathrm{bjet}, \mathrm{LR\ jet}) > 1.1)$	-		≥ 1	0	≥ 1	≥ 1	0	≥ 1
DNN top	-		0			1		
$N(\mathrm{top_{had}}, \mathrm{NN} > 0.2)$	1		-					
N_{bjet}	1	≥ 2	-					
$N_{\mathrm{light\text{-}jet}}$	≥ 2	≥ 1	-					
$\mathrm{top_{had}}$ candidate	Max DNN Score		LR jet					
$\mathrm{top_{lep}}$ candidate	$\ell + \mathrm{j}$	$\ell + \mathrm{bj}$	$\ell + \mathrm{bj}$	$\ell(+\mathrm{j})$	$\ell + \mathrm{bj}$	$\ell + \mathrm{bj}$	$\ell(+\mathrm{j})$	$\ell + \mathrm{bj}$
Event NN selection	See Table 5.15							

The definition of the leptonic top in the different categories is provided in the last row of Table 5.12. It is always defined to be the visible decay products of the leptonic top quark based on the objects available. When a b-quark jet is present, it along with the lepton is chosen: 'l+bj'. In the absence of a b-quark jet, the leading p_{T} non b-tagged jet is used: 'l+j'. In the boosted regime there is no requirement on the number of small R jets, hence it is possible there is no jet to pair with the lepton and is hence described by 'l(+j)'.

Events that pass all the above defined selections are then fed into classification networks used to distinguish if a given event is coming from a known SM process or a new physics process. Binary classifiers are chosen such that they sort events into two target classes: 'Bkg' for all the different SM processes listed in Section 5.2 and 'Signal' for new physics processes. Two types of classifiers, one for DM signal processes and one for stop signal processes are trained separately.

The signal processes across the entire probed phase space also fall into different kinematic regions. The acceptance of these kinematic categories in the signal model phase space also differs. This can be evaluated by plotting the acceptance per model for different analysis categories. Acceptances are computed applying the selections which define the event categories to truth-level objects. Two examples, the High-$E_{\mathrm{T}}^{\mathrm{miss}}$-2b and Boosted-2b selections are shown in Figure 5.24. It can be seen, that the high $E_{\mathrm{T}}^{\mathrm{miss}}$ region is more efficient at accepting signal over the entire mass plane compared to the Boosted-2b, while within the Boosted-2b category, the acceptance increases as one moves to the high $\tilde{t}_1$ mass signal models.

This signal acceptance has to be studied in conjunction with the background rejection efficiency to understand the sensitivity brought about by each category. However, within an analysis category, optimal discrimination between signal and background is desired. It is expected that the background compositions in the different analysis categories have different proportions, which is demonstrated in Section 5.6. Hence, the discrimination task differs in each analysis category.

Additionally, kinematic variables are used to describe the event to the DNN. Hence, dedicated signal and background classifiers are trained for each analysis category. The classification task can be optimised independently in each analysis region and a statistical analysis is performed combining all analysis categories to provide the best sensitivity. Since the DM signal events lie mainly in the high-$E_{\mathrm{T}}^{\mathrm{miss}}$ categories, only two DM classifiers are trained. Whereas, stop classifiers are trained in all eight analysis categories.

5.5.2 Event Discrimination DNN

DNN Input variables

Both top quark 4-vectors and $E_{\mathrm{T}}^{\mathrm{miss}}$ are provided to the network. Additionally, the visible decay products of the $t\bar{t}$ pair, namely the individual lepton and b-quark jets are also provided. It is assumed that the $t\bar{t}$ + $E_{\mathrm{T}}^{\mathrm{miss}}$ system essentially describes the complete event. It is described to the DNN using the 4-vectors of the leptonic and hadronic top along with the 2-D $E_{\mathrm{T}}^{\mathrm{miss}}$ vector reconstructed in the event. Transformations are applied to exploit the expected symmetries of the event similar to what has been described for the DNN to identify hadronically decaying top quarks in Section 5.4.3. The $t\bar{t}$ +$E_{\mathrm{T}}^{\mathrm{miss}}$ object triplet is Lorentz boosted into the rest frame in the transverse plane, $p_{\mathrm{T}}(t+\bar{t}+E_{\mathrm{T}}^{\mathrm{miss}})=0$. A rotation is done around the z-axis such that the $E_{\mathrm{T}}^{\mathrm{miss}}$ vector points into the positive x-direction as can be seen is Figure 5.25. At this point there remains a longitudinal degree of freedom due to the forward-backward symmetry of proton-proton collisions at the LHC. To exploit this symmetry, a mirror transformation is performed such that for a hadronic top quark with a negative z-component, the $t\bar{t}$ +$E_{\mathrm{T}}^{\mathrm{miss}}$ system is rotated by π around the x-axis. For hadronic top quarks with a positive z-component, no rotation is performed. This yields seven remaining non-trivial parameters listed in Table 5.13 as a result of the transformations depicted in Figure 5.25.

Table 5.13: List of the seven non-trivial input variables for the event NNs.

Object	Vector Component
$E_{\mathrm{T}}^{\mathrm{miss}}$	E
t_{had}	E
	p_x
	p_y
	p_z
t_{lep}	E
	p_z

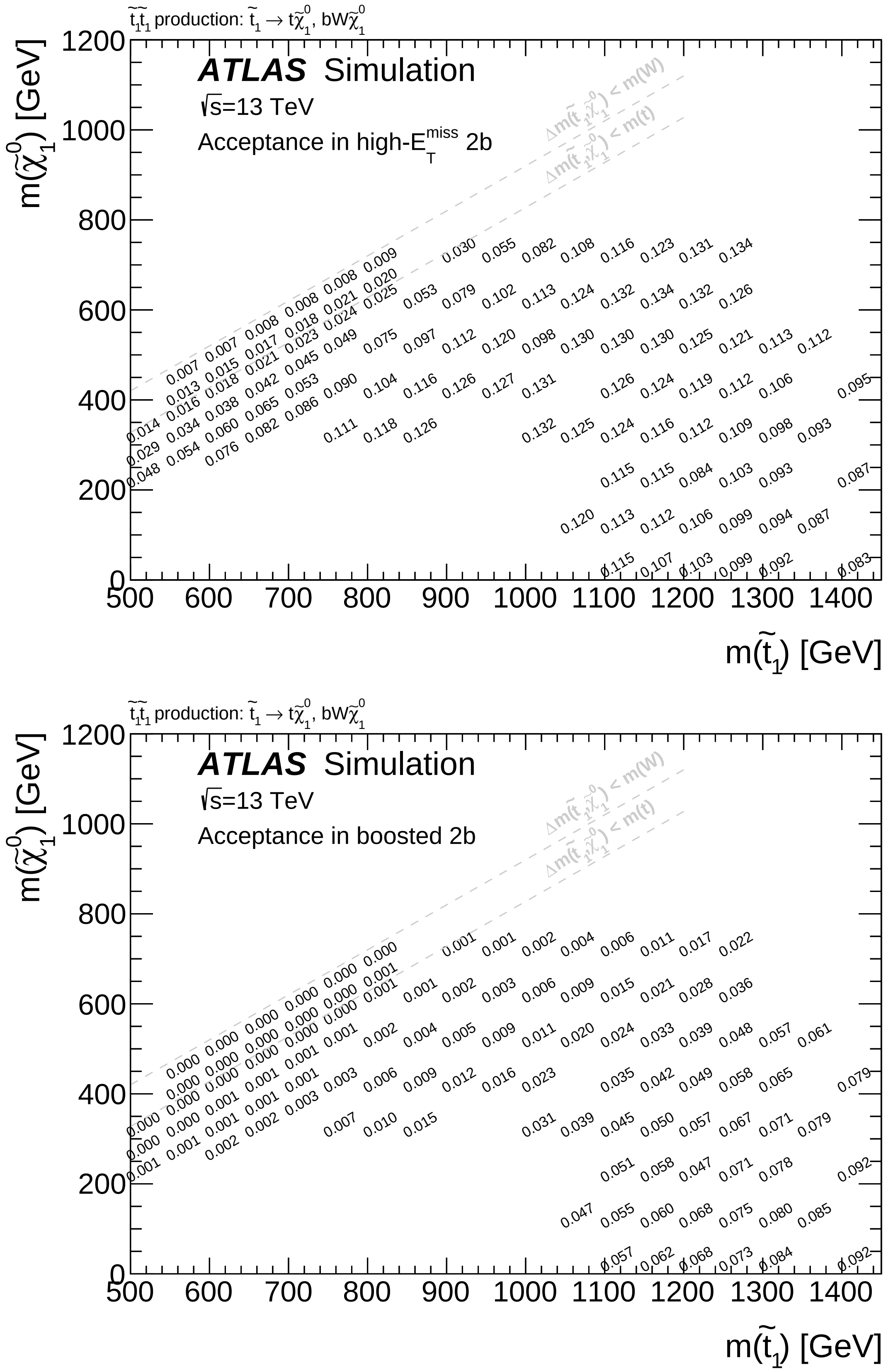

Figure 5.24: Acceptances for all models in the $\tilde{t}_1$-$\tilde{\chi}_1^0$ mass plane are shown for the High-$E_{\mathrm{T}}^{\mathrm{miss}}$-2b category (top) and for the union of the Boosted-2b-1t and Boosted-2b-0t categories (bottom).

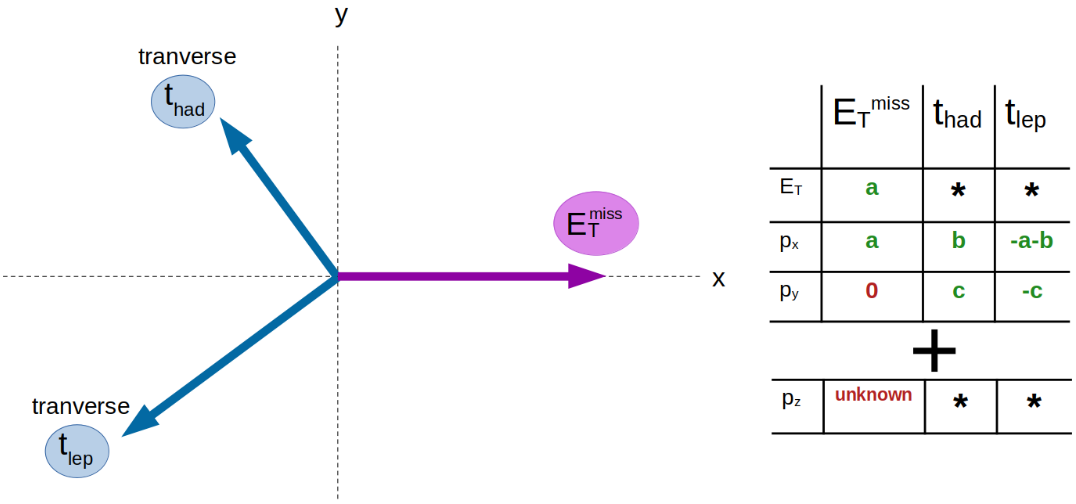

	E_T^{miss}	t_{had}	t_{lep}
E_T	a	*	*
p_x	a	b	-a-b
p_y	0	c	-c
p_z	unknown	*	*

Figure 5.25: Orientation of the $t\bar{t}$ $+E_{\mathrm{T}}^{\mathrm{miss}}$ system to capture all relative kinematics of the three-object system after the transformations explained in the text are applied. A '*' is used to show the parameters that remain unchanged after the transformation.

Furthermore, some high level kinematic variables are provided to the network in addition to the $t\bar{t}$ $+E_{\mathrm{T}}^{\mathrm{miss}}$ kinematics such as:

- $\mathbf{E}_{\mathrm{T}}^{\mathrm{miss}}$ **significance** - This variable quantifies the likelihood that the observed $E_{\mathrm{T}}^{\mathrm{miss}}$ in an event is due to a genuine physical process (like the production of invisible particles such as neutrinos or dark matter) rather than being a result of detector noise or experimental uncertainties. A higher $E_{\mathrm{T}}^{\mathrm{miss}}$ significance indicates that the observed $E_{\mathrm{T}}^{\mathrm{miss}}$ is more likely to be a genuine physical effect rather than a statistical fluctuation or experimental noise. The $E_{\mathrm{T}}^{\mathrm{miss}}$ significance distributions of two major background process ($t\bar{t}$ and W+jets) and four benchmark stop signals are shown in Figure 5.26. An object based calculation for $E_{\mathrm{T}}^{\mathrm{miss}}$ significance explained in Section 3.3.3 is used to calculate the $E_{\mathrm{T}}^{\mathrm{miss}}$ significance in each event. Backgrounds events with incorrectly high amounts of $E_{\mathrm{T}}^{\mathrm{miss}}$ can be differentiated from signal events with such a variable as demonstrated in Figure 3.21.

- $\mathbf{\Delta R(b,b)}$ - Mainly provides discrimination against the W+jets background. The geometrical separation for $t\bar{t}$ and signal events ($t\bar{t}$ $+E_{\mathrm{T}}^{\mathrm{miss}}$) is larger than for W+jets where the additional jets can have gluon splitting $b\bar{b}$ pairs as demonstrated in Figure 5.27.

- $\mathbf{m_T(l,E_{\mathrm{T}}^{\mathrm{miss}})}$ - The transverse mass of the lepton and $E_{\mathrm{T}}^{\mathrm{miss}}$ for SM processes with one lepton cuts off at the mass of the W boson corresponding to the case that the $E_{\mathrm{T}}^{\mathrm{miss}}$ is coming entirely from the neutrino. For the signal processes, the $E_{\mathrm{T}}^{\mathrm{miss}}$ originates from both neutrino and new particles and is expected to have higher values. The distribution of $m_T(l,E_{\mathrm{T}}^{\mathrm{miss}})$ for two major background processes ($t\bar{t}$ and W+jets) and four benchmark stop signals is shown in Figure 5.28, the definition of which is:

$$m_T(\vec{p}_T^{\,\ell},\vec{E}_T^{\mathrm{miss}}) = \sqrt{2|\vec{p}_T^{\,\ell}|E_{\mathrm{T}}^{\mathrm{miss}}(1-\cos\Delta\phi(\vec{p}_T^{\,\ell},\vec{E}_T^{\mathrm{miss}}))} \tag{5.4}$$

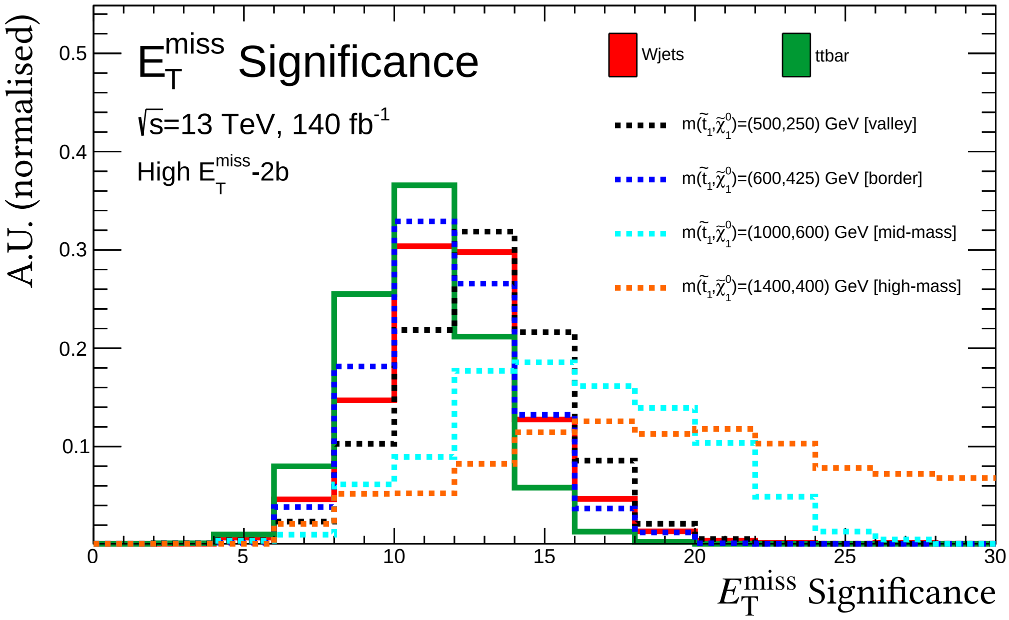

Figure 5.26: Distribution of E_T^{miss} significance in the High-E_T^{miss}-2b analysis region comparing the shapes of two main backgrounds ($t\bar{t}$, W+jets) and some benchmark signal mass points in the stop mass plane.

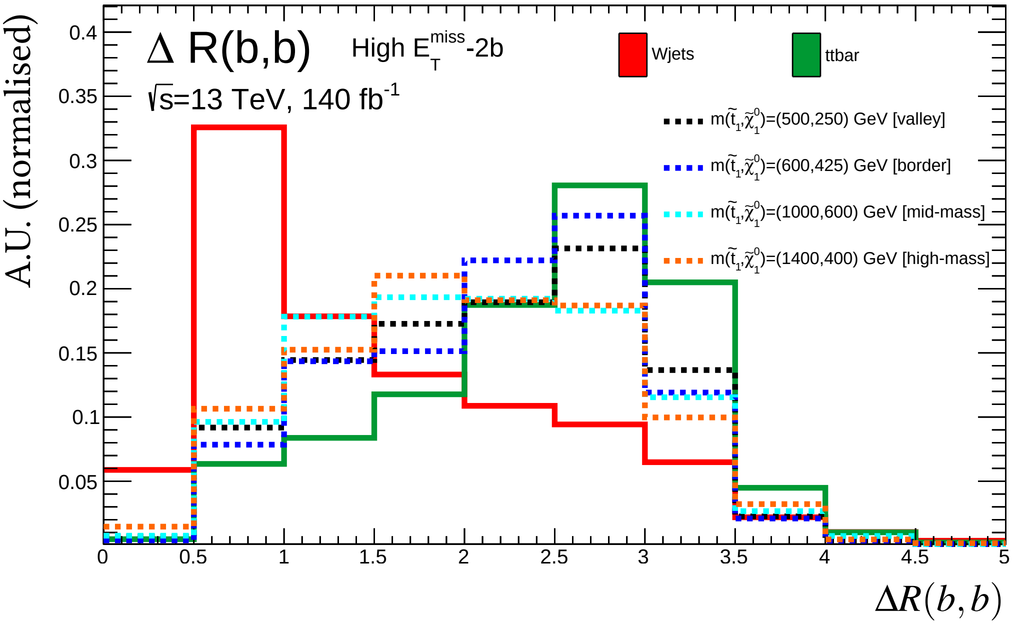

Figure 5.27: Distribution of $\Delta R(b,b)$ in the High-E_T^{miss}-2b analysis region comparing the shapes of two main backgrounds ($t\bar{t}$, W+jets) and some benchmark signal mass points in the stop mass plane.

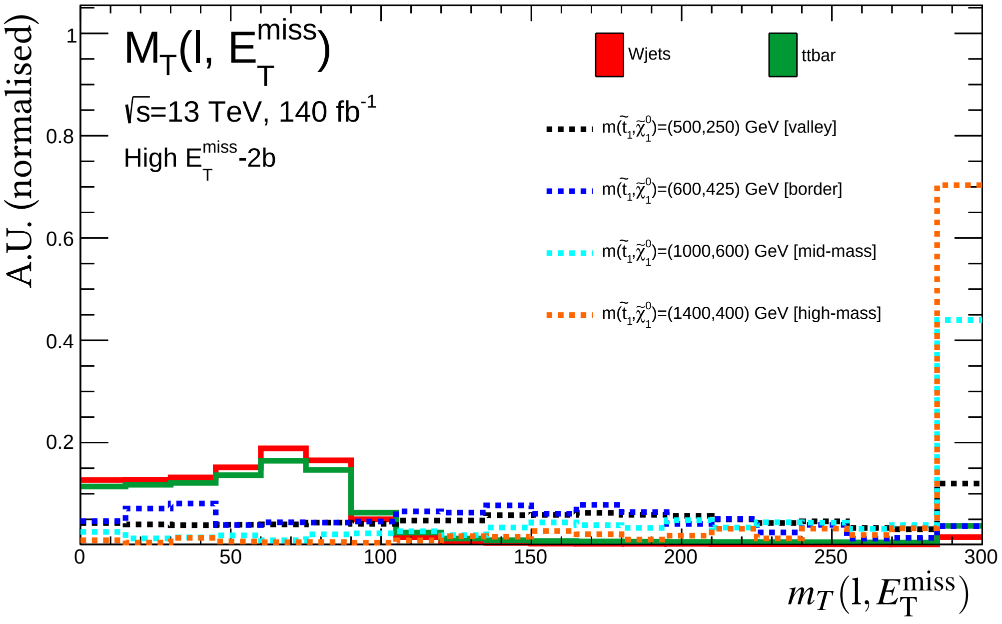

Figure 5.28: Distribution of $m_T(l, E_T^{miss})$ in the High-E_T^{miss}-2b analysis region comparing the shapes of two main backgrounds ($t\bar{t}$, W+jets) and some benchmark signal mass points in the stop mass plane.

For the high-E_T^{miss} categories containing resolved top quarks, additional top specific high-level input variables are provided to the DNN:

- **Resolved top DNN score** - The score of the multiplet chosen in the event is provided to quantify the quality of the reconstructed hadronic top quark as shown in Figure 5.29. The W+jets events are particularly well separated from the $t\bar{t}$ signal events as they don't consist of real top quarks. This is because, the jet combinatorics in the W+jets events that are selected as a top quark have low scores in the top DNN variable.

- **$\mathbf{m_{T2}}$ Variables**: m_{T2} has been employed in various SUSY searches by both ATLAS and CMS [206]. It proves useful in characterising events where the E_T^{miss} arises from the semi-visible decay of two physics objects, as is in the case of a pair of $\tilde{t}_1$ quarks. Its mathematical definition is:

$$m_{T2}(\vec{p}_T^{\,1}, \vec{p}_T^{\,2}, \vec{E}_T^{\,miss}) = \min_{\vec{E}_T^{\,miss,1} + \vec{E}_T^{\,miss,2} = \vec{E}_T^{\,miss}} \left\{ \max \left[m_T(\vec{p}_T^{\,1}, \vec{E}_T^{\,miss,1}), m_T(\vec{p}_T^{\,2}, \vec{E}_T^{\,miss,2}) \right] \right\} , \tag{5.5}$$

where the minimization is conducted over all trial momenta, $\vec{E}_T^{\,miss,1}$ and $\vec{E}_T^{\,miss,2}$ that satisfy the E_T^{miss} constraint ($\vec{E}_T^{\,miss,1} + \vec{E}_T^{\,miss,2} = \vec{E}_T^{\,miss}$). Similar to the m_T distributions, true E_T^{miss} particles distort these distributions more significantly compared to SM particles.

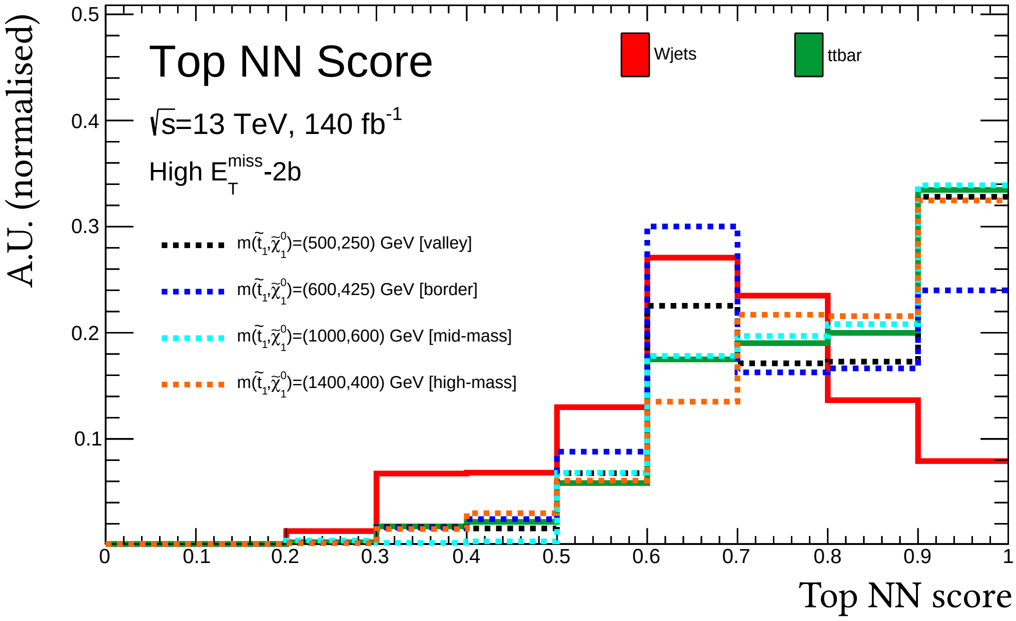

Figure 5.29: Distribution of the resolved top NN score in the High-$E_{\mathrm{T}}^{\mathrm{miss}}$-2b analysis region comparing the shapes of two main backgrounds ($t\bar{t}$, W+jets) and some benchmark signal mass points in the stop mass plane.

- $\mathbf{m_{T2}(b_1, b_2, E_T^{miss})}$ - distributes the $E_{\mathrm{T}}^{\mathrm{miss}}$ between the two b-quark jets such that a pair of particles decay to the b-quark jets and $E_{\mathrm{T}}^{\mathrm{miss}}$ as depicted in Figure 5.30. Consequently, in $t\bar{t}$ events this has a cut-off at the top quark mass as shown in Figure 5.31.
- $\mathbf{m_{T2,\mathrm{min}}(b+l, b, E_T^{miss})} = \min\left[m_{T2}(b_1+l, b_2, E_{\mathrm{T}}^{\mathrm{miss}}), m_{T2}(b_1, b_2+l, E_{\mathrm{T}}^{\mathrm{miss}})\right]$ - An additional variation of m_{T2} along with the lepton is computed.

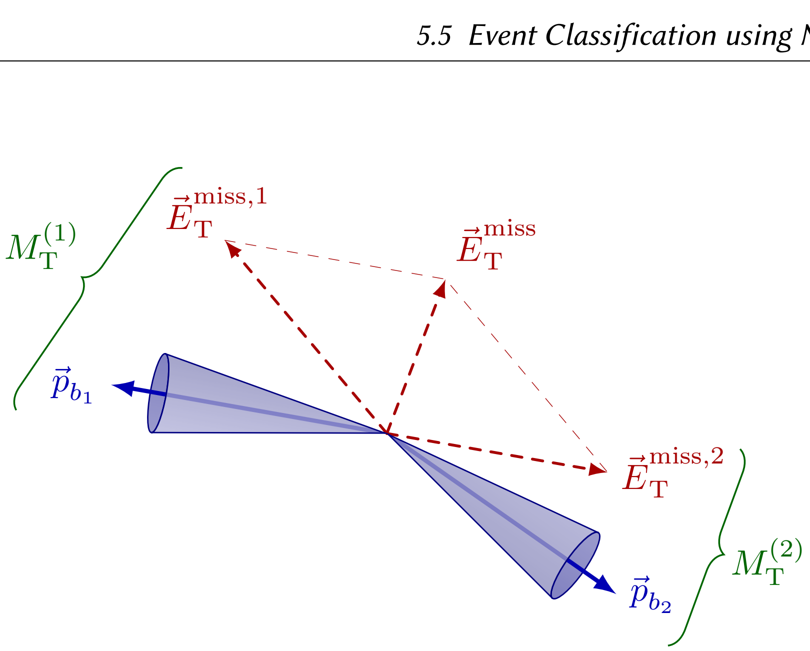

Figure 5.30: Illustration of the $m_{T2}(b_1, b_2, E_T^{miss})$ variable, defined to distribute the E_T^{miss} in the event between the two b-quark jets such that a each particle in a pair of particles decay semi-invisible to a b-quark jet and an invisible particle, adapted from the general m_{T2} variable illustrated in [76].

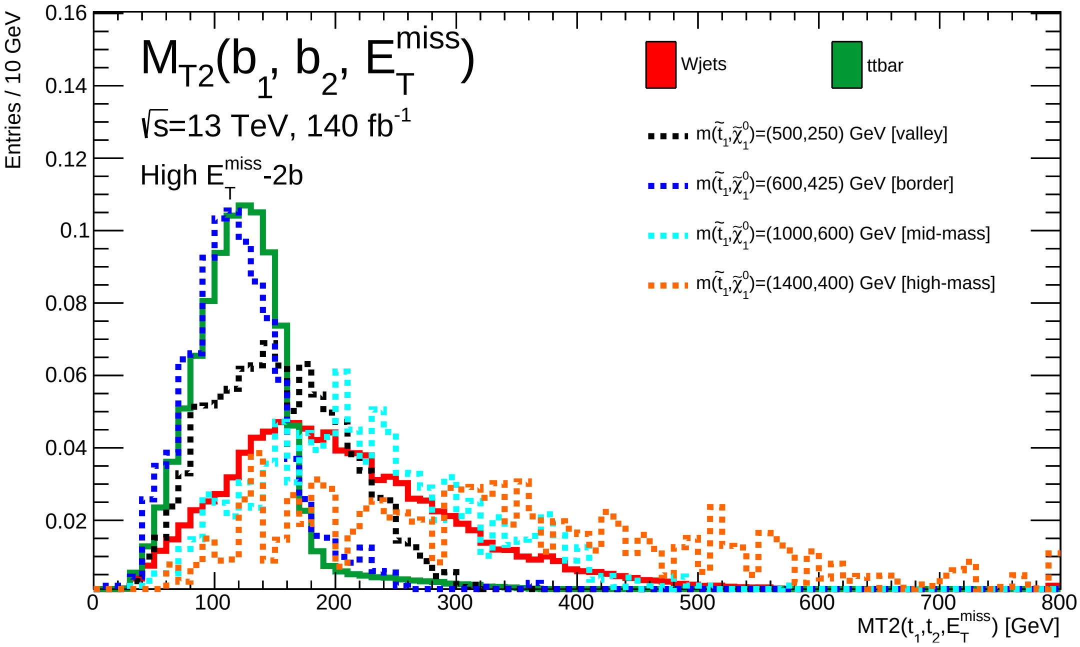

Figure 5.31: Distribution of $m_{T2}(b_1, b_2, E_T^{miss})$ in the High-E_T^{miss}-2b analysis region comparing the shapes of two main backgrounds ($t\bar{t}$, W+jets) and some benchmark signal mass points in the stop mass plane.

These high-level variables are somewhat redundant as they can be calculated from the lower level variables described previously. However, the network needs a large training dataset and large size to achieve such higher level learning. The size of the training dataset available is limited. Approximately one million signal events for each of the high-$E_{\mathrm{T}}^{\mathrm{miss}}$ category networks and roughly 50,000 to 100,000 events for each of the boosted category networks are available. The DNN event inputs per analysis category are summarised in Table 5.14.

Table 5.14: Lists of input variables for the stop- and DM-NNs in each event category.

Category		High-$E_{\mathrm{T}}^{\mathrm{miss}}$		Boosted		
		1b	2b	1bhad-1t (-0t)	1bhad-1t (-0t)	2b-1t (-0t)
$E_{\mathrm{T}}^{\mathrm{miss}}$	E	✓	✓	✓	✓	✓
	Significance	✓	✓	✓	✓	✓
$\mathrm{top}_{\mathrm{had}}$	p_x	✓	✓	✓	✓	✓
	p_y	✓	✓	✓	✓	✓
	p_z	✓	✓	✓	✓	✓
	E	✓	✓	✓	✓	✓
	top-NN output	✓	✓			
$\mathrm{top}_{\mathrm{lep}}$	p_z	✓	✓	✓	✓	✓
	E	✓	✓	✓	✓	✓
lepton	p_x	✓	✓	✓	✓	✓
	p_y	✓	✓	✓	✓	✓
	p_z	✓	✓	✓	✓	✓
	E	✓	✓	✓	✓	✓
b-jet in $\mathrm{top}_{\mathrm{had}}$	p_x	✓	✓		✓	✓
	p_y	✓	✓		✓	✓
	p_z	✓	✓		✓	✓
	E	✓	✓		✓	✓
b-jet in $\mathrm{top}_{\mathrm{lep}}$	p_x	✓	✓	✓	✓	✓
	p_y	✓	✓	✓	✓	✓
	p_z	✓	✓	✓	✓	✓
	E	✓	✓	✓	✓	✓
$p_{\mathrm{T}}(t+\bar{t}+E_{\mathrm{T}}^{\mathrm{miss}})$		✓	✓	✓	✓	✓
$\Delta R(b,b)$		✓	✓	✓	✓	✓
$m_T(\ell,E_{\mathrm{T}}^{\mathrm{miss}})$		✓	✓	✓	✓	✓
$m_{T2}(b,b,E_{\mathrm{T}}^{\mathrm{miss}})$		✓	✓			
$m_{T2,\mathrm{min}}(b+\ell,b,E_{\mathrm{T}}^{\mathrm{miss}})$		✓	✓			

DNN Strategy

For the background processes, events from all SM process are grouped together weighted by their expected cross section. This yields a 'Bkg' target class in the DNN that is representative of the SM processes as they appear at the LHC. For the signal events, ideally, a different DNN should be trained for each mass point, yielding too many classifiers, each with a different background distribution that would need to be studied. A simpler approach where all the independent signal processes are grouped together is implemented. Hence, a training is performed where the signal processes are weighted relative to their expected cross sections.

This is motivated by the fact that events with high $\tilde{t}_1$-$\tilde{\chi}_1^0$ or $\chi_{\text{Med}} - \chi_\chi$ masses are the easiest to discriminate, given that the kinematic properties of these signal events is significantly different from SM events. However, such events have low cross sections and are produced less frequently as the $\sqrt{s}$ required to produce high mass particles is higher. Alternatively, the kinematic properties of the signal events with low $\tilde{t}_1$-$\tilde{\chi}_1^0$ or $\chi_{\text{Med}} - \chi_\chi$ masses are much closer to SM processes. However, these have a higher production cross section, yielding a greater set of events. By providing cross-section weighting to the signals, the more difficult to discriminate events automatically have a higher effective weight as compared to the high mass events.

This can be demonstrated by evaluating the performance of a network in different regions of the mass plane. Taking, for example, a DNN classifier trained to distinguish all stop events from all background events, the ROC curves are plotted for three subcategories of mass. Three different mass regions are defined: 'stop valley', 'stop midmass' and 'stop highmass' as seen in Figure 5.32. The performance of the classifier evolves over the mass plane as expected.

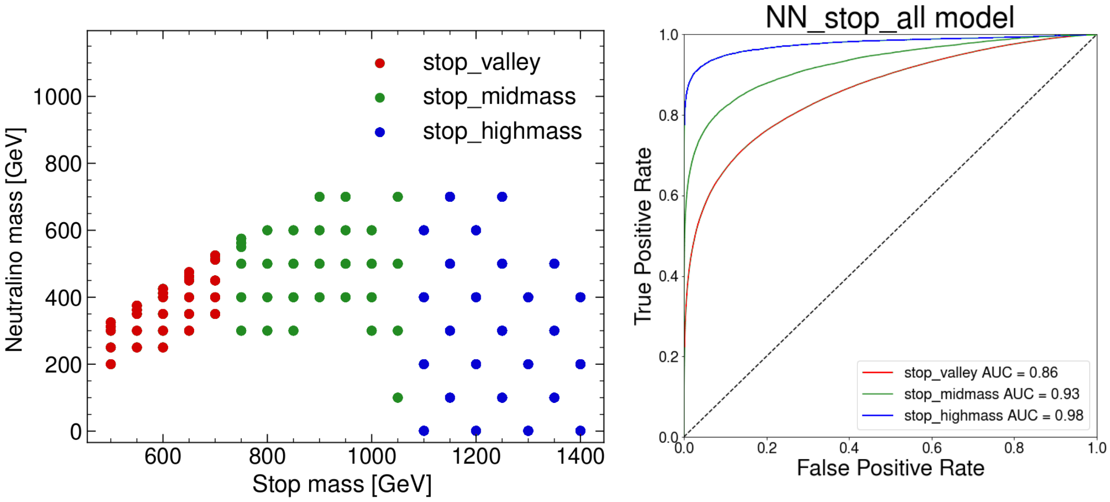

Figure 5.32: Divisions in the stop mass plane to categorise models into "stop valley", "stop midmass" and "stop highmass" and the ROC curves of these subsets for the stop vs SM classifier.

Studies are performed by training more granular NN classifiers targetting subsets of the signal phase space as documented in Appendix A. It is concluded that the performance for sub-sections of the phase space does not significantly reduce when all the signal models are grouped together and only one classifier is trained as compared to dedicated classifiers.

The same network design as for the top DNN is used. A Keras implementation is used and the network consists of four fully connected hidden layers with 64 nodes per layer. The training is done on a CPU and the maximum number of allowed epochs are 200. Early stopping is used to stop the training when the performance of the network doesn't improve for the last 15 iterations.

The resulting NN output distributions of this approach are shown in Figure 5.33 and Figure 5.34. The classification power for different categories of signal models is retained with one DNN classifier. In the SUSY phase space, signal processes with large $\tilde{t}_1$ masses have the highest NN scores, while processes with small $\Delta m(\tilde{t}_1, \tilde{\chi}_1^0)$ have lower classification power. In the DM phase space, a similar mass dependence is observed. Additionally, DM events produced with pseudoscalar mediators are easier to distinguish from SM when compared to those produced with scalar mediators.

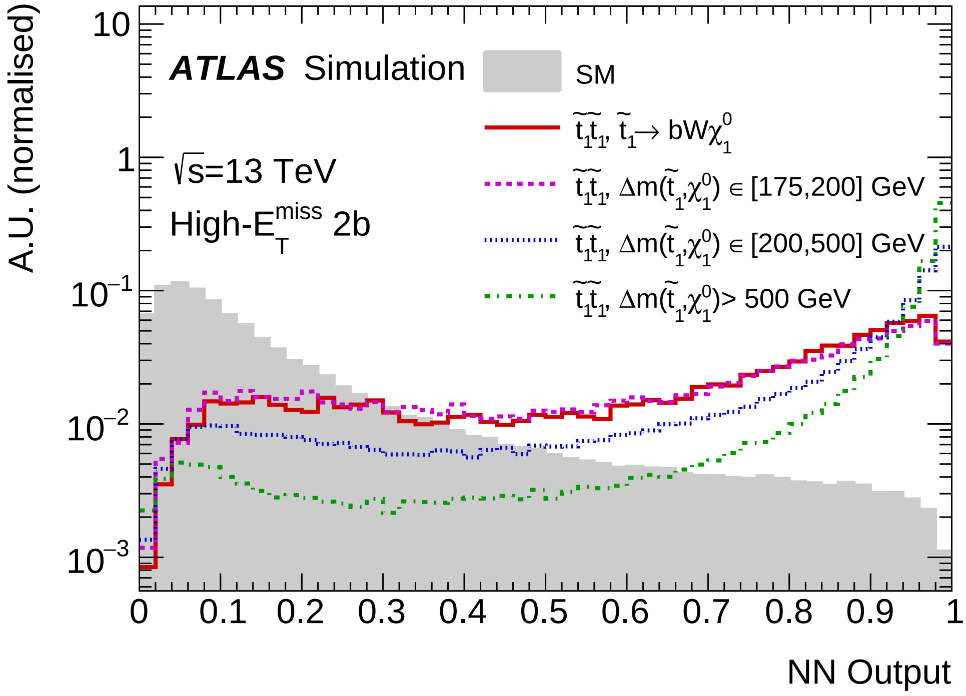

Figure 5.33: Expected distributions of events as a function of the output value of the stop-NN in the High-E_T^{miss}-2b category. The distribution of the SM background processes is compared with classes of signal models. The $\tilde{t}_1\tilde{t}_1$ models are grouped according to $\Delta m(\tilde{t}_1, \tilde{\chi}_1^0)$ and the $\tilde{t}_1$ decay mode. Distributions are normalised to the same integral. This plot is also published in [2].

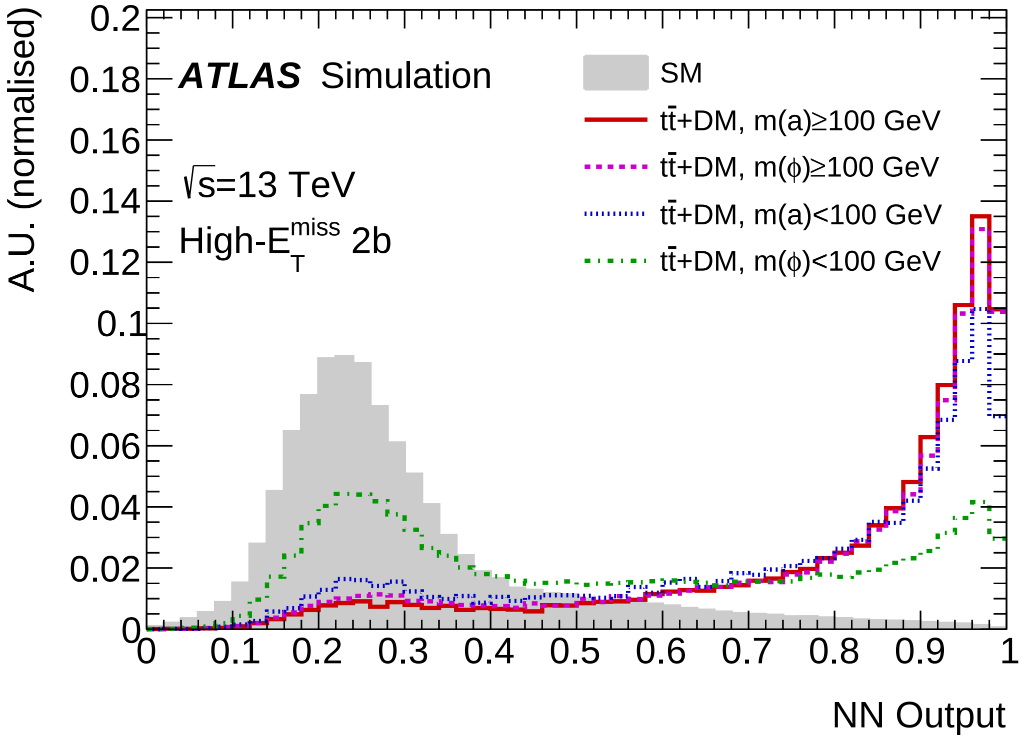

Figure 5.34: Expected distributions of events as a function of the output value of the DM-NN in the High-$E_{\mathrm{T}}^{\mathrm{miss}}$-2b category. The distribution of the SM background processes is compared with classes of signal models. The $t\bar{t}$+DM models with a scalar ϕ or pseudoscalar a mediator are shown for mediator masses larger or smaller than 100 GeV and $m(\chi) = 1$ GeV. Distributions are normalised to the same integral. This plot is also published in [2].

The $t\bar{t}$ events are henceforth sub-divided into two subcategories: "$t\bar{t}$-1L" and "$t\bar{t}$-2L" where $t\bar{t}$-2L consists of $t\bar{t}$ events with two true leptons and $t\bar{t}$-1L consists of events with zero or one true leptons. This is done because the $t\bar{t}$-2L events are closer to signal events kinematically as explained below.

- $t\bar{t}$-2L: Di-leptonically decaying $t\bar{t}$ events comprise a significant contribution of the $t\bar{t}$ background in the analysis categories. Additionally they look more like signal events and need to be understood separately. This is because the event selection requires that one — and only one — lepton is present in the event. Hence, the $t\bar{t}$-2L events that enter into the event selection are mainly those where one of the two leptons is missed in the event reconstruction. This missed lepton can be a result of misidentification or as a result of lying outside the detector acceptance. The reconstruction efficiency of electrons and muons are very high as demonstrated in Section 3.3.3. Hence, in the more likely case where the lepton is missed entirely by the detector, it is incorrectly grouped into the $E_{\mathrm{T}}^{\mathrm{miss}}$ of the event, making it look more like the signal events.

- $t\bar{t}$-1L: Events with semileptonically decaying $t\bar{t}$ are expected to have the same physics objects in the final state as the signal and therefore comprise a significant fraction of the $t\bar{t}$ background. However, the requirement on high $E_{\mathrm{T}}^{\mathrm{miss}}$ in the event selection aims to retain events where the $E_{\mathrm{T}}^{\mathrm{miss}}$ originates from particles additional to the neutrino. This implies that the semileptonic $t\bar{t}$ events that pass the event selection are more likely to have a hard ISR to boost the $t\bar{t}$ $+E_{\mathrm{T}}^{\mathrm{miss}}$ system in the event. A very small fraction of $t\bar{t}$-0L events where a lepton is incorrectly reconstructed, for example by mis-identifying a jet as a lepton, are included inside the $t\bar{t}$-1L category.

5.5.3 Control, Validation and Signal Regions

Each event category is split into a CR, VR and SR. The CR is defined to be a region with negligible contributions from signal events and is used to improve modelling of the background processes. The SR is the region with highest purity of signal events. An intermediate region between the CR and SR is used to check the validity of the background corrections derived in the CR when applied to the SR. This region is called the Validation Region (VR).

The NN score has an increasing number of signal events and decreasing number of background events, as the score moves from 0 to 1. The CR, VR and SRs are defined as a function of NN score by defining thresholds on the fraction of signal over background events. A value of S/B, where S describes the number of signal events, and B the number of background events, is plotted as a function of the NN score. $\sqrt{B}$ is plotted as a proxy of statistical uncertainty and the number of bins in each region is chosen such that a smooth $\sqrt{B}$ distribution is obtained. As an example, this distribution in the High-$E_{\mathrm{T}}^{\mathrm{miss}}$-2b and Boosted-2b-1t analysis categories is shown in Figure 5.35 for the stop signal with $m(\tilde{t}_1) = 500\,\mathrm{GeV}$ and $m(\tilde{\chi}_1^0) = 250\,\mathrm{GeV}$.

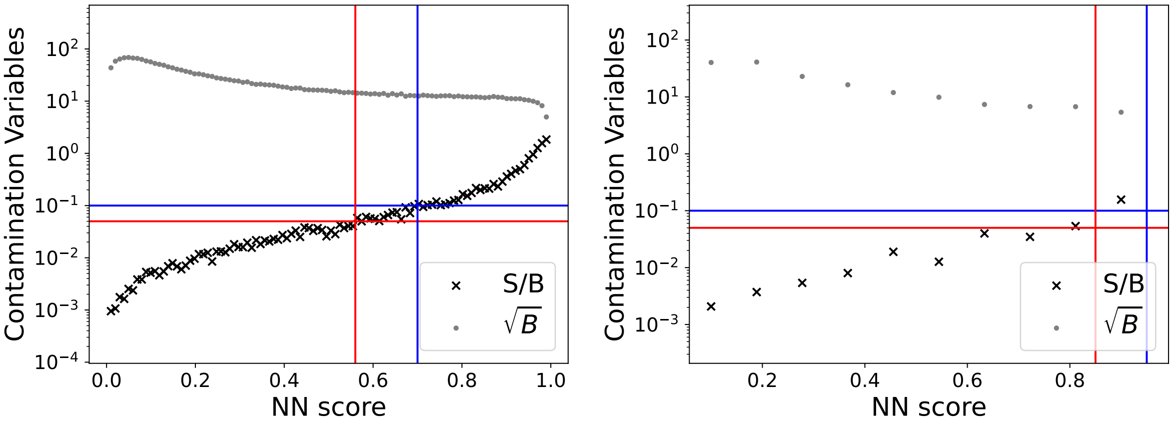

Figure 5.35: The distributions of S/B and $\sqrt{B}$ as a function of NN score for the stop signal with $m(\tilde{t}_1) = 500\,\mathrm{GeV}$ and $m(\tilde{\chi}_1^0) = 250\,\mathrm{GeV}$ in two analysis categories (a) High-$E_{\mathrm{T}}^{\mathrm{miss}}$-2b and (b) Boosted 2b-1t. The red lines correspond to a threshold of $S/B = 0.05$ defining the end of the CR and start of the VR. The blue lines correspond to a threshold of $S/B = 0.1$ defining the end of the VR and start of the SR.

The bin at which the S/B value reaches 0.05, denoted by the red lines, is defined as the upper end of the CR. After this point, the VR begins and is set to end at a value of $S/B = 0.1$, denoted by the blue lines. The rest of the NN score range is defined to be the SR, from the NN score value that achieves a 10% contamination to an NN score value of one. In certain event categories, a lower threshold is established for the CR, leading to the rejection of events falling below this threshold, which are subsequently excluded from further analysis. These discarded events exhibit background compositions that are not reflective of the background events in the SR and may include multijet events that are not simulated.

As an entire grid of signal events is available for each signal model, the distribution S and hence S/B is different for each signal point. To select the representative signal with which this cut-off will be set, the entire signal grid is evaluated. This means that for each signal, the S/B distribution is plotted and the bin at which the threshold of 0.05 (0.1) for the CR (VR) is reached is selected. This corresponds to a maximum signal contamination of 5%(10%) in in the CR (VR). As an example, this strategy is illustrated for the High-$E_{\mathrm{T}}^{\mathrm{miss}}$-2b and Boosted-2b-1t analysis categories for the stop grid in Figure 5.36. The value of NN score at which the relevant threshold is reached is plotted for each model considered. Some models never reach this threshold, as shown in blue. Models that were excluded in the previous 1L full Run-2 ATLAS result [4] are not considered when setting these thresholds. The minimum value of NN score required to reach the relevant threshold for the leftover mass points is chosen as the threshold for the CR, VR or SR.

This yields CRs, VRs, and SRs that are orthogonal and encompass the entire range of the NN output value above a specified minimum threshold. A summary of these selections, along with the signal acceptance efficiencies in the SRs, is provided in Table 5.15.

Table 5.15: Summary of the selections on the stop-NN and DM-NN output values that define CRs, VRs and SRs. Signal efficiencies, computed as the fraction of signal events in a given category with a NN output value in the range accepted in the SR, are also reported. The quoted range encompasses efficiencies estimated for all signals across the simulated parameter space. In boosted categories, only efficiencies for $\tilde{t}_1\tilde{t}_1$ signals with $\Delta m(\tilde{t}_1, \tilde{\chi}_1^0) > 500\,\mathrm{GeV}$ are quoted. This table is also published in [2].

	stop-NN				DM-NN			
Category	CR Range	VR Range	SR Range	Eff.	CR Range	VR Range	SR Range	Eff.
High-$E_{\mathrm{T}}^{\mathrm{miss}}$-1b	$[0.2, 0.64)$	$[0.64, 0.79)$	$[0.79, 1.0]$	0.4-0.9	$[0.3, 0.69)$	$[0.69, 0.87)$	$[0.87, 1.0]$	0.3-0.4
High-$E_{\mathrm{T}}^{\mathrm{miss}}$-2b	$[0.1, 0.56)$	$[0.56, 0.70)$	$[0.70, 1.0]$	0.5-0.9	$[0.3, 0.60)$	$[0.60, 0.76)$	$[0.76, 1.0]$	0.6-0.8
Boosted 1bhad-1t	$[0.0, 0.65)$	$[0.65, 0.80)$	$[0.80, 1.0]$	0.5-0.9				
Boosted 1bhad-1t	$[0.0, 0.65)$	$[0.65, 0.85)$	$[0.85, 1.0]$	0.6-0.9				
Boosted 2b-1t	$[0.0, 0.75)$	$[0.75, 0.95)$	$[0.95, 1.0]$	0.6-0.8				
Boosted 1bhad-0t	$[0.0, 0.70)$	$[0.70, 0.85)$	$[0.85, 1.0]$	0.6-0.8				
Boosted 1bhad-0t	$[0.0, 0.75)$	$[0.75, 0.95)$	$[0.95, 1.0]$	0.4-0.8				
Boosted 2b-0t	$[0.0, 0.65)$	$[0.65, 0.80)$	$[0.80, 1.0]$	0.6-0.9				

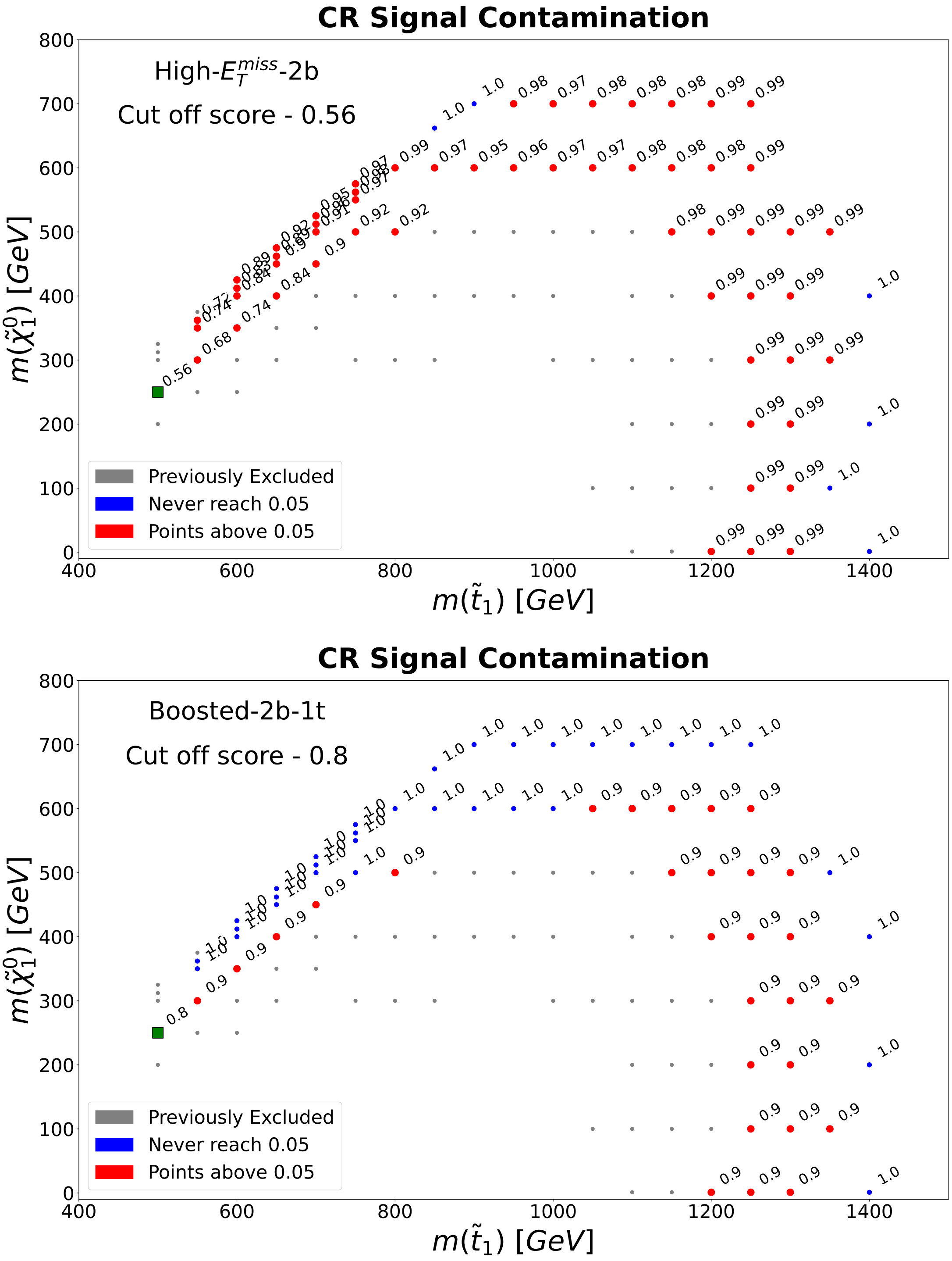

Figure 5.36: At each signal point, the score at which the 0.05 threshold of S/B is reached is shown. The signals shown in blue never reach the 0.05 threshold. The points in grey have been excluded in the previous 1L full Run-2 ATLAS result [4] and are not considered when choosing the NN threshold. From the red points, where 0.05 contamination is reached between the NN score range from zero to one, the minimum score value that crosses this threshold is marked in green. The top graph shows the High-$E_{\mathrm{T}}^{\mathrm{miss}}$-2b analysis region and the bottom shows the Boosted-2b-1t analysis region.

5.6 Background Modelling Studies

In the different control regions, as depicted in Figure 5.37, the dominating background is generally $t\bar{t}$. The sub-dominant background is either W+jets or singletop depending on the analysis region.

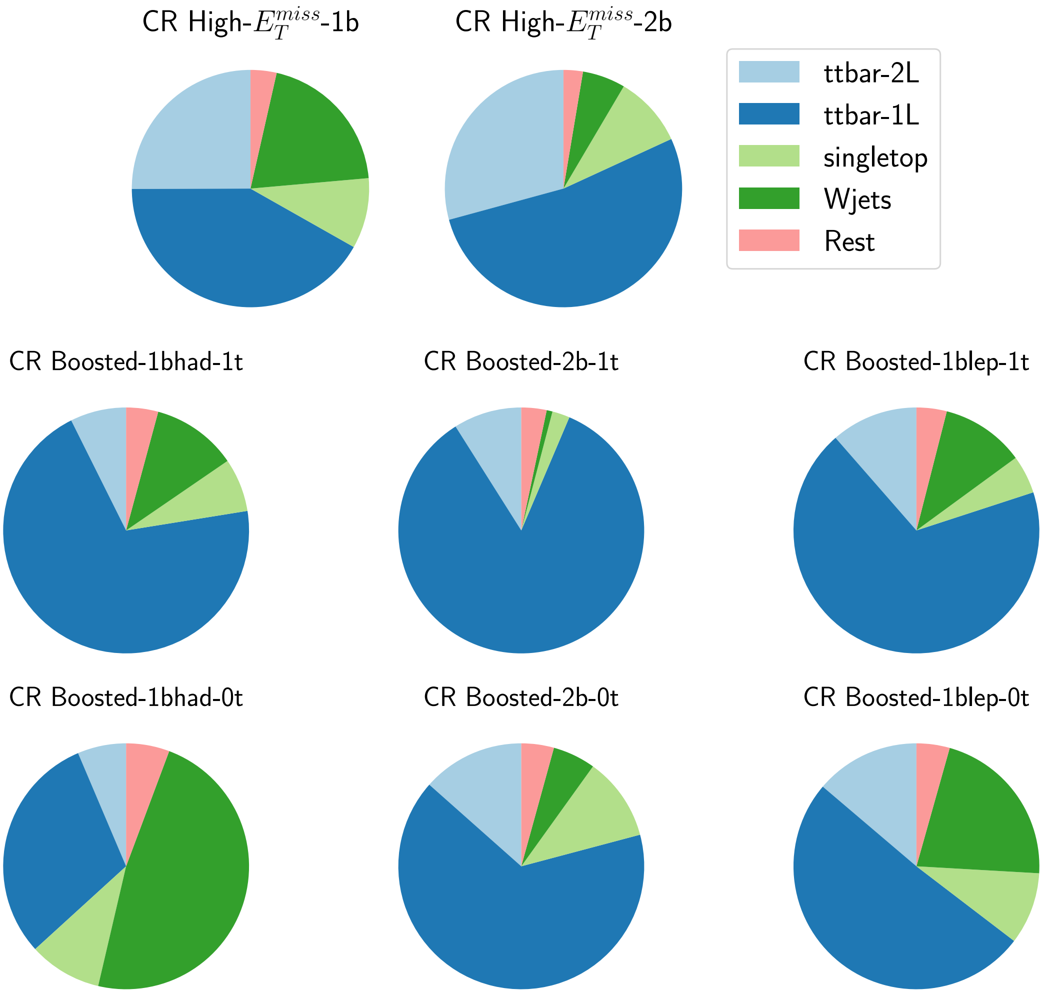

Figure 5.37: Pie charts depicting the compositions of the main SM processes in the eight different CRs defined for the stop fit.

The contributions of these different background processes are first estimated by simulation but need to be corrected to represent real data as described in Section 4.1. It is important that the most up-to-date simulated samples available are used for the SM processes. For the $t\bar{t}$ and singletop processes, studies have been performed on newly simulated samples that became available during the course of this analysis and are summarised below.

5.6.1 Modelling of $t\bar{t}$ events

Initially, the default NLO Powheg $t\bar{t}$ sample was used in this analysis. It is known that this generator is not able to describe some kinematic distributions well, for example $t\bar{t}$ events with high p_{T}. As new theoretical calculations became available for the $t\bar{t}$ process, iterative steps were taken to correct the NLO predictions where possible. The following alternatives are studied:

- The TTbarNNLOReweighter package [207] provides a 3x1D event reweighting tool where a reweighting is performed based on three distributions: top p_{T}, $t\bar{t}$ mass and $t\bar{t}$ p_{T}. For top p_{T} and $t\bar{t}$ mass, new NNLO-QCD+NLO-EW predictions [208] are used and for $t\bar{t}$ p_{T}, the NNLO-QCD predictions from the MATRIX software are used.
- A new sample for the production of $t\bar{t}$ events was simulated using the Sherpa 2.2.12 [150] generator using NLO matrix elements for up to one extra parton and LO matrix elements for up to four extra partons. This sample offers improved modelling compared to the NLO Powheg sample, in particular for $t\bar{t}$ events produced with high p_{T}, where the modelling is known to be bad.

The $t\bar{t}$ p_{T} distribution is used to probe which configuration provides the best agreement with data as shown in Figure 5.38. The High-$E_{\mathrm{T}}^{\mathrm{miss}}$-2b Control Regions are shown before any data-driven background corrections are applied. The Sherpa sample provides the best description and is chosen as the nominal sample for the $t\bar{t}$ background. The discrepancy at events with $t\bar{t}$ pair produced with high p_{T} (visible in all three samples) is likely due to an overestimation of other backgrounds. One possible reason is the single-top contribution. This background is further studied in Section 5.6.2 and an independent strategy is developed to correct this.

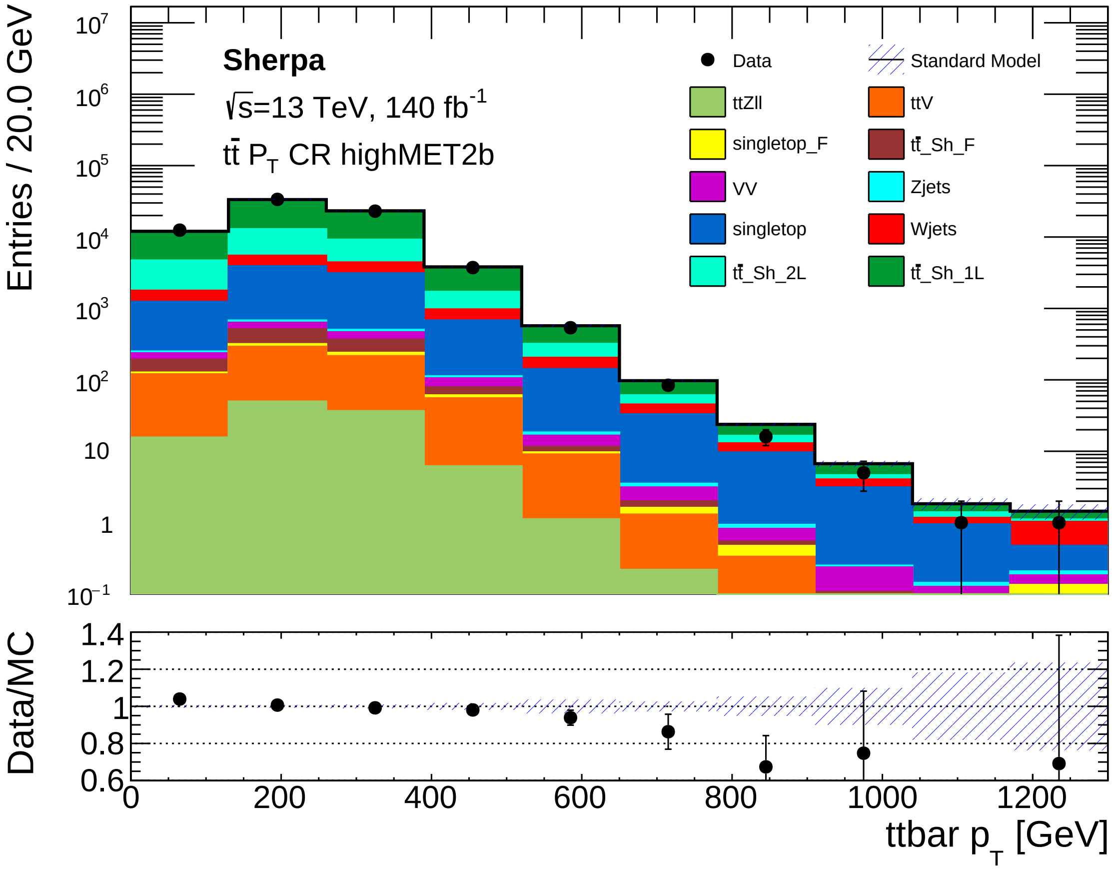

(a) Sherpa

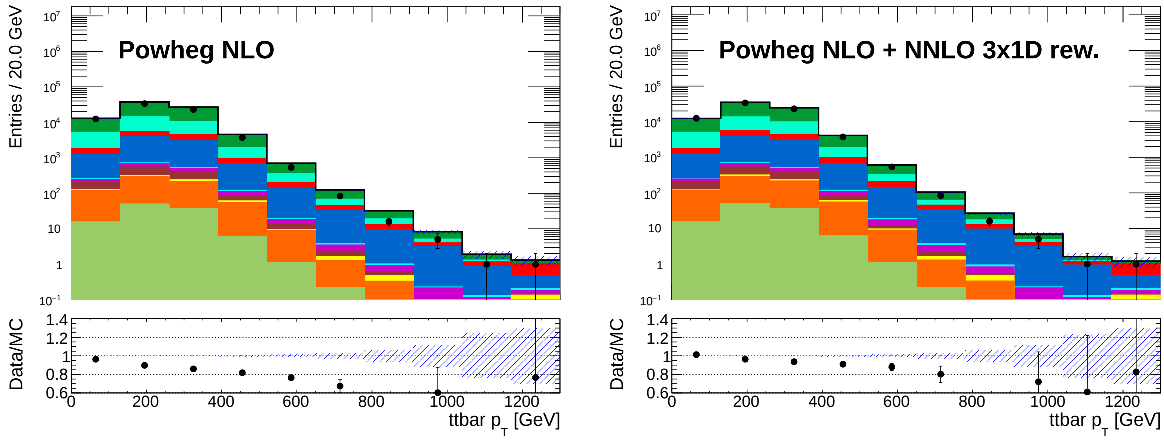

(b) Powheg NLO

(c) Powheg NLO + NNLO 3x1D reweight

Figure 5.38: Distributions of the momentum of the $t\bar{t}$ system in the CR before any data-driven background corrections are applied. Different predictions for the $t\bar{t}$ events are compared: (a) Sherpa, (b) Powheg, and (c) Powheg with the 3D reweighting. Error bars include only statistical uncertainties. The legend in (a) is applicable to the plots (b) and (c).

5.6.2 Singletop Modelling - Fixed vs Dynamic Scale

The singletop process covers three SM production modes shown in Figure 5.5. The calculation of the cross section of the Wt production mode is challenging because it has an interference with the $t\bar{t}$ process. The same final state $WWbb$ is produced for $tWb \to WWbb$ at NLO and interferes with $t\bar{t} \to WWbb$ at LO [194, 209]. Feynman diagrams depicting these two processes are shown in Figure 5.39. Hence, within the sample describing the the Wt process, the overlapping contribution from the $t\bar{t}$ process and interference have to be dealt with.

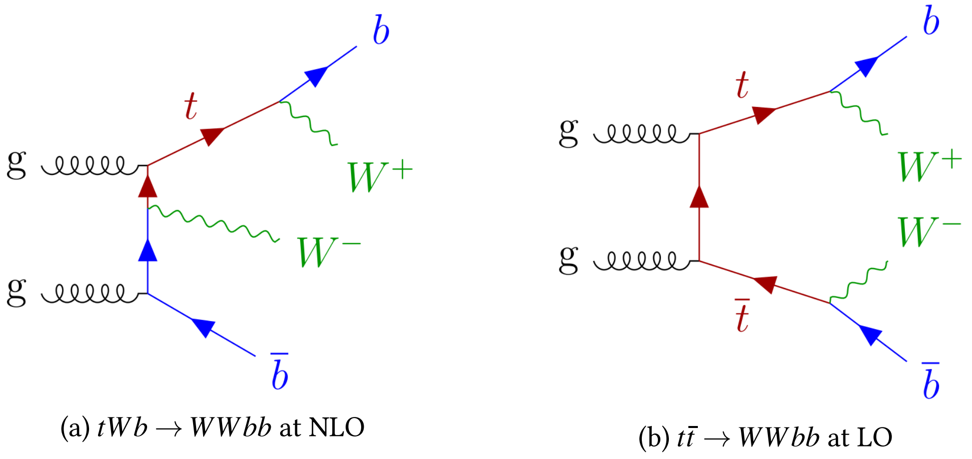

(a) $tWb \to WWbb$ at NLO

(b) $t\bar{t} \to WWbb$ at LO

Figure 5.39: Feynman diagrams representing the (a) single-resonant term (single-top - S) and (b) doubly resonant (top-pair, D) terms, taken from [209].

The matrix element for the $WWbb$ final state can be broken down into the single-resonant term (single-top - S) shown in Figure 5.39a, the doubly resonant term (top-pair, D) shown in Figure 5.39b, and an interference term (I) between S and D. Two methods of addressing this interference are available:

- **Diagram Removal (DR):** In the Diagram Removal approach, one simply eliminates all diagrams that are doubly resonant, when performing the NLO Wt ME calculation. This method eliminates both the top pair (D) and the interference (I) terms entirely from the generated events.
- **Diagram Subtraction (DS):** The Diagram Subtraction method involves modifying the NLO Wt cross section with a subtraction term. This “ad-hoc” subtraction is specifically designed to locally cancel out the top pair (D) contribution. The interference term (I) is included in the simulation.

For some observables, the DS method better represents observed data while for others the DR method is better [194]. This is a result of assumptions introduced in the calculation that make the resulting distributions behave differently in different kinematic regimes. Hence, both schemes are tested and in SUSY searches, one is used as the nominal prediction and the other as a systematic variation. In this analysis the DR scheme is used as nominal and DS is used as a variation to describe the systematic uncertainty obtained as a result of this choice.

Additionally, during the course of this analysis, an attempt was made to improve the theoretical treatment of the Wt process. Previously used samples were generated by fixing both the factorisation renormalisable scales to a fixed value of the top mass. The newly generated samples allow for a dynamic scale of $H_T/2$, where H_T is the sum of the transverse mass of all outgoing objects. This yielded 'Dynamic Scale' Wt samples within Powheg that were tested and compared with the previous version of 'Fixed Scale' Wt samples. When a distribution of $t\bar{t}$ p_{T} is studied, a p_{T} dependence emerges for the different schemes as shown in Figure 5.40. Across the entire range of NN score, the dynamic scales have a slightly lower yield than the ones produced with fixed scales as shown in Figure 5.41. This is observed for the DM NN score plotted in the High-$E_{\mathrm{T}}^{\mathrm{miss}}$-2b and the stop NN score plotted in the Boosted-2b-1t analysis categories. The DS variation also has an lower prediction of yields when compared to the DR for both dynamic and fixed scales. In this analysis the dynamic scales samples are chosen with the DR scheme used as nominal and DS is used as a systematic variation.

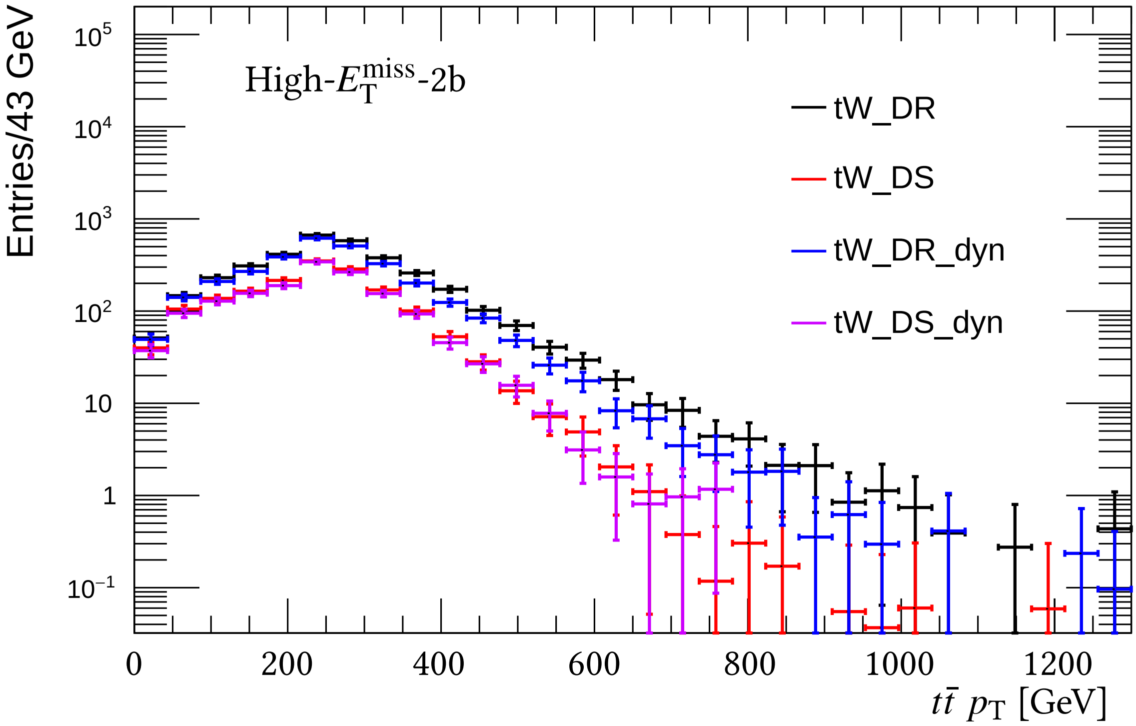

Figure 5.40: The singletop yield with DR and DS schemes for both fixed and dynamic scale samples as a function of $t\bar{t}$ p_{T} in the High-$E_{\mathrm{T}}^{\mathrm{miss}}$-2b region.

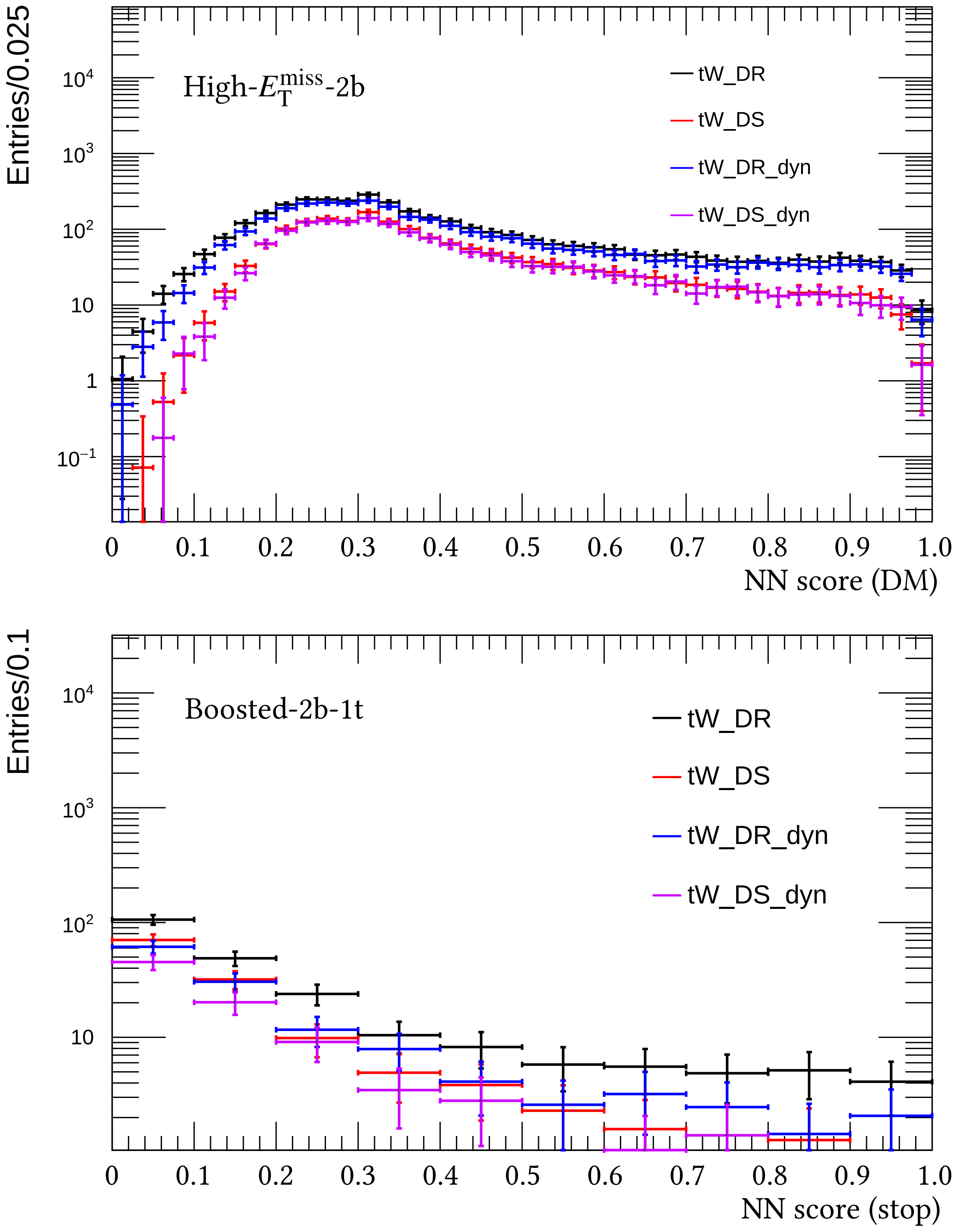

Figure 5.41: The singletop yield with DR and DS schemes for both fixed and dynamic scale samples as a function of the DM NN score in the High-$E_{\mathrm{T}}^{\mathrm{miss}}$-2b (top) region and the stop NN score in the Boosted-2b-1t (bottom) region.

5.6.3 ttZ($\to \nu\nu$) Modelling

Validation of the predictions for the $ttZ(\to \nu\nu)$ irreducible background is performed using events enriched in $ttZ(\to ll)$. The distributions of NN output values across the three-lepton categories is especially useful to study modelling of signal-like events in data before the SRs are unblinded. These events undergo the selection criteria outlined in Section 5.5.1, with one change such that events with exactly three signal leptons without any additional baseline lepton are accepted. Among these three leptons, two must share the same flavour but have opposite electric charges. Furthermore, the invariant mass of these two leptons should align with the leptonic decay of a Z boson, falling within the range of $m_{\ell\ell} \in [81, 101]$ GeV to further ensure that a high purity of SM events are studied.

To identify $ttZ(\to ll)$ events with kinematic properties resembling those of the $ttZ(\to \nu\nu)$ events accepted in the SRs, the three-lepton events are reclassified as one-lepton events. This is achieved by performing a modified missing transverse momentum calculation, to include the vectorial sum of the two leptons from the Z boson decay. Figure 5.42 illustrates the observed distributions of events as a function of the stop-NN output value in the high-$E_{\mathrm{T}}^{\mathrm{miss}}$ three-lepton categories. These distributions align well with theoretical predictions, which do not incorporate data-driven corrections. A similar agreement is observed for the DM-NN output values. The three-lepton selection in the boosted regions is not used due to the insufficient number of events it yields for meaningful validation.

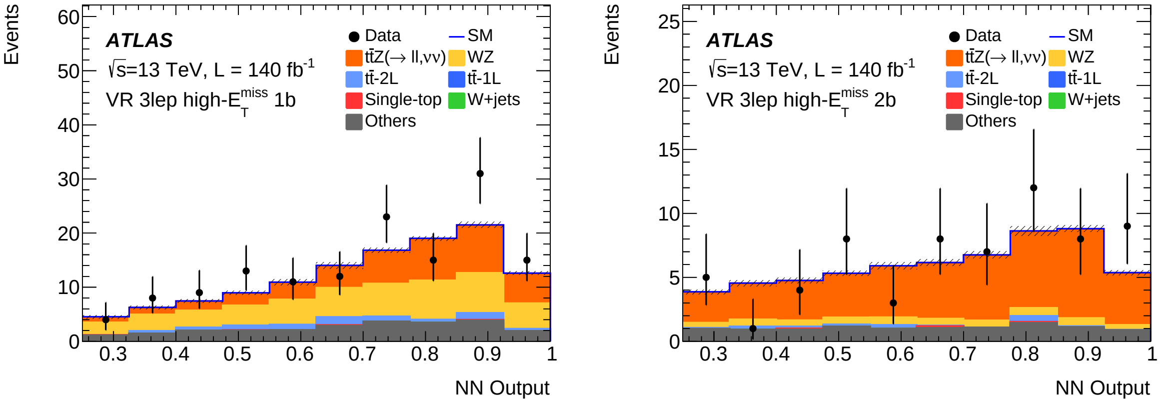

Figure 5.42: Comparison of observed and expected distributions of the stop-NN output values in high-$E_{\mathrm{T}}^{\mathrm{miss}}$ three-lepton events with one (left) and two or more (right) b-tagged jets. The figures display only statistical uncertainties, and no data-driven corrections are applied to background predictions, taken from [2].

5.7 Statistical Interpretation

To yield a quantitative value representing the level of agreement between observed data and a given hypothesis, likelihood based fits are performed. A summary of the ideas used is presented in this section and a more detailed explanation can be found in [210]. The implementation is done using the statistical analysis package HistFitter [211], using RooFit [212] and RooStats [213].

5.7.1 Global Likelihood Definition

A statistical 'test model' is constructed to describe a given hypothesis and the corresponding likelihood function, denoted by $L(\vec{n}|\vec{f}(\vec{\theta}))$, is defined. This is a measure of the probability that the test model ($\vec{f}$ as a function of parameters $\vec{\theta}$) describes the configuration observed in data ($\vec{n}$). In this analysis, a global likelihood function is defined to describe the event yields across all the different analysis categories. Events are binned in a chosen 'fit variable' within each analysis region. Each analysis region is described by N number of bins in the fit variable $\vec{x} = (x_1, x_2, x_3....x_N)$, wherein x_i represents the central value of the i^{th} bin. The observed data is presented in a histogram using the same binning in the fit variable $\vec{x}$ yielding $\vec{n} = (n_1, n_2, n_3....n_N)$. The expected yield of events in each bin is described by:

$$E(x_i) = \mu_{\text{sig}} \cdot s_i + b_i \tag{5.6}$$

where s_i is the number of expected signal events for the model under consideration and b_i is the sum of the expected contributions from SM processes. The free parameter μ_{sig} is included in the model and used to quantify the 'signal strength' where the setting $\mu_{\text{sig}} = 1$ corresponds the nominal event yield predicted by the new physics model. The total background yield b_i can be divided into individual background process contributions. An example where four different background processes contribute to the total background yield is shown here:

$$b_i = \mu_A \cdot b_A + \mu_B \cdot b_B + b_C + b_D \tag{5.7}$$

Here, additional parameters μ_A and μ_B are used to scale the overall predictions of two dominant backgrounds, b_A and b_B respectively, and sub-dominant backgrounds b_C and b_D are added without such scaling parameters. The parameters μ_A and μ_B are called Normalisation Factors (NFs) and are free parameters defined within the test model.

Next, the statistical and systematic uncertainties are included into the model. It is assumed that the observed yields are independent across bins implying that the events in different bins are statistically uncorrelated. The Poisson distribution is used to model the event yield in each bin as the distribution best suited for counting experiments. To address the statistical uncertainties on the predictions, in each bin, one "MC-stat" parameter is assigned to the whole prediction ($s_i + b_i$) to account for the uncertainty from the limited number of Monte Carlo events used to build the histograms. Owing to the Poisson nature of event yields, these MC-stat uncertainties are uncorrelated across bins.

The predicted events are represented by template histograms in which bin yields can be partially correlated. This is because the template histogram is essentially a discretised representation of the Probability Density Function (PDF) which models the expected distribution of events for the chosen variable x and yields the values s_i and b_i. The PDF is affected by underlying experimental and theoretical uncertainties in Monte Carlo simulations, the effects of which can be correlated across bins. To capture these uncertainties, the model is parametrised by a set of systematic uncertainties. These systematic uncertainties along with the MC-stat parameters are together called Nuisance Parameters (NPs) and complete the description of the test model.

The yield in each bin for the test model is given by:

$$E(x_i) = \mu_{\mathrm{sig}} \cdot [f_s(\vec{\theta})]_i + [f_b(\vec{\mu}_{\mathrm{bkg}}, \vec{\theta})]_i \tag{5.8}$$

where f_s and f_b are the PDF for signal and background processes that depend on the vector $\vec{\theta}$ which is the vector of NPs. The vector $\vec{\mu}_{\mathrm{bkg}}$ is the vector of NFs used to normalise overall background yields and μ_{sig} is the signal strength. The signal and background yields in the i^{th} bin of the distribution are given by $s_i = [f_s(\vec{\theta})]_i$ and $b_i = [f_b(\vec{\mu}_{\mathrm{bkg}}, \vec{\theta})]_i$ respectively. The global likelihood for N_{bins} can be expressed as a product of the independent Poisson distributions in each bin:

$$L(\vec{n}, \vec{\theta^0} | \vec{\mu}, \vec{\theta}) = \prod_{i=1}^{N_{bins}} P(n_i | \mu_{\mathrm{sig}} \cdot f_s(\vec{\theta}) + f_b(\vec{\mu}_{\mathrm{bkg}}, \vec{\theta})) \times C_{syst}(\vec{\theta^0}, \vec{\theta}) \tag{5.9}$$

where $P(n_i | \mu_{\mathrm{sig}} \cdot f_s(\vec{\theta}) + f_b(\vec{\mu}_{\mathrm{bkg}}, \vec{\theta}))$ is the Poisson distribution in each bin. The vector $\vec{n}$ describes the vector of observed data yields in the different bins $(n_1, n_2, n_3 .... n_N)$ and $\vec{\theta}$ describes the vector of NPs used to parametrise the model. The vector $\vec{\mu}$ includes μ_{sig} and $\vec{\mu}_{\mathrm{bkg}}$. An additional term $C_{syst}(\vec{\theta^0}, \vec{\theta})$ is introduced to define Gaussian constraints on the NPs describing systematic uncertainties.

Experimental and theoretical systematic uncertainties are estimated from auxiliary measurements or theoretical prescriptions. The source of these uncertainties is varied by a $\pm 1\sigma$ around the previously estimated/prescribed value. These uncertainties are propagated through the analysis and alternative templates for the fit variable are built. This results in “up” and “down” variations on the event yields for each background category or signal process. Finally, a parameter θ_i is added to the fit model to parametrise the impact of this uncertainty. This parameter is defined to have a Gaussian constraint with the central value defined by the nominal event yield and the Gaussian width defined by the up and down variations on the event yield. A parameter value of zero for θ_i corresponds to the nominal event yield and a value of ± 1 corresponds to an event yield varied by $\pm 1\sigma$ as a consequence of the uncertainty it describes.

$$C_{syst}(\vec{\theta^0}, \vec{\theta}) = \prod_{j=1}^{M_{systs}} \frac{1}{\sqrt{2\pi}\sigma_j} exp(-\frac{(\theta_j - \theta_{j0})^2}{2\sigma_j^2}) \tag{5.10}$$

Once the global likelihood function is defined, a likelihood fit can be performed. This fit attempts to calculate values of the model parameters $(\vec{\mu}, \vec{\theta})$ that maximise the value of the likelihood function. In practice the negative log of the likelihood function is minimised. The configuration of model parameters that attain this goal is denoted by $(\hat{\vec{\mu}}, \hat{\vec{\theta}})$, called the Maximum Likelihood Estimate (MLE) and is assumed to be an accurate, unbiased, unconditional description of the data. If the central value of a given NP in the MLE is away from zero, the deviation is called a 'pull'. As an example, if a NP describing an alternative theoretical prescription is pulled, it can indicate that the data agrees better with the alternative hypothesis as compared to the nominal. If the width (σ) of the Gaussian constraint describing a given NP is less than one after the fit, it is called a 'constraint' and can point to an under-parametrised model or a better estimate of the uncertainty associated with that specific NP.

Two kinds of fits are performed in this analysis: a background-only fit and a model-dependent fit. In the CRs, where no signal is expected to be present, the background-only hypothesis is expected to describe the data accurately. Hence, the global likelihood function defined above with a fixed $\mu_{\mathrm{sig}} = 0$ is fit and values of NFs and NPs that maximise the likelihood are obtained. This is the background-only fit result and yields NFs and NPs that best describe the observed data in the CRs. The post-fit values of the NFs and NPs, calculated in the CRs, are used to build post-fit distributions of the background predictions. These corrected distributions are then compared to observed data in the VRs, and the agreement between observed data and simulated background events is evaluated. If reasonable agreement is obtained, it is concluded that the extrapolation of NFs and NPs to SRs is a valid way to correct predictions of SM events in the SR and the background model is well defined.

In the case of model-dependent fits, the probability that a given signal model is compatible with the observed data needs to be evaluated. For this, hypothesis testing is performed as a function of μ_{sig} as described in Section 5.7.2. Fits need to be performed for different values of μ_{sig}, called conditional fits, wherein the likelihood has to be maximised for a range of incremental values of μ_{sig}. A validation is performed for the model-dependent fits as well, wherein resulting parameters (μ_{sig}, $\vec{\mu}_{\mathrm{bkg}}$ and NPs) are applied to the VRs to validate the fit.

5.7.2 Hypothesis Testing Strategy

According to the Neyman-Pearson lemma [214], the optimal discriminator to compare two hypotheses (H_0, H_1) is a likelihood ratio. In general, H_0 describes the null hypothesis and H_1 an alternative hypothesis. To test H_0 against H_1, the likelihood ratio is defined by λ as:

$$\lambda = \frac{L(\vec{n}|H_0)}{L(\vec{n}|H_1)}. \tag{5.11}$$

In this thesis, exclusion fits are performed to evaluate which signal models can be rejected with a 95% confidence level or a p-value ≤ 0.05. The exclusion fits are performed after verifying that no excesses are present after unblinding the SRs. This is evaluated, at first qualitatively, by looking at the SRs in the background-only fit and confirming that no (or moderate) excesses are present in data over the sum of events from SM processes. To get a quantitative estimate, the μ_{sig} value that maximises the unconditional likelihood (MLE) is considered. This is denoted the best-fit μ_{sig} and its compatibility with zero is evaluated.

For the exclusion fits, H_0 is defined as the presence of background+signal, while H_1 describes the background-only hypothesis. A likelihood ratio involving a process known as 'profiling' is used, wherein a the ratio is defined as a function of the Parameter of Interest (POI) and all other nuisance parameters are profiled out. Here, the POI is μ_{sig} which is expected to be positive when a new signal process is present and the profile likelihood ratio is defined as:

$$\lambda(\mu_{\text{sig}}) = \frac{L(\vec{n}|\mu_{\text{sig}}, \hat{\hat{\vec{\theta}}})}{L(\vec{n}|\hat{\mu}_{sig}, \hat{\vec{\theta}})}, \;\; \hat{\mu}_{sig} > 0 \tag{5.12}$$

A modified ratio would be required for negative values of μ_{sig} to not benefit from downward fluctuations in data. However, in the exclusion fits performed here, μ_{sig} is constrained to be positive. The numerator describes a conditional likelihood, where $\hat{\hat{\vec{\theta}}}$[4] is the configuration of model parameters that maximises the likelihood for a given μ_{sig}. The denominator is the unconditional maximised likelihood, obtained by the configuration of parameters $(\hat{\mu}_{sig}, \hat{\vec{\theta}})$ or MLE described before. Given that the value of μ_{sig} has been verified to be compatible with zero prior to doing the exclusion fit, it is assumed that the MLE is the best description of the background-only hypothesis and represents H_1. Here, μ_{sig} is the Parameter Of Interest (POI) and the profile likelihood ratio depends on the POI. This is done so that the compatibility of different values of μ_{sig} with the observed data can be tested and an upper limit on μ_{sig} can be obtained.

To extract a p-value for the signal+background hypothesis, the test statistic $t_{\mu_{\text{sig}}} = -2\ln\lambda(\mu_{\text{sig}})$ based on Equation 5.11 is used. In the asymptotic regime (sufficiently high number of events), according to Wilk's theorem [215], the distribution of the test statistic is known to follow a χ^2 distribution. Consequently, a p-value and significance (Z) can be directly calculated from it:

$$p_{\mu_{\text{sig}}} = \int_{t_{\mu_{\text{sig}},obs}}^{\infty} f(t_{\mu_{\text{sig}}}|\mu_{\text{sig}})\, dt_{\mu_{\text{sig}}}, \qquad Z = \Phi^{-1}(1 - p_{\mu_{\text{sig}}}), \tag{5.13}$$

where f is the PDF of the test statistic ($t_{\mu_{\text{sig}}}$) and $t_{\mu_{\text{sig}},obs}$ is the value of the test statistic observed in data. The Z value describes how many standard deviations away from the mean of a standard normal distribution would yield a one-sided tail integral equal to the p-value. For searches in particle physics, it is standard to exclude a new physics process (signal) if the signal+background hypothesis has a p-value ≤ 0.05, corresponding to $Z = 1.64$. In comparison, to claim the discovery of a new process, the threshold is higher, requiring the null-hypothesis to be rejected with $Z = 5$, corresponding to a p-value of 2.8×10^{-7}. In this scenario, the hypotheses naming convention used above would be switched and H_0 would be the background-only hypothesis, to be rejected in favour of H_1 the background+newly discovered signal.

---

[4] The definition of $\vec{\theta}$ is extended here to include all parameters in the model ($\vec{\mu}_{\text{bkg}}$ and NPs) besides μ_{sig}

The upper limit (UL) on μ_{sig} corresponds to the maximum signal strength that still yields a p-value ≤ 0.05. An UL μ_{sig} of 0.1 means that the signal process is excluded even for a cross section ten times smaller than the nominal one. This characterises the 'depth' of the exclusion and is calculated for all models evaluated in this search.

For the stop grid, an exclusion contour is constructed based on the CL_s value [216] which serves as an improved p-value. The CL_s value ensures that a signal is only excluded in the case that the data is compatible with the background only hypothesis. This is relevant in the case that both background-only and background+signal hypotheses have test statistic distributions that are very close, which can happen for signal processes with small cross sections. In this case the p-value test can incorrectly reject a signal process that the analysis is in-fact not sensitive to. As a solution to this, a reduced p-value or CL_s is used instead:

$$CL_s = \frac{p_{\mu_{\text{sig}}}}{1 - p_0} = \frac{CL_{s+b}}{CL_b}, \tag{5.14}$$

where p_0 quantifies the agreement of data with the background only hypothesis by setting $\mu_{\text{sig}} = 0$ in Eq. 5.13. Figure 5.43 illustrates how dividing $p_{\mu_{\text{sig}}}$ by $1 - p_0$ prevents the exclusion of a weak signal. The CLs value is calculated for each point in the stop grid and a 2D interpolation is performed to obtain a 95% exclusion contour in the stop-neutralino plane excluding signals with a $CL_s < 0.05$.

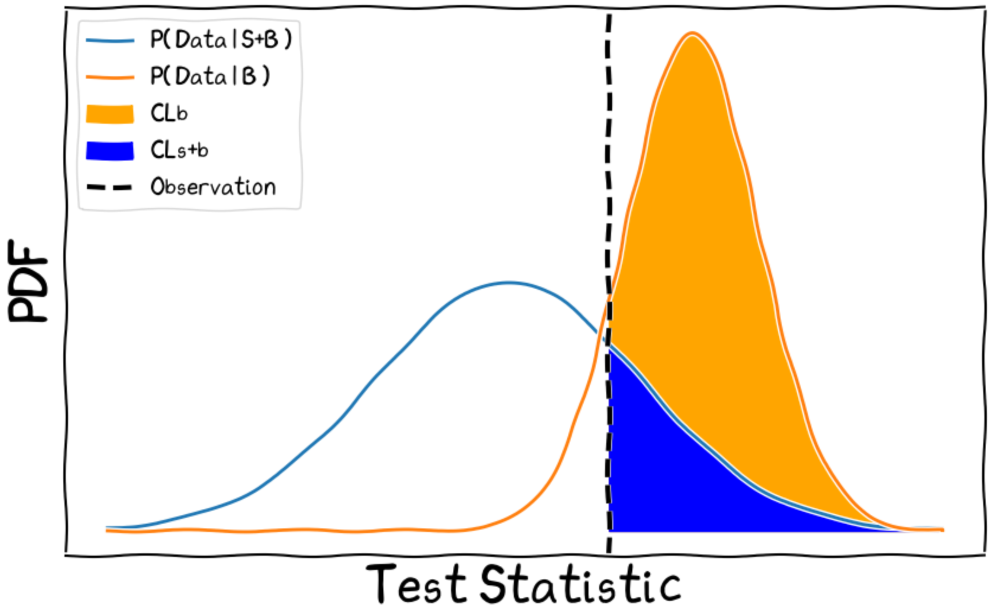

Figure 5.43: Illustration of CL_{s+b} and CL_b values used to calculate the CL_s value.

To calculate upper limits on μ_{sig}, a scan of the CL_s value over μ_{sig} is performed. Starting with a pre-defined range or grid of μ_{sig} values, the likelihood function is evaluated for each

μ_{sig} in conjunction with the profiled nuisance parameters that maximise the likelihood for that specific μ_{sig} value. This results in a profile likelihood ratio $\lambda(\mu_{\text{sig}})$ for each μ_{sig}, quantifying the goodness-of-fit of the data under the signal-plus-background hypothesis relative to the best-fit background-only hypothesis. Subsequently, the confidence level CL_s is computed for each μ_{sig}.

In practice, this scan is often performed using pseudo-data to yield an expected CL_s distribution illustrated in Figure 5.44. A red line at a $CL_s = 0.05$ is shown such that all μ_{sig} values that yield a value of $CL_s \leq 0.05$ can be excluded by the scan shown in Figure 5.44. Throughout the course of the analysis, efforts are made to enhance sensitivity, meaning excluding lower values of the POI or μ_{sig} in this case. Upon unblinding the data, the observed CL_s is computed using real data.

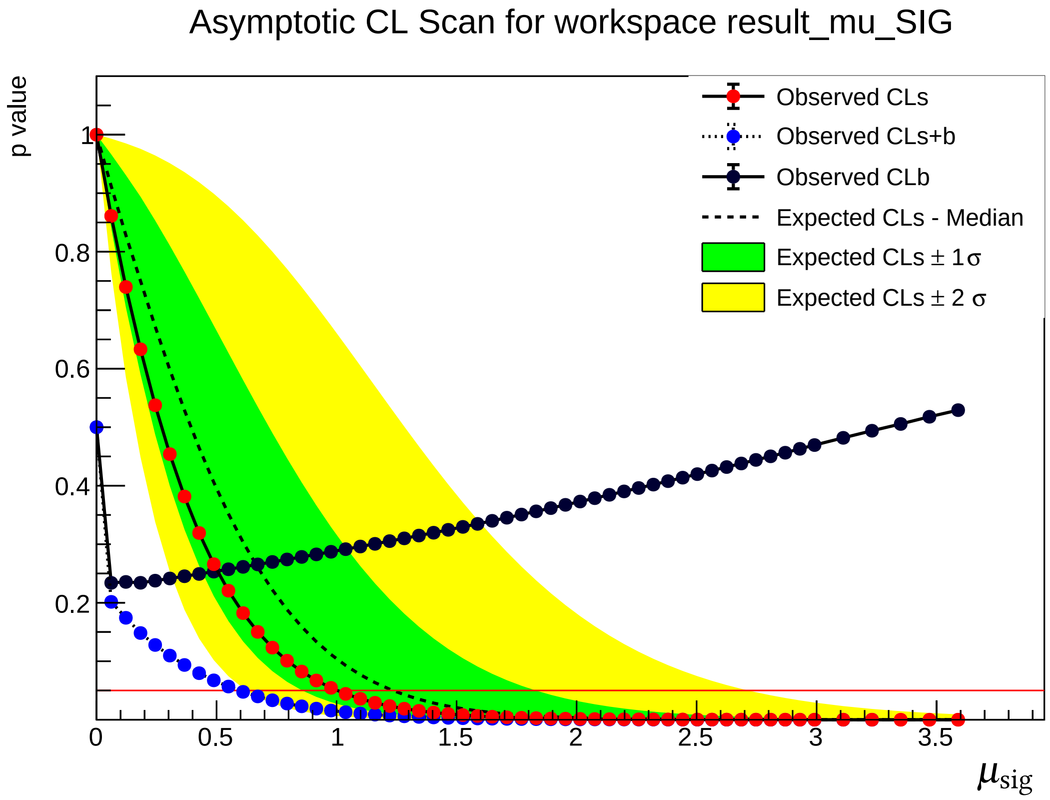

Figure 5.44: An example of a CL_s scan as a function of μ_{sig}.

5.7.3 Statistical Model

Using the concepts explained in Sections 5.7.1-5.7.2, the statistical test model is constructed. The total background contribution is split into the following categories:

- $t\bar{t}$-1L: the fraction of $t\bar{t}$ with ≤ 1 truth leptons in which the selected reconstructed lepton is prompt[5].
- $t\bar{t}$-2L: the fraction of $t\bar{t}$ with ≥ 2 truth leptons in which the selected reconstructed leptons are prompt.
- singletop: the fraction of singletop events in which the selected reconstructed lepton is prompt.
- Fakes (top): the fraction of $t\bar{t}$ and singletop events in which the selected reconstructed lepton is not reconstructed as a prompt lepton[6]. This is a very small contribution.
- W+jets: all W+jets events.
- $t\bar{t}Z(\rightarrow \ell\ell, \nu\nu)$: the $t\bar{t}Z$ events in which the Z boson decays either into charged leptons or neutrinos.
- WZ: Diboson production where one W boson and one Z boson is produced
- Others: this includes other minor background contributions, such as Z+jets, $t\bar{t}W$, $t\bar{t}H$.

Explicit NFs are considered to correct the yields of the three leading background processes: $t\bar{t}$, W+jets and singletop. The other backgrounds are used as predicted by simulation as they have smaller contributions and constrained via theoretical uncertainties.

The CRs which are defined purely on the NN score, as described before, do not reach 100% purity in a single background process. To control the predictions of individual background processes in the SRs, a determination of the individual processes in the CRs must be obtained. A binned distribution of the NN score in the Control Region does not discriminate well enough between the different background processes and instead a variable with better separation between the different SM processes in the CR is chosen.

For $t\bar{t}$ events, the variable $m_T(l, E_{\mathrm{T}}^{\mathrm{miss}})$ is exploited to distinguish between $t\bar{t}$-1L and $t\bar{t}$-2L events. The $t\bar{t}$-2L events have a much larger value of $m_T(l, E_{\mathrm{T}}^{\mathrm{miss}})$ than the $t\bar{t}$-1L events. This is expected because the $t\bar{t}$-2L events have a $E_{\mathrm{T}}^{\mathrm{miss}}$ that is incorrectly reconstructed to be too high coming from a missed lepton and a second neutrino. The W+jets and $t\bar{t}$-1L distributions are still quite degenerate in the $m_T(l, E_{\mathrm{T}}^{\mathrm{miss}})$ distribution because they have, as expected, an end-point around the mass of the W boson. To discriminate W+jets events from $t\bar{t}$, the $m_T(l, E_{\mathrm{T}}^{\mathrm{miss}})$ is multiplied by the charge of the lepton in the event. This captures the effect that W+jets events have a charge asymmetry at the LHC as a result of proton-proton collisions. A larger

---

[5] indicates the channel where the top decays promptly to a lepton and not via a τ-lepton

[6] Most electrons and muons originating from τ-leptons are reconstructed as prompt electrons and muons

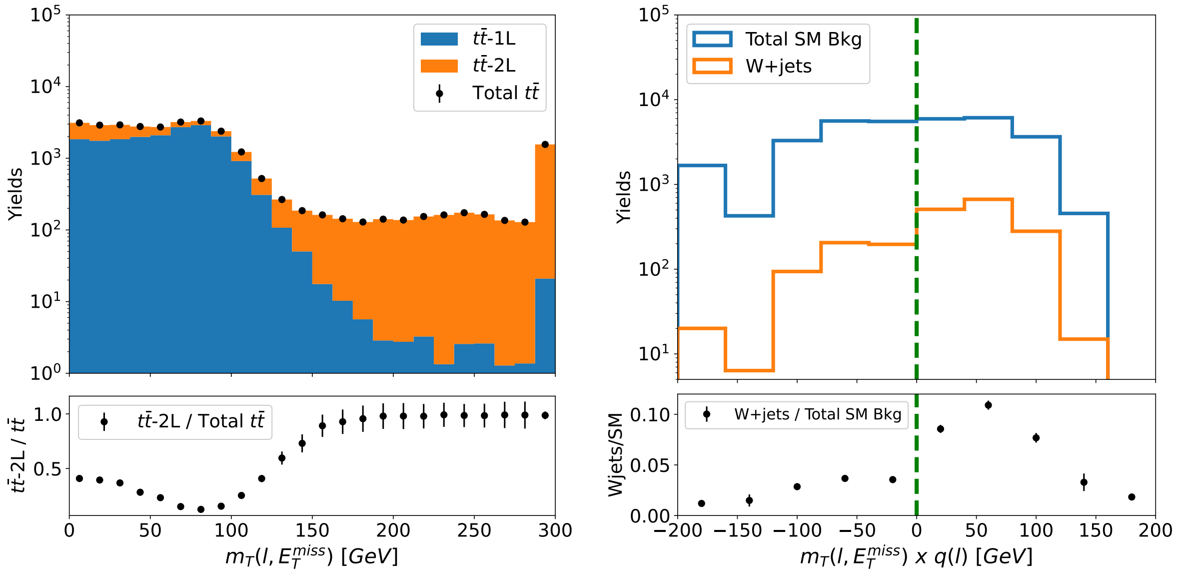

(a) (b)

Figure 5.45: (a) The distribution of $m_T(l, E_{\mathrm{T}}^{\mathrm{miss}})$ in the High-$E_{\mathrm{T}}^{\mathrm{miss}}$-2b CR illustrates how this variable provides different profiles for the $t\bar{t}$-1L (blue) and $t\bar{t}$-2L (orange) processes. (b) The distribution of $m_T(l, E_{\mathrm{T}}^{\mathrm{miss}}) \times q(l)$ with the proportion of W+jets events as compared to the overall SM yield illustrating the charge asymmetry that can be exploited.

fraction of events is produced with positively charged W bosons than negatively charged ones when protons are collided with protons. Hence, the variable $m_T(l, E_{\mathrm{T}}^{\mathrm{miss}}) \times q(l)$ can provide discrimination simultaneously for $t\bar{t}$-1L, $t\bar{t}$-2L and W+jets events as shown in Figure 5.45.

For the singletop background, m_{T2} variables are exploited in the regions where the yield of singletop events is significant to give high purity singletop CRs. This occurs in the Boosted-2b CRs with and without a top tagged *LR* jet, wherein a cut of 300 GeV on the $m_{T2,\mathrm{min}}(b+l, b, E_{\mathrm{T}}^{\mathrm{miss}})$ is used as depicted in Figure 5.46. Below $m_{T2} = 300$ GeV, the binned $m_T(l, E_{\mathrm{T}}^{\mathrm{miss}}) \times q(l)$ distribution is used and for the events above $m_{T2} = 300$ GeV, one bin with the total event yields is used.

In the Signal Regions, the binned NN score provides the ideal fit variable differentiating signal and background templates. A summary of the NFs used is shown in Table 5.16. For $t\bar{t}$ and W+jets, different NFs are used in the high $E_{\mathrm{T}}^{\mathrm{miss}}$ and boosted categories as they select events at different energies which may need different corrections. The same NFs are used in categories which differ by bjet multiplicity. The binning in CRs is chosen in order to capture the differences in distributions between different background contributions while keeping the number of bins as low as possible. In the two Boosted-2b High-MT2 CRs, given the small number of events, only one bin is used. In the SRs, the ranges of the NN output values are split into bins of equal width. The number of bins in each SR is chosen such that an increasing

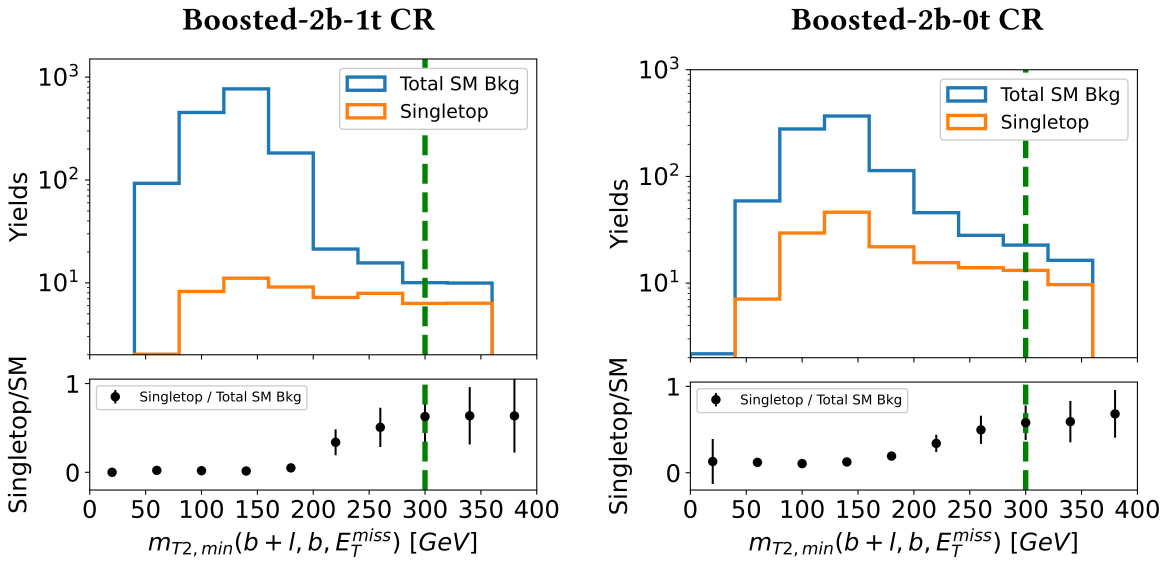

(a)

(b)

Figure 5.46: The $m_{T2,\mathrm{min}}(b+l,b,E_{\mathrm{T}}^{\mathrm{miss}})$ distribution for singletop events and total SM background events in the (a) Boosted-2b-1t and (b) Boosted-2b-0t CRs depicting the increase in purity of singletop events at high values of $m_{T2,\mathrm{min}}(b+l,b,E_{\mathrm{T}}^{\mathrm{miss}})$.

S/B can be exploited. This is done by using the maximum number of equally sized bins that allow a non-zero yield of background events in each bin, yielding a maximum S/B in the right most bin.

For the stop fits, CRs and SRs in all eight analysis categories are used. For DM fits, the boosted SRs are dropped because a negligible number of DM signal events are expected to lie in these regions. Table 5.17 and Table 5.18 give an overall summary of these two fit configurations, showing the number of regions (and bins therein) being considered in each type of fit.

Table 5.16: Summary of the statistical model listing the variables used in the different fit regions and the configuration of NFs applied to the different background contributions. This table is also published in [2].

Category	Fit variable		Normalisation Factors						
	CR	SR	$\mathrm{NF}^{\text{High-met}}_{\text{top-1L}}$	$\mathrm{NF}^{\text{Boosted}}_{\text{top-1L}}$	$\mathrm{NF}^{\text{High-met}}_{\text{top-2L}}$	$\mathrm{NF}^{\text{Boosted}}_{\text{top-2L}}$	$\mathrm{NF}^{\text{High-met}}_{W}$	$\mathrm{NF}^{\text{Boosted}}_{W}$	$\mathrm{NF}_{\text{singletop}}$
High-$E_{\mathrm{T}}^{\mathrm{miss}}$-1b	$m_T(l,E_{\mathrm{T}}^{\mathrm{miss}})\times q(\ell)$	NN	✓		✓		✓		✓
High-$E_{\mathrm{T}}^{\mathrm{miss}}$-2b	$m_T(l,E_{\mathrm{T}}^{\mathrm{miss}})\times q(\ell)$	NN	✓		✓		✓		✓
Boosted-1bhad-1t	$m_T(l,E_{\mathrm{T}}^{\mathrm{miss}})\times q(\ell)$	NN		✓		✓		✓	✓
Boosted-1bhad-1t	$m_T(l,E_{\mathrm{T}}^{\mathrm{miss}})\times q(\ell)$	NN		✓		✓		✓	✓
Boosted-2b-1t	$m_T(l,E_{\mathrm{T}}^{\mathrm{miss}})\times q(\ell)$ (low-m_{T2}) Yield (High-m_{T2})	NN		✓		✓		✓	✓
Boosted-1bhad-0t	$m_T(l,E_{\mathrm{T}}^{\mathrm{miss}})\times q(\ell)$	NN		✓		✓		✓	✓
Boosted-1bhad-0t	$m_T(l,E_{\mathrm{T}}^{\mathrm{miss}})\times q(\ell)$	NN		✓		✓		✓	✓
Boosted-2b-0t	$m_T(l,E_{\mathrm{T}}^{\mathrm{miss}})\times q(\ell)$ (low-m_{T2}) Yield (High-m_{T2})	NN		✓		✓		✓	✓

Table 5.17: Summary of the number of regions used in the fit for the stop search. All regions are orthogonal and fit simultaneously. This table illustrates the large number of regions and bins therein fit simultaneously. Details of individual plots are shown and discussed in Section 5.8.1.

Region	CR (low NN)	SR (high NN)
High-$E_{\mathrm{T}}^{\mathrm{miss}}$-1b	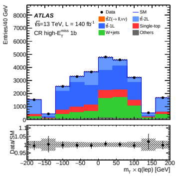	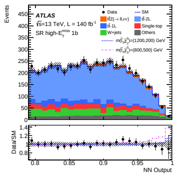
High-$E_{\mathrm{T}}^{\mathrm{miss}}$-2b	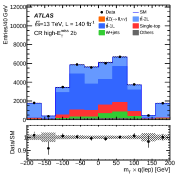	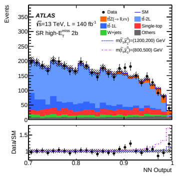
Boosted-2b-1t	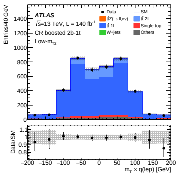 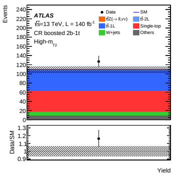	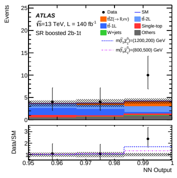
Boosted-2b-0t	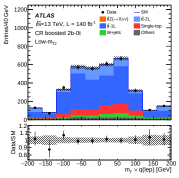 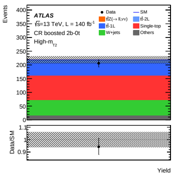	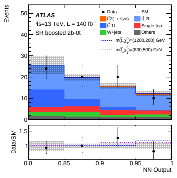
Boosted-1b-1t	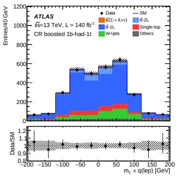	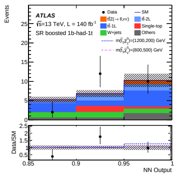
Boosted-1b-0t	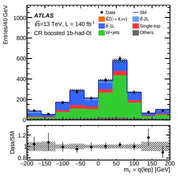	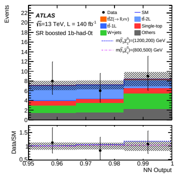
Boosted-1blep-1t	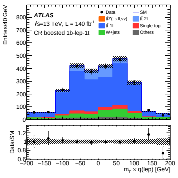	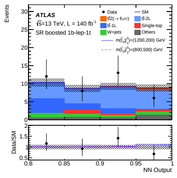
Boosted-1blep-0t	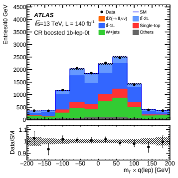	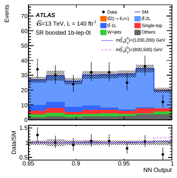

Table 5.18: Summary of the number of regions used in the fit for the DM search. All regions are orthogonal and fit simultaneously. This table illustrates the large number of regions and bins therein fit simultaneously. Details of individual plots are shown and discussed in Section 5.8.1.

Region	CR (low NN)	SR (high NN)
High-E_T^{miss}-1b	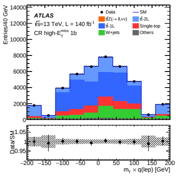	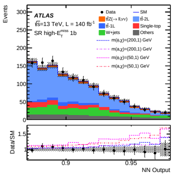
High-E_T^{miss}-2b	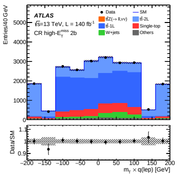	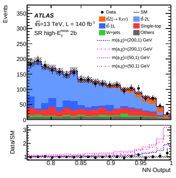
Boosted-2b-1t	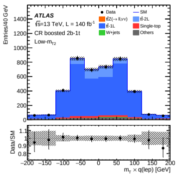 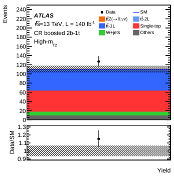	
Boosted-2b-0t	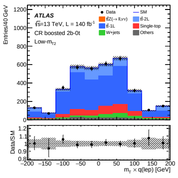 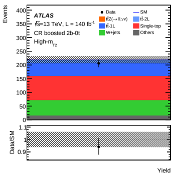	
Boosted-1b-1t	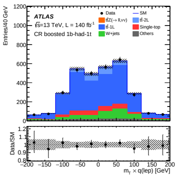	
Boosted-1b-0t	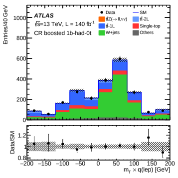	
Boosted-1blep-1t	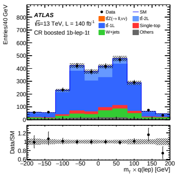	
Boosted-1blep-0t	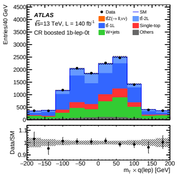	

5.7.4 Systematic Uncertainties

Systematic uncertainties are divided into detector and theory systematic uncertainties. Detector systematic uncertainties cover a broad range of inefficiencies in event collection, detector resolution and object reconstruction algorithms, while theory systematic uncertainties cover modelling uncertainties within the event simulation for the different background and signal processes. The following detector systematic uncertainties have been considered:

- **Pileup Reweighting:** Pileup modelling affects the reconstruction of objects and, consequently, event selection. The level of pileup can vary from event to event, leading to differences in the calculated pileup values between data and simulation. To address this discrepancy, re-weighting of the MC events to the data is performed. Uncertainties arising from the process of reweighting are considered [217].
- **JVT and fJVT Systematics:** The JVT and fJVT algorithms outlined in Section 3.3.3 are used to suppress pileup jets. Uncertainties stemming from these algorithms are included in the fit model [118, 119].
- **Electron and Muon Systematics:** Uncertainties from energy scale and resolution calibration, in addition to those from electron and muon reconstruction, identification, and isolation algorithms are included [112, 113, 133].
- **B-tagging Systematics:** The systematic uncertainties derived from calibrating the DL1r algorithm at the 77% selection, explained in Section 3.3.3, are extracted and applied [129]. Two variations, one for PFlow (bTag) and the other for $\mathrm{VR}_{\mathrm{track}}$ jets (bTrkTag) are used.
- **Jet Systematics:** Jet reconstruction in the LHC environment requires careful calibration to correct the reconstructed objects to match true jet properties as explained in Section 3.3.3. Uncertainties related to jet energy scale and resolution in the reconstruction of small-R jets, JES and JER are considered, while for Large-R jets, JES, JER and jet mass scale (JMS) uncertainties are considered [125].
- **$\mathbf{E}_{\mathrm{T}}^{\mathrm{miss}}$ calculation:** While most uncertainties in $E_{\mathrm{T}}^{\mathrm{miss}}$ are handled by treating the uncertainties of the measured objects, the soft term introduces additional uncertainties to the overall $E_{\mathrm{T}}^{\mathrm{miss}}$ calculation. This soft term accounts for contributions to $E_{\mathrm{T}}^{\mathrm{miss}}$ from low-momentum objects that might not be associated with any reconstructed object. The uncertainty of this term is calculated using in-situ methods using $Z \to \mu\mu$ events without additional jets, comparing simulation to data and included in the fit [137].

In order to reduce the complexity of the fit, a “pruning” of experimental uncertainties is performed. This means that detector systematic uncertainties with negligible impact for specific processes and specific categories are not considered in the fit model. The threshold for this is set such that an experimental uncertainty is only considered if it leads to a variation greater than 10% of the statistical uncertainty in any bin of the fit variable distribution.

Theory systematic uncertainties are considered for the $t\bar{t}$, singletop, W+jets, $t\bar{t}\,Z(\to \ell\ell)$ and signal processes, a summary of which uncertainty is considered for each process is shown in Table 5.19. For all remaining processes, a conservative uncertainty of 30% on the overall normalisation is applied [218, 219].

Table 5.19: Summary of the theoretical uncertainties used in the test model for the various background process.

	$\mathbf{t\bar{t}}$	W**+jets**	**Singletop**	$\mathbf{t\bar{t}\,Z(\to ll)}$	**Signal**
Scales	✓	✓	✓	✓	✓
PDFs	✓	✓	✓	✓	✓
EW corrections	✓	✓			
CKKW	✓	✓			
QSF	✓	✓			
Lund	✓				
ISR			✓		✓
DR vs DS			✓		
Heavy Flavour		✓			

- **Scales (Factorisation and Renormalisation):** Factorisation scales (μ_F) separate short-distance and long-distance physics in perturbative QCD calculations, while renormalisation scales (μ_R) are used to regulate divergences arising in loop calculations, allowing for finite and physically meaningful predictions. The choice of these scales is not well defined and a few variations from the nominal are used to acknowledge the effect of this choice as an uncertainty. For the simulated samples used, 7-point QCD variations of μ_R and μ_F are available and paired such that they can be associated to three independent NPs. Two versions of these variations exist: ME only and ME+PS where the variation is done only on the matrix element or coherently on the matrix element and parton shower respectively. For $t\bar{t}$, the ME only scheme is used[7], while for others, the ME+PS scheme is used.

- **PDF:** Predictions for cross sections and other observables carry uncertainties based on the PDF set used in the Monte Carlo simulation. Several variations of the PDF set are available and the envelope of all variations in each bin of the final discriminating distribution is used. This is applied to $t\bar{t}$, W+jets, singletop, $t\bar{t}\,Z(\to \ell\ell)$ and signal events.

- **EW corrections:** For Sherpa [150] generated samples ($t\bar{t}$ and W+jets), approximate NLO EW corrections are available atop the nominal sample using different prescriptions. The impact of different prescriptions in the estimation of approximate NLO EW corrections is accounted for as additional systematic uncertainties. The electroweak and QCD components can be combined using an additive, multiplicative, or exponentiated

---

[7] At the time, ME+PS variations for $t\bar{t}$ events were still being studied and could not be used in the time-frame of the analysis.

prescription [220]. The additive prescription is used as nominal and applied to the nominal predictions, while the differences between the additive and the alternative prescriptions are accounted for as systematic uncertainties.

- **CKKW:** The importance of combining ME and PS calculations is described in Section 3.3.2. The CKKW matching scheme is used to achieve this and variations of the ME+PS matching parameter (CKKW) are included in the model [102, 103]. Merging scale variations of $\pm 10\,\mathrm{GeV}$ around $30\,\mathrm{GeV}$ nominal are considered.
- **QSF:** The resummation scale (QSF) is employed for the resummation of soft gluon emissions. SHERPA provides systematic QSF variation factors that can be adjusted relative to the nominal sample and are used as such in the model.
- **Lund:** For $t\bar{t}$, uncertainties related to the fragmentation model are accounted for by using the Lund string as an alternative model.
- **ISR:** The modelling of ISR jets is an important part of ATLAS event simulation as described in Section 3.3.2. For signal events with large $E_{\mathrm{T}}^{\mathrm{miss}}$, the presence of ISR ensures that the events have enough energy to pass the trigger selections, making this modelling parameter important. The singletop events produced at the LHC that fall in this phase space also contain considerably high energy ISR jets. Hence the ISR modelling uncertainties are considered for both signal and singletop.
- **Singletop DR vs DS:** For singletop, the difference between the DR and DS prescriptions is explained in Section 5.6.2. The dynamic scale DR variation is used as the nominal and the difference of the dynamic scale DS variation as compared to the dynamic scale DR variation is considered as a systematic uncertainty.
- **W+jets Heavy Flavour (HF):** For W+jets, a relative uncertainty of 30% is assigned to cover variations between the W+jets predictions in event categories with one b-tagged jet and those with two or more b-tagged jets. This uncertainty accounts for variations in the production of a W boson in association with heavy-flavour quarks [221].

The statistical test model contains NFs for $t\bar{t}$, singletop and W+jets, therefore the NPs used to describe systematic uncertainties for $t\bar{t}$, singletop, W+jets can have correlations with NFs. The impact from theoretical uncertainties on the total normalisations of these backgrounds is reduced by “normalising” these uncertainties such that the total yields of these backgrounds in all CRs are not affected by theoretical uncertainties. Additionally, it is ensured that the correlation scheme at the end of the fit is analysed.

The theoretical uncertainties on $t\bar{t}$ and W+jets events are assigned such that they have the same correlation scheme as the NFs shown in Table 5.16. This implies that the uncertainties are treated separately for $t\bar{t}$-1L, $t\bar{t}$-2L and W+jets and further split for the high-$E_{\mathrm{T}}^{\mathrm{miss}}$ and boosted categories. For W+jets, the 30% HF uncertainty serves as an extrapolation uncertainty of W+jets events from the event categories with one b-quark jet to two b-quark jets.

5.8 Fit Results

5.8.1 Background-only Fit

Before unblinding the data in the SRs, the background only fit is performed by fitting simulated background process in the CRs and extracting the resulting fit parameters and applying them to the VRs. The results of this fit indicated that the background estimate was accurate and the SRs could be unblinded. After unblinding, it was observed that no significant excesses were present in the data and a background-only fit could then be performed including the data in the SRs, providing an improved description of the data in all fit regions. The 'full' background fit is shown here where the CRs and SRs are included in the fit along with intermediate VRs wherein the fit parameters extracted from the CRs and SRs are applied to the distributions in the VRs.

The post-fit values of the NFs for the background-only fit in the stop and DM fit setups are reported in Figure 5.47. The singletop NF has a large uncertainty given that its interference with $t\bar{t}$ is hard to model. The post-fit distributions in the CRs, VRs and SRs for both the DM and stop fits are shown in Figures 5.48-5.53.

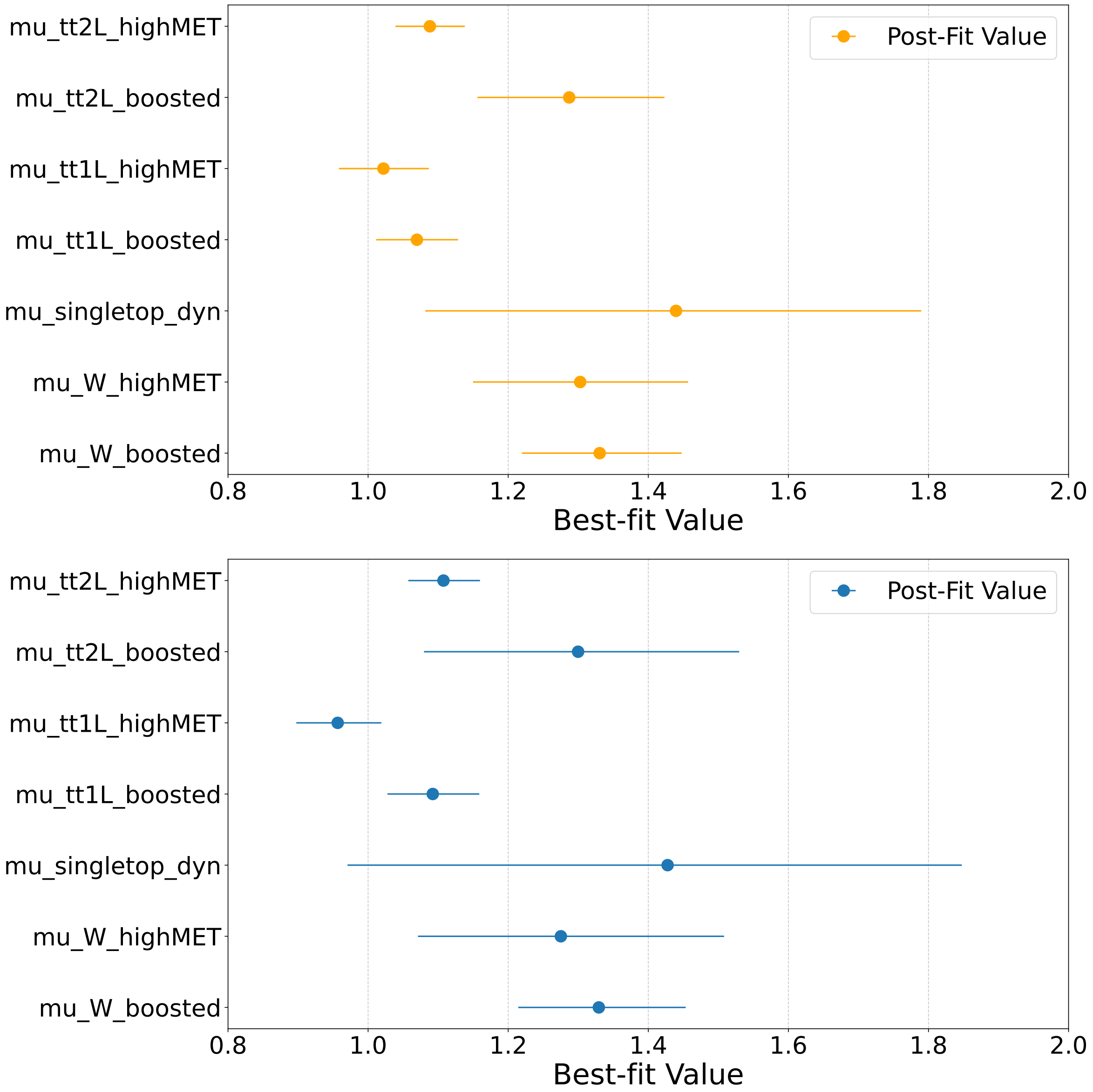

Figure 5.47: Best-fit values of the normalisation factors in the background-only stop (top) and DM (bottom) fits with SRs.

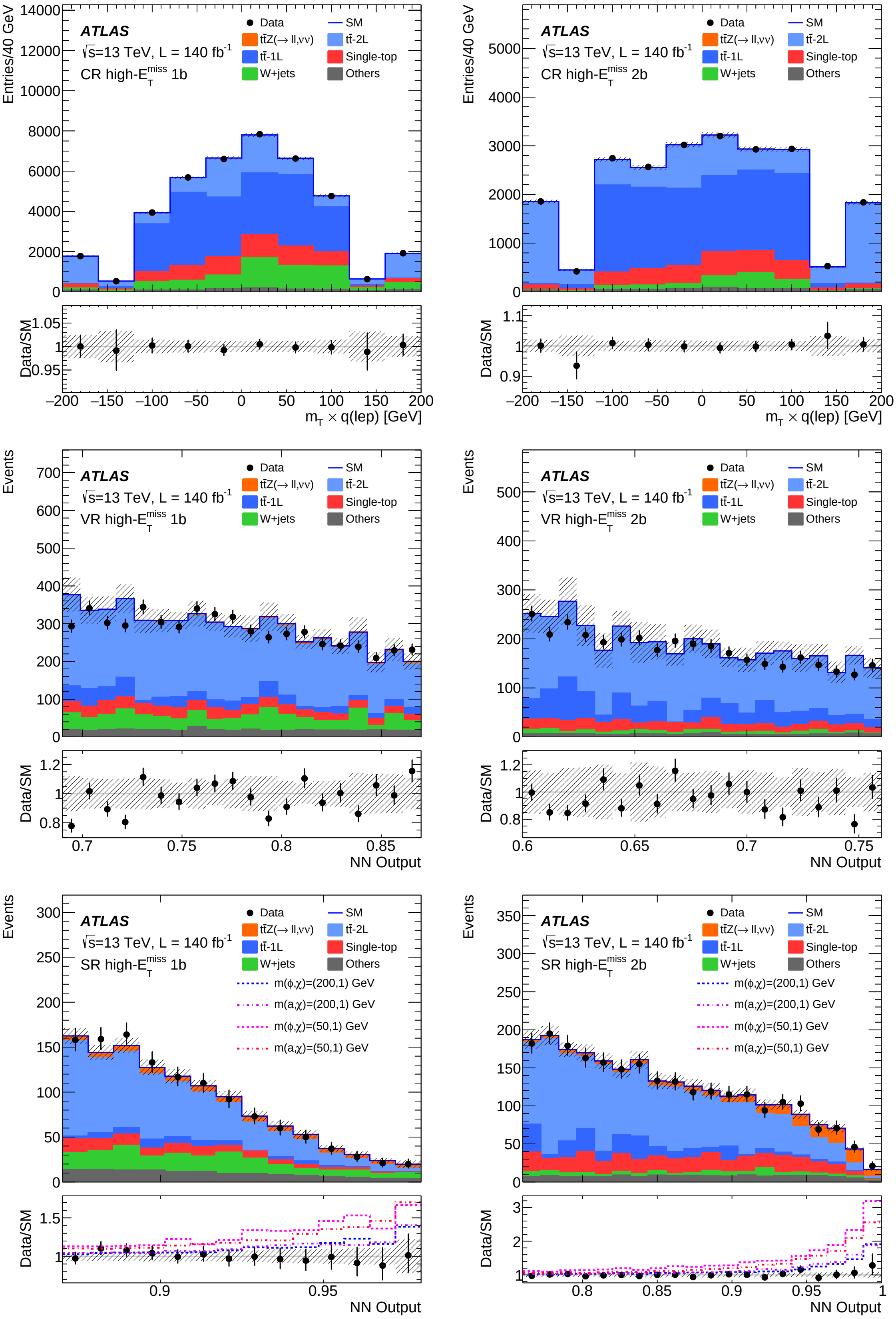

Figure 5.48: Observed and expected distributions in the High-$E_{\mathrm{T}}^{\mathrm{miss}}$ DM CRs (top), VRs (middle) and SRs (bottom) after the background-only fit with SRs in the DM fit setup, also published in [2].

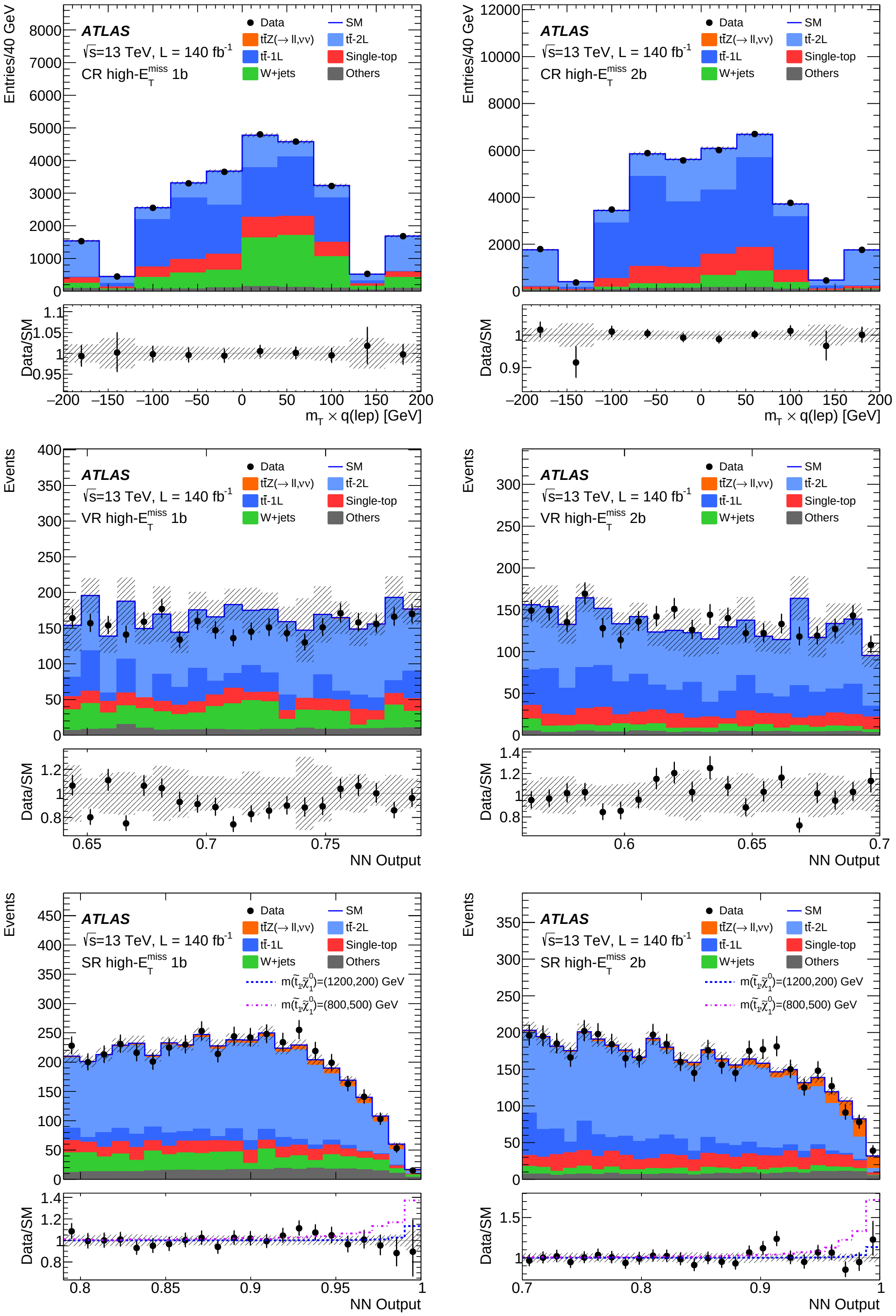

Figure 5.49: Observed and expected distributions in the High-$E_{\mathrm{T}}^{\mathrm{miss}}$ stop CRs (top), VRs (middle) and SRs (bottom) after the background-only fit with SRs in the stop fit setup, also published in [2].

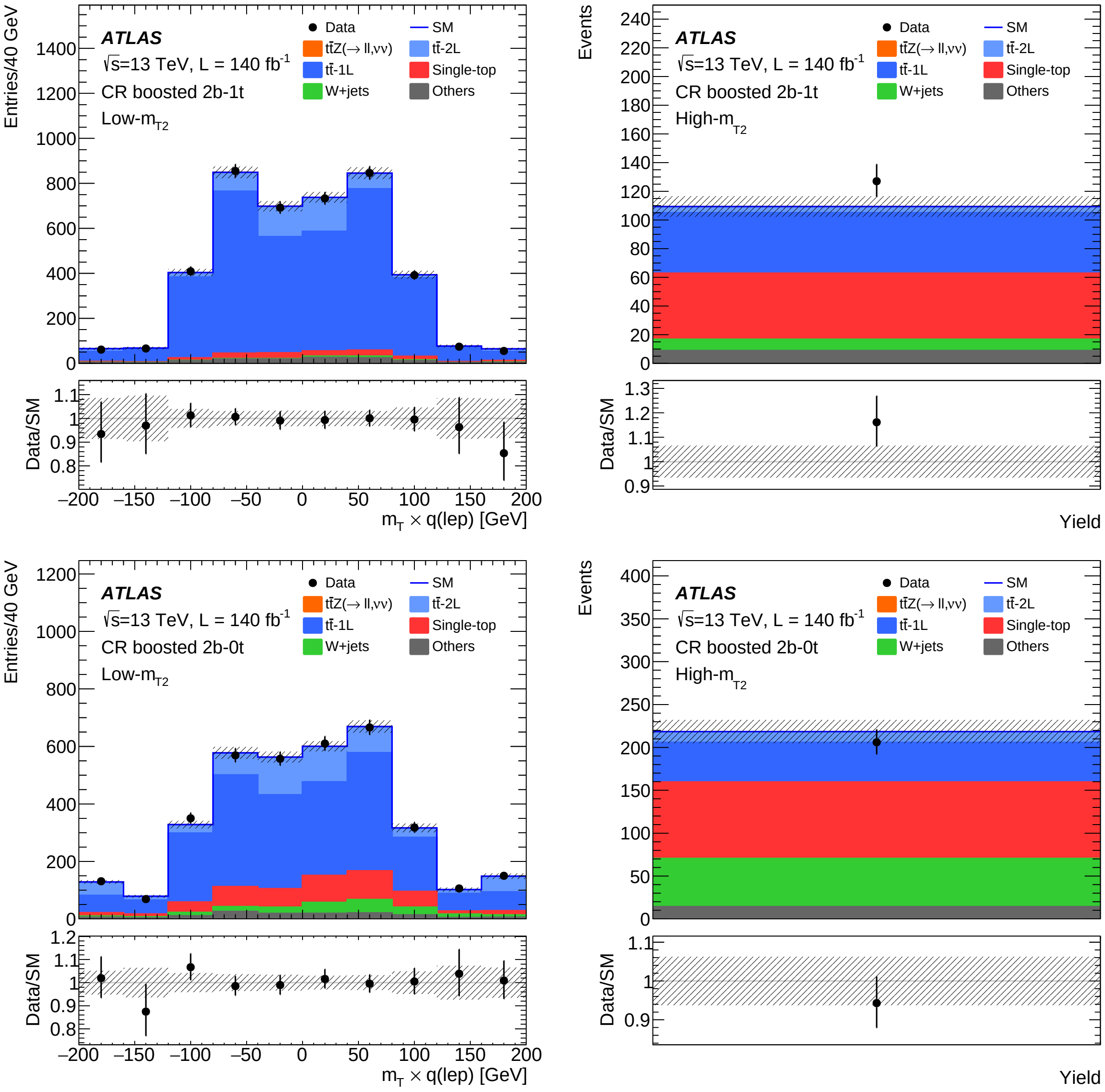

Figure 5.50: Observed and expected distributions in the Boosted-2b stop CRs after the background-only fit with SRs in the stop fit setup, also published in [2].

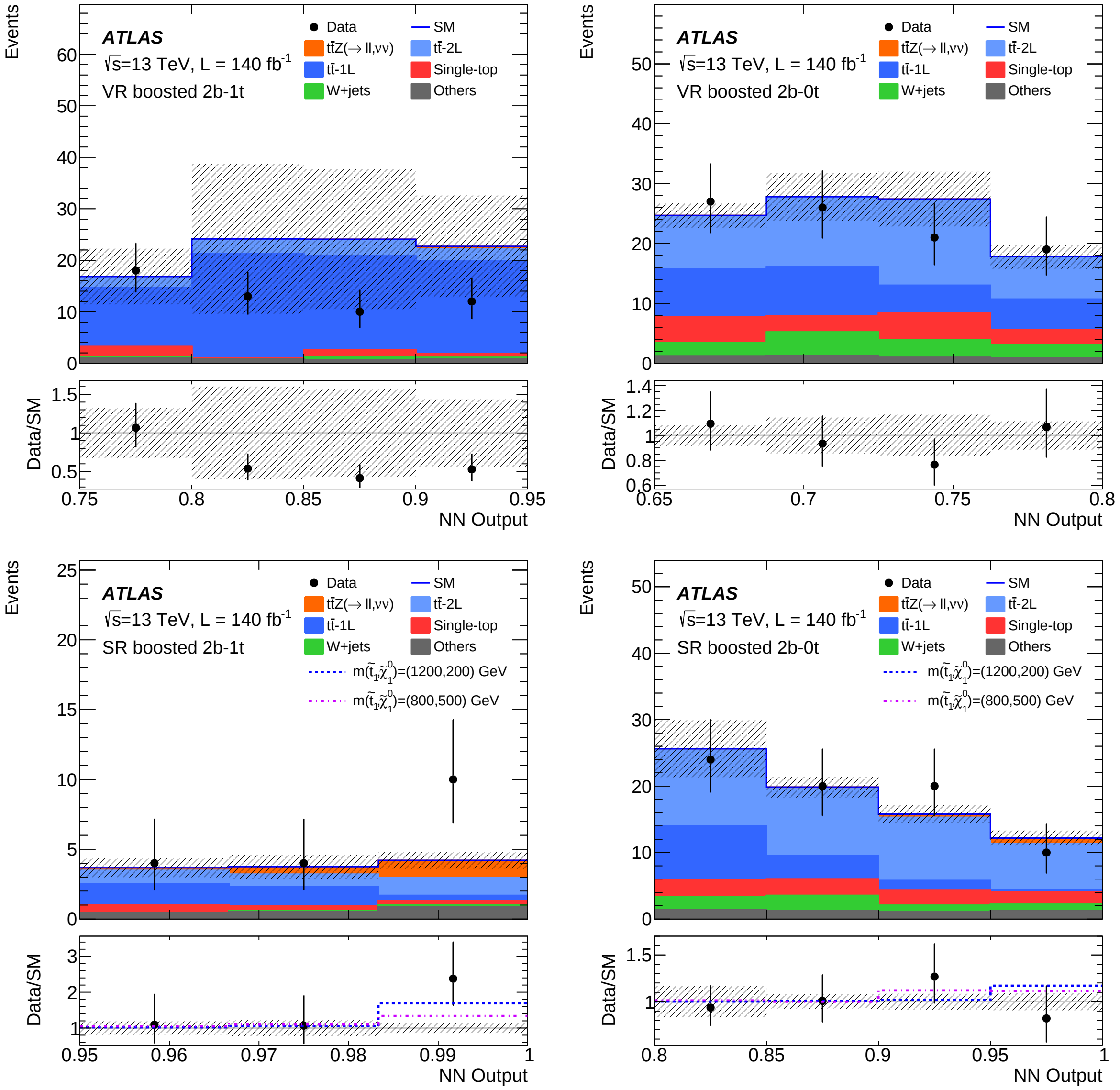

Figure 5.51: Observed and expected distributions in the Boosted-2b stop VRs (top) and SRs (bottom) after the background-only fit with SRs in the stop fit setup, also published in [2].

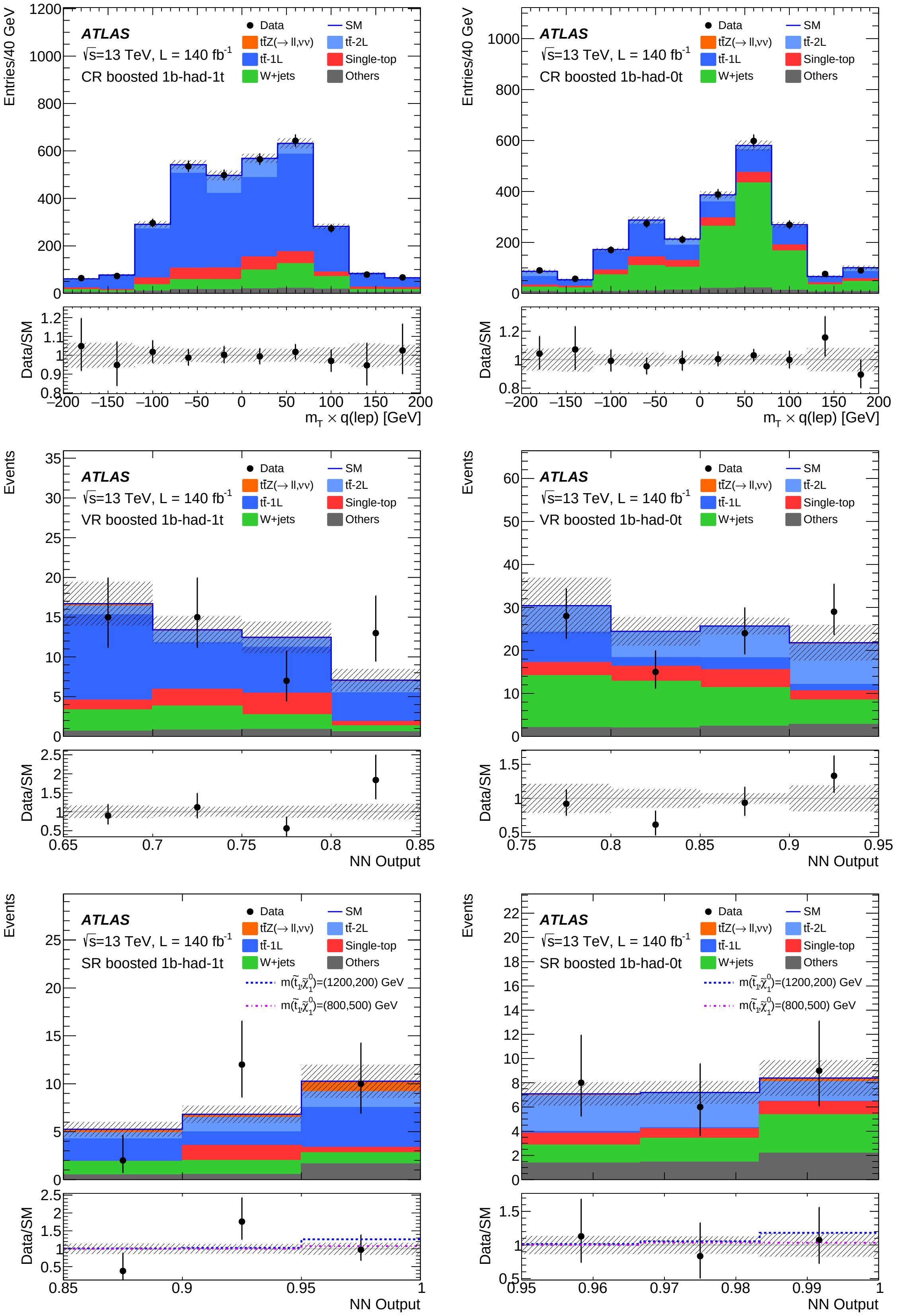

Figure 5.52: Observed and expected distributions in the Boosted-1bhad stop CRs (top), VRs (middle) and SRs (bottom) after the background-only fit with SRs in the stop fit setup, also published in [2].

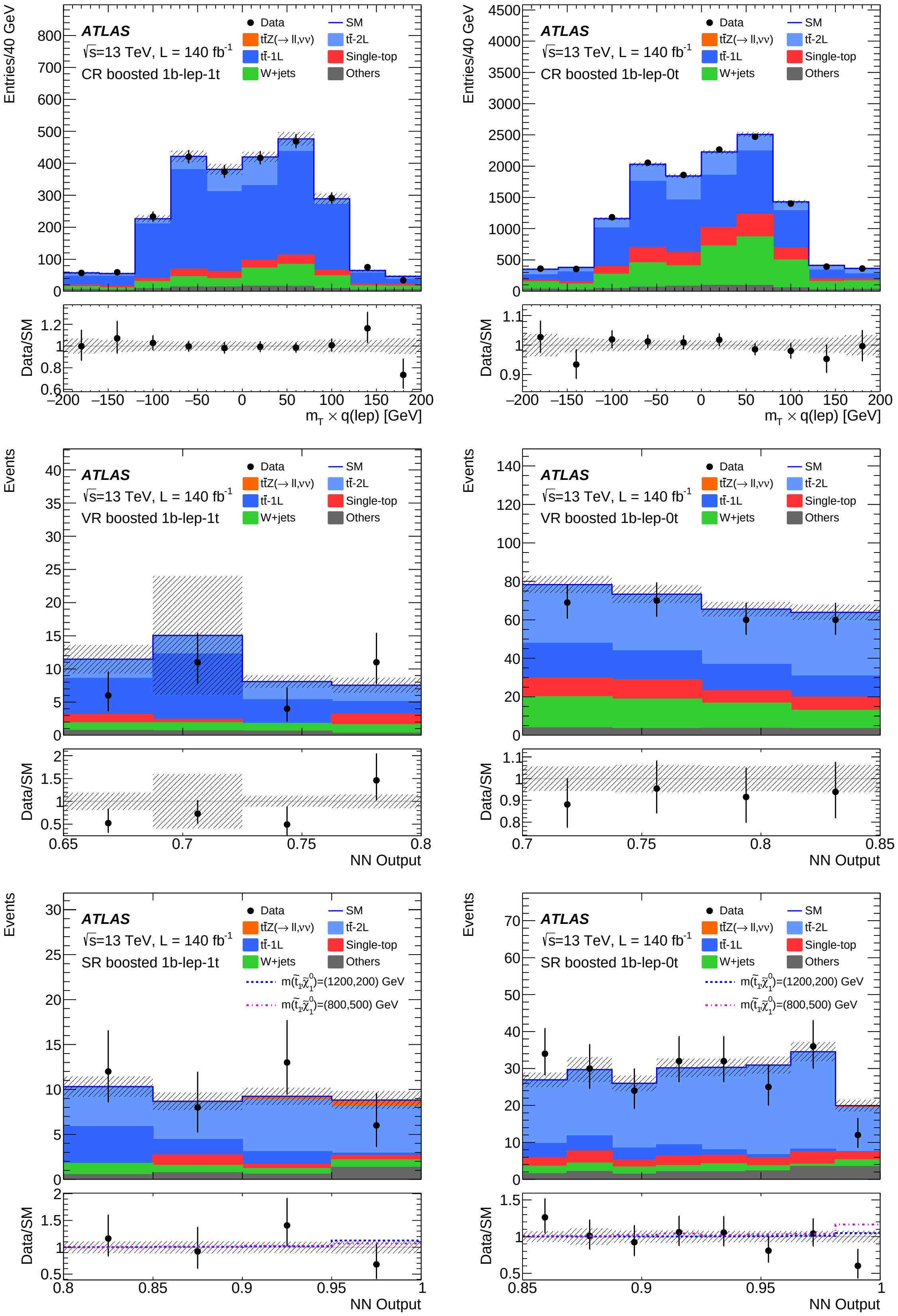

Figure 5.53: Observed and expected distributions in the Boosted-1blep stop CRs (top), VRs (middle) and SRs (bottom) after the background-only fit with SRs in the stop fit setup, also published in [2].

Looking at the post-fit distributions in Figures 5.48-5.53, it can be concluded that, overall, the data agrees well with a background-only hypothesis across the CRs, VRs and SRs. The VRs are not included in fit so that they can continue to be independent cross-checks. Hence, they have larger unconstrained error bars on the SM stack (hashed error bars) than the CRs and SRs. Some key observations in the SRs are summarized below:

- The largest excess ($\simeq 1.7\sigma$) is observed in the last bin of the Boosted-2b-1t SR in the stop fit shown in Figure 5.51.
- In both the DM and stop fit, an excess of ($\simeq 1\sigma$) is observed in the last bin of the High-$E_{\mathrm{T}}^{\mathrm{miss}}$-2b SRs shown in Figure 5.48 and Figure 5.49 respectively.
- At lower NN score, a slight excess incompatible with the population of signal events (expected to be largest in the last bin) is observed in the Boosted-1bhad-1t SR, shown in Figure 5.52.

These excesses are too small to reject a background only hypothesis. Their agreement with the presence of signal are investigated using model dependant fits in Section 5.8.2 and Section 5.8.3.

5.8.2 Interpretation for Stop Searches

For an interpretation using stop signal models, a hypothesis test as described in Section 5.7.2 is carried out. A statistical model is constructed to contain all background processes and one signal model at a time. The value of μ_{sig} in a fit of data to this s+b hypothesis is studied for every stop signal. This quantifies the overall compatibility of the excesses for each stop signal. The setting $\mu_{\text{sig}} = 1$ corresponds to the nominal event yield predicted by the new physics model, hence a post-fit value of zero signifies data incompatible with the presence of the given model. Figure 5.54 shows values of μ_{sig} and its deviation from zero of μ_{sig} for the signals across the $m(\tilde{t}_1)$-$m(\tilde{\chi}_1^0)$parameter space in the full fit to data both in the CRs and in the SRs.

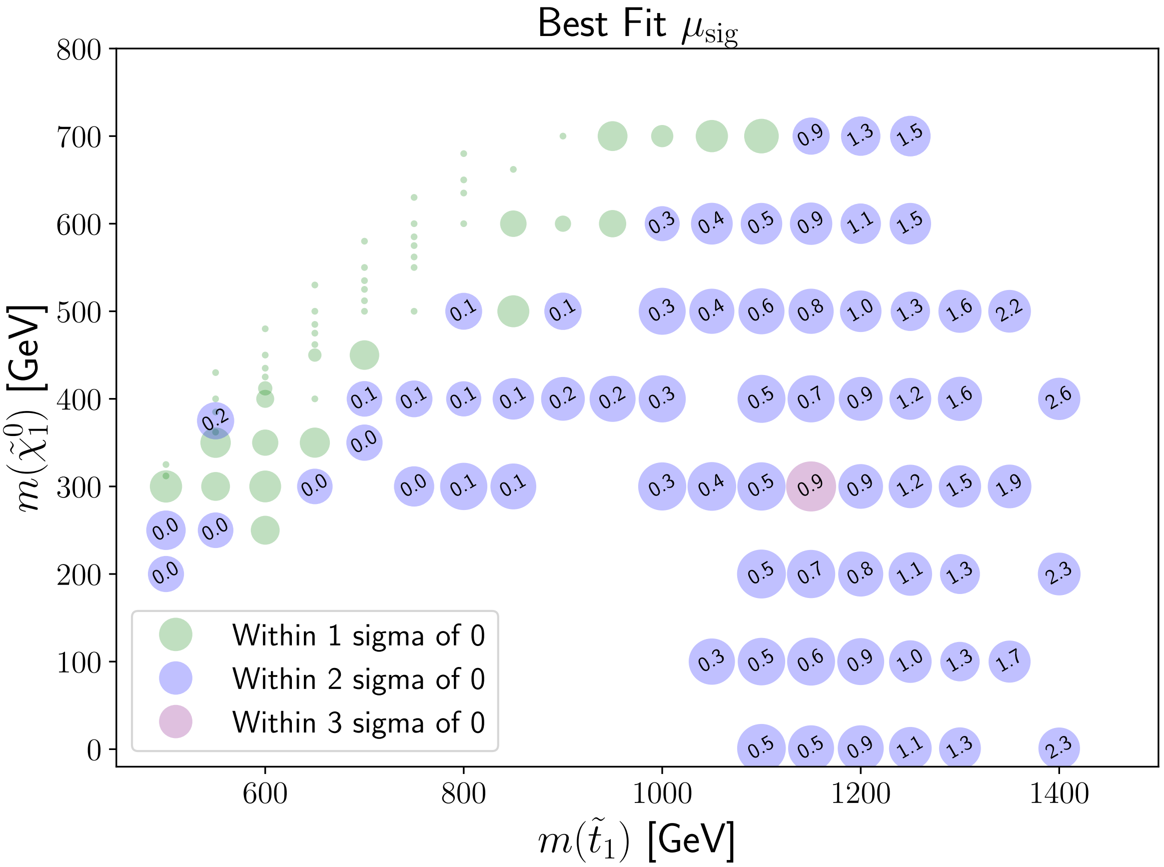

Figure 5.54: Best-fit values of the signal strengths from the full fit to data in all CRs and SRs. Signal strengths μ_{sig} that are within 1 sigma of zero are not denoted with text. The size of the circle representing each μ_{sig} is proportional to its Z-score value, indicating its compatibility with zero.

Signals in the three-body regime and for mass splitting $\Delta m(\tilde{t}_1, \tilde{\chi}_1^0) \sim m(t)$ are fit with a signal strength compatible with zero within one standard deviation. As one moves to high $m(\tilde{t}_1)$ and low $m(\tilde{\chi}_1^0)$ masses, the value of μ_{sig} increases but is still compatible within two standard deviations with zero. This is compatible with the small excesses observed in the

Boosted-2b-1t and High-$E_{\mathrm{T}}^{\mathrm{miss}}$-2b analysis categories of the background-only fit. However, there is no evidence for a significant excess compatible with one of the signals under study, so exclusion limits are set.

Additionally, a $\mathrm{CL_s}$ value explained in Section 5.7.2 is derived for each signal model. This quantifies the confidence with which the background+signal hypotheses can be rejected in favour of the background only hypothesis. A 95% CL exclusion contour corresponding to a $\mathrm{CL_s} < 0.05$ is derived by interpolating the $\mathrm{CL_s}$ values across the $m(\tilde{t}_1)$-$m(\tilde{\chi}_1^0)$ plane. Figure 5.55 shows the expected and observed exclusion contours as a function of $m(\tilde{t}_1)$ and $m(\tilde{\chi}_1^0)$ for the $\tilde{t}_1 \to t\tilde{\chi}_1^0$ (2-body) and $\tilde{t}_1 \to bW\tilde{\chi}_1^0$ (3-body) scenarios.

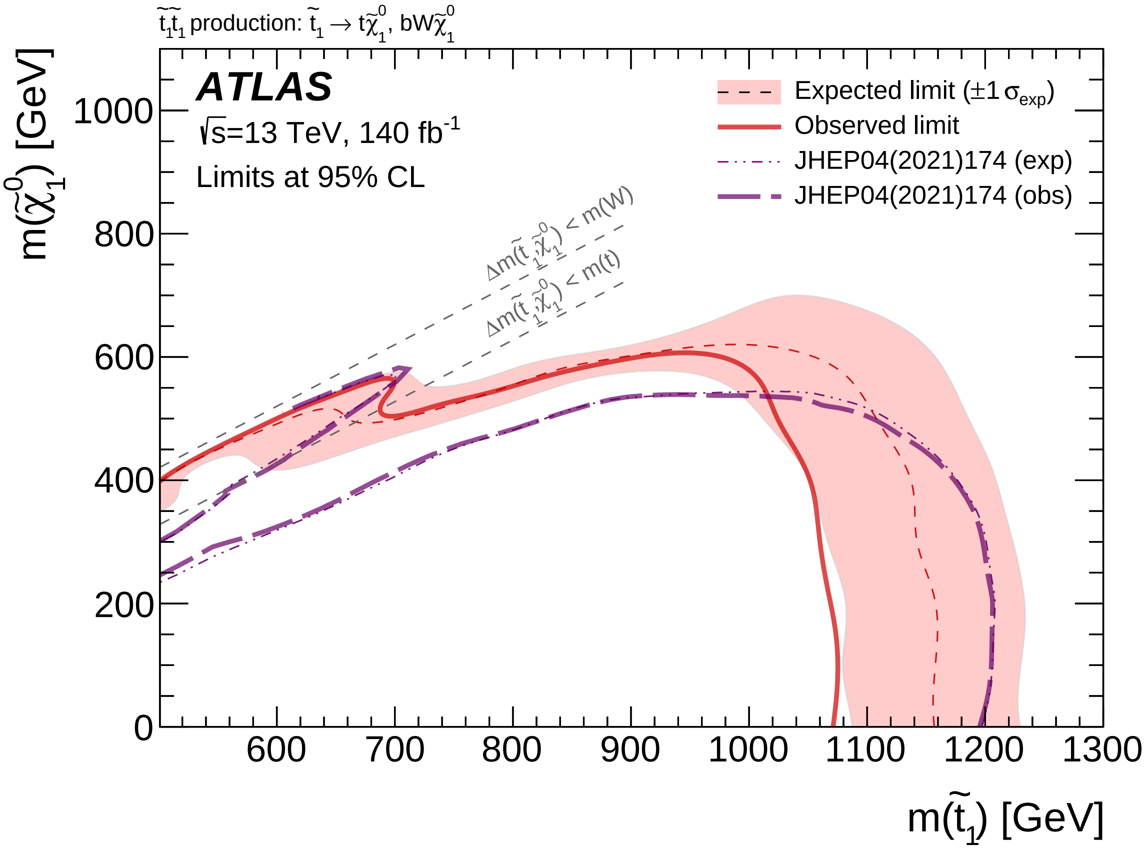

Figure 5.55: Expected and observed 95% CL excluded regions in the plane of $m(\tilde{t}_1)$ and $m(\tilde{\chi}_1^0)$ for $\tilde{t}_1\tilde{t}_1$ production, assuming either a $\tilde{t}_1 \to t\tilde{\chi}_1^0$ or $\tilde{t}_1 \to bW\tilde{\chi}_1^0$ decay with a branching ratio of 100%. Models that lie within the contours are excluded. The red band indicates the $\pm1\sigma$ variation of the expected limit. The diagonal dashed lines indicate the kinematic threshold of the stop decay modes. Also shown is the region excluded by the previous 1L full Run-2 ATLAS result [4]. This plot is also published in [2].

At high neutralino masses, the observed and expected limits are very similar and significantly improve on the limits from the previous 1L full Run-2 ATLAS result [4], even improving on the limits in the three-body regime which was not specifically targeted in the design of this analysis. In this regime, the expected limits are very comparable with those from the 1L CMS result [10] shown with the red dotted lines in Figure 5.56. At high stop masses, the expected limits are very close to those from the previous 1L full Run-2 ATLAS result [4]. This is expected since the sensitivity in this mass range is dominated by the statistical power the analysed data set and less dependent of the analysis strategy. The observed limits are not as strong as the expected limits because of the small observed excess in data.

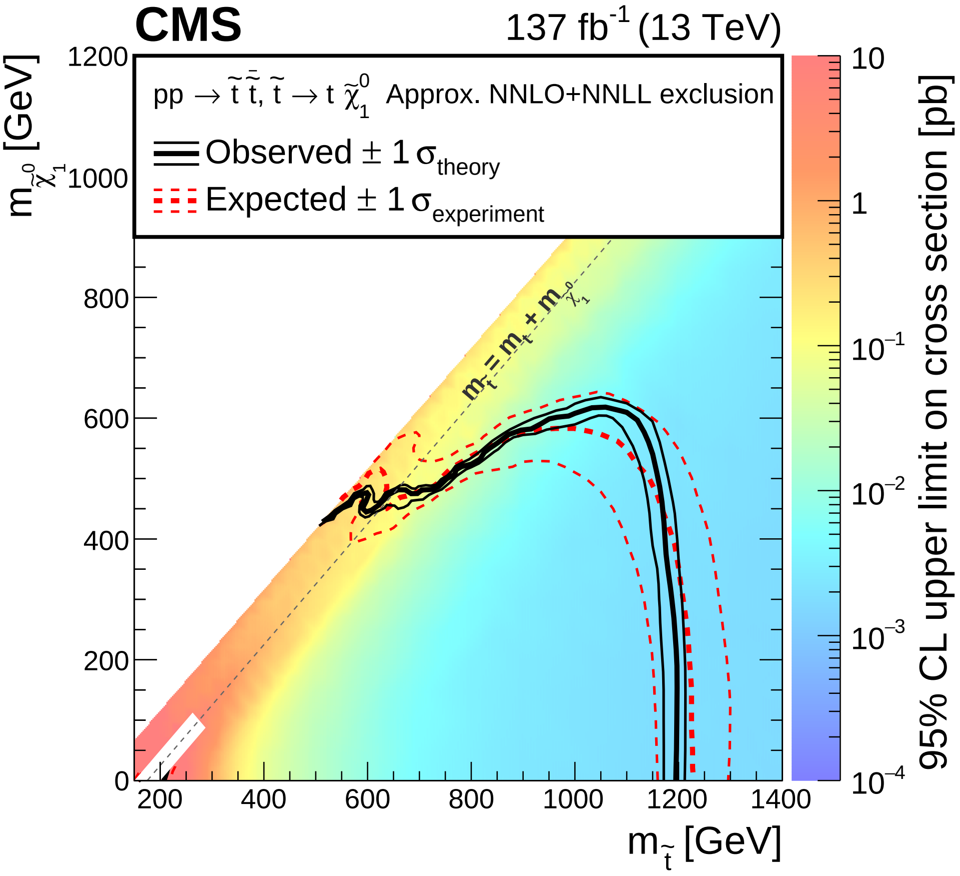

Figure 5.56: Expected and observed limits in the m($\tilde{t}_1$)-m($\tilde{\chi}_1^0$) mass plane, from the CMS 1L result [8].

The comparison of the expected limits from this search and the previous 1L full Run-2 ATLAS result [4] highlights the capability of the unified ML based approach used in this search. It yields sensitivity to a wider range in parameter space without the need to design SRs targetting specific signal models. Improved background modelling used in this analysis also contributes to the improvements in the result.

The reconstruction strategies also impact the sensitivity of the result. Studying the influence of the various NPs on the parameter of interest (μ_{sig}) is essential to understand what uncertainties affect the overall analysis. The "impact" of an NP is a measure that evaluates how much the parameter of interest varies when the NP is adjusted within its uncertainty range [222]. Mathematically, the impact is defined as:

$$\text{impact}(\theta) = \Delta\mu^{\pm}_{\text{sig}} = \hat{\hat{\mu}}_{\text{sig},(\theta_0 \pm \sigma)} - \hat{\mu}_{\text{sig}} \tag{5.15}$$

where, $\hat{\hat{\mu}}_{\text{sig},(\theta_0 \pm \sigma)}$ represents the MLE of μ_{sig} where the value θ is set to the expectation value plus or minus one standard deviation. $\hat{\mu}_{\text{sig}}$ denotes the MLE of $\hat{\mu}_{\text{sig}}$ when all parameters are estimated simultaneously.

A high impact value for an NP indicates that small variations in the NP can lead to significant changes in the parameter of interest, highlighting the importance of estimating this NP accurately. A study of the impact of the different sources of uncertainties on the signal sensitivity are shown in Figure 5.57 and Figure 5.58 for two benchmark signals close to the reach of the exclusion limits. The uncertainty on the signal strength is largely dominated by the statistical uncertainties of the data, including the uncertainties on the NFs. Among the systematic uncertainties, the ones with highest impact are related to the theoretical modelling uncertainties on the background prediction.

- The 30% uncertainty on the overall normalisation of the "Other" background category is typically the uncertainty with the highest impact. The Other category includes $t\bar{t}\,V$ (which is not $t\bar{t}\,Z(\to \ell\ell)$, where ℓ includes both charged and neutral leptons), VV, Z+jets, ttH, and other minor processes like tZ production, the tWZ production, and the production of three and four top quarks. Among these, the largest contributions in the SRs are $t\bar{t}\,V$ and VV, with the $t\bar{t}\,V$ background dominating in the regions with two b-tagged jets and VV dominating in the regions with one b-tagged jet.
- Uncertainties in the modelling of the $t\bar{t}$ and W+jets backgrounds have a substantial impact. These uncertainties have a large size and the high impact is thus expected.
- Among the experimental systematic uncertainties, some related to jet energy scale and b-tagging efficiency also have a high impact.

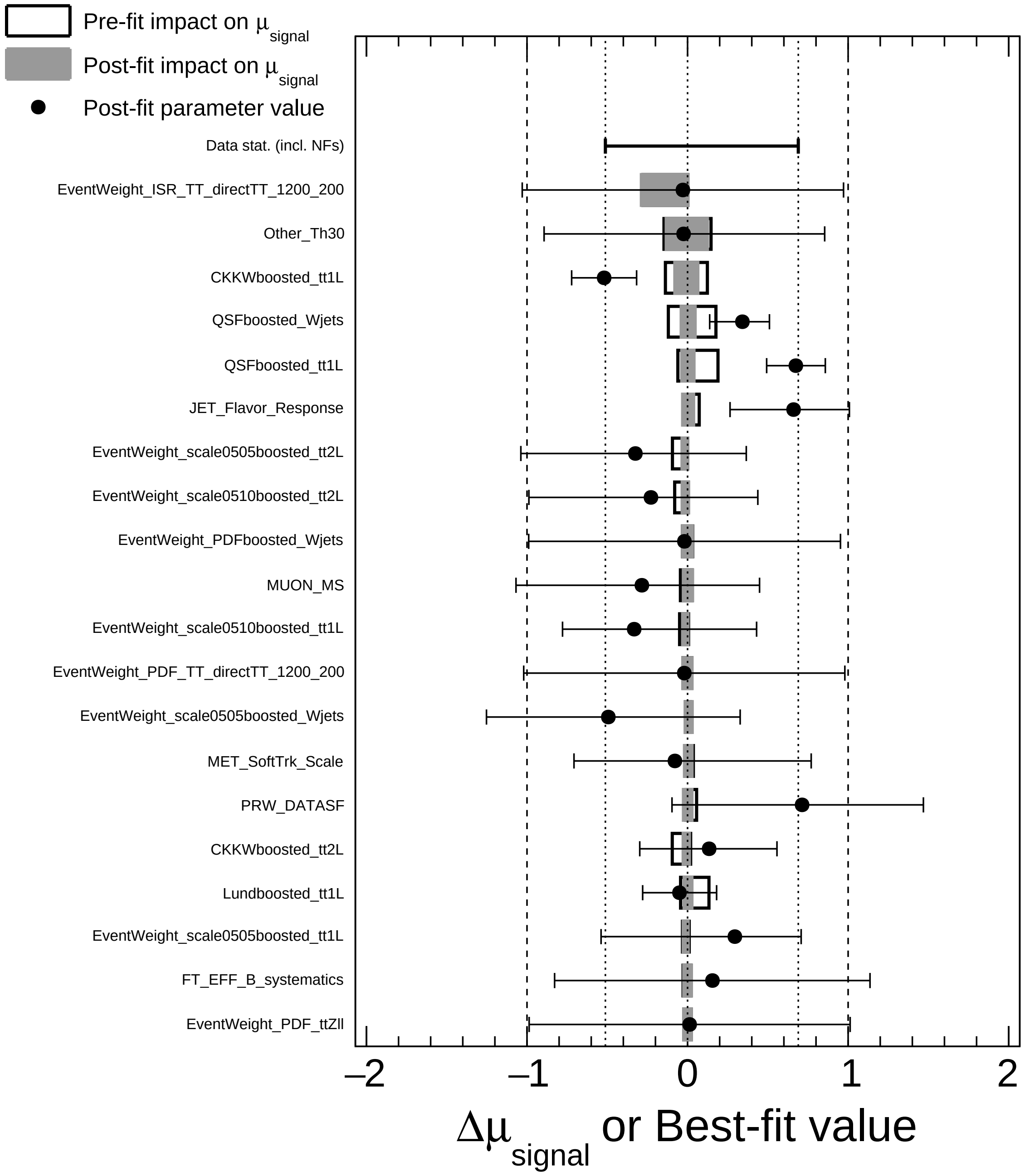

Figure 5.57: Post-fit values of the NPs for the stop fit ranked from top to bottom based on their impact on the determination of the signal strength for two points close to the reach of the exclusions limits: $(m_{\tilde{t}_1}, m_{\tilde{\chi}_1^0}) = (1200, 200)$ GeV. Only the 20 NPs with highest impact on the signal strength are shown. The impact of the NFs is included in the impact from the statistical uncertainty of the data. The postfit values of NPs are not shown if they are outside the range of the x-axis.

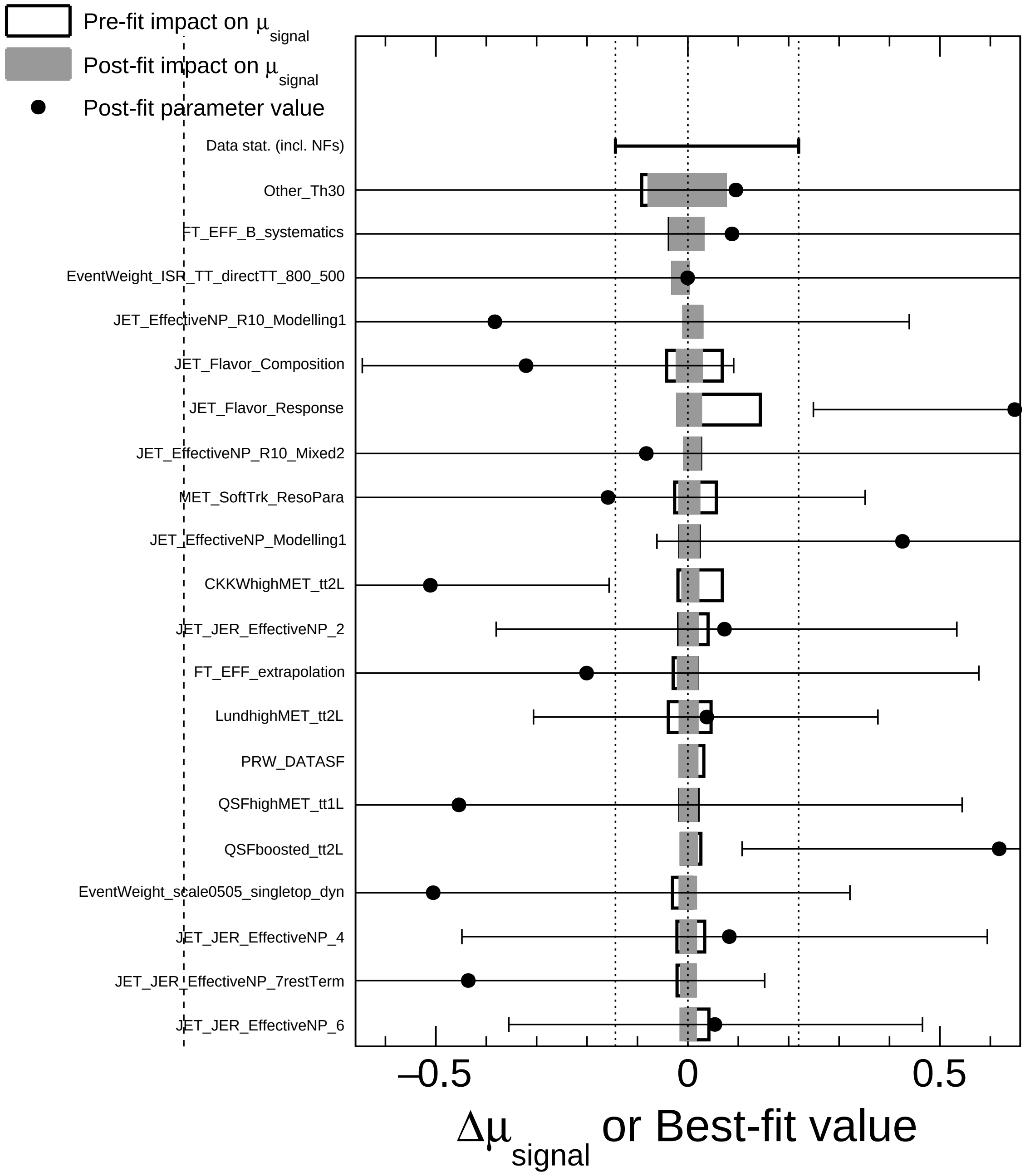

Figure 5.58: Post-fit values of the NPs for the stop fit ranked from top to bottom based on their impact on the determination of the signal strength for two points close to the reach of the exclusions limits: $(m_{\tilde{t}_1}, m_{\tilde{\chi}_1^0}) = (800, 500)$ GeV. Only the 20 NPs with highest impact on the signal strength are shown. The impact of the NFs is included in the impact from the statistical uncertainty of the data. The postfit values of NPs are not shown if they are outside the range of the x-axis.

5.8.3 Interpretation for Dark Matter Searches

As done in the interpretation for stop searches in Section 5.8.3, Figure 5.59 shows the best-fit values of the signal strengths for the signals across the parameter space in the full fit to data both in the CRs and in the SRs. The small excess at high NN output values in the High-$E_{\mathrm{T}}^{\mathrm{miss}}$-2b SR observed in the background-only fit (Section 5.8.1) is compatible with a possible signal with a signal strength different from zero at a significance between one and two standard deviations. No strong dependence on the mediator mass is observed.

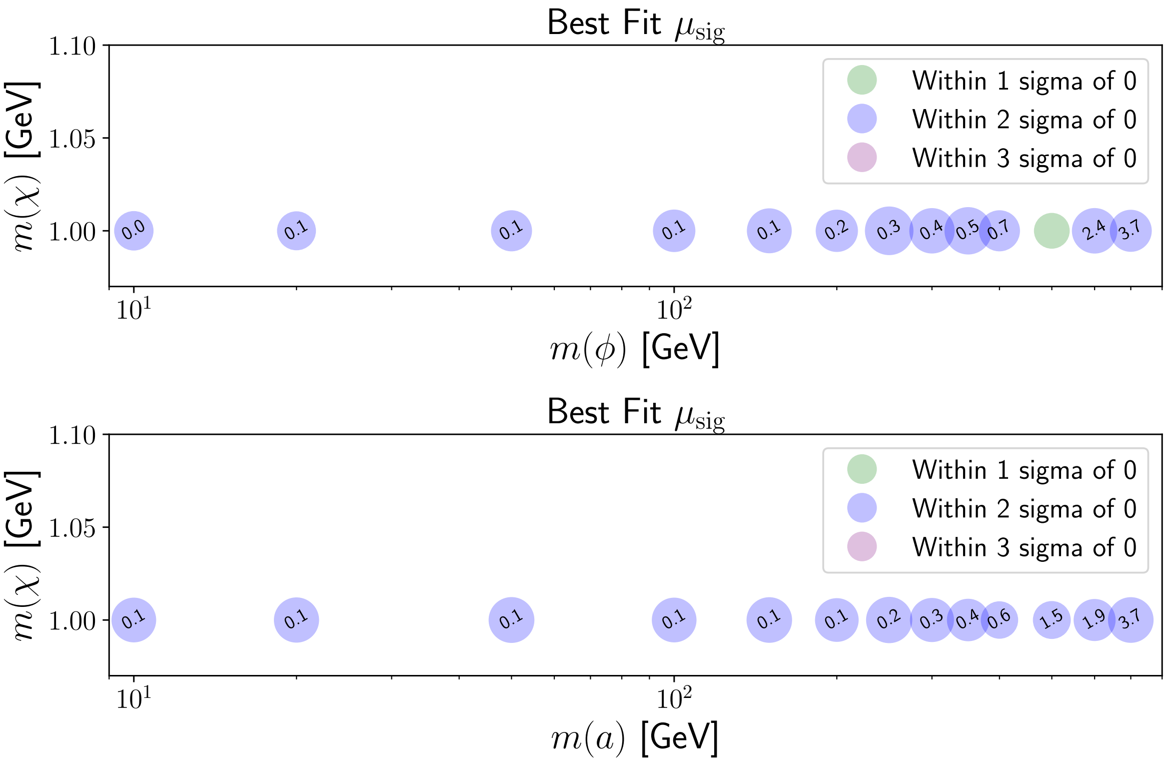

Figure 5.59: Best-fit values of the signal strengths from the full fit to data in all CRs and SRs for signals with a scalar (top) or a pseudoscalar (bottom) mediator and $m(\chi) = 1\,\mathrm{GeV}$.

Figure 5.60 and Figure 5.61 show the observed and expected exclusion limits for the DM search with all systematic and statistical uncertainties and compare these limits with those from the previous 1L full Run-2 ATLAS result [4]. The observed upper limits are worse than the expected upper limits due to the small excess of events in data.

The expected exclusion limits obtained by this improved 1L analysis exceed those obtained by the combination of 0L+1L+2L searches for the same spin-0 mediators using the full Run-2 ATLAS dataset [6], shown in Figure 5.62.

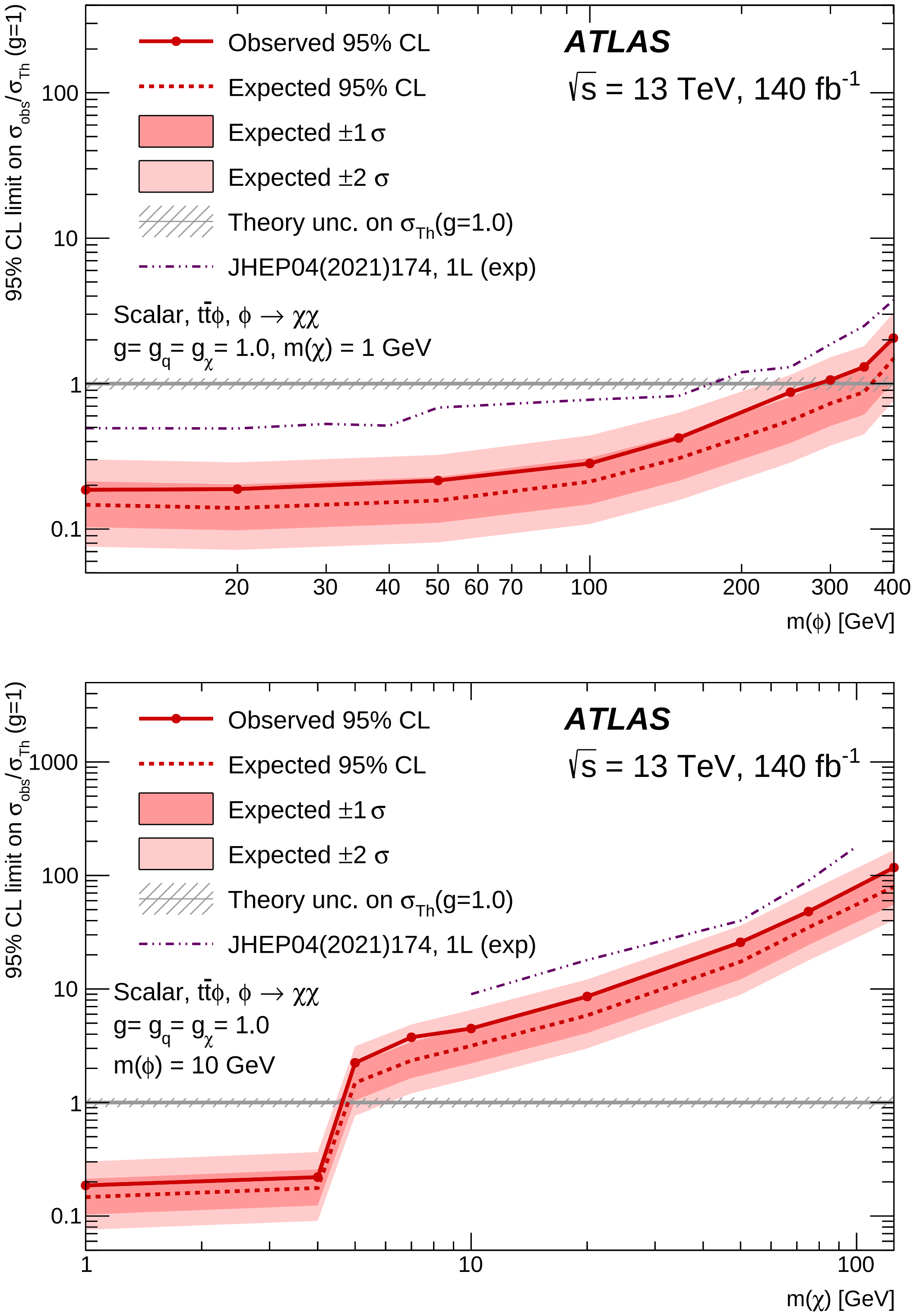

Figure 5.60: Upper limit at 95% CL on the ratio of the $t\bar{t}$+DM production cross-section to the theoretical cross-section of a scalar mediator. Limits are shown as a function of $m(\phi)$ assuming $m(\chi) = 1\,\text{GeV}$ (top), or as a function of $m(\chi)$ assuming $m(\phi) = 10\,\text{GeV}$ (bottom). All limits are computed assuming $g = 1$. Limits from the previous 1L full Run-2 ATLAS result [4] are also shown to demonstrate the improvement of the analysis. These plots are also published in [2].

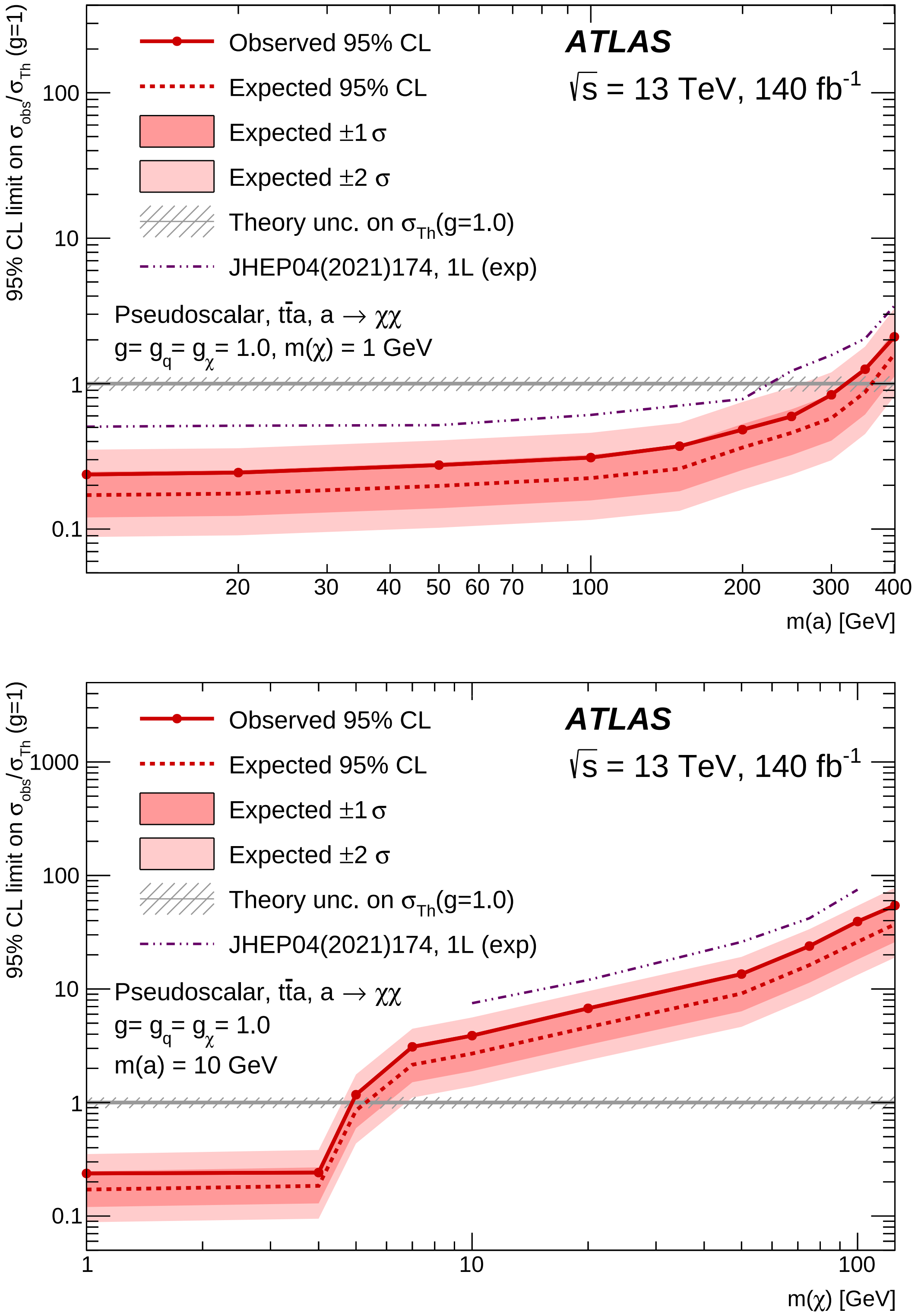

Figure 5.61: Upper limit at 95% CL on the ratio of the $t\bar{t}$+DM production cross-section to the theoretical cross-section under the hypothesis of a pseudoscalar mediator. Limits are shown as a function of $m(a)$ assuming $m(\chi) = 1\,\text{GeV}$ (top), or as a function of $m(\chi)$ assuming $m(a) = 10\,\text{GeV}$ (bottom). Limits from the previous 1L full Run-2 ATLAS result [4] are also shown to demonstrate the improvement of the analysis. These plots are also published in [2].

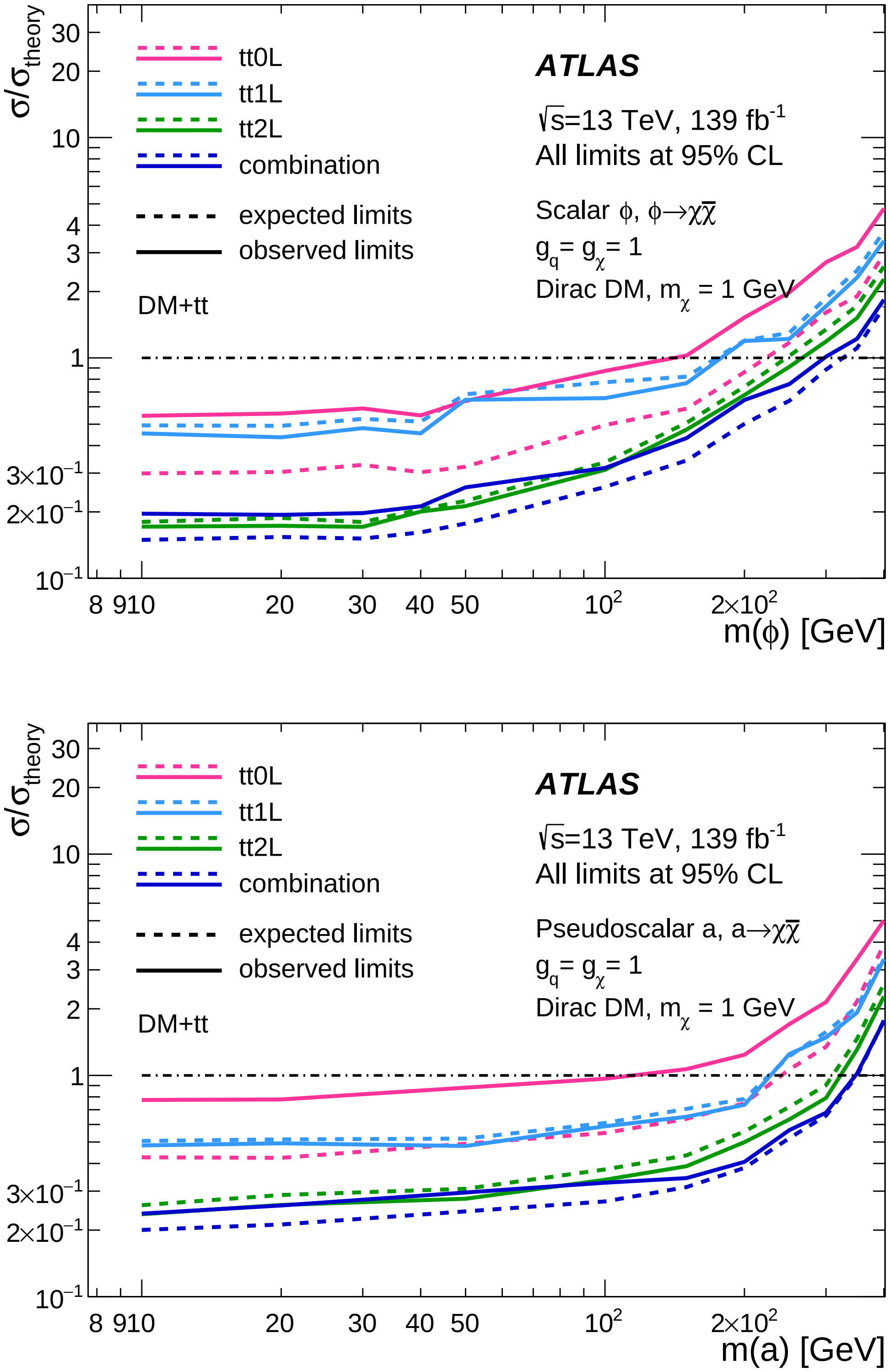

Figure 5.62: Exclusion limits for scalar (top) and pseudoscalar (bottom) mediator DM models as functions of the mediator mass $m(\phi)$ or $m(a)$ with a dark matter mass $m_\chi = 1$ GeV. A combined 0L+1L+2L is shown. Only DM production with top-quark pairs is considered. Limits are at 95% CL and given as ratios to a coupling assumption of $g = g_q = g_\chi = 1$. Solid (dashed) lines represent observed (expected) exclusion limits for each channel and their combination, taken from [4].

Summaries of the impact of the different sources of uncertainties to the signal sensitivity are shown in Figure 5.63 and Figure 5.64 for different benchmark signals. As for the stop fit, the uncertainty on the signal strength is largely dominated by the statistical uncertainties. Among the systematic uncertainties, the ones with highest impact are mainly related to theoretical uncertainties on the background determination, but they also include uncertainties on the jet energy scale and on the b-tagging efficiency.

To provide an overview of the impact of all uncertainties for both stop and DM fits, Table 5.20 reports the total uncertainties on the μ_{sig} for a few benchmark signals with a break down in groups of uncertainties. Both stop and DM fits are dominated by statistical uncertainties followed by background modelling uncertainties. The impact of the various subgroups of uncertainties is similar for both stop and DM benchmark models.

Table 5.20: The total uncertainty $\sigma(\mu_{\text{sig}})$ includes contributions from statistical and major systematic uncertainties. Statistical uncertainty is assessed by fixing all fit nuisance parameters, while systematic uncertainty is calculated as $\sigma_{\text{sys}}(\mu) = \sqrt{\sigma^2(\mu_{\text{sig}}) - \sigma^2_{\text{fix}}(\mu_{\text{sig}})}$, with $\sigma_{\text{fix}}(\mu_{\text{sig}})$ obtained when systematic nuisance parameters are fixed. Uncertainty components are presented as percentages of $\sigma(\mu_{\text{sig}})$ for positive μ_{sig} variations only due to potential biases for negative variations. No correlations between components are considered. This table is taken from [2].

	$\tilde{t}_1\tilde{t}_1$, $m(\tilde{t}_1, \tilde{\chi}^0_1)$ GeV		$t\bar{t}$+DM, $m(a, \chi)$ GeV	
	(1000, 600)	(1200, 200)	(50, 1)	(150, 1)
$\mu \pm \sigma(\mu)$ (total uncertainty)	$0.25^{+0.42}_{-0.25}$	$0.8^{+0.7}_{-0.5}$	$0.08^{+0.10}_{-0.08}$	$0.12^{+0.13}_{-0.12}$
Data statistical uncertainty	82 %	74 %	67 %	69 %
Background modelling	45 %	62 %	51 %	48 %
MC statistical uncertainty	25 %	20 %	34 %	33 %
Jet energy scale and resolution	20 %	13 %	29 %	28 %
Flavour tagging efficiency	18 %	10 %	21 %	21 %

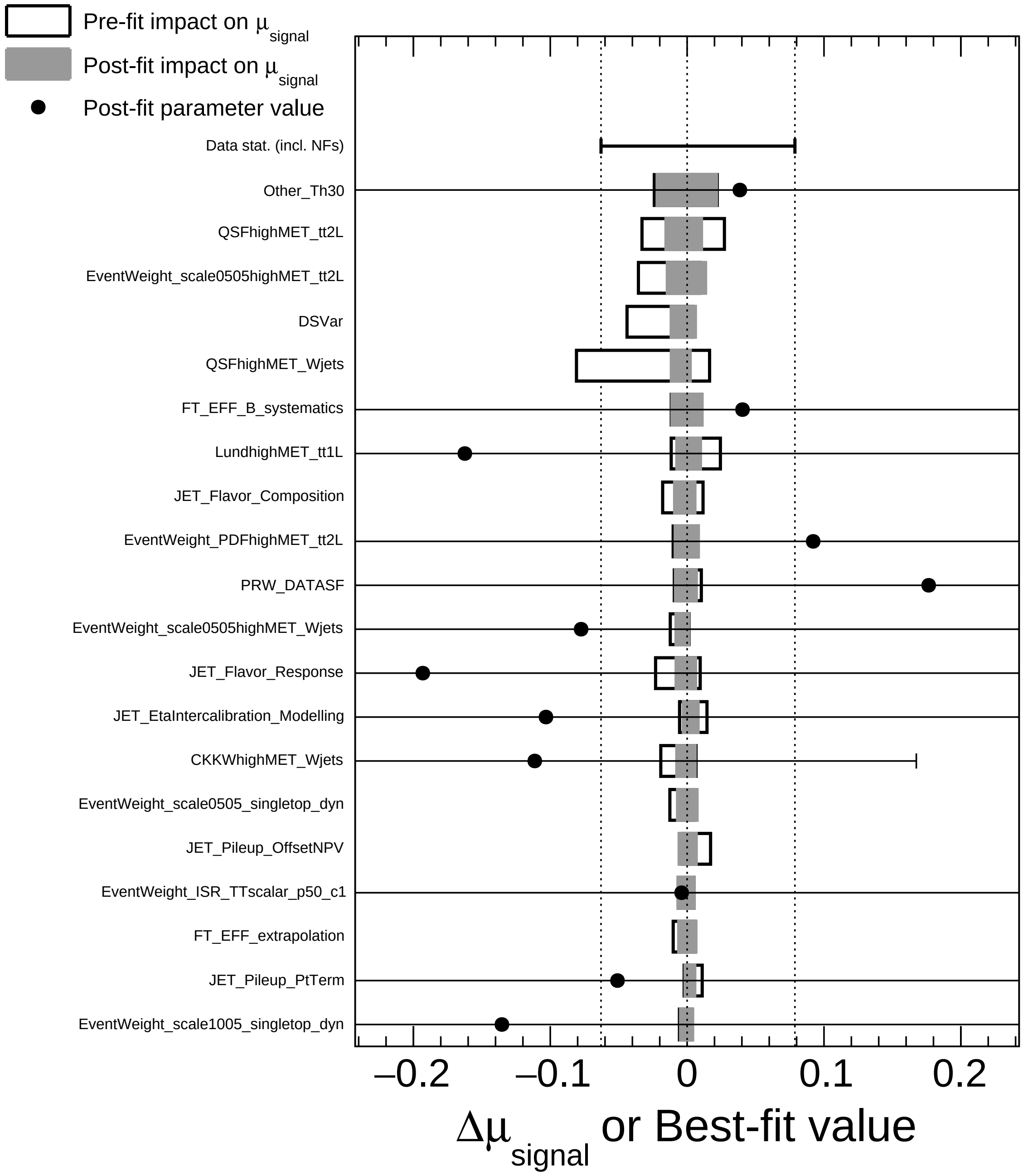

Figure 5.63: Post-fit values of the NPs for the DM fit ranked from top to bottom based on their impact on the determination of the signal strength for signals with a scalar mediator with $m_\phi = 50\,\text{GeV}$ and $m_\chi = 1\,\text{GeV}$. Only the 20 NPs with highest impact on the signal strength are shown. The impact of the NFs is included in the impact from the statistical uncertainty of the data. The postfit values of NPs are not shown if they are outside the range of the x-axis.

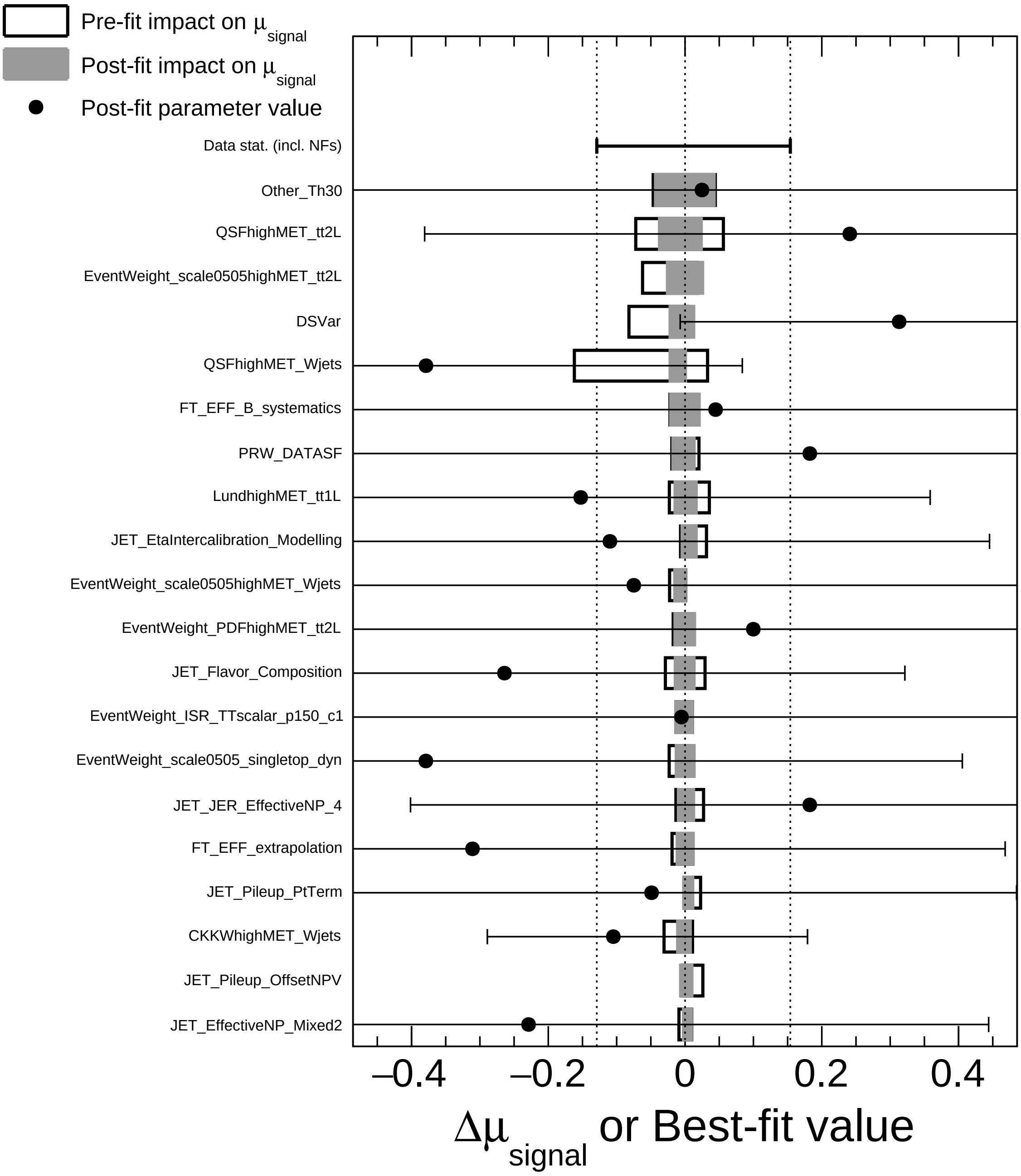

Figure 5.64: Post-fit values of the NPs for the DM fit ranked from top to bottom based on their impact on the determination of the signal strength for signals with a scalar mediator with $m_\phi = 150\,\text{GeV}$ and $m_\chi = 1\,\text{GeV}$. Only the 20 NPs with highest impact on the signal strength are shown. The impact of the NFs is included in the impact from the statistical uncertainty of the data. The postfit values of NPs are not shown if they are outside the range of the x-axis.

5.9 Combinations

This chapter has presented the new Run-2 ATLAS 1-lepton (1L) results for both stop-pair production and spin-0 mediators decaying to DM when produced in association with top-quark pairs. These findings improve upon the results previously presented in [4]. Results for the same models in the 0-lepton (0L) and 2-lepton (2L) channels can be found in [3, 5, 6].

In the search for stop-pair production, the new 1L result provides improved sensitivity in the high neutralino mass region, especially where the mass splitting between the stop quark and the neutralino, $\Delta m = m_{\tilde{t}} - m_{\tilde{\chi}_1^0}$ is close to the top quark mass. On the other hand, the Run-2 ATLAS 0-lepton result [3] provides the best sensitivity for high mass stop quarks. Since both these results use independent selections of events, a statistical combination of the two results can be performed. The new 1L result, presented in this thesis, and the previous Run-2 ATLAS 0-lepton result [3] are statistically combined in [2]. This yields the best limits for stop searches using the ATLAS Run-2 dataset as shown in Figure 5.65.

In the search for dark matter using a simplified model to probe its production in association with top-quark pairs, the exclusion limits from this enhanced 1L analysis surpass those from the combined 0L+1L+2L searches for the same spin-0 mediators using the full Run-2 ATLAS dataset [6]. This prompts an updated ATLAS $t\bar{t}$+DM combination, where the 1L limit from [6] is replaced with the new result presented in this thesis. A statistical combination is performed across all three final states in [2]. The revised ATLAS $t\bar{t}$+DM combination result is shown in Figure 5.66. While the sensitivity of the previous combination result was dominated by the search in the 2-lepton final state, the updated combination is dominated by the the new 1-lepton result.

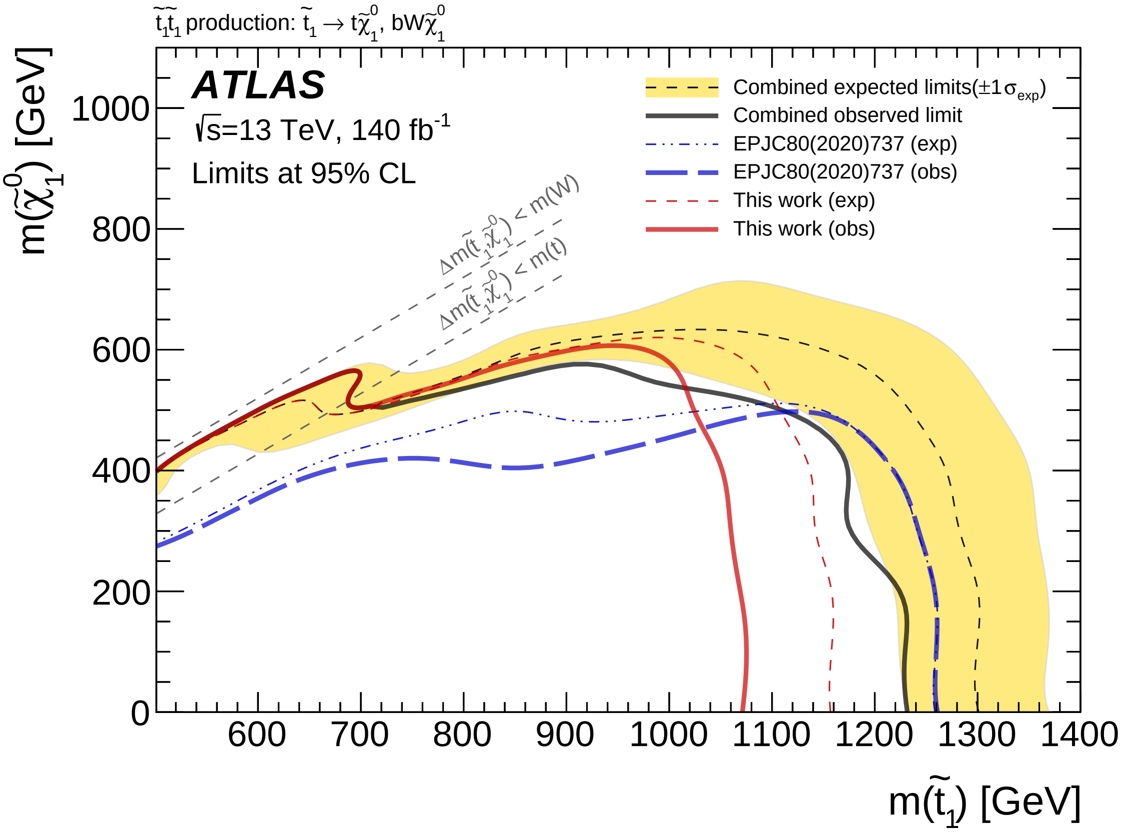

Figure 5.65: The 95% CL excluded regions in the $m(\chi_1^0)$ and $m(\tilde{t}_1)$ plane for $\tilde{t}_1\tilde{t}_1$ production are shown. The results are derived from a statistical combination of the search presented in this chapter and the results in [3]. Excluded models lie outside the contours. The yellow band represents the $\pm 1\sigma$ uncertainty of the combined expected limit, and the diagonal dashed lines mark the kinematic thresholds for the different stop decay modes. This plot is taken from [2].

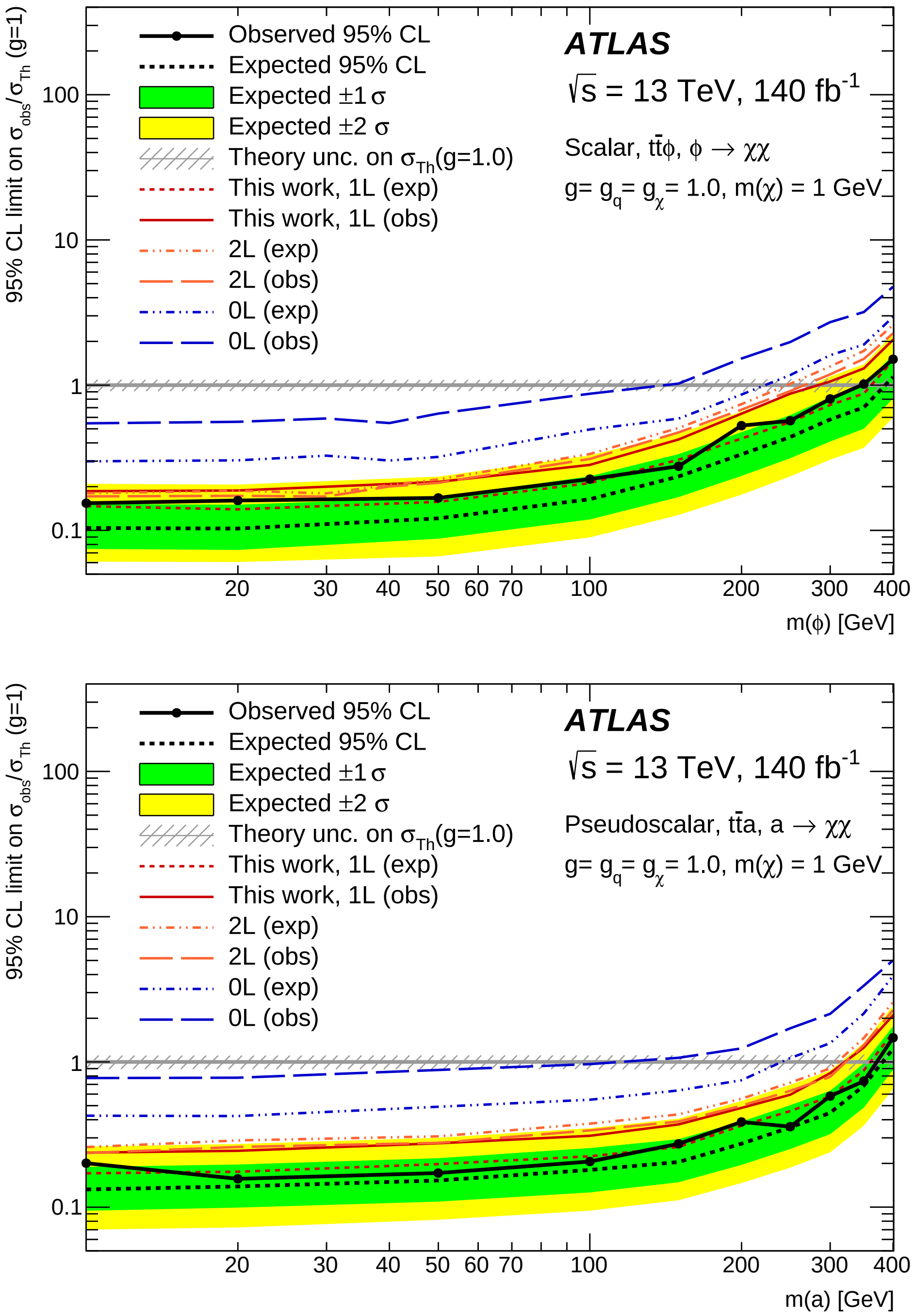

Figure 5.66: Upper limits at 95% CL on the ratio of the $t\bar{t}$+DM production cross-section to the theoretical cross-section are presented under the hypothesis of (top) a scalar or (bottom) a pseudoscalar mediator. Limits are plotted as a function of $m(\phi/a)$ with $m(\chi) = 1$ GeV. All limits are computed assuming $g = 1$. Combined limits from [6] are updated to incorporate the analysis in improved 1L result presented in this chapter. Additionally, individual analysis limits included in the combination are displayed. These plots are taken from [2].

CHAPTER 6

EFT Interpretation: $t\bar{t}\nu\bar{\nu}$ Contact Interactions

This chapter introduces the EFT framework used to interpret data in the context of Contact Interactions (CIs). The specific $t\bar{t}\nu\bar{\nu}$ *CI probed is then explained, followed by the methodologies used to probe this CI using the full Run-2 ATLAS pp dataset. The chapter ends with the presentation of the first upper limits set on this* $t\bar{t}\nu\bar{\nu}$ *CI with the ATLAS detector.*

* * *

The data probed with the previous model-dependent searches is interpreted in the context of a search for new contact interactions between top quarks and neutrinos. This investigation is carried out using the Effective Field Theory (EFT) approach, which provides a more model-independent perspective. In general, the EFT approach is made possible by the fundamental principle of scale separation in particle physics, which recognises that the many known physical processes occur over a wide range of energy scales, and that different physical processes become relevant at different energy scales. This allows physics calculations to be done "locally" focusing on the relevant physics at a given energy scale while addressing any divergencies that may arise from quantum corrections through the renormalization process later.

While current experiments, like those at the LHC, probe energy scales in the TeV range, new physics may lie at a much higher energy scale. Given the lack of experimental evidence for new physics up to the TeV range, there lies motivation to study indirect effects of new physics at higher energy scales, which is made possible by the EFT approach. This approach can provide indirect tests for new physics at high energies without delivering concrete evidence on the nature of this new physics, thus providing model-independent limits.

6.1 The EFT approach

EFT is a well-defined theoretical approach, the main ideas of which are summarized in this section, based on detailed explanations available in [223–225]. If there exists a "full theory" that describes physics at all energy scales, the SM can be thought of as an EFT approximation of the full theory. It neglects physics above a certain scale Λ, but accurately describes physics at energy scales $E \ll \Lambda$ within a certain precision. A specific example of the EFT concept is to consider the Fermi theory of weak interactions as an EFT of SM. For example, in beta decay, which occurs on energy scales well below the mass of the W boson, a four-fermion contact interaction replaces the weak interaction mediated by the "heavy" W boson, as shown in the figure 6.1.

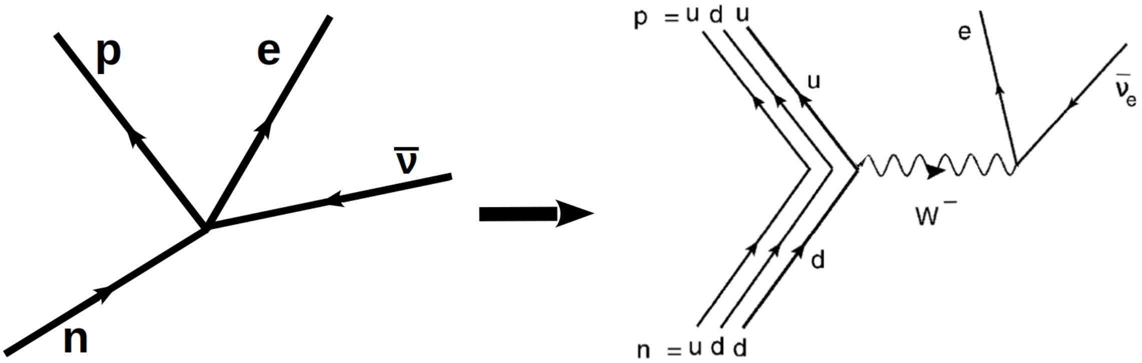

Figure 6.1: Depiction of neutron beta decay occurring at low energies ($E \ll m_W$) on the left, where a neutron transforms into a proton, an electron, and an electron antineutrino. On the right is an illustration of the W boson exchange, showcasing its role in mediating weak force interactions.

Similarly, if a heavy particle exists beyond the reach of the LHC and mediates a new interaction, it can be probed using an approximate point-like interaction at the LHC energy scale. The new physics process is mathematically quantified within an EFT Lagrangian and depends on Λ, which represents the energy scale at which the new physics phenomena become relevant, and Wilson coefficients, which quantify the strength of the new interactions. In the context of an extended SM, a special implementation of EFT called Standard Model Effective Field Theory (SMEFT) is used. In SMEFT, the principles of EFT are used to extend the SM Lagrangian to include higher-dimensional operators that capture the effects of the new physics. An illustrative expression of the SMEFT Lagrangian is given by the formula

$$\mathscr{L}_{\text{SMEFT}} = \mathscr{L}_{\text{SM}} + \sum_{n=5}^{\infty} \frac{1}{\Lambda^{n-4}} \sum_i (\alpha_i O_i)^{(n)}, \tag{6.1}$$

where, $\mathscr{L}_{\text{SM}}$ denotes the SM Lagrangian, Λ represents the energy scale at which new physics becomes relevant, O_i are the operators that describes new, high dimensional interactions between SM particles that come into existence due to new physics appearing at the energy scale Λ, and α_i are the Wilson coefficients that describe the strengths of these interactions. The approximation of the EFT approach is to "integrate out" the degrees of freedom of these new processes/particles and replace them with effective interactions between SM particles. These effective interaction between SM particles, described by the operators in the Lagrangian, describe the low-energy effects of the new processes. Thus, by studying the point-like contact interaction, limits can be placed on Λ and α_i. Both these quantities are not independent, which means that the assumptions made for α_i influence the constraints set on Λ.

6.2 The $t\bar{t}\nu\bar{\nu}$ Contact Interaction

In this analysis, the results obtained in the analysis of the $t\bar{t}$ +$E_{\mathrm{T}}^{\mathrm{miss}}$ final state are interpreted in the EFT framework with four-fermion contact interactions (CIs) between two quarks and two leptons[1]. Using an EFT theoretical framework based on [227–229], the $tt\ell\ell$ Lagrangian for four-fermion operators using SM fields is given as follows:

$$\mathscr{L}_{t\bar{t}\ell\bar{\ell}} = \frac{1}{\Lambda^2} \sum_{i,j=L,R} \Big[V_{ij}^{\ell}(\bar{\ell}\gamma_\mu P_i \ell)(\bar{t}\gamma^\mu P_j t) + S_{ij}^{\ell}(\bar{\ell}P_i\ell)(\bar{t}P_j t) + T_{ij}^{\ell}(\bar{\ell}\sigma_{\mu\nu}P_i\ell)(\bar{t}\sigma^{\mu\nu}P_j t) \Big] \quad (6.2)$$

where Λ is the scale for new physics and $P_{L,R} = (1 \mp \gamma_5)/2$ are the projection operators for left and right-handed fields. The dimensionless Wilson coefficients of the vector, scalar and tensor four-fermion interactions are depicted by V_{ij}^{ℓ}, S_{ij}^{ℓ} and T_{ij}^{ℓ} respectively.

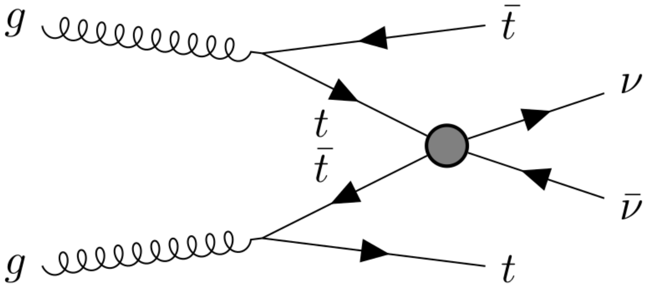

Figure 6.2: Leading-order Feynman diagram of the $t\bar{t}\nu\bar{\nu}$ effective contact interaction.

Constraining the $tt\ell\ell$ Lagrangian for the case where the leptons are only SM neutrinos yields a reduced $t\bar{t}\nu\bar{\nu}$ Lagrangian. Since SM neutrinos are left-handed (LH), only the vector interactions V_{LL} and V_{LR} can be generated in dimension six. Scalar and tensor interactions are generated in higher dimensions, and are therefore suppressed by higher powers of Λ and consequently neglected in this analysis. The reduced $t\bar{t}\nu\bar{\nu}$ Lagrangian for the interaction of interest shown in Figure 6.2, is as follows:

$$\mathscr{L}_{t\bar{t}\nu\bar{\nu}} = \frac{1}{\Lambda^2} \Big[V_{LL}^{\ell}(\bar{\nu}\gamma_\mu P_L \nu)(\bar{t}\gamma^\mu P_L t) + V_{LR}^{\ell}(\bar{\nu}\gamma_\mu P_L \nu)(\bar{t}\gamma^\mu P_R t) \Big] \quad (6.3)$$

Limits on Λ are set considering one coefficient at a time, meaning the interaction of SM neutrinos with left and right-handed top quarks are analysed independently. The simulations

---

[1] While this interaction was originally motivated to investigate flavour anomalies observed in decays such as $b \to s\ell^+\ell^-$ [226], which have since been reduced, this CI remains a good probe to test SM predictions at high energies.

for the $t\bar{t}\nu\bar{\nu}$ CIs involving either V_{LL} and V_{LR} operators were conducted in two separate samples. Additionally, the vector CI can have a constructive or destructive interference with the SM $t\bar{t}Z(\rightarrow \nu\nu)$ process. To account for the interference, two samples for each operator are produced, one representing the pure contribution from new physics (NP) and the other representing the interference with the SM (SM-NP). Therefore, the total cross section for the $t\bar{t}\nu\bar{\nu}$ final state can be parametrized as:

$$\sigma_{\text{tot}} = \sigma_{\text{SM}} + \frac{V_{ij}}{\Lambda^2}\sigma_{\text{SM-NP}} + \frac{V_{ij}^2}{\Lambda^4}\sigma_{\text{NP}} \tag{6.4}$$

where V_{ij} is V_{LL} or V_{LR} based on the interaction being probed, Λ is the scale where the CI becomes relevant and $\sigma_{\text{SM-NP}}$ and σ_{NP} are the cross sections for the SM-NP interference and "pure" NP contributions, respectively. The simulations were performed using MadGraph at leading order (LO) with up to one additional parton, utilizing the model provided by the authors of [227]. For $\Lambda = 1\,\text{TeV}$ and $V_{ij} = \pm 4\pi$ and considering three generations of neutrinos, the computed cross section for the NP contribution for the LL (LR) operator is 384 fb (365 fb). The cross section of the SM-NP contribution for the LL (LR) operator is $\pm 17\,\text{fb}$ ($\mp 6.4\,\text{fb}$), wherein the '$+$' depicts constructive interference and '$-$' the destructive interference. These benchmark values can be used and adapted assuming that they scale the predicted cross sections but do not affect the kinematic distributions of the simulated events.

The distributions of the invariant mass of the two neutrinos show the characteristic pattern of the interference contributions with a discontinuity and a sign flip at the Z boson mass. The true $m(\nu,\nu)$ distribution for the interference and NP contributions are plotted in Figure 6.3 for the High-$E_{\text{T}}^{\text{miss}}$-2b and Boosted-2b analysis categories for both *LL* and *LR* operators.

While the interference contributions are predominantly below $m_{\nu\nu} < 500\,\text{GeV}$, the NP contributions, which are very similar for *LL* and *LR* operators, extend to higher values, well above 1 TeV. This might be a concern for the validity of the EFT approach, which requires that the energy scale of the point-like interaction being studied is well below the scale at which the new physics occurs[2]. To this end, a pragmatic "clipping" approach similar to the one used in [230] is used. Limits are set for three scenarios: full prediction, prediction with a cut $m_{\nu\nu} < 1\,\text{TeV}$ and $m_{\nu\nu} < 2\,\text{TeV}$.

The impact of a selection at $m_{\nu\nu} < 1\,\text{TeV}$ on the NN score distributions is shown in Figure 6.4 and Figure 6.5. The impact of clipping on the SM-NP (interference) contribution is minimal. However, the NP contribution reduces significantly. The biggest effect can be seen looking at events in the the last bin, yielding a reduction of $\sim 40\%$ in the High-$E_{\text{T}}^{\text{miss}}$-2b region and $\sim 50\%$ in the Boosted-2b analysis region. The clipping at 2 TeV is not shown as it rejects only a small fraction of events. This leads to a loss in sensitivity and therefore more conservative limits.

---

[2] In case the new physics is realized in s-channel (e.g. with a Z'-like boson), then signal events should have $m_{\nu\nu} < \Lambda_{\text{excl}}$, where Λ_{excl} is the exclusion limit for Λ. In case of t-channel (e.g. with a single LQ-like particle) constraints are less stringent.

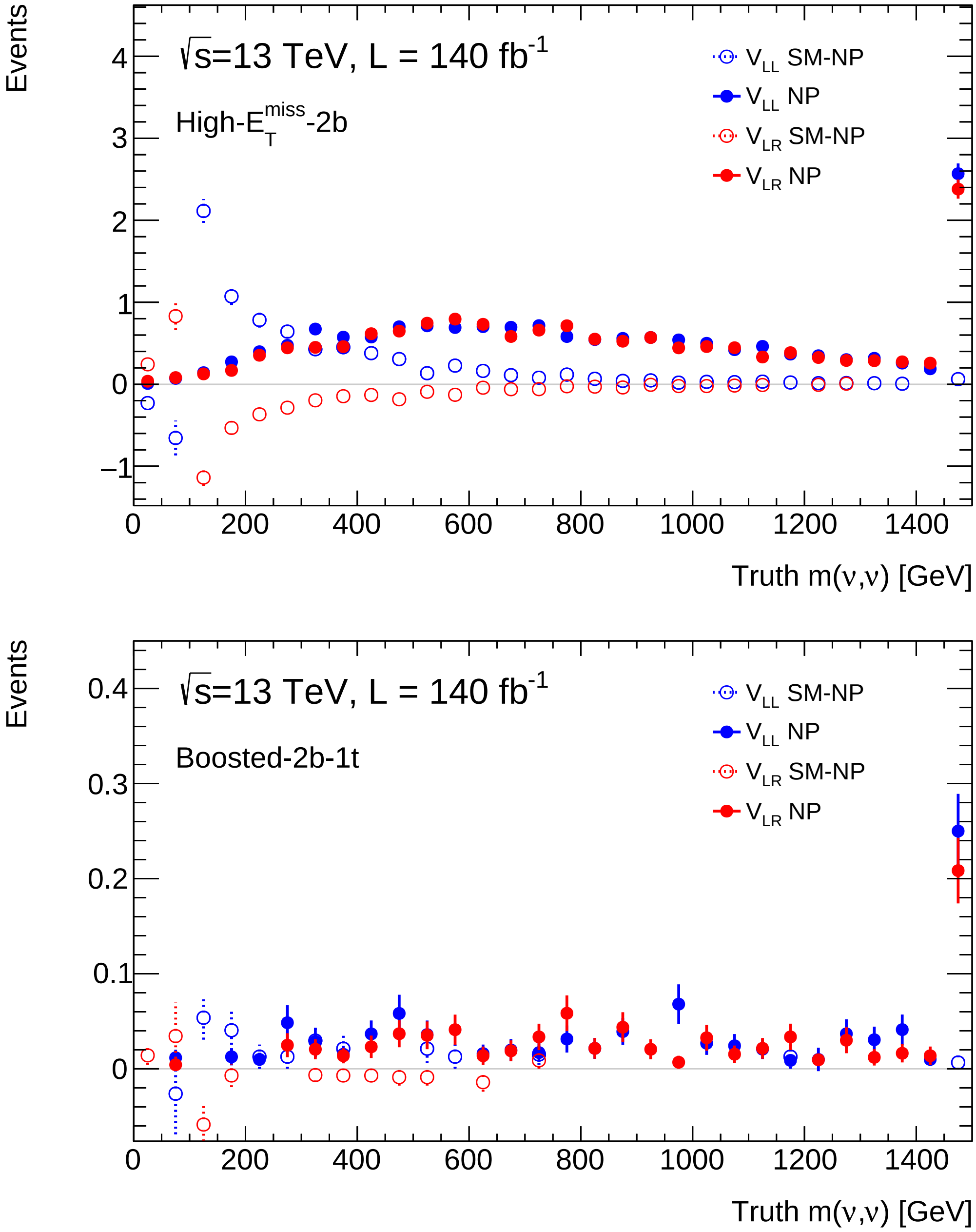

Figure 6.3: Distributions of $t\bar{t}\nu\bar{\nu}$ events in the High-$E_{\mathrm{T}}^{\mathrm{miss}}$-2b (top) and Boosted-2b-1t (bottom) categories showing the true invariant mass of the neutrinos from the $t\bar{t}\nu\bar{\nu}$ interaction, wherein the last bin includes overflow events.

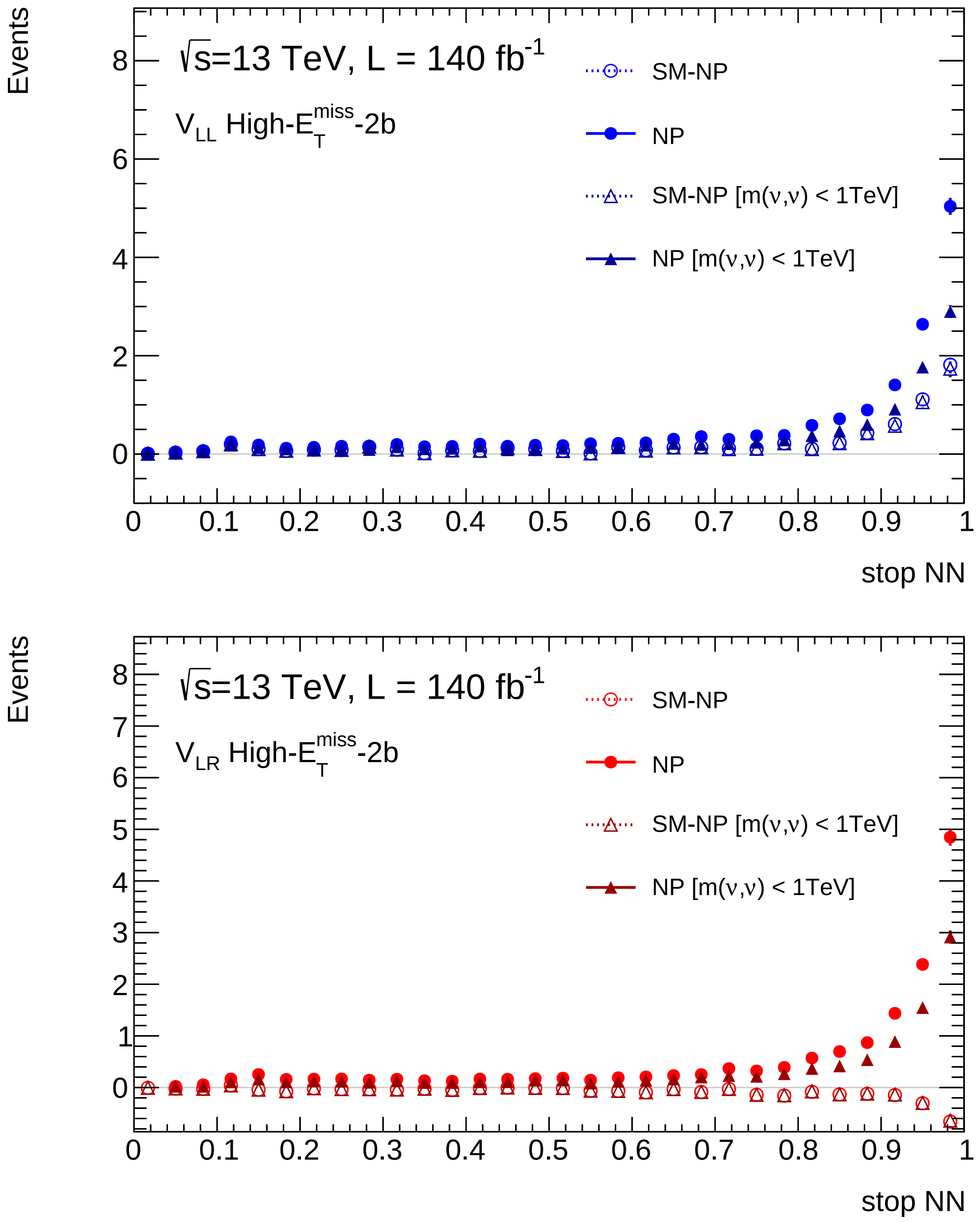

Figure 6.4: NN score distributions of $t\bar{t}\nu\bar{\nu}$ events in the High-$E_{\mathrm{T}}^{\mathrm{miss}}$ 2b category. The NP and the interference contributions for the *LL* and *LR* interactions are shown along with the distributions when a selection on the true invariant mass of the neutrinos below 1 TeV is applied.

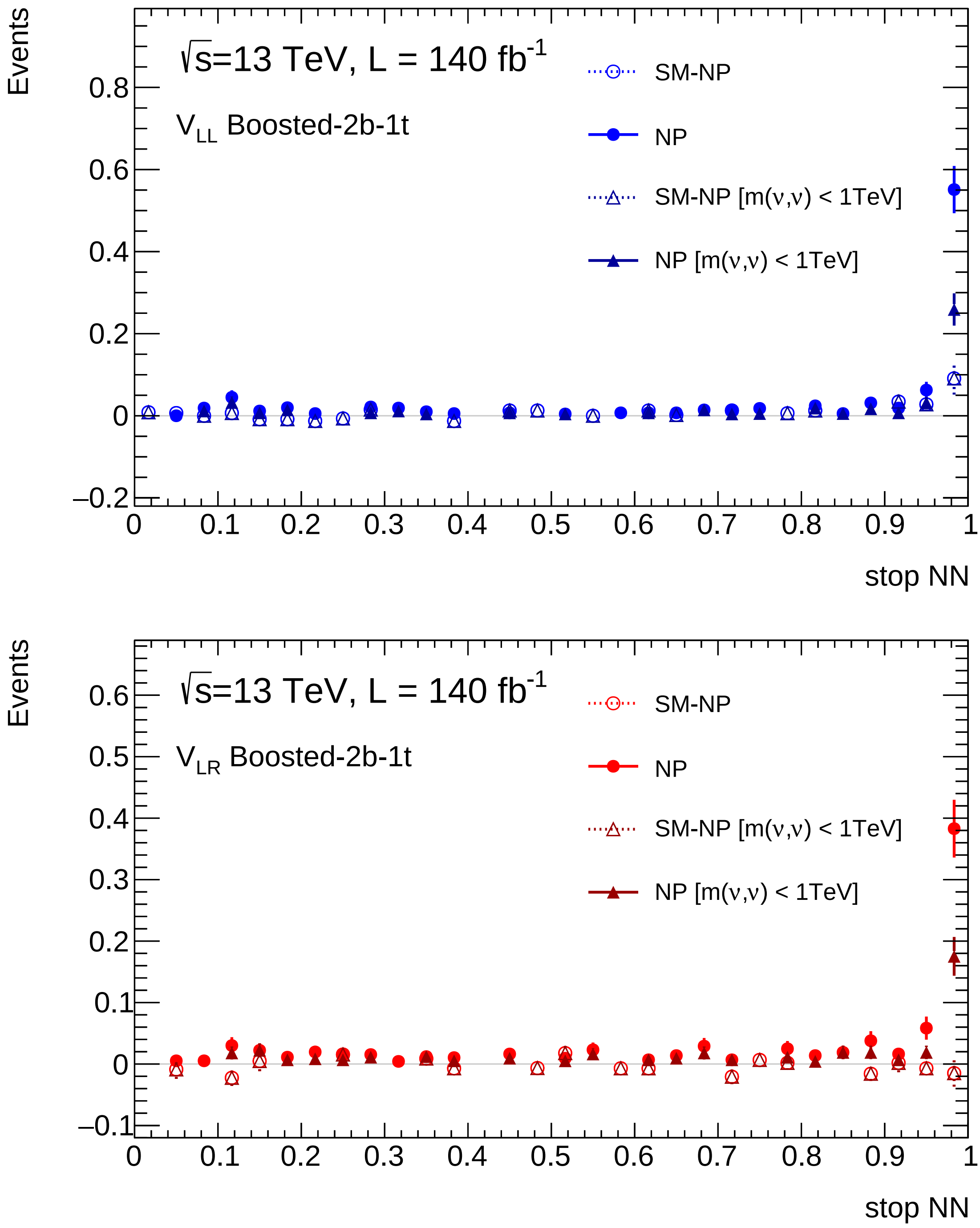

Figure 6.5: NN score distributions of $t\bar{t}\nu\bar{\nu}$ events in the Boosted-2b category. The NP and the interference contributions for the LL and LR interaction are shown along with the the distributions when a selection on the true invariant mass of the neutrinos below 1 TeV is applied.

As shown in [231], applying unitarity constrains weaken bounds on Wilson coefficients. The clipping approach yields conservative limits that are valid given the unitarity constraints of the EFT framework. In the case of visible leptons, a clipping could be done on reconstructed $m_{\ell\ell}$ but this is much more difficult in the case of neutrinos given that $E_{\mathrm{T}}^{\mathrm{miss}}$ only provides part of the picture. In this case, clipping the contribution using the true $m_{\nu\nu}$ distribution ensures that a unitarity violating signal is not incorrectly identified as new physics in this analysis. However, by clipping away a significant contribution of signal, the limits obtained can be conservative.

Fits are conducted using both stop and DM fit configurations. These fits categorize the contribution resulting from a new physics process probed using the $t\bar{t}\nu\bar{\nu}$ contact interaction (CI) operator as the signal contribution which is parametrized using the POI, $\mu = \frac{V_{ij}^2}{\Lambda^4}$. The signal cross-section is then expressed as:

$$\sigma_{\text{signal}} = \pm\sqrt{\mu}\,\sigma_{\text{SM-NP}} + \mu\,\sigma_{\text{NP}} \tag{6.5}$$

The “±” sign corresponds to the sign of the Wilson coefficient V_{ij}, determining whether the interference is constructive or destructive and limits are set for both scenarios. Given that the stop fit setup consists of eight SRs and the DM fit setup only of two SRs, the stop fit is found, as expected, to be more sensitive and is consequently employed for the final result.

6.3 Results

Table 6.1 shows the limits at 95% CL. The upper limits on $\mu = \frac{V_{ij}^2}{\Lambda^4}$ are converted into lower limits on Λ by assuming the magnitudes of the Wilson coefficients $|V_{ij}|$ to be 4π. Results are reported separately for V_{LL} and V_{LR} and for either constructive or destructive interferences. Results are also reported for a signal clipping at 1 TeV and 2 TeV.

The results yield lower limits on Λ around 2 TeV using the EFT approach without any clipping and similar to those with a clipping at 2 TeV. Hence, they fall within the regime where the EFT approach is applicable, given the minimal signal anticipated above $m_{\nu\bar{\nu}} > 2\,\text{TeV}$. The limits with a clipping are at 1 TeV are weaker given the reduced signal yield due to the clipping.

These limits are the first application of EFT to probe $t\bar{t}\nu\bar{\nu}$ operators, expanding the set of results where CIs have been used to examine other $qq\ell\ell$ operators [232–234]. While it is true that meaningful constraints can only be set when assuming $|V_{ij}| = 4\pi$, which is the maximal value of Wilson coefficients typically considered in EFT[3], these results have considerable future outlooks. In this EFT approach with only SM fields, the couplings of the operators with left-handed neutrinos are the same as the couplings of the operators with left-handed charged leptons, so one could eventually consider combining results from this search with the results from a future search for $tt\ell^{\pm}\ell^{\pm}$ CI. On the other hand, one could consider operators with right-handed neutrinos which would yield scalar and tensor operators at dimension six.

---

[3] Larger values of Wilson coefficients may cause the perturbative framework of calculations to break down.

These new operators would be sensitive to physics different from that which can be probed with the left-handed fields and only accessible via the $t\bar{t}$ +$E_{\mathrm{T}}^{\mathrm{miss}}$ final state.

Table 6.1: Constraints on effective $t\bar{t}\nu\bar{\nu}$ contact interactions involving all three generations of left-handed neutrinos based on the results of the stop search. Constraints are set independently for different effective vector operators and for different hypotheses about the sign of the Wilson coefficient which leads to a constructive or destructive interference with $t\bar{t}Z(\rightarrow \nu\bar{\nu})$. Observed (expected) limits at 95% CL are reported for $\sqrt{|V_{ij}|}/\Lambda$ and for Λ, for the full phase space and for specified regions of the true invariant mass of the neutrino pair, assuming $|V_{ij}| = 4\pi$. Limits corresponding to $\pm 1\sigma$ variations of the expected limits are also reported. This table is also published in [2].

Wilson coefficient	Observed (Expected) upper limit on $\sqrt{\lvert V_{ij}\rvert}/\Lambda$ [TeV $^{-1}$]	Observed (Expected) lower limit on Λ for $\lvert V_{ij}\rvert = 4\pi$ [TeV]
$V_{LL} > 0$	$1.59\ (1.44\ ^{+0.14}_{-0.13})$	$2.23\ (2.47\ ^{+0.24}_{-0.22})$
$m_{\nu\bar{\nu}} < 1\,\mathrm{TeV}$	$1.84\ (1.66\ ^{+0.16}_{-0.15})$	$1.93\ (2.14\ ^{+0.21}_{-0.19})$
$m_{\nu\bar{\nu}} < 2\,\mathrm{TeV}$	$1.62\ (1.46\ ^{+0.15}_{-0.10})$	$2.18\ (2.42\ ^{+0.24}_{-0.21})$
$V_{LL} < 0$	$1.66\ (1.52\ ^{+0.14}_{-0.12})$	$2.13\ (2.33\ ^{+0.20}_{-0.19})$
$m_{\nu\bar{\nu}} < 1\,\mathrm{TeV}$	$1.96\ (1.80\ ^{+0.15}_{-0.14})$	$1.81\ (1.97\ ^{+0.16}_{-0.15})$
$m_{\nu\bar{\nu}} < 2\,\mathrm{TeV}$	$1.70\ (1.56\ ^{+0.13}_{-0.12})$	$2.08\ (2.28\ ^{+0.19}_{-0.18})$
$V_{LR} > 0$	$1.67\ (1.53\ ^{+0.13}_{-0.13})$	$2.12\ (2.32\ ^{+0.21}_{-0.19})$
$m_{\nu\bar{\nu}} < 1\,\mathrm{TeV}$	$1.92\ (1.78\ ^{+0.16}_{-0.14})$	$1.84\ (1.99\ ^{+0.17}_{-0.17})$
$m_{\nu\bar{\nu}} < 2\,\mathrm{TeV}$	$1.70\ (1.56\ ^{+0.14}_{-0.12})$	$2.08\ (2.27\ ^{+0.20}_{-0.19})$
$V_{LR} < 0$	$1.63\ (1.49\ ^{+0.14}_{-0.13})$	$2.17\ (2.38\ ^{+0.22}_{-0.20})$
$m_{\nu\bar{\nu}} < 1\,\mathrm{TeV}$	$1.86\ (1.72\ ^{+0.17}_{-0.14})$	$1.91\ (2.06\ ^{+0.19}_{-0.18})$
$m_{\nu\bar{\nu}} < 2\,\mathrm{TeV}$	$1.66\ (1.52\ ^{+0.17}_{-0.12})$	$2.13\ (2.33\ ^{+0.21}_{-0.20})$

CHAPTER 7

Conclusions

In this thesis, a novel search for new physics in association with top-quark pairs using the complete ATLAS Run-2 pp dataset at $\sqrt{s} = 13\,\text{TeV}$ has been presented. Events compatible with the semileptonic decay of a pair of top quarks and the presence of missing transverse energy ($E_{\text{T}}^{\text{miss}}$) have been used for the search. Direct production of a pair of stop quarks and the production of spin-0 mediators in association with a pair of top quarks, that decay into dark matter particles, have been specifically probed. Additionally, effective $t\bar{t}\nu\bar{\nu}$ contact interactions have been explored as probes for new physics.

A novel inclusive analysis approach based on neural networks has been presented. This approach defines event categories using the multiplicities and kinematic properties of jets, b-tagged jets, and $E_{\text{T}}^{\text{miss}}$. Instead of focusing on specific signal model parameters, a comprehensive training across the parameter space has been performed, resulting in signal regions sensitive to a wide spectrum of new physics models simultaneously. Additionally, a novel method for reconstructing hadronic top-quark decays using neural networks has been developed.

Significant improvements in the sensitivity to stop-pair production have been achieved for the 1-lepton (1L) channel, especially in the region where the mass splitting between the stop quark and the neutralino, $\Delta m = m_{\tilde{t}} - m_{\tilde{\chi}_1^0}$ are close to the top quark mass, when compared to the previous 1L full Run-2 ATLAS result [4]. Large improvements in sensitivity to spin-0 mediators decaying to dark matter particles have also been observed across the parameter spectrum. No statistically significant deviations from the Standard Model (SM) expectation have been observed, leading to the establishment of exclusion limits at a 95% confidence level.

A simplified SUSY scenario wherein the stop quark and the neutralino are the lightest particles in the MSSM, and decoupled from the rest of the MSSM mass spectrum has been probed. Stop pair production has been studied wherein either a $\tilde{t}_1 \to t\tilde{\chi}_1^0$ or $\tilde{t}_1 \to bW\tilde{\chi}_1^0$ decay with a branching ratio of 100% is possible. Stop-quarks have been excluded for masses up to 1080 GeV, while neutralinos have been excluded for masses up to 600 GeV. The exclusion zones have expanded, with the maximum excluded neutralino mass increasing by about 80 GeV when compared to the previous 1L full Run-2 ATLAS result [4]. A combination has been performed using this new 1L result and the previous 0-lepton (0L) result [3] to provide the best limits for the search of stop pair production with the ATLAS Run-2 dataset [2].

In the search for dark matter, a simplified model for probing dark matter production in association with top-quark pairs has been used. A scalar or pseudoscalar particle serves as a mediator connecting the SM and dark sector. Assuming strengths of the couplings of the mediator to SM particles (g_q) and to dark matter particles (g_χ) as $g = g_q = g_\chi = 1$, models with scalar (pseudoscalar) mediators with masses up to 250 (300) GeV have been excluded. Additionally, at lower mediator masses, models with production cross sections as low as 0.19 (0.24) times the nominal predictions have been excluded. This new and improved 1L result has been used to provide a combined 0L+1L+2L ATLAS result for scalar and pseudoscalar mediators produced with top-quark pairs and decaying to dark matter [2]. The 1L result has provided the dominating contribution to the combined result.

The data has also been interpreted within the framework of effective $t\bar{t}\nu\bar{\nu}$ contact interactions. Assuming the maximal value of $|V_{ij}| = 4\pi$, lower limits on the energy scale of new physics Λ between 2.12 TeV and 2.23 TeV have been set. With a clipping at 1 TeV to ensure the validity of the EFT approach, weaker limits have been obtained. These limits serve as the first constraints using EFT to probe $t\bar{t}\nu\bar{\nu}$ operators.

What sets this analysis apart is the absence of dedicated signal region optimization for specific new physics models. This streamlined approach not only simplifies the analysis but also facilitates the re-use of this analysis for probing future models that yield the same final state. This has been demonstrated by yielding the first ever limits on the effective $t\bar{t}\nu\bar{\nu}$ contact interactions using networks trained for stop quark searches.

This analysis has shown how improved analysis techniques can enhance the reach of a previously explored dataset. It has yielded stronger exclusions in signal models that are challenging to probe and slight excesses in the statistically limited regime of high stop masses. Additionally, this simplified approach yields a straightforward validation of background modelling. This analysis has also benefited from the availability of new and improved modelling of top quark production processes during the course of this search.

The integration of Machine Learning techniques in searches for new physics is becoming increasingly important. This thesis stands as one of many projects advancing the application of ML in physics tasks. Exciting advancements in the use of neural networks for top quark reconstruction are ongoing, with the development of even more complex architectures than those presented in this thesis. The innovative exploration of the dataset being collected at the LHC with Machine Learning (ML) techniques is proving to be an intriguing way to understand the universe.

Bibliography

[1] ATLAS collaboration, *Search for new phenomena with top-quark pairs in final states with one lepton, jets and missing transverse momentum using 140* fb^{-1} *of data at* $\sqrt{s} = 13$ *TeV with the ATLAS detector*, Tech. Rep. ATLAS-CONF-2023-043, CERN, Geneva (2023).

[2] The ATLAS Collaboration, *Search for new phenomena with top-quark pairs and large missing transverse momentum using* $140 fb^{-1}$ *of pp collision data at* $\sqrt{s} = 13\,\mathrm{TeV}$ *with the ATLAS detector*, *Journal of High Energy Physics* **2024** (2024) .

[3] ATLAS Collaboration, *Search for a scalar partner of the top quark in the all-hadronic* $t\bar{t}$ *plus missing transverse momentum final state at* $\sqrt{s} = 13$ *TeV with the ATLAS detector*, *Eur. Phys. J. C* **80** (2020) 737 [`arXiv:2004.14060`].

[4] ATLAS Collaboration, *Search for new phenomena with top quark pairs in final states with one lepton, jets, and missing transverse momentum in pp collisions at* $\sqrt{s} = 13$ *TeV with the ATLAS detector*, *JHEP* **04** (2020) 174 [`arXiv:2012.03799`].

[5] ATLAS Collaboration, *Search for new phenomena in events with two opposite-charge leptons, jets and missing transverse momentum in pp collisions at* $\sqrt{s} = 13$ *TeV with the ATLAS detector*, *JHEP* **04** (2021) 165 [`arXiv:2102.01444`].

[6] ATLAS Collaboration, *Constraints on spin-0 dark matter mediators and invisible Higgs decays using ATLAS 13 TeV pp collision data with two top quarks and missing transverse momentum in the final state*, *Eur. Phys. J. C* **83** (2023) 503 [`arXiv:2211.05426`].

[7] CMS Collaboration, *Search for top squark production in fully-hadronic final states in proton–proton collisions at* $\sqrt{s} = 13$ *TeV*, *Phys. Rev. D* **104** (2021) 052001 [`arXiv:2103.01290`].

[8] CMS Collaboration, *Search for direct top squark pair production in events with one lepton, jets, and missing transverse momentum at* 13 *TeV with the CMS experiment*, *JHEP* **05** (2020) 032 [`arXiv:1912.08887`].

[9] CMS Collaboration, *Search for top squark pair production using dilepton final states in pp collision data collected at sqrts* $=$ 13 *TeV*, *Eur. Phys. J. C* **81** (2021) 3 [`arXiv:2008.05936`].

[10] CMS Collaboration, *Combined searches for the production of supersymmetric top quark partners in proton–proton collisions at* $\sqrt{s} = 13$ *TeV*, *Eur. Phys. J. C* **81** (2021) 970 [`arXiv:2107.10892`].

[11] D. Griffiths, *Introduction to Elementary Particles*, John Wiley & Sons, New York, USA (1987).

[12] R.L.e.a. Workman, *Review of Particle Physics*, *Progress of Theoretical and Experimental Physics* **2022** (2022) .

[13] E. Noether, *Invariante Variationsprobleme*, *Nachrichten von der Gesellschaft der Wissenschaften zu Göttingen. Mathematisch-Physikalische Klasse* (1918) 235.

[14] S.L. Glashow, *Partial-symmetries of weak interactions*, *Nuclear Physics* **22** (1961) 579.

[15] A. Salam and J. Ward, *Electromagnetic and weak interactions*, *Physics Letters* **13** (1964) 168.

[16] F. Englert and R. Brout, *Broken Symmetry and the Mass of Gauge Vector Mesons*, *Physical Review Letters* **13** (1964) 321–323.

[17] P. Higgs, *Broken symmetries, massless particles and gauge fields*, *Physics Letters* **12** (1964) 132–133.

[18] P.W. Higgs, *Broken Symmetries and the Masses of Gauge Bosons*, *Physical Review Letters* **13** (1964) 508–509.

[19] P.W. Higgs, *Spontaneous Symmetry Breakdown without Massless Bosons*, *Physical Review* **145** (1966) 1156–1163.

[20] G.S. Guralnik, C.R. Hagen and T.W.B. Kibble, *Global Conservation Laws and Massless Particles*, *Physical Review Letters* **13** (1964) 585–587.

[21] F. Englert, R. Brout and M.F. Thiry, *Vector mesons in presence of broken symmetry*, *Il Nuovo Cimento A Series 10* **43** (1966) 244–257.

[22] T.W.B. Kibble, *Symmetry Breaking in Non-Abelian Gauge Theories*, *Phys. Rev.* **155** (1967) 1554.

[23] S. Weinberg, *A Model of Leptons*, *Phys. Rev. Lett.* **19** (1967) 1264.

[24] M. Thomson, *Modern Particle Physics*, Cambridge University Press (2013).

[25] F. Halzen, A.D. Martin and N. Mitra, *Quarks and Leptons: An Introductory Course in Modern Particle Physics*, *American Journal of Physics* **53** (1985) 287.

[26] M.E. Peskin and D.V. Schroeder, *An Introduction to Quantum Field Theory*, Westview Press (1995).

[27] G. Busoni, *The Standard Model Lagrangian (Yukawa sector)*, 2023.

[28] N. Aghanim, Y. Akrami, M. Ashdown, J. Aumont, C. Baccigalupi, M. Ballardini et al., *Planck2018 results: VI. Cosmological parameters*, *Astronomy & Astrophysics* **641** (2020) A6.

[29] U. Amaldi, W. de Boer and H. Fürstenau, *Comparison of grand unified theories with electroweak and strong coupling constants measured at LEP*, *Physics Letters B* **260** (1991) 447–455.

[30] D.I. Kazakov, *Beyond the Standard Model (In Search of Supersymmetry)*, 2001. `arXiv:hep-ph/0012288`.

[31] S.P. MARTIN, *A SUPERSYMMETRY PRIMER*, in *Perspectives on Supersymmetry*, pp. 1–98, WORLD SCIENTIFIC (1998), DOI.

[32] I. Melzer-Pellmann and P. Pralavorio, *Lessons for SUSY from the LHC after the first run*, *The European Physical Journal C* **74** (2014) .

[33] G. Weiglein, *The MSSM at present and future colliders*, 2000. `arXiv:hep-ph/0001044`.

[34] G. Isidori and D.M. Straub, *Minimal flavour violation and beyond*, *The European Physical Journal C* **72** (2012) .

[35] L. Girardello and M. Grisaru, *Soft breaking of supersymmetry*, *Nuclear Physics B* **194** (1982) 65.

[36] N. Polonsky, *The μ-Parameter of Supersymmetry*, 1999. `arXiv:hep-ph/9911329`.

[37] T. Aaltonen, A. Abulencia, J. Adelman, A. Affolder, T. Akimoto, M. Albrow et al., *Searches for direct pair production of supersymmetric top and supersymmetric bottom quarks in p^+p^- collisions at s = 1.96 TeV*, *Physical Review D* **76** (2007) .

[38] F. Zwicky, *Die Rotverschiebung von extragalaktischen Nebeln*, *Helvetica Physica Acta* **6** (1933) 110.

[39] V.C. Rubin, N. Thonnard and J. Ford, W. K., *Rotational properties of 21 SC galaxies with a large range of luminosities and radii, from NGC 4605 /R = 4kpc/ to UGC 2885 /R = 122 kpc/*, *The Astrophysical Journal* **238** (1980) 471.

[40] D. Clowe, A. Gonzalez and M. Markevitch, *Weak-Lensing Mass Reconstruction of the Interacting Cluster 1E 0657–558: Direct Evidence for the Existence of Dark Matter**, *The Astrophysical Journal* **604** (2004) 596.

[41] P.A.R. Ade, N. Aghanim, M. Arnaud, M. Ashdown, J. Aumont, C. Baccigalupi et al., *Planck2015 results: XIII. Cosmological parameters*, *Astronomy &; Astrophysics* **594** (2016) A13.

[42] T. Lin, *TASI lectures on dark matter models and direct detection*, 2019. `arXiv:1904.07915`.

[43] M. Milgrom, *A modification of the Newtonian dynamics as a possible alternative to the hidden mass hypothesis*, *The Astrophysical Journal* **270** (1983) 365.

[44] A. Arbey and F. Mahmoudi, *Dark matter and the early Universe: A review*, *Progress in Particle and Nuclear Physics* **119** (2021) 103865.

[45] D. Abercrombie et al., *Dark Matter benchmark models for early LHC Run-2 Searches: Report of the ATLAS/CMS Dark Matter Forum*, *Phys. Dark Univ.* **27** (2020) 100371.

[46] M.R. Buckley, D. Feld and D. Gonçalves, *Scalar simplified models for Dark Matter*, *Phys. Rev. D* **91** (2015) 015017.

[47] The ATLAS Collaboration, *Constraints on mediator-based dark matter and scalar dark energy models using* $\sqrt{s} = 13$ *TeV pp collision data collected by the ATLAS detector*, *Journal of High Energy Physics* **2019** (2019) .

[48] *LEP design report*, Report, CERN, Geneva (1984), https://cds.cern.ch/record/102083.

[49] T. Berners-Lee, R. Cailliau, J. Groff and B. Pollermann, *World-Wide Web: The Information Universe*, *Internet Research* **2** (1992) 52–58.

[50] L. Evans and P. Bryant, *LHC Machine*, *Journal of Instrumentation* **3** (2008) S08001.

[51] The ATLAS Collaboration, *The ATLAS experiment at the CERN large hadron collider*, *Journal of Instrumentation* **3** (2008) S08003.

[52] The CMS Collaboration, *The CMS experiment at the CERN LHC*, *Journal of Instrumentation* **3** (2008) S08004.

[53] The ALICE Collaboration, *The ALICE experiment at the CERN LHC*, *Journal of Instrumentation* **3** (2008) S08002.

[54] The LHCb Collaboration, *The LHCb detector at the LHC*, *Journal of Instrumentation* **3** (2008) S08005.

[55] The TOTEM Collaboration, *The TOTEM Experiment at the CERN Large Hadron Collider*, *Journal of Instrumentation* **3** (2008) S08007.

[56] The LHCf Collaboration, *The LHCf detector at the CERN Large Hadron Collider*, *Journal of Instrumentation* **3** (2008) S08006.

[57] MoEDAL collaboration, *Technical Design Report of the MoEDAL Experiment*, Tech. Rep. CERN-LHCC-2009-006, MoEDAL-TDR-001 (2009).

[58] P.A. et al, *The COMPASS experiment at CERN*, *Nuclear Instruments and Methods in Physics Research Section A: Accelerators, Spectrometers, Detectors and Associated Equipment* **577** (2007) 455.

[59] N.e.a. Abgrall, *NA61/SHINE facility at the CERN SPS: beams and detector system*, *Journal of Instrumentation* **9** (2014) P06005–P06005.

[60] S. Maury, *The Antiproton Decelerator (AD)*, *Hyperfine Interactions* **109** (1997) .

[61] W. Oelert, *The ELENA Project at CERN*, *Acta Physica Polonica B* **46** (2015) 181.

[62] G. Audi et al., *The NUBASE2016 evaluation of nuclear properties*, *Chinese Physics C* **41** (2017) 030001.

[63] G. Barreau et al., *MEDICIS-Promed: A new facility for the production of innovative radionuclides for medical research*, *EPJ Web of Conferences* **131** (2016) 08001.

[64] F. Gunsing et al., *The n_TOF facility: Neutron beams for challenging measurements*, *European Physical Journal A* **55** (2019) 4.

[65] M. Aguilar et al., *The Alpha Magnetic Spectrometer (AMS) on the International Space Station: Part I – Results from the test flight on the space shuttle*, *Physics Reports* **366** (2002) 331.

[66] S. Andriamonje et al., *An improved limit on the axion–photon coupling from the CAST experiment*, *Journal of Cosmology and Astroparticle Physics* **2007** (2007) 010.

[67] P. Pugnat et al., *First results from the OSQAR photon regeneration experiment*, *Physics Letters B* **681** (2009) 8.

[68] E. Lopienska, *The CERN accelerator complex, layout in 2022. Complexe des accélérateurs du CERN en janvier 2022*, .

[69] B. Salvachua, *Overview of Proton-Proton Physics during Run 2*, .

[70] F. Siegert, *Monte-Carlo Event Generation for the LHC*, Ph.D. thesis, Durham University, 2010.

[71] J. Elmsheuser and A. Di Girolamo, *Overview of the ATLAS distributed computing system*, *EPJ Web of Conferences* **214** (2019) 03010.

[72] T. Maeno, K. De, T. Wenaus, P. Nilsson, G.A. Stewart, R. Walker et al., *Overview of ATLAS PanDA Workload Management*, *Journal of Physics: Conference Series* **331** (2011) 072024.

[73] V. Garonne, M. Barisits, T. Beermann, M. Lassnig, C. Serfon, W. Guan et al., *Experiences with the new ATLAS Distributed Data Management System*, *Journal of Physics: Conference Series* **898** (2017) 062019.

[74] Worldwide LHC Computing Grid, *Worldwide lhc computing grid*, 2024.

[75] J. Pequenao, “Computer generated image of the whole ATLAS detector.” `https://cds.cern.ch/record/1095924`, 2008.

[76] I. Neutelings, “Images from tikz.net.”

[77] L. Masetti, *ATLAS Inner Detector: Commissioning with Cosmics Data*, *European Physical Society Europhysics Conference on High Energy Physics* (2010) .

[78] J. Pequenao, "Computer generated image of the ATLAS inner detector." `https://cds.cern.ch/record/1095926`, 2008.

[79] T.A. et al, *Status of design and construction of the Transition Radiation Tracker (TRT) for the ATLAS experiment at the LHC*, *Nuclear Instruments and Methods in Physics Research Section A: Accelerators, Spectrometers, Detectors and Associated Equipment* **522** (2004) 131.

[80] A. "Vogel, *ATLAS Transition Radiation Tracker (TRT): Straw Tube Gaseous Detectors at High Rates*, Tech. Rep. ATL-INDET-PROC-2013-005, CERN, Geneva (2013).

[81] ATLAS collaboration, *Operational Experience of the ATLAS SCT and Pixel Detector*, .

[82] A. Bingül, *The ATLAS TRT and its Performance at LHC*, *Journal of Physics: Conference Series* **347** (2012) 012025.

[83] J. Pequenao, "Computer Generated image of the ATLAS calorimeter." `https://cds.cern.ch/record/1095927`, 2008.

[84] P. Puzo, *ATLAS calorimetry*, *Nuclear Instruments and Methods in Physics Research Section A: Accelerators, Spectrometers, Detectors and Associated Equipment* **494** (2002) 340.

[85] N. Amram and E. Etzion, *Hough Transform Track Reconstruction in the Cathode Strip Chambers in ATLAS*, .

[86] The ATLAS Collaboration, *Commissioning of the ATLAS Muon Spectrometer with cosmic rays*, *The European Physical Journal C* **70** (2010) 875–916.

[87] H. ten Kate, *The ATLAS superconducting magnet system at the Large Hadron Collider*, *Physica C: Superconductivity* **468** (2008) 2137.

[88] A. Yamamoto, Y. Makida, R. Ruber, Y. Doi, T. Haruyama, F. Haug et al., *The ATLAS central solenoid*, *Nuclear Instruments and Methods in Physics Research Section A: Accelerators, Spectrometers, Detectors and Associated Equipment* **584** (2008) 53.

[89] T.A. collaboration, *Operation of the ATLAS trigger system in Run 2*, *Journal of Instrumentation* **15** (2020) P10004.

[90] ATLAS Collaboration, *2015 start-up trigger menu and initial performance assessment of the ATLAS trigger using Run-2 data*, Tech. Rep. ATL-DAQ-PUB-2016-001, CERN, Geneva (2016).

[91] ATLAS Collaboration, *Trigger Menu in 2016*, Tech. Rep. ATL-DAQ-PUB-2017-001, CERN, Geneva (2017).

[92] ATLAS Collaboration, *Trigger Menu in 2017*, Tech. Rep. ATL-DAQ-PUB-2018-002, CERN, Geneva (2018).

[93] ATLAS Collaboration, *Trigger menu in 2018*, Tech. Rep. ATL-DAQ-PUB-2019-001, CERN, Geneva (2019).

[94] The ATLAS Collaboration, *Luminosity determination in pp collisions at $\sqrt{s} = 13$ tev using the atlas detector at the lhc*, *The European Physical Journal C* **83** (2023) 982.

[95] ATLAS Collaboration, "Integrated luminosity versus time (run 2)." `https://atlas.web.cern.ch/Atlas/GROUPS/DATAPREPARATION/PublicPlots/2018/DataSummary/figs/intlumivstimeRun2.png`, 2018.

[96] ATLAS Collaboration, "Mean number of interactions per bunch crossing (2015-2018)." `https://atlas.web.cern.ch/Atlas/GROUPS/DATAPREPARATION/PublicPlots/2018/DataSummary/figs/mu_2015_2018.png`, 2018.

[97] J. Bauer and T. Muller, *Prospects for the observation of electroweak top quark production with the cms experiment*, .

[98] G. Altarelli and G. Parisi, *Asymptotic freedom in parton language*, *Nuclear Physics B* **126** (1977) 298–318.

[99] G. Altarelli, *Partons in quantum chromodynamics*, *Physics Reports* **81** (1982) 1–129.

[100] V.N. Gribov and L.N. Lipatov, *Deep inelastic ep scattering in perturbation theory*, https://cds.cern.ch/record/427157*Sov. J. Nucl. Phys.* **15** (1972) 438.

[101] Y.L. Dokshitzer, *Calculation of the Structure Functions for Deep Inelastic Scattering and e^+e^- Annihilation by Perturbation Theory in Quantum Chromodynamics*, *Soviet Physics JETP* **46** (1977) 641.

[102] S. Catani, F. Krauss, B.R. Webber and R. Kuhn, *Qcd matrix elements + parton showers*, *Journal of High Energy Physics* **2001** (2001) 063–063.

[103] S. Höche, F. Krauss, S. Schumann and F. Siegert, *Qcd matrix elements and truncated showers*, *Journal of High Energy Physics* **2009** (2009) 053–053 [`arXiv:0903.1219`].

[104] S.A. et al, *Geant4—a simulation toolkit*, *Nuclear Instruments and Methods in Physics Research Section A: Accelerators, Spectrometers, Detectors and Associated Equipment* **506** (2003) 250.

[105] The ATLAS Collaboration, *The ATLAS Simulation Infrastructure*, *The European Physical Journal C* **70** (2010) 823.

[106] J. Pequenao and P. Schaffner, "How ATLAS detects particles: diagram of particle paths in the detector." `https://cds.cern.ch/record/1505342`, 2013.

[107] ATLAS Collaboration, *The atlas inner detector commissioning and calibration*, *The European Physical Journal C* **70** (2010) 787–821.

[108] The ATLAS Collaboration, *Electron reconstruction and identification in the ATLAS experiment using the 2015 and 2016 LHC proton–proton collision data at* $\sqrt{s} = 13\,\text{TeV}$, *The European Physical Journal C* **79** (2019) .

[109] F. Cavallari, *Performance of calorimeters at the lhc*, *Journal of Physics: Conference Series* **293** (2011) 012001.

[110] Straessner, Arno, *The ATLAS and CMS Experiments at the LHC*, in *Electroweak Physics at LEP and LHC*, pp. 137–165, Springer Berlin Heidelberg (2010), DOI.

[111] A. Collaboration, "Tracking tutorial."

[112] ATLAS Collaboration, *Electron and photon performance measurements with the ATLAS detector using the 2015–2017 LHC proton–proton collision data*, *JINST* **14** (2019) P12006 [`arXiv:1908.00005`].

[113] "Electron efficiency with full Run2."
`https://atlas.web.cern.ch/Atlas/GROUPS/PHYSICS/PLOTS/EGAM-2022-02`, 2022.

[114] M. Cacciari, G.P. Salam and G. Soyez, *The anti-*k_t *jet clustering algorithm*, *JHEP* **04** (2008) 063 [`arXiv:0802.1189`].

[115] C. Collaboration, *Jets in CMS and the Determination of Their Energy Scale*, 2024.

[116] M. Cacciari, G.P. and G. Soyez, *FastJet user manual*, *Eur. Phys. J. C* **72** (2012) 1896 [`arXiv:1111.6097`].

[117] *Characterisation and mitigation of beam-induced backgrounds observed in the atlas detector during the 2011 proton-proton run*, *Journal of Instrumentation* **8** (2013) P07004.

[118] ATLAS Collaboration, *Performance of pile-up mitigation techniques for jets in pp collisions at* $\sqrt{s} = 8$ *TeV using the ATLAS detector*, *Eur. Phys. J. C* **76** (2016) 581 [`arXiv:1510.03823`].

[119] ATLAS collaboration, *Forward jet vertex tagging using the particle flow algorithm*, Tech. Rep. ATL-PHYS-PUB-2019-026, CERN, Geneva (2019).

[120] ATLAS Collaboration, *Optimisation of large-radius jet reconstruction for the ATLAS detector in* 13 *TeV proton–proton collisions*, *Eur. Phys. J. C* **81** (2020) 334 [`arXiv:2009.04986`].

[121] T. Barillari et al., *Local Hadronic Calibration*, Tech. Rep. ATL-LARG-PUB-2009-001-2, ATL-COM-LARG-2008-006, ATL-LARG-PUB-2009-001, CERN, Geneva (2008).

[122] D. Krohn, J. Thaler and L.-T. Wang, *Jet Trimming*, *JHEP* **02** (2010) 084 [`arXiv:0912.1342`].

[123] D. Krohn, J. Thaler and L.-T. Wang, *Jets with Variable R*, *JHEP* **06** (2009) 059 [`arXiv:0903.0392`].

[124] E. Hansen, "Jet Reconstruction and Calibration in ATLAS." `https://indico.cern.ch/event/868940/contributions/3813697/`, July 31, 2020.

[125] ATLAS Collaboration, *Jet energy scale and resolution measured in proton–proton collisions at $\sqrt{s} = 13$ TeV with the ATLAS detector*, *Eur. Phys. J. C* **81** (2020) 689 [`arXiv:2007.02645`].

[126] ATLAS collaboration, *Performance of the ATLAS Secondary Vertex b-tagging Algorithm in 900 GeV Collision Data*, Tech. Rep. ATLAS-CONF-2010-004, CERN, Geneva (2010).

[127] ATLAS Collaboration, *ATLAS b-jet identification performance and efficiency measurement with $t\bar{t}$ events in pp collisions at $\sqrt{s} = 13$ TeV*, *Eur. Phys. J. C* **79** (2019) 970 [`arXiv:1907.05120`].

[128] ATLAS Collaboration, *ATLAS flavour-tagging algorithms for the LHC Run 2 pp collision dataset*, `arXiv:2211.16345`.

[129] ATLAS collaboration, *Calibration of the ATLAS b-tagging algorithm in $t\bar{t}$ semi-leptonic events*, Tech. Rep. ATLAS-CONF-2018-045, CERN, Geneva (2018).

[130] The ATLAS Collaboration, *Atlas flavour-tagging algorithms for the lhc run 2 pp collision dataset*, *The European Physical Journal C* **83** (2023) .

[131] S. Rettie, *Muon identification and performance in the ATLAS experiment*, Tech. Rep. ATL-PHYS-PROC-2018-052, CERN, Geneva (2018), DOI.

[132] ATLAS Collaboration, *Muon reconstruction performance of the ATLAS detector in proton–proton collision data at $\sqrt{s} = 13$ TeV*, *Eur. Phys. J. C* **76** (2016) 292 [`arXiv:1603.05598`].

[133] ATLAS Collaboration, *Muon reconstruction and identification efficiency in ATLAS using the full Run 2 pp collision data set at $\sqrt{s} = 13$ TeV*, *Eur. Phys. J. C* **81** (2021) 578 [`arXiv:2012.00578`].

[134] ATLAS collaboration, *Reconstruction, Identification, and Calibration of hadronically decaying tau leptons with the ATLAS detector for the LHC Run 3 and reprocessed Run 2 data*, Tech. Rep. ATL-PHYS-PUB-2022-044, CERN, Geneva (2022).

[135] ATLAS collaboration, *Measurement of the tau lepton reconstruction and identification performance in the ATLAS experiment using pp collisions at $\sqrt{s} = 13$ TeV*, Tech. Rep. ATLAS-CONF-2017-029, CERN, Geneva (2017).

[136] ATLAS collaboration, *Performance of missing transverse momentum reconstruction for the ATLAS detector in the first proton-proton collisions at at $\sqrt{s} = 13$ TeV*, Tech. Rep. ATL-PHYS-PUB-2015-027, CERN, Geneva (2015).

[137] The ATLAS Collaboration, *Performance of missing transverse momentum reconstruction with the ATLAS detector using proton–proton collisions at $\sqrt{s}$= 13 TeV*, *The European Physical Journal C* **78** (2018) .

[138] ATLAS collaboration, *Object-based missing transverse momentum significance in the ATLAS detector*, Tech. Rep. ATLAS-CONF-2018-038, CERN, Geneva (2018).

[139] ATLAS collaboration, *Top cross section summary plots - November 2023*, Tech. Rep. ATL-PHYS-PUB-2023-038, CERN, Geneva (2023).

[140] C. Borschensky, M. Krämer, A. Kulesza, M. Mangano, S. Padhi, T. Plehn et al., *Squark and gluino production cross sections in pp collisions at $\sqrt{s} = 13$, 14, 33 and 100 TeV*, *The European Physical Journal C* **74** (2014) .

[141] U. Haisch, P. Pani and G. Polesello, *Determining the CP nature of spin-0 mediators in associated production of dark matter and pairs*, *Journal of High Energy Physics* **2017** (2017) 131.

[142] Particle Data Group collaboration, *Review of Particle Physics*, *PTEP* **2022** (2022) 083C01.

[143] F. Déliot and P.V. Mulders, *Top quark physics at the LHC*, *Comptes Rendus. Physique* **21** (2020) 45.

[144] ATLAS collaboration, *Production of electroweak bosons in association with jets with the ATLAS detector. Production of electroweak bosons in association with jets with the ATLAS detector*, Tech. Rep. ATL-PHYS-PROC-2017-225, CERN, Geneva (2017).

[145] G.J. Besjes, M. Baak, D. Côté, A. Koutsman, J.M. Lorenz and D. Short, *HistFitter: a flexible framework for statistical data analysis*, *Journal of Physics: Conference Series* **664** (2015) 072004.

[146] K. Albertsson, P. Altoe, D. Anderson, J. Anderson, M. Andrews, J.P.A. Espinosa et al., *Machine learning in high energy physics community white paper*, 2019. `arXiv:1807.02876`.

[147] T. Wiederer, “Neural Networks in Javascript.” Retrieved from `https://webkid.io/blog/neural-networks-in-javascript/`, 2016.

[148] S. Ruder, *An overview of gradient descent optimization algorithms*, 2017. `arXiv:1609.04747`.

[149] D. Gonçalves, D. López-Val, K. Mawatari and T. Plehn, *Automated third generation squark production to next-to-leading order*, *Phys. Rev. D* **90** (2014) 075007.

[150] E. Bothmann et al., *Event generation with Sherpa 2.2*, *SciPost Phys.* **7** (2019) 034 [`arXiv:1905.09127`].

[151] S. Schumann and F. Krauss, *A parton shower algorithm based on Catani–Seymour dipole factorisation*, *JHEP* **03** (2008) 038 [`arXiv:0709.1027`].

[152] S. Höche, F. Krauss, M. Schönherr and F. Siegert, *A critical appraisal of NLO+PS matching methods*, *JHEP* **09** (2012) 049 [`arXiv:1111.1220`].

[153] S. Höche, F. Krauss, M. Schönherr and F. Siegert, *QCD matrix elements + parton showers. The NLO case*, *JHEP* **04** (2013) 027 [`arXiv:1207.5030`].

[154] T. Gleisberg and S. Höche, *Comix, a new matrix element generator*, *JHEP* **12** (2008) 039 [`arXiv:0808.3674`].

[155] F. Buccioni, J.-N. Lang, J.M. Lindert, P. Maierhöfer, S. Pozzorini, H. Zhang et al., *OpenLoops 2*, *Eur. Phys. J. C* **79** (2019) 866 [`arXiv:1907.13071`].

[156] F. Cascioli, P. Maierhöfer and S. Pozzorini, *Scattering Amplitudes with Open Loops*, *Phys. Rev. Lett.* **108** (2012) 111601 [`arXiv:1111.5206`].

[157] A. Denner, S. Dittmaier and L. Hofer, *COLLIER: A fortran-based complex one-loop library in extended regularizations*, *Comput. Phys. Commun.* **212** (2017) 220 [`arXiv:1604.06792`].

[158] The NNPDF Collaboration, R.D. Ball et al., *Parton distributions for the LHC run II*, *JHEP* **04** (2015) 040 [`arXiv:1410.8849`].

[159] M. Beneke, P. Falgari, S. Klein and C. Schwinn, *Hadronic top-quark pair production with NNLL threshold resummation*, *Nucl. Phys. B* **855** (2012) 695 [`arXiv:1109.1536`].

[160] M. Cacciari, M. Czakon, M. Mangano, A. Mitov and P. Nason, *Top-pair production at hadron colliders with next-to-next-to-leading logarithmic soft-gluon resummation*, *Phys. Lett. B* **710** (2012) 612 [`arXiv:1111.5869`].

[161] P. Bärnreuther, M. Czakon and A. Mitov, *Percent-Level-Precision Physics at the Tevatron: Next-to-Next-to-Leading Order QCD Corrections to $q\bar{q} \to t\bar{t} + X$*, *Phys. Rev. Lett.* **109** (2012) 132001 [`arXiv:1204.5201`].

[162] M. Czakon and A. Mitov, *NNLO corrections to top-pair production at hadron colliders: the all-fermionic scattering channels*, *JHEP* **12** (2012) 054 [`arXiv:1207.0236`].

[163] M. Czakon and A. Mitov, *NNLO corrections to top pair production at hadron colliders: the quark-gluon reaction*, *JHEP* **01** (2013) 080 [`arXiv:1210.6832`].

[164] M. Czakon, P. Fiedler and A. Mitov, *Total Top-Quark Pair-Production Cross Section at Hadron Colliders Through $O(\alpha_S^4)$*, *Phys. Rev. Lett.* **110** (2013) 252004 [`arXiv:1303.6254`].

[165] M. Czakon and A. Mitov, *Top++: A program for the calculation of the top-pair cross-section at hadron colliders*, Comput. Phys. Commun. **185** (2014) 2930 [`arXiv:1112.5675`].

[166] E. Re, *Single-top Wt-channel production matched with parton showers using the POWHEG method*, Eur. Phys. J. C **71** (2011) 1547 [`arXiv:1009.2450`].

[167] P. Nason, *A new method for combining NLO QCD with shower Monte Carlo algorithms*, JHEP **11** (2004) 040 [`arXiv:hep-ph/0409146`].

[168] S. Frixione, P. Nason and C. Oleari, *Matching NLO QCD computations with parton shower simulations: the POWHEG method*, JHEP **11** (2007) 070 [`arXiv:0709.2092`].

[169] S. Alioli, P. Nason, C. Oleari and E. Re, *A general framework for implementing NLO calculations in shower Monte Carlo programs: the POWHEG BOX*, JHEP **06** (2010) 043 [`arXiv:1002.2581`].

[170] T. Sjöstrand, S. Ask, J.R. Christiansen, R. Corke, N. Desai, P. Ilten et al., *An introduction to PYTHIA 8.2*, Comput. Phys. Commun. **191** (2015) 159 [`arXiv:1410.3012`].

[171] N. Kidonakis, *Two-loop soft anomalous dimensions for single top quark associated production with a W^- or H^-*, Phys. Rev. D **82** (2010) 054018 [`arXiv:1005.4451`].

[172] N. Kidonakis, *Top Quark Production*, in *Proceedings, Helmholtz International Summer School on Physics of Heavy Quarks and Hadrons (HQ 2013)*, pp. 139–168, DOI [`arXiv:1311.0283`].

[173] M. Aliev, H. Lacker, U. Langenfeld, S. Moch, P. Uwer and M. Wiedermann, *HATHOR – HAdronic Top and Heavy quarks crOss section calculatoR*, Comput. Phys. Commun. **182** (2011) 1034 [`arXiv:1007.1327`].

[174] P. Kant, O.M. Kind, T. Kintscher, T. Lohse, T. Martini, S. Mölbitz et al., *HatHor for single top-quark production: Updated predictions and uncertainty estimates for single top-quark production in hadronic collisions*, Comput. Phys. Commun. **191** (2015) 74 [`arXiv:1406.4403`].

[175] C. Anastasiou, L. Dixon, K. Melnikov and F. Petriello, *High-precision QCD at hadron colliders: Electroweak gauge boson rapidity distributions at next-to-next-to leading order*, Phys. Rev. D **69** (2004) 094008 [`arXiv:hep-ph/0312266`].

[176] J. Alwall, R. Frederix, S. Frixione, V. Hirschi, F. Maltoni, O. Mattelaer et al., *The automated computation of tree-level and next-to-leading order differential cross sections, and their matching to parton shower simulations*, JHEP **07** (2014) 079 [`arXiv:1405.0301`].

[177] LHC Higgs Cross Section Working Group collaboration, *Handbook of LHC Higgs Cross Sections: 4. Deciphering the Nature of the Higgs Sector*, `arXiv:1610.07922`.

[178] M. Beneke, M. Czakon, P. Falgari, A. Mitov and C. Schwinn, *Threshold expansion of the* $gg(q\bar{q}) \to Q\bar{Q} + X$ *cross section at* $\mathcal{O}(\alpha_s^4)$, *Phys. Lett. B* **690** (2010) 483 [`arXiv:0911.5166`].

[179] W. Beenakker, C. Borschensky, M. Krämer, A. Kulesza and E. Laenen, *NNLL-fast: predictions for coloured supersymmetric particle production at the LHC with threshold and Coulomb resummation*, *JHEP* **12** (2016) 133 [`arXiv:1607.07741`].

[180] W. Beenakker, M. Krämer, T. Plehn, M. Spira and P. Zerwas, *Stop production at hadron colliders*, *Nucl. Phys. B* **515** (1998) 3 [`arXiv:hep-ph/9710451`].

[181] W. Beenakker, S. Brensing, M. Krämer, A. Kulesza, E. Laenen and I. Niessen, *Supersymmetric top and bottom squark production at hadron colliders*, *JHEP* **08** (2010) 098 [`arXiv:1006.4771`].

[182] W. Beenakker, C. Borschensky, R. Heger, M. Krämer, A. Kulesza and E. Laenen, *NNLL resummation for stop pair-production at the LHC*, *JHEP* **05** (2016) 153 [`arXiv:1601.02954`].

[183] O. Mattelaer and E. Vryonidou, *Dark-matter production through loop-induced processes at the LHC: the s-channel mediator case*, *Eur. Phys. J. C* **75** (2015) 133.

[184] M. Backović, M. Krämer, F. Maltoni, A. Martini, K. Mawatari and M. Pellen, *Higher-order QCD predictions for dark matter production at the LHC in simplified models with s-channel mediators*, *Eur. Phys. J. C* **75** (2015) 482.

[185] ATLAS Collaboration, *The ATLAS Simulation Infrastructure*, *Eur. Phys. J. C* **70** (2010) 823 [`arXiv:1005.4568`].

[186] S. Agostinelli et al., *GEANT4 – a simulation toolkit*, *Nucl. Instrum. Meth. A* **506** (2003) 250.

[187] D.J. Lange, *The EvtGen particle decay simulation package*, *Nucl. Instrum. Meth. A* **462** (2001) 152.

[188] *ATLAS Pythia 8 tunes to 7 TeV data*, Tech. Rep. ATL-PHYS-PUB-2014-021, CERN, Geneva (2014).

[189] R.D. Ball, V. Bertone, S. Carrazza, C.S. Deans, L. Del Debbio, S. Forte et al., *Parton distributions with LHC data*, *Nuclear Physics B* **867** (2013) 244–289.

[190] T. Sjöstrand, S. Mrenna and P. Skands, *A brief introduction to PYTHIA 8.1*, *Comput. Phys. Commun.* **178** (2008) 852 [`arXiv:0710.3820`].

[191] ATLAS collaboration, *The Pythia 8 A3 tune description of ATLAS minimum bias and inelastic measurements incorporating the Donnachie-Landshoff diffractive model*, Tech. Rep. ATL-PHYS-PUB-2016-017, CERN, Geneva (2016).

[192] P. Artoisenet, R. Frederix, O. Mattelaer and R. Rietkerk, *Automatic spin-entangled decays of heavy resonances in Monte Carlo simulations*, *JHEP* **03** (2013) 015 [`arXiv:1212.3460`].

[193] J. Butterworth et al., *PDF4LHC recommendations for LHC Run II*, *J. Phys. G* **43** (2016) 023001 [`arXiv:1510.03865`].

[194] S. Frixione, E. Laenen, P. Motylinski, C. White and B.R. Webber, *Single-top hadroproduction in association with awboson*, *Journal of High Energy Physics* **2008** (2008) 029–029.

[195] ATLAS collaboration, *Studies on top-quark Monte Carlo modelling for Top2016*, Tech. Rep. ATL-PHYS-PUB-2016-020, CERN, Geneva (2016).

[196] S. Frixione, P. Nason and G. Ridolfi, *A Positive-weight next-to-leading-order Monte Carlo for heavy flavour hadroproduction*, *JHEP* **09** (2007) 126 [`arXiv:0707.3088`].

[197] H.B. Hartanto, B. Jäger, L. Reina and D. Wackeroth, *Higgs boson production in association with top quarks in the POWHEG BOX*, *Phys. Rev. D* **91** (2015) 094003 [`arXiv:1501.04498`].

[198] T. Sjöstrand, S. Ask, J.R. Christiansen, R. Corke, N. Desai, P. Ilten et al., *An introduction to PYTHIA 8.2*, *Comput. Phys. Commun.* **191** (2015) 159 [`arXiv:1410.3012`].

[199] The ATLAS Collaboration, *Performance of the missing transverse momentum triggers for the ATLAS detector during Run-2 data taking*, *Journal of High Energy Physics* **2020** (2020) .

[200] The ATLAS Collaboration, *Performance of electron and photon triggers in ATLAS during LHC Run 2*, *The European Physical Journal C* **80** (2020) .

[201] The ATLAS Collaboration, *Performance of the ATLAS muon triggers in Run 2*, *Journal of Instrumentation* **15** (2020) P09015–P09015.

[202] M. Cacciari, G.P. Salam and G. Soyez, *The catchment area of jets*, *JHEP* **2008** (2008) 005.

[203] F. Chollet et al., *Keras*, 2015.

[204] ATLAS Collaboration, *Performance of top-quark and W-boson tagging with ATLAS in Run 2 of the LHC*, *Eur. Phys. J. C* **79** (2019) 375 [`arXiv:1808.07858`].

[205] ATLAS collaboration, *Boosted hadronic vector boson and top quark tagging with ATLAS using Run 2 data*, Tech. Rep. ATL-PHYS-PUB-2020-017, CERN, Geneva (2020).

[206] A.M. Sirunyan, A. Tumasyan, W. Adam, F. Ambrogi, T. Bergauer, J. Brandstetter et al., *Searches for physics beyond the standard model with the M_{T2} variable in hadronic final states with and without disappearing tracks in proton–proton collisions at $\sqrt{s} = 13\,TeV$*, *The European Physical Journal C* **80** (2020) .

[207] M. Pinamonti et al., "TTbarNNLOReweighter." `https://gitlab.cern.ch/pinamont/TTbarNNLOReweighter`, Accessed: 2024-01-21.

[208] M. Czakon, D. Heymes, A. Mitov and et al., *Top-pair production at the LHC through NNLO QCD and NLO EW*, *Journal of High Energy Physics* **2017** (2017) 186.

[209] J. Roggel, *Search for vector-like partners of the top and bottom quarks with the ATLAS experiment*, Ph.D. thesis, Wuppertal U., 2022.

[210] G. Cowan, K. Cranmer, E. Gross and O. Vitells, *Asymptotic formulae for likelihood-based tests of new physics*, *Eur. Phys. J. C* **71** (2011) 1554 [`arXiv:1007.1727`].

[211] M. Baak et al., *HistFitter software framework for statistical data analysis*, `arXiv:1410.1280`.

[212] W. Verkerke and D.P. Kirkby, *The RooFit toolkit for data modeling*, *eConf* **C0303241** (2003) MOLT007 [`arXiv:physics/0306116`].

[213] L. Moneta et al., *The RooStats Project*, *PoS* **ACAT2010** (2010) 057 [`arXiv:1009.1003`].

[214] J. Neyman and E.S. Pearson, *On the Problem of the Most Efficient Tests of Statistical Hypotheses*, *Phil. Trans. Roy. Soc. Lond. A* **231** (1933) 289.

[215] S.S. Wilks, *The Large-Sample Distribution of the Likelihood Ratio for Testing Composite Hypotheses*, *The Annals of Mathematical Statistics* **9** (1938) 60–62.

[216] A.L. Read, *Presentation of search results: the CL_s technique*, *Journal of Physics G: Nuclear and Particle Physics* **28** (2002) 2693.

[217] The ATLAS Collaboration, *Reconstruction of primary vertices at the ATLAS experiment in Run 1 proton–proton collisions at the LHC*, *The European Physical Journal C* **77** (2017) .

[218] ATLAS Collaboration, "Multi-boson simulation for 13 TeV ATLAS analyses." ATL-PHYS-PUB-2016-002, 2016.

[219] ATLAS Collaboration, "Modelling of the $t\bar{t}H$ and $t\bar{t}V\,(V = W,Z)$ processes for $\sqrt{s} = 13$ TeV ATLAS analyses." ATL-PHYS-PUB-2016-005, 2016.

[220] S. Kallweit, J.M. Lindert, P. Maierhöfer, S. Pozzorini and M. Schönherr, *NLO electroweak automation and precise predictions for W+multijet production at the LHC*, 2015. `arXiv:1412.5157`.

[221] ATLAS Collaboration, "ATLAS simulation of boson plus jets processes in Run 2." ATL-PHYS-PUB-2017-006, 2017.

[222] E. Gross, *Practical Statistics for High Energy Physics*, *CERN Yellow Reports: School Proceedings* (2018) Vol 3 (2018): Proceedings of the 2017 European School of High.

[223] A.V. Manohar, *Effective Field Theories*, 1995. `arXiv:hep-ph/9508245`.

[224] A.V. Manohar, *Introduction to Effective Field Theories*, 2018. `arXiv:1804.05863`.

[225] I. Brivio and M. Trott, *The standard model as an effective field theory*, *Physics Reports* **793** (2019) 1.

[226] D. London and J. Matias, *B Flavor Anomalies: 2021 Theoretical Status Report*, *Annual Review of Nuclear and Particle Science* **72** (2022) 37.

[227] Y. Afik, S. Bar-Shalom, K. Pal, A. Soni and J. Wudka, *Multi-lepton probes of new physics and lepton-universality in top-quark interactions*, *Nuclear Physics B* **980** (2022) 115849.

[228] Y. Afik, S. Bar-Shalom, J. Cohen, A. Soni and J. Wudka, *High p_T correlated tests of lepton universality in lepton(s) + jet(s) processes; An EFT analysis*, *Phys. Lett. B* **811** (2020) 135908 [`arXiv:2005.06457`].

[229] Y. Afik, S. Bar-Shalom, J. Cohen and Y. Rozen, *Searching for New Physics with $b\bar{b}\ell^+\ell^-$ contact interactions*, *Phys. Lett. B* **807** (2020) 135541 [`arXiv:1912.00425`].

[230] The ATLAS Collaboration, *Differential cross-section measurements of the production of four charged leptons in association with two jets using the ATLAS detector*, *Journal of High Energy Physics* **2024** (2024) .

[231] E.d.S. Almeida, O.J.P. Éboli and M.C. Gonzalez-Garcia, *Unitarity constraints on anomalous quartic couplings*, *Phys. Rev. D* **101** (2020) 113003.

[232] ATLAS Collaboration, *Search for new non-resonant phenomena in high-mass dilepton final states with the ATLAS detector*, *JHEP* **11** (2020) 005 [`arXiv:2006.12946`].

[233] ATLAS Collaboration, *Search for new phenomena in final states with two leptons and one or no b-tagged jets at $\sqrt{s} = 13$ TeV using the ATLAS detector*, *Phys. Rev. Lett.* **127** (2021) 141801 [`arXiv:2105.13847`].

[234] ATLAS Collaboration, *Search for new phenomena in events with same-charge leptons and b-jets in pp collisions at $\sqrt{s} = 13$ TeV with the ATLAS detector*, *JHEP* **12** (2018) 039 [`arXiv:1807.11883`].

List of Figures

List of Tables

CHAPTER A

Event NN Studies

Studies were performed to see if it is beneficial to train networks for different kinds of signal processes. For instance, networks were trained separately for pseudoscalar DM models and scalar DM models and compared to a model trained on all DM models at once. To judge the performance across different mass points, the phase space is divided by on-shell and off-shell regions. It is further divided into low and high mediator mass in the on-shell region and low and high DM mass in the off-shell region as shown in Figure A.1. The ROC curves are then plotted for these sub-divisions to compare the different strategies. From Figure A.2 it is clear that the performance does not differ greatly between the two approaches. It is also concluded that the high (mediator/DM) mass models are easier to distinguish than the low (mediator/DM) mass DM models. A further configuration is tested, where the training dataset consists of only high mass models grouped together for pseudo and scalar DM processes as the signal target category. Similarly, two different models are trained with only low mass pseudoscalar mass points as signal yielding the ‘lowmassDMpseudo’ classifier and low mass scalar mass points as ‘lowmassDMscalar’ classifier. The bkg category for all these trainings remains the same and consists of all SM background processes. The evaluation of this approach is shown in Figure A.3 and the discrimination power does not significantly improve by training models on specific regions of phase space.

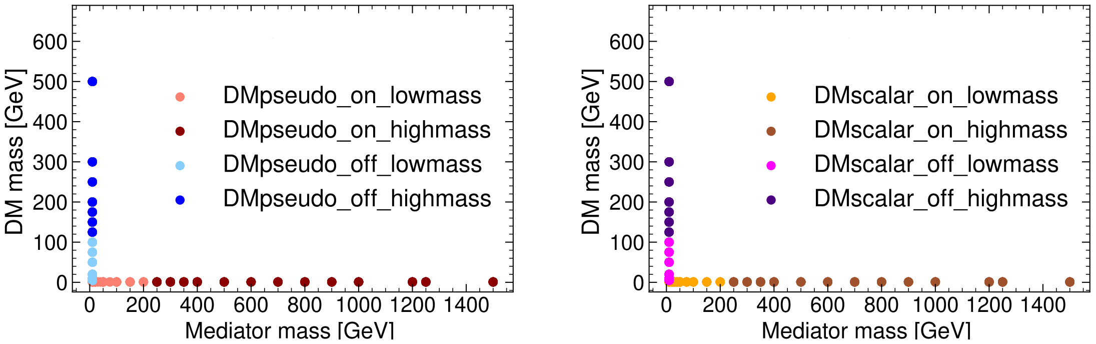

Figure A.1: Pseudoscalar and scalar DM mass phase space with the definition of the onshell-off-shell and lowmass -highmass categories.

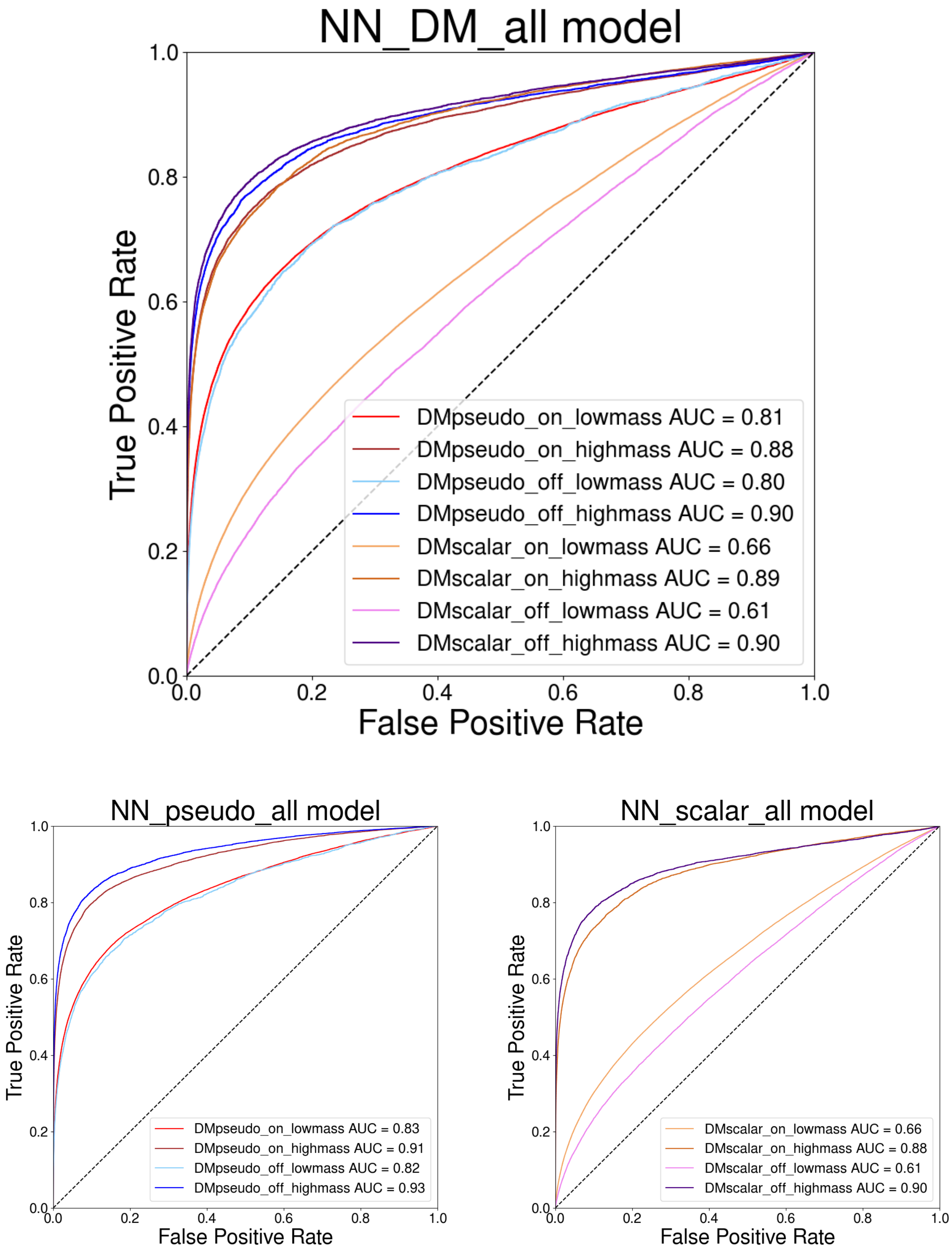

Figure A.2: ROC curves for three different training configurations of the DM classifier: "NN_DM_all" is trained to discriminate all DM signals from all SM processes. "NN_psuedo(scalar)_all" is trained to discriminate pseudoscalar(scalar) DM mediator models from all SM.

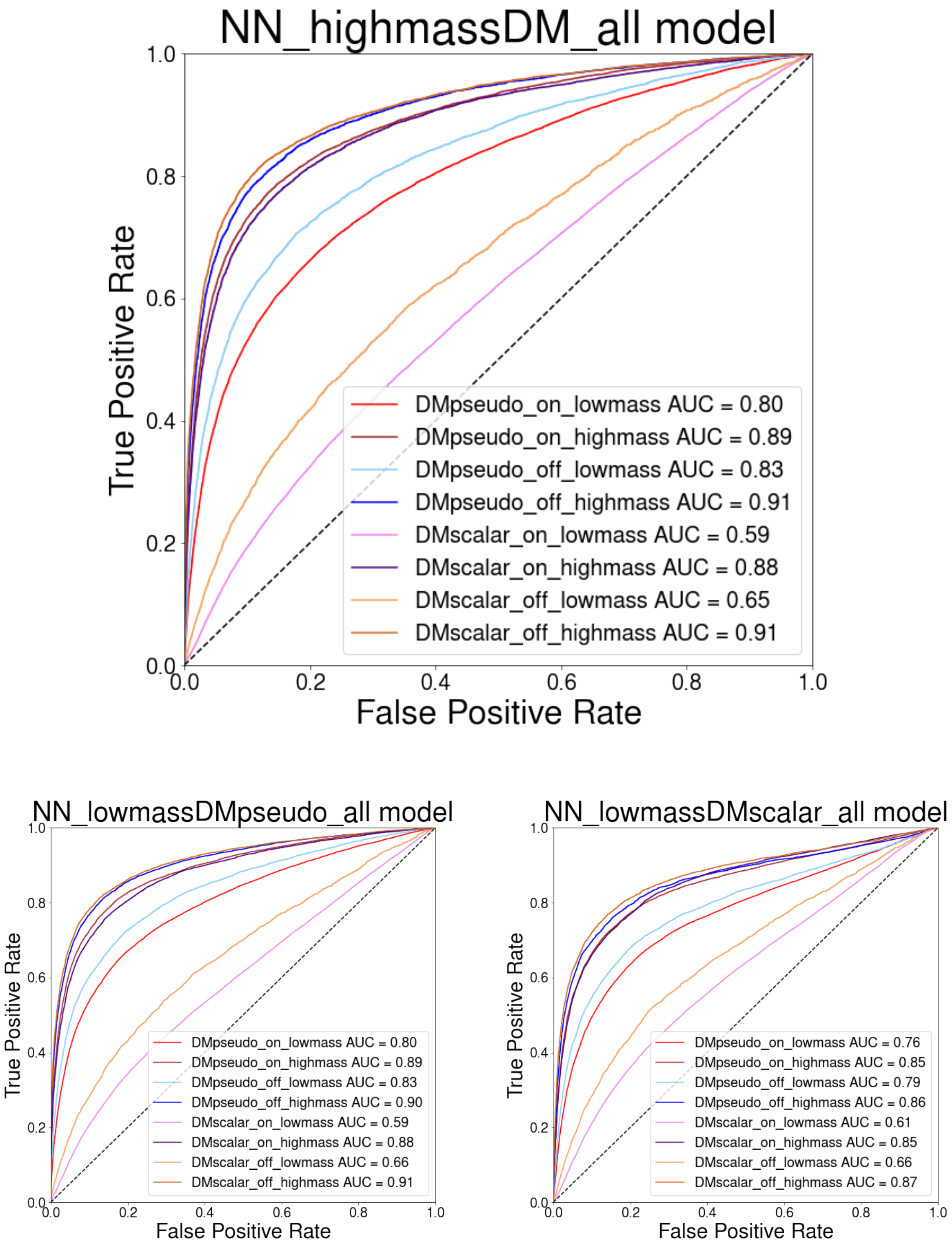

Figure A.3: ROC curves for even finer training configurations of the DM classifier. Pseudoscalar and scalar highmass models are grouped together and one classifier is trained. On the other hand, two different classifiers are trained for the lowmass models for scalar and pseudoscalar mediator models.

Acknowledgements

I would like to express my heartfelt gratitude to Silvan Fischbacher, my partner, for his unwavering emotional support throughout my PhD journey. During my move from the US to Germany, especially during the challenging times of the COVID-19 pandemic, he not only stood by me as my emotional anchor but helped me immensely to adapt to my new environment and culture. He is also a constant source of comfort, lifting my spirits and supporting me through the most demanding working days.

I would like to express my heartfelt gratitude to my family for their steady support. Despite the distance, their support from afar has been crucial. My sister Tania Gurdasani, in the US, and my parents Beena Gurdasani and Sunil Gurdasani, in Dubai, have been my pillars of strength. A special thank you goes to my sister and mother for diligently proofreading my thesis and offering invaluable feedback.

I am deeply grateful to Silvan's family, with special heartfelt mentions to Urs Fischbacher and Helene Arnet, for warmly welcoming me into their lives and making me feel like a part of their family. They have lined my time in Germany and Switzerland with joyful experiences.

I would like to express my heartfelt gratitude to Dr. Christian Weiser and Dr. Daniele Zanzi for their unwavering support and guidance throughout my education in particle physics. Working closely with Daniele was an enriching experience, with daily discussions and collaborative efforts that truly enhanced my understanding of the field. The writing of this thesis would have not been possible without the guidance of Dr. Christian Weiser.

I am honoured to be a part of the ATLAS SUSY community at CERN and highlight my thanks to Javier Montejo and Rosa Simoniello for their leadership during my time in the SUSY group. A special shout-out to Vangelis Kourlitis and Claudia Merlassino for their camaraderie and support. I would like to thank Luigi Longo for his support which technical aspects of the SUSY analysis. Additionally, I express my gratitude to the entire ATLAS community for their collective encouragement and inspiration. My time at CERN was full of valuable experiences, and during this time, I want to especially highlight my participation in ATLAS operations through the SCT community. It was a wonderful period where I had the chance to work hands-on with the great ATLAS detector.

I am deeply indebted to the Group of Prof. Karl Jakobs for offering me the invaluable opportunity to conduct my thesis within the group. Special mention goes to Chris Skorek, who assisted me in every possible way, especially with administration and emotional support to deal with the many immigration challenges further worsened by the COVID-19 pandemic. My PhD journey would not have been possible without the generous funding from the GRK

and BMBF. Additionally, I extend my gratitude to the computing resources of the Black Forest Grid (BFG) and the BFG administration team, as well as the computing resources at CERN, for making the technical possible.

I am grateful for the unwavering support of my friends in Freiburg, Ilia Kalaitzidou, Aranza Espinoza, and Charlotte Clossé. I cannot list the countless memories I have made with Ilia while enjoying many a drink, discussing life and physics. Aranza has truly shaped my time in Freiburg with her amazing personality. I am grateful to have shared so many milestones in both the PhD, personal life and my move to Germany with her. While my meeting with Charlotte is a story I will always cherish, my friendship with her has comprised of so many wonderful moments of growth, introspection and real fun! I cannot thank her enough for inviting me to a coffee on my first day in Freiburg and I definitely could not have imagined that she would be by my side as I printed out my final thesis.

At the beginning of my PhD, my days and weeks were filled with great memories shared with Krzysztof Bozek, Stephen Jiggins, and Benedict Winter. I want to thank them for making an extra effort to include me into the social aspects of the Jakobs group despite the challenges posed by the COVID-19 pandemic. I also extend this acknowledgement to those members of the group with whom I have been side-by-side throughout my PhD up till the very end - Ilia Kalaitzidou, Jose Pretel and Roman Küsters, who have now become lifelong friends. A special thank you to Roman for proof reading my thesis and providing me support during the last steps of the writing process. My PhD experience was further enriched when my friendship with Jose, that started in a German class, grew during our time attending the AEPSHEP school in Korea and continued through to us sharing our thesis writing time.

I fondly remember the plentiful beers and enriching discussions with other members of the Jakobs group, the GRK, and the physics institute, which added a sense of camaraderie and community to my PhD journey with special mentions to Alex Froch, Shalu Solomon, Prasham Jain and Naman Bhalla.

My stay at CERN would not have been the same without my swimming evenings and relaxing coffees with Leena Diehl and cheery moments with Francesco Carnevali. Thank you Cristiano Sebastiani for introducing me to many many cool Geneva hangouts and Juhee Song for exploring CERN and Geneva social life with me. Special mentions to Claudia Merlassino, Sara Alderweireldt, Luigi Longo and John Anders.

I am also grateful to my mentors in and around my career, including Valerie Lang and Eluned Smith, for their guidance and support. I would like to mention additionally my special cohort of PhD students with whom I was learning German and from whom I drew immense support. I also want to acknowledge the friendships I forged during the summer schools and conferences I participated in over the years. My roommates in Freiburg and Geneva, Jonna Müller, Jonna Gorges, and Kevin Leche, deserve special mention for enduring my periods of intense work and providing a supportive environment.

I would also like to express my heartfelt gratitude to the ETH cosmology research group, whom I got to know during my weekends in Zurich visiting my partner Silvan. Special mentions to Marta Spinelli, Bea Moser, Virginia Ajani, Arne Thomsen, Janis Fluri, and Alex Reeves, with whom I shared many evenings and weekends, navigating both the highs and lows of our academic experiences.

Finally, I want to acknowledge the Purdue CMS group as my intermediate step between Biophysics and Particle Physics. I also want to highlight the supportive Purdue PhD community, with special thanks to Bhagya Subrayan for being a constant ray of sunshine since I met her in 2018. I'm especially grateful to Horia Petrache, my first academic mentor during my Biophysics research journey who gave me the first nudge and opportunity to delve into physics research.

Freiburg, September 2024
Simran Gurdasani